STATISTICAL MECHANICAL THEORY OF STRUCTURE AND MISCIBILITY OF POLYMER NANOCOMPOSITES: EFFECTS OF DENSITY, FILLER SHAPE, AND CHEMICAL HETEROGENEITY

BY

LISA MICHELLE HALL

DISSERTATION

Submitted in partial fulfillment of the requirements
for the degree of Doctor of Philosophy in Chemical Engineering
in the Graduate College of the
University of Illinois at Urbana-Champaign, 2009

Urbana, Illinois

Doctoral Committee:

Professor Kenneth S. Schweizer, Chair
Professor Charles F. Zukoski
Professor Steve Granick
Assistant Professor Charles M. Schroeder

Abstract

Motivated by increasing interest in various types of nanoparticles or fillers added to polymers to enhance the material properties, the Polymer Reference Site Interaction Model (PRISM) theory is applied to study the structure and miscibility of polymer nanocomposites (PNCs). Spherical fillers are studied in homopolymers of varying density and interfacial interaction strengths, with specific favorable comparisons to experimental scattering results. Also discussed briefly are copolymers composed of two types of monomer which interact differently with the filler. The polymer induced depletion attraction is dominant and causes phase separation if interfacial attractions are weak. Complete miscibility can be achieved at moderate interfacial attraction strengths, due to a sterically stabilizing bound polymer layer. The bound layer remains with a strong interfacial attraction, but phase separation is induced by polymer bridging between nanoparticles. For copolymers, the bridging attraction is strongly affected by chemistry and monomer spatial arrangement (random versus alternating). The effect of nanoparticle dimensionality is explored by comparing rod, disk, and cube shaped fillers. Nanoparticle interactions on several length scales are relevant in the depletion regime. The bound polymer layer present in the miscible and bridging regimes damps out order on these length scales in favor of increased order on an averaged filler length scale. The effect of nanoparticle chemical heterogeneity was briefly explored by investigation of fillers composed of two tangentially connected spheres with different polymer interfacial attraction strengths or with an added inter-nanoparticle site-site attraction. Such heterogeneous diatomic fillers exhibited additional structural features and particle clustering compared to analogous homogeneous nanoparticles. Motivated by recent experimental interest in carbon nanotubes, thin rod particles were further investigated. Adding a strong rod-rod attraction relevant to nanotubes predictably

leads to a strongly attractive potential of mean force at contact, especially when there is little bound polymer. In the stabilized and bridging regimes, miscibility can persist until a stronger rod-rod attraction if it is of shorter spatial range than the polymer-rod interfacial attraction. An initial investigation of these attractive rods in a random copolymer revealed that replacing the homopolymer with copolymer can significantly reduce miscibility.

Acknowledgments

I am grateful for and have greatly benefited from the thoughtful instruction and council of my adviser, Prof. Ken Schweizer, throughout my graduate career. I also appreciated the many helpful discussions I have had with other members of the Schweizer group. I would not have been able to complete this project without the love and support of my family and friends, including Glenn and Lauren, and especially my husband Greg and our parents.

Table of Contents

Chapter 1

Introduction

1.1 Motivation and Goals

Nanoparticles are added to polymers to modify the material properties of the resulting polymer nanocomposites (PNCs). For example, nanoparticles have been shown to have interesting effects on the polymer glass transition[1–4] and mechanical properties.[5–14] The effects of the nanoparticle on the matrix persist for $\sim 3-30$ nm from the surface, resulting in a significant volume of interfacially modified polymer at a relatively low volume fraction of nanoscale fillers.[15]

Many types of nanoparticles and polymers are currently available, raising the possibility of tuning PNC properties for specific applications by varying, for example, polymer chemistry, filler shape and size, or polymer-filler interfacial attraction. In some systems, a significant shift in polymer properties near the nanoparticle surface can be measured.[10,11] Therefore, it is not surprising that changing the surface chemistry or grafting polymer to the particles can significantly affect the polymer-particle interaction and the bulk properties of the composite.[3,6,16]

A theoretical analysis of these systems could suggest design rules that guide the choice of polymer and particle shapes and chemistries to create novel PNCs with specific spatial structure and properties. To maximize the effect of the nanoparticles on the polymer matrix, good spatial dispersion is often desired.[15,17] To this end, an understanding of the conditions which allow particle miscibility in the polymer melt is crucial, and is a key purpose of this thesis. Description of the structure of the polymer around the particles is a first step as polymers can either mediate a contact depletion attraction, create a repulsive and stabilizing adsorbed layer, or "bridge" between particles resulting in formation of polymer-nanoparticle complexes or networks. Theoretical

structure and miscibility results for the fundamental system of hard spheres in a homopolymer melt provide the context for description of more complex types of PNCs and can be quantitatively compared with scattering experiments and simulations to evaluate the accuracy of the theory.

Nonspherical fillers are of increasing recent interest due to their potential to affect the polymer matrix on multiple length scales and at lower volume fractions than can be achieved with spherical fillers.[15] Experiments have especially focused on rod-like carbon nanotubes[16,18,19] and plate-like exfoliated clay particles.[20] Questions to be addressed by the study of aspherical fillers include: (i) how the various nanoparticle length scales and surface area-to-volume ratios affect the real and Fourier space statistical structure as quantified by pair correlation functions and structure factors, (ii) the influence of filler shape on the formation of stabilizing bound polymer layers, (iii) how many body effects at elevated nanoparticle volume fractions are influenced by filler shape and the spatial overlap of perturbed polymer layers, and (iv) how both entropically and enthalpically driven phase separation are modified by nanoparticle shape. Of special relevance to nanocomposites containing carbon nanotubes (CNTs) are the competing effects of filler-filler and polymer-CNT attraction strengths on PNC structure. Because CNTs experience a strong attraction of $\sim 0.5eV$ per nanometer of length, they tend to strongly aggregate and bundle, and much experimental effort has been devoted to improving their dispersion.[21] Therefore, a goal of theoretical work in this area is to determine which types of (potentially experimentally tunable) chemical interactions best promote miscibility of thin attractive rods in polymer melts.

Novel spherical and aspherical fillers include those which are "chemically heterogeneous", or composed of chemically different parts. For instance, nanocrystals of CdS have been grown on colloidal nanocrystals of Fe_3O_4 to create diatomic molecule like heterostructures of various shapes and sizes.[22,23] "Janus" particles can be created by chemically modifying only one hemisphere of a hard particle.[24] Such particles in a ho-

mopolymer melt have the potential to form clusters or micelles of controlled size and shape, with unknown but likely novel implications for the polymer structure and PNC properties. Another heterogeneous particle created recently consists of a gold nanorod with polymer tethers added to both ends, which changes the end-end interactions.[25] This system is similar to a triblock copolymer, suggesting that small clusters of rod ends may assemble to create a percolated rod network within the homopolymer matrix.

A chemically heterogeneous polymer, or copolymer, may also be used as the matrix material. The consequences of polymer heterogeneity on the adsorbed layer and polymer-mediated particle interactions may not always be intuitive. In recent experiments at Oak Ridge National Laboratory, surface modified carbon nanotubes were added to a melt of random copolymers composed of two monomer types, only one of which had a specific interaction with the nanotubes. Interestingly, an intermediate copolymer composition yielded decreased nanotube bundling relative to that of either homopolymer alone.[26] Therefore, a theoretical investigation of such systems might identify possible non-monotonic trends in miscibility as a function of copolymer architecture and chemistry.

1.2 Prior Work

Considerable theoretical[27–38] and simulation[39,40] work has been devoted to various colloid-polymer solutions, which provide a starting point for understanding the interactions of colloids in a dense polymer matrix. One of the basic effects of adding colloids to a polymer solution is that the existence of the impenetrable surface disrupts polymer packing, and thus theoretical studies of polymers near a flat surface[41–47] are useful in understanding polymer-mediated effective interparticle interactions. Scheutjens and Fleer have reported the effect of a polymer-wall attraction: with no favorable enthalpic interaction, the polymer maximizes its entropy by avoiding the constraint of the wall, causing depletion between parallel walls. However, a favorable enthalpic

interaction can overcome this entropic effect, causing the polymer to adsorb on the surface and either stabilize the surfaces from coming together or create polymer bridges between them.[46] This depletion, stabilization, and bridging behavior is paralleled in dense PNC melt systems but with distinctive (sometimes qualitative) differences due to the short density fluctuation correlation length, near incompressibility, and significant monomer scale order in a dense polymeric liquid.

Monte Carlo,[48–51] molecular dynamics,[52–57] and dissipative particle dynamics[58] simulation methods have also been applied to study dense PNCs. A few simulations have been performed on PNCs with aspherical particles, including Monte Carlo and molecular dynamics studies of platelets[59,60] and a molecular dynamics study elucidating the effect of shape by comparing systems with icosahedral, rod, and plate nanoparticles at the same volume fraction of 0.05.[61] The latter study considered nanoparticles composed of bonded sites of the same size as the polymer monomers, and a modest interfacial attraction was introduced. The rods and icosahedra were well dispersed, although sheets tended to aggregate in a parallel configuration with some intercalated polymer between them. The statistical ordering of polymers around the fillers is shape dependent, with an increasing number of particle-polymer contacts and polymer bridges as the nanoparticle shape changes from sheets to icosahedra to rods. The simulations also predict significant differences in viscosity and tensile strength of the composite depending on nanoparticle shape.[61] Overall, due to the complexity of PNCs and the importance of different length scales, simulations can be very expensive and difficult or impossible to equilibrate, especially at significant nanoparticle volume fractions and realistic filler sizes. Thus simulations must focus on relatively small particles, low nanoparticle volume fractions, short chains, lower than meltlike densities, and/or explore a very limited amount of parameter space.

Complementary theoretical work on PNCs was recently reviewed.[62] Several versions of density functional theory (DFT) have been extensively applied to dilute spherical

nanoparticles in a nonadsorbing concentrated polymer solution.[29,63–65] The polymer induces a depletion attraction which becomes deeper with an increasing polymer concentration or particle size. DFT also allows addition of a polymer-particle attraction, which mitigates depletion and can induce a small bridging attraction.[30] Self consistent mean field theory (SCMFT) calculations have found a depletion attraction between spheres in a concentrated nonadsorbing polymer solution, and adsorbing polymer can create an interparticle repulsion.[48,66–68]

Aspherical fillers have been the focus of only a few theoretical studies. Continuum percolation theory has been employed to study rod-like particles of variable flexibility with effective interactions chosen to mimic a polymer melt. The volume fraction of percolation is lowered by increasing the nanotube stickiness or increasing length polydispersity.[69] Percolation of nanotubes in semidilute polymer solutions has been investigated using SCMFT.[70] Rod miscibility depends on the detailed nature of polymer adsorption, and both depletion and polymer-induced bridging are predicted. Due to strong direct inter-rod attractions for nanotubes, dispersability is suggested to be achievable only kinetically via a repulsive barrier in the polymer-mediated potential of mean force (PMF). Polymer SCMFT has also been used to study parallel clay platelets dissolved in a polymer melt.[71] The platelets were predicted to not disperse ("exfoliate") unless the clay surface was mostly covered by grafted polymer and intercalants. However, SCMFT is highly coarse grained in the sense that it does not properly capture total density fluctuations and liquid state packing effects on the monomer length scale which are critical in concentrated solutions and melts.[72,73]

Much of the experimental and theoretical work involving chemically heterogeneous PNCs has focused on block copolymers. Chemically different blocks of a copolymer can microphase separate, and the filler may segregate into one of the microdomains. Thus the filler takes on microphase order, which can be different than that of the copolymer alone, producing rich and interesting phase behavior.[74] SCMFT and DFT,

as well as other theoretical methods, have been applied to such systems.[75,76] However, the microphase separation of copolymers is not a topic of this thesis. Thus, only copolymers whose monomers are chemically similar (which can not microphase separate in the dilute particle limit) except in their interaction with the nanoparticle are studied. This case has apparently not been studied in prior simulation or theoretical work.

Simulations, DFT, and SCMFT have only explored a small region of the possible phase space of polymer-filler mixtures, and have often focused on polymer solutions rather than the melt. They have never been used to determine phase diagrams. Liquid state theory can therefore advance the microscopic understanding of dense PNCs by calculation of detailed real and Fourier space structure and phase behavior for a large range of nanoparticle shapes, sizes, and chemical properties.

PRISM theory is a microscopic, statistical-mechanical approach developed to describe the structure and thermodynamics of polymers,[72,73,77] and is explained in Chapter 2. PRISM structure predictions for polymer melts[78,79] compare well with experiments and simulations.[80] PRISM theory has also been applied to the study of colloid-polymer solutions.[81–87] The predicted thermodynamic and phase behavior of these solutions compares well with experiments.[87–89] More recently, PRISM theory has been extended and applied to polymer nanocomposites.[90–100] Its predictions show good agreement with molecular dynamics simulations in the 1- and 2-particle limits,[95,96] and the effect of particles on the collective polymer structure appears similar to recent scattering experiments.[101] PRISM theory is an ideal choice for the study of PNC systems, as it is computationally inexpensive yet allows a good representation of the monomer scale liquid-like structure relevant to dense polymer nanocomposites. As described further in Chapter 2, PRISM theory can treat spherical and aspherical nanoparticles and chemically heterogeneous systems. Thus, the structure of the many types of polymer and particle PNCs of interest experimentally may be relatively quickly and efficiently investigated in both real and Fourier space, and calculations of phase diagrams are

possible.

1.3 Polymer Nanocomposite Structure

Several important length scales are involved in determining the structure of the model PNCs studied in this thesis. The polymer is modeled as a freely-jointed chain of elementary units, each of diameter d. The average global size is described by its radius of gyration R_g. The filler is composed of one or more tangentially connected sites of diameter D, typically of order or larger than the polymer R_g. Particles can experience order on the site diameter, total molecule size, and other intermediate length scales, depending on their shape. The dense polymer melt has liquid-like ordering on the scale of the monomer diameter which persists even at high volume fractions of particles, though adding particles quantitatively reduces monomer-scale order and can imprint D-scale order onto polymer correlations.[90,93] The monomer scale, instead of the R_g scale, is the most important length scale of ordering in the dense melt, and therefore the effects of polymer chain length on dense PNC structure are typically small. The specifics of how polymer organizes around the particle depend on these length scales as well as the polymer-particle interfacial attraction.[90,93] To maximize its entropy, the polymer should retain its random configuration and avoid the surface of the particle. The compromise between this effect and the added enthalpic interfacial cohesion plays a crucial role in determining the state of dispersion of particles. A basic understanding of filler organization begins with the potential of mean force (PMF) between 2 dilute fillers, shown in Figure 1.1. If the interfacial attraction is small, entropic considerations cause polymer to be depleted from the particle surface, resulting an attractive PMF at contact. At intermediate attraction strength, enthalpic considerations become more important and a layer of polymer adsorbs on the particle surface, thereby stabilizing the particles via a repulsive PMF. An even stronger attraction can induce a local minimum in the PMF corresponding to particle attraction via bridging, i.e. partial sharing of

bound polymer layer between two or more particles.

The effects of depletion, stabilization, and bridging are discussed in greater detail in Chapter 3, and phase diagrams are presented. Chapter 3 also explores the effect of nanoparticle shape by comparing the structure and miscibility of PNCs containing pseudo 1- 2- and 3- dimensional fillers. Chapter 4 presents a comparison of spherical particle results to small angle x-ray scattering experiments, including a discussion of the effects of chemical modification of interfacial cohesion and solvent dilution. Thin rodlike fillers with a variable rod-rod attraction, motivated by carbon nanotube composites, are examined in Chapter 5, which also includes discussion of rods in a random copolymer melt. Chapter 6 studies the effect of chemical heterogeneity. Heterogeneous polymer with spherical nanoparticles, as well as heterogeneous diatomic fillers in a homopolymer melt, are considered. Finally, Chapter 7 summarizes the results of this thesis and considers possible future directions.

1.4 Figures

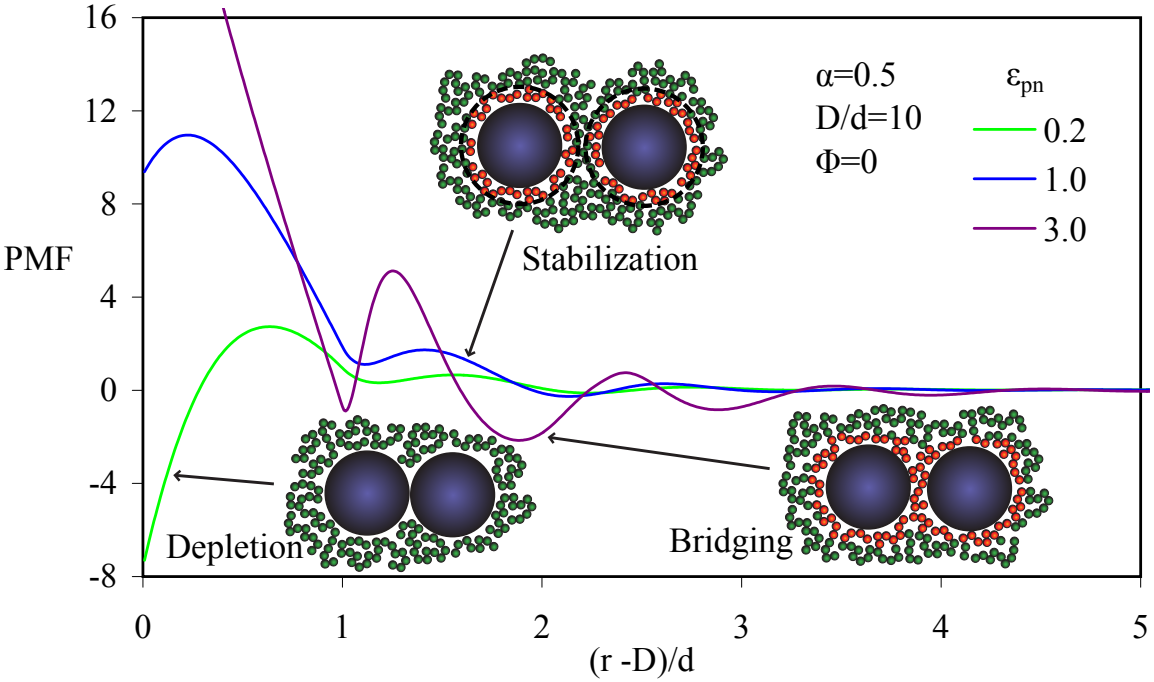

Figure 1.1: Potential of mean force (units of thermal energy, kT) between dilute hard spheres in a polymer melt as a function of surface-to-surface separation at a packing fraction of 0.4, including conceptual sketches of the behavior, where the polymer is a hard freely jointed chain of 100 monomers, the particle:monomer diameter ratio $D/d = 10$, and an added interfacial attraction is exponential with range $\alpha = 0.5d$ and variable strength ϵ_{pn} in units of kT.

Chapter 2

Theory and Methods

The Polymer Reference Interaction Site Model (PRISM) theory[72,73,77] is used to calculate the structure and thermodynamic properties of polymer nanocomposites. In this thesis, the polymer is a freely-jointed-chain consisting of N segments with diameter d and bond (persistence) length $l = 4d/3$, corresponding to a persistence length typical of many flexible polymers. The fillers are spheres of diameter D or other shapes made of tangentially-connected spherical sites of diameter D. Given the total system volume fraction η_t and filler volume fraction Φ, the site number density ρ of each species can be calculated: $\rho_p = 6(1-\Phi)\eta_t/(\pi d^3)$ and $\rho_n = 6\Phi\eta_t/(\pi D^3)$, where the subscript p denotes a polymer segment and n denotes a nanoparticle (or nanoparticle site, in the case of aspherical fillers). The monomer diameter d is chosen to be unity and all dimensions are in units of monomer diameter unless otherwise noted. All energies are in units of the thermal energy, kT.

2.1 PRISM Equations

PRISM theory is an extension of the Reference Interaction Site Model (RISM) theory for small rigid molecules to polymers in which end effects are ignored (monomers are assumed to all have identical interchain correlation functions).[79] Soon after it was developed, the theory was extended to polymer mixtures.[102] Each molecule is composed of sites, and given the site densities and intramolecular correlations, the theory is used to calculate the intermolecular pair correlations. The equations for polymer nanocomposites with spherical fillers, or with each filler site assumed to be equivalent, are essentially formally the same as those for a blend of two homopolymers. For PNCs with a chemically heterogeneous polymer or filler, two types of inequivalent sites exist

within a species, which increases the number of correlation functions and adds a nonzero intramolecular correlation for the heterogeneous species. The relative positions of sites within a molecule are described by the intramolecular probability distribution function ω. The matrix Ornstein-Zernike or Chandler-Andersen equation, Equation 2.1, relates the site-site intermolecular pair correlation function, g, to the site-site intermolecular direct correlation function C, and can be considered the definition of the direct correlation function.

$$H(k) = \Omega(k)C(k)[\Omega(k) + H(k)] \tag{2.1}$$

Here, $H(k)$ and $C(k)$ are matrices containing the Fourier transforms of $\rho_i\rho_j h_{ij}(r) = \rho_i\rho_j(g_{ij}(r) - 1)$ and $C_{ij}(r)$, respectively. $\Omega(k)$ is the matrix containing $\omega(k)$ weighted by the site densities such that $\Omega_{ij}(k \to 0) = \rho_i N_j$, where N_j is the number of sites of type j in the molecule. Based on the normalization of ω in Equation 2.17, as used for this thesis, for the diagonal terms $\Omega_{ii} = \rho_i\omega_i$ and for the cross terms $\Omega_{ij} = (\rho_i + \rho_j)\omega_{ij}$.

When the polymer and particle are both chemically homogeneous, there are only two types of sites; polymer (p) and nanoparticle (n). Equation 2.1 can then be written as 3 coupled equations, which in practice are rearranged to give $h_{ij}(k)$ as a function of $C_{ij}(k)$.

$$h_{pp}(k) = \frac{\omega_p(k)^2\left(C_{pp}(k) - \rho_n\omega_n(k)C_{pp}(k)C_{nn}(k) + \rho_n\omega_n(k)C_{pn}(k)^2\right)}{\lambda} \tag{2.2}$$

$$h_{nn}(k) = \frac{\omega_n(k)^2\left(C_{nn}(k) - \rho_p\omega_p(k)C_{pp}(k)C_{nn}(k) + \rho_p\omega_p(k)C_{pn}(k)^2\right)}{\lambda} \tag{2.3}$$

$$h_{pn}(k) = \frac{\omega_p(k)\omega_n(k)C_{pn}(k)}{\lambda} \tag{2.4}$$

$$\lambda = 1 - \rho_p\omega_p(k)C_{pp}(k) - \rho_n\omega_n(k)C_{nn}(k) + \rho_p\omega_p(k)\rho_n\omega_n(k)\left(C_{pp}(k)C_{nn}(k) - C_{pn}(k)^2\right) \tag{2.5}$$

In the case that either the polymer or particle is chemically hetergeneous, there are 3 types of sites, and Equation 2.1 can be written as 6 coupled integral equations, which

include the nonzero off-diagonal ω_{ij} describing the intramolecular correlation between the different sites of the heterogeneous species. For the copolymer cases considered, the polymer has two types of sites which have different interfacial attraction strengths with the nanoparticle, which is chemically homogeneous. For the heterogeneous diatomic filler considered, the two filler sites have either different interfacial attraction strengths with the homopolymer sites, or only one of the diatomic sites is attracted to its counterpart on the other diatomics.

Many thermodynamic properties can be calculated from $g(r)$. The potential of mean force (PMF or W_{nn}) quantifies the polymer-mediated interaction between two nanoparticles in real space and is given by:

$$W_{nn}(r) = -\ln(g_{nn}(r)) \tag{2.6}$$

The mixture bulk modulus, K_B is given at volume (V) and pressure (P) as:[90]

$$K_B = -V\left(\frac{\partial P}{\partial V}\right)_T = \frac{\rho_p}{N} - \rho_p^2 C_{pp}(k \to 0) + \frac{\rho_n}{N_n} - \rho_n^2 C_{nn}(k \to 0) - 2\rho_p \rho_n C_{pn}(k \to 0) \tag{2.7}$$

The Fourier-space structure factors S_{pp}, S_{nn}, and S_{pn} are:

$$S'(k) = \Omega(k) + H(k) = (I - \Omega(k)C(k))^{-1}\Omega(k) \tag{2.8}$$

where I is the identity matrix and S' is the unnormalized version of S: $S'_{ij} = S_{ij}\sqrt{\rho_i \rho_j}$. For nonspherical fillers, a representation of collective nanoparticle structure can be made in a "spherical particle" spirit which removes much of the differences between shapes by computing the ratio $S_{nn}(k)/\omega_n(k)$, which equals unity in the dilute limit. This approach is commonly adopted by experimentalists, and it also theoretically ap-

proximates the nanoparticle center-of-mass (CM) structure factor:[103,104]

$$S_{CM}(k) = \frac{S_{nn}(k)}{\omega_n(k)} \tag{2.9}$$

In the idealized incompressible random phase approximation (IRPA)[105] potentially relevant at relatively low wavevectors, the three partial structure factors are equivalent after scaling by a constant,[77]

$$K_{pp}S'_{pp} = K_{nn}S'_{nn} = -K_{pn}S'_{pn} \tag{2.10}$$

where $K_{ij} = \nu_i\nu_j/(\eta_t\sqrt{\nu_p\nu_n})$ and ν_i is the site volume of species i. The total structure factor is

$$S_{tot} = K_{pp}S'_{pp} + K_{nn}S'_{nn} - 2K_{pn}S'_{pn} \tag{2.11}$$

which is zero by definition of the IRPA.

In the two particle limit (when $\Phi \to 0$), the second virial coefficient, B_2, is calculated from the PMF and is usually normalized by 4 times the filler volume (the limit for hard spheres in a vacuum, $B_{2,HS}$),

$$\overline{B_2} = \frac{B_2}{B_{2,HS}} = \frac{-2\pi\int_0^\infty (g_{nn}(r)-1)\, r^2 dr}{4N_n\pi D^3/6} = \frac{-3h_{nn}(k\to 0)}{4N_n\pi D^3} \tag{2.12}$$

where N_n is the number of filler sites. This normalization was used for spheres and the relatively small shapes studied, but in the study of long rods, B_2 was instead normalized by the B_2 calculated for hard rods in a vacuum using the HNC closure, as motivated further in Chapter 5. A lowest order virial analysis[92] yields the following criterion for spinodal phase separation ($1/S_{ij}(k=0) = 0$):

$$1 - \rho_n\rho_p S_{pp}(k=0;\rho_n\to 0)\left(\frac{\partial C_{pp}}{\partial \rho_n}\right)_{\rho_n\to 0} + \frac{2\rho_n}{N_n}B_2 = 0 \tag{2.13}$$

Neglecting the interfacial polymer-filler contribution (second term in Equation 2.13) results in a simple criterion for phase separation at the volume fraction Φ_s:[92]

$$\Phi_s = -\left(8\overline{B_2}\eta_t\right)^{-1} \tag{2.14}$$

For spherical fillers it has been shown that the full spinodal calculation at finite volume fractions yields important differences from the simple virial analysis, but Equation 2.14 is qualitatively accurate at low nanoparticle volume fractions as intuitively expected.[98] Therefore, we expect that a negative $\overline{B_2}$ is a reliable indicator of impending phase separation at low volume fractions, while a positive $\overline{B_2}$ correlates with stability and the homogeneous phase.

2.2 Closure Relations

Approximate closures relate the functions $h_{ij}(r)$, $C_{ij}(r)$, and the site-site potential functions, $U_{ij}(r)$, and render the PRISM theory mathematically solvable. Prior work has compared molecular dynamics simulations and PRISM theory in the 1 and 2 particle limits[90,96] and showed good agreement based on the Percus-Yevick (PY) closure, Equation 2.15, for polymer-polymer and polymer-nanoparticle interactions, and the hypernetted chain closure, Equation 2.16, for nanoparticle-nanoparticle interactions.

$$C(r) = (e^{-U(r)} - 1)(1 + h(r) - C(r)) = (e^{-U(r)} - 1)(1 + \gamma(r)) \tag{2.15}$$

$$C(r) = e^{(h(r)-C(r)-U(r))} - 1 - h(r) + C(r) = e^{(\gamma(r)-U(r))} - 1 - \gamma(r) \tag{2.16}$$

Inside the hard core, $U_{ij}(r) = \infty$, so both closures reduce to the exact result: $h(r) = -1$, or $g(r) = 0$. For the numerical solution of the PRISM equations, each $C_{ij}(r)$ is written as a function of $\gamma_{ij}(r) \equiv h_{ij}(r) - C_{ij}(r)$.

2.3 Intramolecular Correlation Functions

The shape of each rigid or statistically averaged molecule is described by its intramolecular correlation function, $\omega_{ij}(r)$,

$$\omega_{ij}(r) = \frac{1}{N_{norm}} \sum_{\alpha,\gamma=1}^{N} \omega_{\alpha\gamma}(r) \tag{2.17}$$

where $\omega_{\alpha\gamma}(r)$ is a normalized probability density of finding sites γ of type i and α of type j a distance r apart on the same molecule, and N_{norm} is a normalization factor equal to N_i for $i = j$ and $N_i + N_j$ for $i \neq j$. A chemically heterogeneous species is described by 3 intramolecular correlation functions: one for each type of site and a cross term which describes how the two types of sites are connected.

For a homogeneous freely-jointed-chain polymer, the Fourier transform of $\omega(r)$ is:[79]

$$\omega_{pp}(k) = \left(1 - \frac{\sin(kl)}{kl}\right)^{-2} \left(1 - \left(\frac{\sin(kl)}{kl}\right)^{2} - \frac{2\sin(kl)}{N_p kl} - \frac{2}{N_p}\left(\frac{\sin(kl)}{kl}\right)^{N_p+1}\right) \tag{2.18}$$

where l is the distance between adjacent sites. Possible nonideal filler-induced conformational changes are ignored, and have been argued previously to be perturbative.[73,80] A recent fully self consistent[73] implementation of PRISM theory for a spherical nanoparticle mixture supports the latter statement given changes of polymer radius of gyration of $\sim 10\%$ are found at filler volume fractions of $\sim 20\%$.[106] The degree of polymerization, N_p, is 100 for the bulk of this thesis, and it is shown that changing N_p has only a small effect on PNC structure.

The three site-site $\omega(k)$ functions for an AB block copolymer with a variable probablility of A-A and B-B block connectivity (versus A-B block connectivity) along the chain were reported by Sung and Yethiraj.[107] Here only the case of single monomer "blocks" is explored, though the "monomer correlation strength" λ is varied. This quantity is defined by $\lambda \equiv p_{AA} + p_{BB} - 1$, where p_{ij} is the probablility that a monomer

of type i is followed by one of type j. Three cases are investigated in this thesis; the alternating copolymer ($\lambda = -1$), the random copolymer ($\lambda = 0$), and the polymer blend limit ($\lambda \to 1$). The corresponding $\omega_{ij}(k)$ for an ideal FJC with A and B monomers are:

$$\omega_{ii}(k) = \frac{1}{N_i} N_{tot} f_i + \frac{2}{N_i} \sum_{\tau=1}^{N_{tot}+1} (N_{tot} - \tau) \left(f_i^2 + f_i \left(1 - f_i\right) \lambda^\tau \right) \left(\frac{sin\left(kl\right)}{kl} \right)^\tau \tag{2.19}$$

$$\omega_{AB}(k) = \frac{2}{N_{tot}} \sum_{\tau=1}^{N_{tot}+1} (N_{tot} - \tau) f_A f_B (1 - \lambda^\tau) \left(\frac{sin(kl)}{kl} \right)^\tau \tag{2.20}$$

where N_i is average number of i monomers in a chain, N_{tot} is the total number of monomers in a chain, and f_i is the fraction of i monomers.

For rigid molecules, $\omega_{ij}(k)$ is easy to calculate from Equation 2.17 by counting how many sites (delta functions in real space) the average site would see at a distance x from itself. The delta functions in real space are equal to $\sin(kx)/(kx)$ in k space. For a sphere (a delta function at the origin in r space), $\omega_{nn}(k) = 1$.

The 1, 2, and 3-dimensional shapes considered are each composed of 8 sites, where the sites are length L from adjacent bonded sites. The 1-dimensional shape is a rigid rod, the 2-dimensional shape is a disk composed of a square of sites plus one site nested in each of its sides, and the sites of the 3-dimensional shape are at the corners of a cube. The intramolecular structure factors are:

8-site rod:

$$\omega_{nn}(k) = 1 + \frac{7}{4}\frac{\sin\left(kL\right)}{kL} + \frac{3}{2}\frac{\sin\left(2kL\right)}{2kL} + \frac{5}{4}\frac{\sin\left(3kL\right)}{3kL} + \frac{\sin\left(4kL\right)}{4kL} + \frac{3}{4}\frac{\sin\left(5kL\right)}{5kL} + \frac{1}{2}\frac{\sin\left(6kL\right)}{6kL} + \frac{1}{4}\frac{\sin\left(7kL\right)}{7kL} \tag{2.21}$$

8-site disk:

$$\omega_{nn}(k) = 1 + 3\frac{\sin(kL)}{kL} + \frac{1}{2}\frac{\sin\left(\sqrt{2}kL\right)}{\sqrt{2}kL} + 3\frac{\sin\left(2kL\sin\left(5\pi/12\right)\right)}{2kL\sin\left(5\pi/12\right)} + \frac{1}{2}\frac{\sin\left(kL\left(1+\sqrt{3}\right)\right)}{kL\left(1+\sqrt{3}\right)} \tag{2.22}$$

8-site cube:

$$\omega_{nn}(k) = 1 + 3\frac{\sin(kL)}{kL} + 3\frac{\sin\left(\sqrt{2}kL\right)}{\sqrt{2}kL} + \frac{\sin\left(\sqrt{3}kL\right)}{\sqrt{3}kL} \tag{2.23}$$

A rod of N_n sites is described by:

$$\omega_{nn}(k) = \frac{1}{N_n} + \frac{2}{N_n}\sum_{\tau=1}^{N_n}\left(N_n - \tau\right)\frac{\sin(\tau kL)}{\tau kL} \tag{2.24}$$

For heterogeneous AB diatomic molecules, each site is simply a sphere, so $\omega_{AA} = \omega_{BB} = 1$, but the connectivity between the sites is:

$$\omega_{AB}(k) = \frac{\sin(kL)}{kL} \tag{2.25}$$

In this work, the bond length L for filler shapes is always equal to the site diameter D.

2.4 Site-Site Potential Functions

Intermolecular interactions are given by pair decomposable site-site potentials $U_{ij}(r)$. Monomer-monomer interactions are hard core, and monomer-nanoparticle interactions are hard core with an exponential attraction. Particle-particle interactions are hard core with an exponential attraction added for some systems.

$$U_{pp}(r) = \begin{array}{ll} \infty & , \ r < d \\ 0 & , \ r \geq d \end{array} \tag{2.26}$$

$$U_{nn}(r) = \begin{cases} \infty & , \ r < D \\ -\epsilon_{nn} e^{-(r-D)/\alpha_{nn}} & , \ r \geq D \end{cases} \tag{2.27}$$

$$U_{pn}(r) = \begin{cases} \infty & , \ r < r_c \\ -\epsilon_{pn} e^{-(r-r_c)/\alpha_{pn}} & , \ r \geq r_c \end{cases} \tag{2.28}$$

where $r_c = (d + D)/2$ is the monomer-nanoparticle distance of closest approach (contact). For spherical fillers, $D/d = 5$, 10, and 15 are studied, while the diatomic molecule site size is $D/d = 5$, and other aspherical shapes were composed of smaller sites of $D/d = 2$. The parameter ϵ is the strength, and α is the range, of the exponential site-site attractive potential. For heterogeneous species, the forms of the potentials are the same but the strength or range can be different for different sites. The shape of the exponential attraction is similar to the attraction calculated by Henderson and coworkers between a Lennard-Jones particle and a colloid represented by a continuum of Lennard-Jones particles.[90,91,108] The chemistry of the model enters via the adjustable ϵ and α. Because the polymer interactions are hard core, ϵ_{pn} represents the net enthalpic gain of transfering a monomer from the pure melt to contact with the particle, including any possible enthalpic loss of favorable polymer-polymer contacts. This quantity is not generally directly measurable in experiments, and in this thesis ϵ_{pn} is varied from small fractions of kT to multiple kT. It seems sensible the spatial range of the attraction, α_{pn}, is somewhat smaller than, or of the same size as, the monomer diameter (which in real units is of the order of a nanometer).[109] The shortest range studied, $\alpha_{pn} = 0.25$, mimics a specific attraction such as hydrogen bonding or charge transfer, while $\alpha_{pn} = 0.5$ or 1 are more relevant to a van der Walls attraction.[91]

2.5 Polymer and Filler Packing Fraction

The simple model of a constant total particle plus polymer packing fraction of $\eta_t = 0.4$, which mimics a dense polymer melt, is used in the majority of this thesis. Basic

results for spherical particles under this assumption are presented in Chapter 3. In Chapter 4, the experimental comparison for large ($D/d = 10$) spherical fillers shows that adjusting η_t as nanoparticles are added to mimic equation-of-state effects operative a constant pressure (as fully described in Chapter 4) results in significantly better quantitative agreement with experimental scattering data.[99] However, in the case of nonspherical fillers, their more complex geometry renders the proper method of η_t adjustment unclear. Furthermore, for the comparitive study of rods, disks, and cubes, and the study of longer rods, the polymer and nanoparticle site size disparity is small ($D/d = 2$), so the effect of adjusting packing fraction will be small. Moreover, very large nanoparticle packing fractions are not relevant for most PNCs based on nonspherical fillers, and at small Φ again the total packing fraction adjustment has little effect. The high aspect ratio nanoparticle Φ is also kept low to avoid any discussion of the isotropic-nematic phase transition, which could occur at high rod or disk packing fractions. Hence, $\eta_t = 0.4$ is fixed for aspherical particle systems. For rods, disks, and cubes, calculations are presented only up to $\eta_n = 0.4\Phi = 0.12$. The study of long rods focuses on the dilute rod limit. The study of heterogeneous diatomic fillers, however, does consider a somewhat larger site size of $D/d = 5$, and investigates the entire volume fraction range from dilute particle to dilute polymer at constant $\eta_t = 0.4$.

2.6 Computational Approach

2.6.1 Iterative Solution Methods

The PRISM equations are solved iteratively starting with a guess of $\gamma_{pp,m}(r)$, $\gamma_{nn,m}(r)$, and $\gamma_{pn,m}(r)$, where m denotes the number of the current iteration and $\gamma_{ij}(r) \equiv h_{ij}(r) - C_{ij}(r)$. If an initial guess from a similar previously solved system is not available, the zero vector is used. This guess is substituted into the closures, Equations 2.15 and 2.16, (since the potential is known, the right hand side of these equations is a function of only $\gamma = h - C$) to obtain $C_{ij,m,new}(r)$, which is converted to k space by a fast Fourier

transform (FFT). The $C_{ij,m,new}(k)$ can then be substituted into the PRISM equations, Equations 2.2, 2.3, and 2.4 or their analogs for heterogeneous systems ($\omega(k)$ and ρ for all species are known), yielding $h_{ij,m,new}(k)$. The Fourier transform is linear, so $\gamma_{ij,m,new}(k) = h_{ij,m,new}(k) - C_{ij,m,new}(k)$. The FFT is used to convert the new γ to r space, and it is compared to the γ guess–which, if they are the same within some tolerance, is said to be converged. Otherwise, the results are used to choose the next guess, $\gamma_{ij,m+1}$, and the procedure is repeated. The choice of this next γ guess depends on the iterative method used.

The Picard iterative method is easy to implement: the new γ found is used as the next γ guess; however, this method must be modified using both the old and new guesses and a mixing parameter, x, to obtain convergence for all but the simplest systems:

$$\gamma_{ij,m+1} = (1 - x)\gamma_{ij,m} + x\gamma_{ij,m,new} \tag{2.29}$$

For some systems, such as those at high volume fractions or near phase separation, the mixing parameter must be very small to obtain convergence; in this case, the γ changes little during each iteration and many iterations are required, which can result in extremely slow convergence and long computation times.

Another common way to numerically solve coupled nonlinear equations is Newton's method, but since each function is represented by many points, this requires calculation of huge matrices. The size of the matrices can be reduced by instead representing $\gamma_{ij}(r)$ as a sum of basis functions with variable coefficients, so that the equations are simplified and the iterative method must solve for only the coefficients. Wavelets are an effective choice of basis set because they are localized in both r and k space.[110] Even if basis functions are not used, special mathematical tricks and approximations allow the efficient use of modified Newton's methods for a large number of points.[111] These methods can be quite complex, but publically available programs such as KINSol[112] include the necessary mathematical and computing tricks to use a modified Newton's

iteration for a large number of points.

In this work, functions are described by a discrete number of points (16384 or more) and the serial version of KINSol is used to solve the PRISM equations. The KINSol program is designed to use an inexact Newton's method to solve an equation $F(y_m) = E_m$, where y_m is the m^{th} guess of the solution vector and E_m is the error vector. When E_m equals the zero vector within some tolerance, the system is considered converged. The KINSol program requires only y_0 and the ability to call $F(y_m)$ to obtain E_m; details of the method can be found in the files which accompany the KINSol program and in a recent paper describing this software.[112] In order to adapt the present system to KINSol's expectations, the vectors $\gamma_{pp,m}(r)$, $\gamma_{nn,m}(r)$, and $\gamma_{pn,m}(r)$ (or all 6 site-site γ vectors in the heterogeneous polymer or particle case) are placed end-to-end to make the one vector y_m. Therefore, $F(y_m) = E_m = y_{m,new} - y_m$, where $y_{m,new}$ is $\gamma_{pp,m,new}$, $\gamma_{nn,m,new}$, and $\gamma_{pn,m,new}$, calculated as described above and placed end-to-end. Using KINSol's inexact Newton's method has proven much faster than the Picard iterative method, and has rendered possible the study of systems and scientific questions which are intractable using the Picard method.

Unless otherwise noted, r space functions were represented by points spaced at intervals of $dr = 0.02d$, and results were converged within a maximum tolerance of 10^{-10} on the largest point value of the error E_m. Spinodal phase separation is reported where non-convergence was obtained using the prior solution as a guess while incrementing in ϵ_{pn} at $+/-0.0001$, if this value coincided closely with the extrapolation of $1/S_{nn}(k = 0)$ and $1/S_{pp}(k = 0)$ to zero based on the last converged results. Some of the systems may have been able to be converged slightly further if even smaller increments had been attempted. Specifics of the convergence method such as the size of the Krylov space (typically 40) or use of the convergence method "Linesearch" instead of "Inexact Newton" in the KINSol program,[112] as well as how long the program was allowed to run to find a solution, were varied using discretion to speed up some of the calculations

while making reasonably sure that non-convergence was only declared for those systems which could not have been converged even if these parameters were changed. Typically, the "Inexact Newton" method was used with a maximum number of iterations of 500. The change from convergence to non-convergence generally appeared rapidly and was easy to identify: either the error E_m increased to a huge value, or after a period of time during which nearby systems would have converged, the magnitude of the current error E_m was oscillating and no longer decreasing steadily.

2.6.2 Multiple Solutions

None of the iterative numerical methods guarantee a solution, nor that the solution found is unique. Some systems converge to a solution much more easily than others; using a γ guess of the zero vector often works at moderate interfacial attraction values near $\Phi = 0$. Otherwise, a γ from a previously converged system at a slightly different Φ or ϵ_{pn} is used as the guess. Some systems do not converge even if a γ guess of a very similar system is used; as non-convergence is approached in Φ or ϵ_{pn}, usually the $k = 0$ value of the structure factors $S_{pp}(k)$ and $S_{nn}(k)$ begins to increase sharply. This is a sign that the mixture is nearing phase separation, and as the equations are not physically applicable in the phase-separated regime, it is assumed that, as Φ or ϵ_{pn} is changed in small increments, the last system that can be converged is near phase separation.

Sometimes a system nearing phase separation converges on a "solution" which gives structure factors $S_{pp}(k)$ and/or $S_{nn}(k)$ that are negative at low k. These results are clearly unphysical, and are not reported here. However, occasionally the same system will converge to a physical result if a better guess for γ is used (for example, if the γ from a previous Φ is used but Φ is increased in smaller increments). In some cases, two solutions can be converged for the same system which have relatively similar correlation functions in real space, but one of the solutions has a long range tail in $g_{nn}(r)$ which can

be is much longer range than the filler diameter even in the dilute filler limit; therefore, this solution is discarded on physical grounds. The difference of this system from the true physical solution is most readily seen in $C_{nn}(k)$ at low wavevectors, where a peak at $k = 0$ and following oscillations are seen before both solutions are identical at large k. For spherical fillers, the alternate solution seems to only be found with the solution methods used here if the mixture is very near depletion (low ϵ_{pn}) phase separation, but for aspherical fillers the two solutions can be found more easily. Generally, the solution with the extra peak in $C_{nn}(k)$ has a large negative $\overline{B_2}$ which increases to meet that of the other solution at depletion or bridging "phase separation", after which no solution can be found. Mathematically, it is likely that these two solution branches meet at a square root branch point which is not literally the spinodal boundary because $S_{nn}(0)$ remains finite. A detailed analysis proved this point for a one component system with the HNC closure and Lennard-Jones potential,[113,114] but the extension of such analysis to the multicomponent, mixed closure system used for PNCs is an unsolved problem which is not attempted in this thesis. Whether or not it is possible for the theory to predict that all $S_{ij}(k \to 0)$ actually diverge, as nonconvergence is approached for most systems, a large zero wavevector peak appears. As the theory applies only to homogeneous systems, the lack of an available solution could be construed to imply that a heterogeneous, phase separated system exists instead. The quantities $1/S_{ij}(k \to 0)$ of the last few converged data points (incrementing by small changes in ϵ_{pn} or Φ) can be extrapolated to zero to predict spinodal phase separation, as is done experimentally with small angle scattering data, and the result of such an extrapolation is generally similar to the last converged data; we discuss spinodal results only in such cases.

Chapter 3

Spherical Particle Miscibility and Fundamental Effects of Shape

A key question in the field of polymer nanocomposites is how to ensure that the polymer and nanoparticle will mix.[17,21] Good filler dispersion eases processing and is widely believed to result in optimal property enhancement. Related questions include how the polymer-mediated filler interactions change with particle chemistry and volume fraction throughout the miscibility window, and how phase separation and structure vary with filler shape. In this chapter, the miscibility and structure of PNCs with spherical nanoparticles and with pseudo 1- 2- and 3-dimensional fillers is investigated.

PRISM theory describes only equilibrium homogeneous systems. However, the limit of spinodal phase separation can be found by observance of non-convergence of the PRISM equations combined with an increasing $S_{nn}(0)$ and $S_{pp}(0)$, the inverse of which can be extrapolated to zero (the condition for spinodal phase separation) to estimate the location of the phase boundary. A phase diagram can then be plotted showing where immiscibility occurs. Clearly, some infinitesimal amount of either component should be able to mix, so the system is miscible as $\Phi \to 0$ and as $\Phi \to 1$. However, interesting effects of nanoparticles are observed even at low volume fractions, and nanoparticles are usually considered simply as minority component additives to the polymer, so experimental studies typically focus on relatively low volume fractions of particles of 0.3 or less.[1–9,17,101] Novel fillers such as carbon nanotubes are expensive and can have drastic effects at low volume fractions, so are especially likely to be used at low volume fractions. Therefore the focus of the aspherical work in this thesis is relatively low Φ. Spherical nanoparticle calculations, however, were performed for the entire range from nearly pure polymer to nearly pure hard spheres. The latter limit is of interest in colloid science as it corresponds to dense particle suspensions with dilute polymer additives. It is also directly relevant to the recent experimental studies of

the silica-polyethylene oxide and silica-polytetrahydrofuran systems by Anderson and Zukoski, as discussed in the subsequent chapter. In this chapter, the spinodal phase diagram is presented for spherical particles over the entire volume fraction range and, to explore the effects of filler shape, for rod, disk, and cube shaped particles at volume fractions up to 0.3. The degree of polymerization $N = 100$ and the total system packing fraction $\eta_t = 0.4$ is constant at all particle volume fractions. Investigation of real and Fourier space correlations for each of these systems reveals the composite structure in the depletion, sterically stabilized, and polymer bridging regimes.

The spherical particle calculations in this chapter were performed before all other results in this thesis, and slightly different numerical parameters were used than those reported in Chapter 2. For these spherical particle results, r space functions were represented by 131072 points spaced at intervals of $dr = 0.001d$, and results at $D/d = 5$ and 10 were converged within an L^2 tolerance of 10^{-10} (the L^2 function norm of the error E_m described in Chapter 2 is less than 10^{-10}). However, many $D/d = 15$ systems would not reach this tolerance, so the slightly higher tolerance of 10^{-9} was used for all $D/d = 15$ results. The phase boundaries reported for the spherical particles generally refer to the last Φ which could be converged when the increment in Φ was 1 in the the fourth significant digit–for example, if in an increasing Φ trial the last Φ converged is reported to be 0.01234, this implies the value 0.01235 was attempted but did not converge to a meaningful result. Because $\Phi = 1$ is the highest value possible, leading 9's after the decimal point were not counted as significant figures. For some spherical particle data, as for all spinodal data for nonspherical particles, ϵ_{pn} was incremented at constant Φ, and the final increment in ϵ_{pn} was $+/-0.0001$.

3.1 Spherical Particle Miscibility

Miscibility is determined by the polymer-induced nanoparticle interactions, and a qualitative picture can be gained by examining the potential of mean force in the dilute

particle limit. At low interfacial attraction strength ϵ_{pn}, a strong depletion attraction exists at particle contact, as shown in Figure 3.1 which presents the PMF for a) a short range $\alpha = 0.25$ and b) a long range $\alpha = 1.0$ attraction. The PMF at an intermediate $\alpha = 0.5$ was given in Figure 1.1, along with conceptual sketches of depletion, stabilization, and bridging behaviors. Depletion is qualitatively similar at both short and long interfacial attraction range α, though a smaller ϵ_{pn} is needed at larger α to cause the same contact minimum in W_{nn}. This is expected because the total enthalpic gain of a monomer-particle contact, the quantity which competes against the entropic depletion effect, is related to the quantity $\alpha\epsilon_{pn}$. At an intermediate ϵ_{pn}, particles are sterically stabilized by a bound polymer layer. Thus a repulsion is observed in Figure 3.1 at $\epsilon_{pn} = 1.0$, which becomes longer range (corresponding to a thicker bound layer) at higher α. Small oscillations exist on the scale of the monomer diameter. At even higher values of ϵ_{pn}, the monomer scale oscillations deepen, and the bound layer repulsion is followed by one or more minima (corresponding to polymer "bridging" between particles), which strengthen with increasing ϵ_{pn}. At $\alpha = 0.25$, a single bridging minimum at an interparticle distance of one monomer diameter is prevalent. The $\alpha = 1.0$ systems experience a longer range repulsion and several subsequent bridging minima corresponding to approximately 3, 4, or 5 monomer layers between particles. Overall, the basic effect of ϵ_{pn} is similar regardless of attraction range: all systems experience depletion, stabilization, and then bridging as ϵ_{pn} is increased.

The second virial coefficient, based on the dilute particle W_{nn}, provides a simple gauge of miscibility as discussed in Chapter 2. Figure 3.2 shows the normalized $\overline{B_2}$ at $D/d = 10$ and $\alpha = 0.25$, 0.5, and 1.0. At intermediate ϵ_{pn}, the repulsive adsorbed polymer layer causes a repulsion between fillers and $\overline{B_2} > 1$, and miscibility is expected. As ϵ_{pn} is lowered, the depletion attraction causes a sharp drop in $\overline{B_2}$ which is expected to result in phase separation at finite volume fractions. Increasing α enhances the total interfacial cohesion at a given ϵ_{pn} and monotonically increases miscibility under

depletion conditions (in the sense that the drop in $\overline{B_2}$ occurs at lower ϵ_{pn}). Raising ϵ_{pn} also causes a sharp drop in $\overline{B_2}$ due to the polymer-induced bridging attraction, though it is not as sudden as that at low ϵ_{pn}. Competing effects of α on the bridging attraction cause the intermediate $\alpha = 0.5$ system to have the widest $\overline{B_2} > 0$ window. The strong bridging minimum in W_{nn} at $1d$ for the $\alpha = 0.25$ system decreases its $\overline{B_2}$ versus the $\alpha = 0.5$ case which has a thicker adsorbed polymer layer system. However, further increasing α only slightly thickens the adsorbed layer while significantly increasing the range of bridging, which again reduces $\overline{B_2}$.

The spinodal phase boundary is plotted versus ϵ_{pn} for $D/d = 5$, 10, and 15 at $\alpha = 0.5$ in Figure 3.3. The spinodal curves at higher Φ were converged by decreasing Φ starting near $\Phi = 1$, while the lower Φ curves were converged by increasing Φ from the $\Phi \to 0$ limit. A few systems on this plot were converged by changing ϵ_{pn} at constant Φ, and line up well with the other data, bolstering confidence in the accuracy of these various methods of finding the phase boundary. Both the high and low ϵ_{pn} spinodal boundaries show decreasing miscibility with increasing D/d. The low ϵ_{pn} boundary sharply curves upwards towards the critical point at $\Phi \approx 0.1$, then curves back slightly slower to reach $\epsilon_{pn} = 0$ around $\Phi \approx 0.8$. The high ϵ_{pn} boundary rises more slowly; the Φ at bridging phase separation is approximately linear in ϵ_{pn} from $\epsilon_{pn} = 3.5$ to 2.0, then the boundary curves upwards towards its critical point at $\Phi \approx 0.9$. The spinodals imply that the onset of bridging phase separation is slower than that of depletion phase separation. This could be due to the fact that the bridging attraction is generally weaker than the depletion attraction, so bridging phase separation is a more subtle phenomenon.

Figure 3.4 shows the spinodal phase diagram for $\alpha = 0.25$, 0.5, and 1.0, compared to the virial calculation (dashed lines) based on the dilute $\overline{B_2}$. At $\epsilon_{pn} = 0$, there is no attraction and the three systems are identical, however, the data point at $\epsilon_{pn} = 0$ was found separately for each α; the slight variation in the three points gives an indication

of the accuracy of the method of determining the spinodal. The low ϵ_{pn} results show increasing miscibility with growing attraction range and are in qualitative agreement with virial calculations,[90,92] shown by dashed lines. This result is expected because a longer attraction range gives a greater total enthalpic gain of a monomer-particle contact, hence a higher α allows the particles to acquire bound polymer layers and be stabilized at a lower ϵ_{pn}.

At very high ϵ_{pn}, the results also qualitatively agree with the virial analysis.[90,92] This is expected because the virial analysis is more accurate at low volume fractions, and the high ϵ_{pn} systems phase separate at low Φ. These very low Φ calculations show miscibility increases from $\alpha = 0.25$ to 0.5, then decreases from $\alpha = 0.5$ to 1.0. This may be due to the competing effects of the weakening of the bridging minimum (which increases miscibility) and the increasing interparticle distance of bridging (which decreases miscibility) which occur with increasing α. At low α, bridging occurs at a very specific distance (one monomer diameter), and the potential of mean force generally shows a deeper, sharper bridging minimum than it does for the $\alpha = 0.5$ case. At $\alpha = 0.5$ there is some effect of bound polymer at a distance of one monomer diameter and several relatively weaker bridging minima are seen at 1, 2, and 3 monomer diameters from the surface. The potential of mean force for $\alpha = 1.0$ shows slightly weaker bridging minima than $\alpha = 0.5$, however, bridging can occur at interparticle separations of 2, 3, 4 or more d. As the bridging distance becomes this large, the particles are effectively larger, so a particle network becomes easier to form at lower volume fractions, decreasing miscibility.

As ϵ_{pn} is decreased so that phase separation occurs at a larger Φ, many-body effects become important and the results no longer agree with the virial analysis. For example, based on the positive B_2 (0.22) of the system at $\Phi = 0$, $\alpha = 0.5$, $D/d = 10$, $\epsilon_{pn} = 3.0$, a virial analysis predicts complete miscibility while Figure 3.4 shows that phase separation occurs for this system just after $\Phi = 0.1513$ and that complete

miscibility is not achieved until ϵ_{pn} is below 0.9. It is also of note that the depletion critical point occurs at a low Φ (less than 0.1 for $D/d = 10$), suggesting that even in the experimentally relevant regime of relatively low volume fraction, in some cases increasing filler loading would increase miscibility. This possibility was not captured in the virial analysis, where miscibility monotonically decreases with filler loading. At the more moderate ϵ_{pn} values, the effect of longer-range bridging decreasing miscibility is enhanced, and small differences in the depth of the bridging minima become less relevant. This effect is proposed as an explanation for the crossing of the $\alpha = 0.25$ and 0.5 curves in Figure 3.4. When phase separation occurs at a relatively high volume fraction above ~ 0.3 or greater, miscibility decreases with increasing attraction range (and therefore with increasing bridging distance). In contrast, the virial calculations predict much greater miscibility for $\alpha = 0.5$ and 1.0, and that the $\alpha = 0.25$ system is the least miscible.[90,92] Many-body effects should be more important for systems with greater effective volume fractions (larger α). Accounting for many-body effects always decreases the predicted miscibility window, but the decrease is the most for $\alpha = 1.0$, while the $\alpha = 0.25$ curve changes the least.

3.2 Spherical Filler Structure with Increasing Volume Fraction

To explore the effect of particle volume fraction at the fixed total packing fraction of $\eta_t = 0.4$, Φ was increased for the very weakly bridging system at $\alpha = 0.5$, $\epsilon_{pn} = 0.9$, and $D/d = 10$. This mixture is of particular interest as it has a positive $\overline{B_2}$ at $\Phi = 0$ but phase separates due entirely to many-body effects at a very high $\Phi = 0.93$. This allows calculations over a wide range of Φ and reveals dramatic changes in real space and structure factor features.

3.2.1 Structure in Real Space

The potential of mean force of the $\alpha = 0.5$, $\epsilon_{pn} = 0.9$, $D/d = 10$ mixture is shown in Figure 3.5–it is almost entirely repulsive at $\Phi = 0$ but develops a very weak bridging attraction as particle concentration increases. The polymer scale oscillations in W_{nn} weaken with increasing Φ while oscillations on a scale slightly larger than the particle diameter (corresponding approximately to the size of the filler plus its bound polymer layer) intensify. For comparison, W_{nn} of pure hard spheres at $\eta_t = 0.4$ is also given, and shows that in the absence of adsorbing polymer there is a greater likelihood of particle-particle contact and particle separations of $1D$ (instead of $1D$ plus a bound layer).

The same trends are observed in the polymer-polymer pair correlation function of Figure 3.6. In the pure polymer limit, the typical lowering of g_{pp} near contact or "correlation hole" indicates that a tagged monomer is less likely to see monomers on other chains at short distances. Superimposed on the correlation hole are monomer scale liquidlike oscillations. Increasing Φ decreases the monomer scale order, though the correlation hole persists, and oscillations on the scale of the filler develop. The polymer-particle pair correlation function also displays decreasing monomer-scale and increasing filler-scale oscillations as nanoparticles are added, plotted in Figure 3.7. In the dilute limit, beyond a strong but short range peak at contact, the oscillations of $g_{pn}(r)$ are approximately centered around the random value of unity. As Φ is increased, the excess of polymer around the particle instead persists for several monomer diameters.

3.2.2 Structure in Fourier Space

The particle collective structure factor for the $\alpha = 0.5$, $\epsilon_{pn} = 0.9$, $D/d = 10$ mixture is shown in Figure 3.8. The predominant feature is the "cage peak" on the scale of $2\pi/k \sim$ the filler diameter plus its bound layer. This peak quantifies the local ordering of the "cage" of particles surrounding a tagged particle. The sharpening of

the cage peak and its shift to higher wavevector with increasing Φ indicates that the nanoparticles are becoming more ordered and closer together even at $\Phi = 0.9$, which is approaching the phase boundary of $\Phi = 0.93$. The particle osmotic compressibility, $S_{nn}(k = 0)$, intuitively decreases as fillers are added, until a sharp $k = 0$ peak develops by $\Phi = 0.9$ due to large, long range concentration fluctuations indicative of impending phase separation.

The corresponding polymer collective structure factor is shown in Figure 3.9. A filler-induced peak not present in the pure polymer melt, reflecting "imprinting" of the nanoparticle spatial order on the polymer via the bound polymer layer. This peak moves to larger wavevector with increasing Φ, demonstrating that the bound layer correlations occur on a shorter real space length scale as particles are closer together at higher Φ. The peak initially increases in intensity with filler volume fraction due to the increased amount of bound polymer; however, at very high Φ the peak intensity slightly decreases. The latter may reflect that, at very high volume fractions, most polymer is already associated with one or more particles, so increasing Φ further simply reduces the amount of polymer. Adding particles initially increases the dimensionless compressibility of the polymer $S_{nn}(k = 0)$; this is expected because, to the otherwise unperturbed polymer matrix, particles appear as added "holes". At intermediate values of Φ, however, the amplitude of polymer concentration fluctuations decreases with increasing Φ. This trend is driven by the bound polymer layer being more structured and harder than the matrix, such that at intermediate Φ adding particles creates a harder enough bound layer to compensate for the softening effect of adding more "holes". Finally at very high Φ, the trend reverses again as the system nears phase separation and $S_{pp}(0) \to \infty$ at the spinodal.

3.2.3 Potential of Mean Force Minimum at Phase Separation

PRISM theory describes equilibrium systems, however, the PMF may be used to gain a qualitative understanding of when kinetic effects become dominant. When the interparticle attraction in the PMF is strong enough (several kT), particles can be irreversibly stuck on experimental time scales, and in this case kinetically stable aggregates or a gel would be expected before equilibrium phase separation is reached.[99] The global minimum of the potential of mean force for the last converged system before spinodal phase separation is plotted versus Φ in Figure 3.10 for various D/d at $\alpha = 0.5$ and in Figure 3.11 for various α at $D/d = 10$. Depletion phase separation requires a much larger negative minimum in $W_{nn}(r)$ than does bridging phase separation because depletion is a shorter-range phenomenon. Many-body interactions also enhance the effect of a minimum in the potential of mean force, so at larger Φ the minimum of $W_{nn}(r)$ need not be as deep to cause phase separation. These trends are similar at various D/d, but as particle diameter increases, a deeper minimum in the PMF is required for phase separation. The depletion minimum is also similar for various α, but as bridging range increases with increasing α, an even less negative minimum in $W_{nn}(r)$ is required for phase separation. This could be due to the increased importance of many-body effects at longer bridging ranges.

3.3 Effect of Filler Shape: Rods, Disks, and Cubes

The coupled and nonadditive consequences of nanoparticle shape and interfacial attractions have been studied for (quasi) 1-, 2-, and 3- dimensional fillers. Like spheres, the aspherical fillers exhibit polymer mediated depletion, stabilization, and bridging behavior. In the latter two cases, clear signatures of the polymer bound layer or bridging are seen in the collective partial structure factors.

The three specific shapes studied, a rod, disk, and cube, each composed of eight identical sites, are shown in Figure 3.12. The space-filling single nanoparticle volumes

are intentionally held fixed, thereby allowing a fair assessment of the effect of shape. The filler site diameter is twice the polymer monomer diameter (d), $D/d = 2$, a choice motivated by carbon nanotubes which typically have a thickness of only a nanometer. An advantage of the $D/d = 2$ choice is that simulations should be tractable which can test the theoretical predictions. The fillers are taken as "hard" in the sense their direct interactions are purely excluded volume, which allows a definitive study of polymer-mediated effective interactions between nonspherical particles as a function of interfacial cohesion strength.

3.3.1 Dilute Nanoparticle Limit

Polymer-mediated interactions between fillers can be quantified by structure (PMF) and thermodynamics (virial coefficient) in the nanoparticle infinite dilution limit.

3.3.1.1 Second virial coefficient

The normalized second virial coefficient is plotted in Figure 3.13 for the three shapes and two values of interfacial attraction range ($\alpha = 0.5$ and 1.0). A composite ordinate variable is employed to quantify interfacial cohesion, $\epsilon_{pn}\alpha$. This choice is motivated by the fact that the integral of the bare monomer-filler attractive potential of Equation 2.28 is roughly proportional to this quantity for the α and D values used here. As observed in prior spherical particle work,[92] the rod, disk, and cube nanoparticles all show a relatively constant $\overline{B_2} > 0$ at intermediate $\epsilon_{pn}\alpha$ corresponding to steric stabilization via the formation of a bound polymer layer. Sharp downturns of $\overline{B_2}$ occur at low $\epsilon_{pn}\alpha$ (contact depletion attraction) and high $\epsilon_{pn}\alpha$ (polymer-induced bridging).

In terms of absolute ϵ_{pn} values, the sterically stabilized regime is broader for the shorter range interfacial attraction, though the corresponding values of $\overline{B_2}$ are smaller than when $\alpha = 1$. This trend is physically due to the thicker bound polymer layer that forms at larger α. The maximum value of $\overline{B_2}$ for rods with the longer range interfacial

attraction implies the rods appear as though they are almost 2.8 times their bare hard core volume. Disks and cubes have less bound polymer and therefore a lower $\overline{B_2}$ in the stabilized regime, presumably due to their lower surface area. Interestingly, the maximum $\overline{B_2}$ for disks and cubes is nearly the same and independent of attraction range. As $\epsilon_{pn}\alpha$ decreases, the amount of bound polymer for all nanoparticle shapes is reduced and the entropic depletion attraction causes a sharp decrease in $\overline{B_2}$. Increasing α slightly reduces this effect for all filler shapes. For the longer range α, the rod $\overline{B_2}$ curve crosses the others; the rod, which has the most bound polymer at intermediate ϵ_{pn}, appears the least stable, while disks are the most miscible. The apparently subtle and competing effects of shape on depletion result in a non-monotonic dependence of nanocomposite stability on particle dimensionality at $\alpha = 0.5$: the disks are most stable, followed by rods, and then cubes.

At high enough $\epsilon_{pn}\alpha$ a minimum in the PMF emerges due to polymer bridging between nanoparticles, resulting in a sudden drop of $\overline{B_2}$. However, $\overline{B_2}$ does not fall as sharply in the bridging regime as in the weak ϵ_{pn} depletion regime. For both values of α, increasing particle dimensionality monotonically decreases stability, with disks being more similar to cubes than rods, as was the case in the sterically stabilized regime. In terms of $\epsilon_{pn}\alpha$, disks and cubes are very similar and not sensitive to attraction range, while rods become much less stable as cohesion range grows.

The value of ϵ_{pn} at which $\overline{B_2} = 0$ is a measure of the onset of filler clustering and impending immiscibility. Results for this crossover value of attraction strength are shown in Table 3.1 at two interfacial attraction ranges. Calculations for spherical fillers of the same size as a site of the nonspherical nanoparticles, and also for a sphere of the same volume as the $N_n = 8$ site fillers, are given for comparison.

There are a number of interesting trends that shed light on the question of how nanoparticle shape (at fixed particle volume) influences depletion, bound layer formation and bridging. On the depletion side at $\alpha = 0.5$, the interfacial attraction

Table 3.1: Interfacial attraction strength (units of thermal energy) at which the second virial coefficient equals zero for the two indicated values of attraction range. Where non-convergence occurs before $\overline{B_2} = 0$, the values were deduced via modest extrapolation.

$\alpha = 0.5$	rod	disk	cube	$D/d = 2$ sphere	$D/d = 4$ sphere
depletion ϵ_{pn}	0.063	0.052	0.11	0.12	0.18
bridging ϵ_{pn}	1.61	0.68	0.60	2.09	3.03
$\alpha = 1.0$	rod	disk	cube	$D/d = 2$ sphere	$D/d = 4$ sphere
depletion ϵ_{pn}	0.021	0.0080	0.017	0.047	0.075
bridging ϵ_{pn}	0.49	0.33	0.32	0.85	1.61

strength required to first achieve stabilization ($\overline{B_2} > 0$) is smallest for disks, with rods larger, and cubes nearly a factor of two greater. This corresponds to a non-monotonic dependence on nanoparticle dimensionality of the "depletion-to-stabilized" crossover. For the longer range attraction, less interfacial attraction is needed as expected, although the disk and cube fillers experience a much larger reduction than the rod; the non-monotonicity with filler dimensionality remains but now the rod requires the most interfacial attraction. The "stabilized-to-bridging" crossover occurs at a high ϵ_{pn} which progressively increases as particle dimensionality decreases. This trend reflects the reduction in bridging efficiency as nanoparticles become less compact, and applies for both attraction ranges.

It is also interesting to contrast the behavior of the nonspherical fillers with the two spherical analogs defined above. The required strengths of interfacial attraction for both crossovers are larger, and relative to each other differ by a factor of ~ 2 or less. The equivalent volume sphere ($D/d = 4$) system clearly differs from its nonspherical analogs more on the bridging side compared to the depletion region, and the difference for the depletion-stabilization crossover becomes larger as the interfacial attraction range grows.

Note that an attraction range equal to a nanoparticle site radius ($\alpha = 1$) is relatively large for real materials that experience dispersive, hydrogen bonding or charge transfer interactions. Therefore, in the rest of this chapter only calculations for $\alpha = 0.5$ are

presented.

3.3.1.2 Potential of mean force

To provide physical insight into the structural origin of the depletion and bridging behaviors, the dilute limit PMF at $\alpha = 0.5$ is plotted in Figures 3.14 and 3.15 with interfacial attraction strength adjusted so that $\overline{B_2} = 0.5$. The latter condition, although arbitrary, represents a thermodynamic calibration of the degree of polymer-mediated attraction between fillers that allows a more informed comparison of the conditions leading to immiscibility for different shapes. In the depletion regime, the contact attraction in Figure 3.14 is deepest for rods, and is followed by a small repulsion and cusps corresponding to distances of intra-nanoparticle bonding correlations. A monotonic weakening of contact attraction occurs with increasing nanoparticle dimensionality, with the disk considerably closer to cubes than rods. Envisioning the various possibilities for the orientation of two particles, rods more often experience a single site-site contact than do disks or cubes, which have many more relative orientations for which multiple sites are in contact. This may explain why a deeper contact minimum (and lower ϵ_{pn}) is required to decrease $\overline{B_2}$ to 0.5 for rods.

Rods are even more different than cubes and disks under the weak bridging conditions of Figure 3.15. The short range repulsion in Figure 3.15 is greatest for rods, then disks and cubes. The repulsion decays most quickly for rods, bolstering the idea that shorter range polymer-mediated correlations occur for these linear objects. The bridging minima (inset) required to reduce $\overline{B_2}$ to 0.5 are weak, but persist for several monomer diameters. The minimum is deepest for cubes with a spatial range of $\sim 5d$. The bridging minimum for the disk is similar to that of cubes but slightly weaker. Rods continue these monotonic trends, but show an extremely weak, even longer range minimum.

Figure 3.16 presents the site-site nanoparticle PMF for ϵ_{pn} in the bound layer or

stabilization regime. The thin lines indicate results in the dilute limit. The inset shows the extremely small polymer induced attractions. In contrast to Figures 3.14 and 3.15, the PMFs are very similar with a polymer mediated repulsion extending 2-3 monomer diameters. The rod experiences shorter range repulsion compared to the more compact shapes. Increasing α to 1 (not shown) increases the thickness of the bound polymer layer, and filler sites experience a longer range repulsion as expected.

3.3.2 Nanoparticle Concentration Effects and Phase Separation

3.3.2.1 Filler PMF and osmotic compressibilities

Figure 3.16 shows the PMF at $\Phi = 0.3$ (thick curves) of systems in the sterically stabilized regime based on dilute virial calculations. Increasing nanoparticle volume fraction in the middle of the miscibility window leads to many body effects which generically reduce the stabilizing effect of bound layers, as previously discovered for spherical fillers.[98] Specifically, the polymer-induced repulsive barrier is lowered, especially for rods, which have an increased probability of site-site contact. These changes reflect the geometric fact that rods are more likely to be near other rods at moderate volume fractions compared to disks or cubes. In polymer science, this aspect is quantified by an overlap volume fraction, $\Phi^* = N_n R^3/R_g^3$, where R is the site radius and R_g the filler radius of gyration. This quantity indicates when the volume a nanoparticle pervades equals the particle space-filling volume, or equivalently the onset of interpenetration for a fractal object like a rod.[105] For the $N_n = 8$ cubes, disks, and rods, $\Phi^* \sim 1.5$, 0.78, and 0.08, respectively; the compact nature of the cube and disk results in unphysically large, and hence irrelevant, values for Φ^*.

To explore the effect of nanoparticle volume fraction on the collective concentration fluctuations ($k = 0$ limit of partial collective structure factors), Figure 3.17 shows the polymer and filler dimensionless osmotic compressibilities under full miscibility conditions. The amplitude of nanoparticle concentration fluctuations initially decreases

linearly for all shapes, with the cube and disk showing a nearly identical and much smaller reduction than rods. For rods beyond $\Phi^* \sim 0.08$, $S_{nn}(k = 0)$ becomes highly nonlinear indicating strong inter-rod repulsions mediated by bound polymer layers. Cubes and disks remain linear to much higher volume fractions, but their $S_{nn}(0)$ curves eventually separate and become nonlinear. The most compact nanoparticle, the cube, has the highest values of $S_{nn}(0)$ since at fixed volume fraction the objects are farther apart.

The collective polymer concentration fluctuation amplitude ($S_{pp}(k = 0)$) trends are also monotonic with nanoparticle dimensionality. The polymer osmotic compressibility increases as particles are first added since the initial dominant effect is to create "holes" in the polymer matrix. This increase of osmotic compressibility is independent of nanoparticle shape since the space-filling volumes of each type of filler are equal. However, the increase of $S_{pp}(0)$ slows with growing volume fraction, and eventually $S_{pp}(0)$ slightly decreases with increasing Φ corresponding to a filler-induced "hardening" of the polymer matrix due to the increasing amount of bound polymer around the nanoparticles.[98] The bending over of $S_{pp}(0)$ occurs at lower Φ as nanoparticle dimensionality is decreased, consistent with the trends displayed by $S_{nn}(0)$.

3.3.2.2 Spinodal phase diagram

Spinodal demixing boundary results are presented in Figure 3.18. They have been determined as the last ϵ_{pn} value at which the PRISM equations numerically converged.[98] It has been previously stated,[98] and verified again here, that this value of ϵ_{pn} usually corresponds closely with the ϵ_{pn} at which $1/S_{nn}(0)$ and $1/S_{pp}(0)$ extrapolate to zero, the definition of a spinodal. However, this condition is not met at very low volume fractions for the present PNCs. The thin lines in Figure 5 show the ϵ_{pn} at which $1/S_{nn}(0) = 0$ based on extrapolation. At lower volume fractions, the thick and thin curves separate, and the reliability of the spinodal prediction is unclear. Therefore,

phase separation is discussed only when this complicating issue is absent, $\Phi = 0.1$ to 0.3.

The effect of nanoparticle volume fraction on phase separation is subtle. Figure 3.18 shows the tendency for depletion phase separation at low ϵ_{pn} is not monotonic with respect to nanoparticle dimensionality. Cubes phase separate earliest, followed by rods, then disks, as expected based on the $\overline{B_2}$ trends (Figure 3.13). Increasing Φ has little effect on the critical value of interfacial cohesion required for depletion phase separation, i.e. the spinodal curves are nearly vertical. The values of ϵ_{pn} where $\overline{B_2} = 0$ in the dilute limit are 0.052, 0.063 and 0.11 for disks, rods and cubes, respectively; the corresponding values for spinodal demixing at $\Phi = 0.16$ (0.30) are $\sim$ 0.043 (0.036), 0.050 (0.042), and 0.11 (0.10). Comparison of these numbers suggests many body effects only modestly contribute to depletion-induced demixing at low volume fraction as intuitively expected.

At high ϵ_{pn}, cubes phase separate first on the bridging side of the phase diagram, followed by disks, then rods, a monotonic trend with nanoparticle dimensionality. The values of ϵ_{pn} where $\overline{B_2} = 0$ are 0.60, 0.68 and 1.61 for cubes, disks and rods, respectively; the corresponding values for spinodal demixing at $\Phi = 0.16$ (0.30) are $\sim$ 0.86 (1.11), 1.12 (1.24), and 1.66 (1.62). Hence, many body effects are again very small for rods. However, the condition $\overline{B_2} = 0$ clearly no longer accurately captures the true demixing behavior of the more compact disks and cubes. The effect of increasing Φ on the bridging spinodal boundary is subtle; cubes become more miscible, as do disks, but rods become slightly less miscible. This effect may be related to the slightly increased volume available to cube and disk PNCs given the nanoparticle sites are more closely packed, which is not as relevant on the depletion side of the phase diagram where immiscibility is driven by stronger, highly local ($< d$) induced interactions. Overall, the miscibility window monotonically broadens as the nanoparticle dimensionality decreases.

3.3.3 Interfacial Correlations and Scattering Patterns

The real space polymer-filler interfacial pair correlations, and Fourier space collective structure, of the polymer nanocomposites at a fixed nanoparticle volume fraction of $\Phi = 0.3$ have been computed at $\epsilon_{pn} = 0.2$, 0.5, and 0.8, corresponding to the weak depletion, steric stabilization, and weak bridging regimes, respectively. Nanoparticle structure factors are presented in the form directly relevant to scattering experiments, $S_{nn}(k)$, and also in a center-of-mass representation, $S_{CM}(k)$, that allows interpretation in the spirit of a spherical particle system. The collective polymer structure factor, $S_{pp}(k)$, is computed, and the questions of microphase-like ordering, imprinting of filler organization on the polymer species, and the validity of an incompressible RPA description, are addressed.

3.3.3.1 Polymer-filler pair correlations

The influence of nanoparticle shape on the organization of polymers around particles is quantified via the non-random part of the interfacial pair correlation function $h_{pn} = g_{pn} - 1$. This quantity is weighted by the surface area factor $(r/r_c)^2$ to better reveal long range correlations. Figure 3.19 shows results at $\Phi = 0.3$ for $\epsilon_{pn} = 0.2$ where there is relatively little bound polymer. For all shapes, h_{pn} is positive at contact ($g_{pn} > 1$), and the corresponding contact value is weakly filler shape dependent with the rod showing the largest value since it is the most open, least "self-shielding" object. Beyond the very local contact region, h_{pn} shows a negative, correlation-hole behavior which is greatest (deepest) for cubes, then disks, then rods. Beyond a few monomer diameters, the only observable features in h_{pn} are small cusps corresponding to intra-nanoparticle correlations.

Increasing the adsorption strength to $\epsilon_{pn} = 0.5$ where bound layers exist (Figure 3.20) predictably increases h_{pn} at contact. Compared with Figure 3.19, each shape shows an increased amplitude of the weighted h_{pn} corresponding to the average loca-

tion of the bound polymer; the cube most dramatically displays a clear peak around 3 monomer diameters which was hardly present at low ϵ_{pn}. The disk shows smaller peaks at $\sim 1.5d$, $2d$ and $4d$, while the primary rod-polymer correlations appear to be at the shortest range of $\sim 1.5 - 2.0d$. The dominant length scale of the interfacial polymer ordering for rod fillers corresponds to a one to two monomer thick region of polymer adsorbed to a nanoparticle site, while the cubes experience bound polymer order on an overall filler size scale. In other words, a cube site may correlate relatively well with the average of the polymer adsorbed to all cube sites to create a single most important ordering length scale.

Calculations have been performed for the even stronger interfacial attraction of $\epsilon_{pn} = 0.8$ where weak bridging begins. The results are not shown since they are similar to Figure 3.20, with all features modestly enhanced relative to the $\epsilon_{pn} = 0.5$ system.

3.3.3.2 Collective structure factors

Partial collective nanoparticle and polymer structure factors, $S_{nn}(k)$ and $S_{pp}(k)$, reveal the average length scales of polymer and particle ordering and these spatially-resolved concentration fluctuations can be measured by scattering experiments. In the dilute filler limit, the nanoparticle structure factor is equal to its purely intramolecular analog which is different for the three shapes. Therefore, the approximate center-of-mass (CM) filler structure factor from Equation 2.9, which equals one in the dilute limit for any shape, is calculated as described in Chapter 2.

Figures 3.21 and 3.22 present the CM and site-site nanoparticle structure factors, and the corresponding polymer structure factors with S_{tot} of Equation 2.11 as an inset, for the three shapes at $\Phi = 0.3$ and $\epsilon_{pn} = 0.2$ corresponding to the depletion side of the phase diagram. At the site level, $S_{nn}(k)$ in Figure 3.21 displays a wide angle cage peak, the intensity of which quantifies local filler site packing order. The latter decreases in the order of disks, rods, cubes, and is not very sensitive to the magnitude

of the interfacial attraction (see below). The nanoparticle CM structure factors exhibit a small degree of order on several length scales. Each has a peak at $2\pi/(kD) \sim 0.9$, with the rod showing the most intense feature along with a shoulder at $2\pi/(kD) \sim 1.9$ and other very weak shoulders. $S_{CM}(k)$ for cubes displays order on the length scales of $2\pi/(kD) \sim 1.8$ (a peak) and 4.2 (a shoulder), while for the disk the relevant length scales are 1.2 (a weak shoulder) and 1.9 (a shoulder).

Figure 3.22 demonstrates that nanoparticles imprint little order on the collective polymer structure factor under depletion conditions and all are of a nearly "diffusive" form corresponding to a peak at $k = 0$ which grows with increasing nanoparticle dimensionality. Only a very weak peak at nonzero low wavevectors (for cubes) or shoulder (for disks and rods) due to fillers is present in $S_{pp}(k)$ for this weakly adsorbing polymer case. The inset shows the total structure factors, S_{tot}, which equal zero in a hypothetical incompressible RPA limit. In the low k regime where the latter approximation should be most accurate, rod PNCs are closest to fulfilling the $S_{tot} = 0$ condition, while cubes and disks each show a small upturn at low wavevector. Overall, however, the shape of the low wavevector regions of $S_{pp}(k)$ and $S_{nn}(k)$ are similar, consistent to a first approximation with the IRPA relations of Equation 2.10.

Figures 3.23 and 3.24 are the analogs of Figures 3.21 and 3.22 but at $\epsilon_{pn} = 0.5$ which corresponds to moderately adsorbing polymer in the middle of the miscibility window. At the site level, one sees from Figure 3.23 that a low angle peak emerges for the rod, but only a very weak peak (or shoulder) for the cube (disk). Hence, the existence of bound layers on these nanoparticles does lead to mesoscopic ordering, but in a strongly shape dependent manner. Moreover, in contrast to the multiple peaks visible in $S_{CM}(k)$ for the different shapes at low ϵ_{pn} (Figure 3.21), the miscible particles all have a smooth, "soft sphere" correlation hole type of form consistent with the presence of a soft adsorbed polymer layer. There are two very weak peaks corresponding to two main length scales of order at ~ 0.9 and $\sim 1.8 - 2.2$.

The polymer structure factors in Figure 3.24 display strongly imprinted features associated with filler-scale order resulting in a low angle microphase-like peak which is most intense for rods and weakest for disks. The microphase peak is at $2\pi/(kD) \sim 2.4$ for rods, and ~ 4.5 and 4.8 for disks and cubes, significantly longer than the nanoparticle CM ordering length scales. As observed at $\epsilon_{pn} = 0.2$, the rods are again rather well described by the IRPA prediction that $S_{pp}(k)$ and $S_{nn}(k)$ have the same shape at low wavevectors, although disks and cubes are not quantitatively well described.

Scattering profiles for systems approaching the bridging side of the phase diagram at $\epsilon_{pn} = 0.8$ are presented in Figures 3.25 and 3.26. At the site level, the low angle region of $S_{nn}(k)$ is now very different for each shape, with the cube showing two small angle peaks, and the disk only shoulders or inflection points. Multiple peaks continue to be seen in $S_{CM}(k)$, but the low wavevector peak is now clearly dominant for all nanoparticle shapes and represents a polymer bridging mediated ordering effect. As at $\epsilon_{pn} = 0.5$, increasing particle dimensionality increases the length scale of filler order. The nanoparticle spatial ordering trends are imprinted on the collective polymer structure factors in Figure 3.26, which all exhibit a low angle microphase peak at a wavevector that decreases as particle dimensionality increases. Again the disk is the most "frustrated" system in that its microphase ordering is the weakest and most diffuse as indicated by the broad nature of $S_{pp}(k)$. The inset shows rods continue to have a small $S_{tot}(k)$ at low wavevectors, though the upturns in S_{tot} at low k for disks and cubes are significantly higher than for the smaller ϵ_{pn} systems of Figures 3.21-3.24. The latter trend implies the IRPA is expected to fail for disks and cubes, as seen directly by comparison of S_{nn} and S_{pp}; however, for the more polymeric rod filler, Equation 2.10 continues to be reasonably accurate.

Similar trends of all the structure factors have been found for the longer range interfacial cohesion case of $\alpha = 1$ (not shown). Given the existence of a more strongly held and thicker bound polymer layer, the nanoparticle and polymer structure factor

peaks shift to lower wavevector, reflecting order on a slightly longer length scale. The overall filler length scale peaks are somewhat more pronounced, and order on other length scales more suppressed, at higher α. The structure factor peaks are sharpest for cubes, followed by disks, and then rods. These trends suggest the averaging effect of bound polymer on nanoparticle ordering length scales occurs more readily with a thicker adsorbed layer.

In summary, the overall picture suggested by Figures 3.21 to 3.26 is that increasing polymer-filler adsorption strength averages out various length scales of nanoparticle ordering in $S_{CM}(k)$ and allows fillers to better imprint their spatial order on the collective polymer structure factor. The latter occurs on a length scale which corresponds with some global nanoparticle plus bound layer size. The average length scale of ordering increases with nanoparticle effective dimensionality, perhaps because the smaller length scale is most important for rods, while the various length scales are relatively similar and their average is longer for cubes. The particle and polymer spatial order is most intense near bridging, though the structure factors are qualitatively similar for miscible systems. This suggests that in the weakly bridged regime, nanoparticles are correlated to polymers in a similar way as under steric stabilization conditions except now the fillers share adsorbed layers. The interesting microphase feature in $S_{pp}(k)$ can be qualitatively understood based on the IPRA for rods, but not generally for the disk and cube nanoparticle systems.

3.4 Summary

The structure and miscibility of spherical and aspherical particles in a homopolymer melt were studied. Phase separation occurs at low interfacial attraction strength due to depletion attraction and at high interfacial attraction due to bridging. The study of spherical particles shows that depletion phase separation is similar at various values of attraction range, and involves contact aggregation of particles. There is little

or no filler-induced polymer order as depletion phase separation is approached–the main structural change is that particles become much more likely to be in contact (aggregation). The mixture becomes less miscible at lower attraction strengths, or equivalently, at higher temperatures, because depletion phase separation maximizes polymer entropy. Therefore, the critical point of depletion phase separation is similar to a typical entropy-driven lower critical solution temperature, and occurs at $\approx 10\%$ filler. The spinodal phase diagram also shows that increasing filler size decreases miscibility, which is expected because the potential of mean force scales approximately with filler diameter,[91] so the depletion attraction is stronger at larger D. Increasing the range of the interfacial attraction increases the net enthalpic gain of a monomer-particle interaction and therefore increases miscibility. At depletion phase separation below the critical point, the minimum in the PMF is large (between -5 and $-11kT$ for systems studied here), so particle contacts are likely irreversible on experimental time scales. This raises the possibility of the system forming kinetically stable aggregates or a gel before equilibrium phase separation is reached.

Spherical filler bridging phase separation is a more complex phenomenon in which particles are attracted to each other by sharing part of their bound polymer layer. At low α, the phenomenon is somewhat like depletion except that the attraction occurs at one monomer diameter separation instead of contact. However, bridging minima are weaker than depletion attractions, and several minima corresponding to various numbers of monomers bridged between particles may be important, especially at higher α. Interestingly, in contrast to the low $\Phi \approx 0.1$ critical point for depletion, the bridging critical point or upper critical temperature occurs at $\approx 95\%$ filler. Because bridged particles still have a strongly held bound layer, they continue to imprint their order on the polymer matrix even as phase separation is approached. The bound layer causes the particles to be effectively larger, so many-body effects may become important at relatively low volume fractions. The increase in effective volume fraction is greater for

smaller particles; at a certain interfacial attraction, the bound layer is approximately the same thickness for various diameter particles, so the bound layer increases the effective particle size by a larger percentage at smaller D/d. These effects are increased for thicker bound layers, and the spinodal phase diagram shows that at $\Phi \sim 0.3$ or greater, increasing α greatly decreases miscibility. Systems which have a positive second virial coefficient at $\Phi = 0$ are predicted by a lowest-order virial analysis to be completely miscible, but the full calculations for some $\alpha = 1.0$ systems show that even when B_2 is positive, many-body effects can cause bridging attractions and phase separation by $\Phi = 0.3$. The minimum in the PMF at bridging phase separation can be large ($< -3kT$), especially for systems which phase separate at low Φ, so bridges between particles may be irreversible on experimental time scales, as particle contacts can be for depletion systems.

The effect of nanoparticle shape on polymer nanocomposite miscibility and real and reciprocal space structure was explored by comparison of rods, disks, and cubes of matched space-filling volume. The overall trends for the second virial coefficient, PMF, small angle scattering patterns, and spinodal boundaries clearly suggest a monotonic variation with effective filler dimensionality, although exceptions exist. As the interfacial attraction strength is varied, cubes are the least miscible on both the depletion and bridging sides of the phase diagram. A subtle effect of shape on depletion behavior is revealed in that the disks are the least susceptible to depletion phase separation. Tendency towards bridging phase separation is monotonic, with rods requiring a much higher interfacial attraction to induce strong bridging. This is likely due to the lower surface area shared between two close non-aligned rods, in contrast to the larger area available and greater number of relevant configurations for polymer mediated bridging as two disks or cubes are brought together in a polymer melt.

Aspherical nanoparticle collective structure factors at low interfacial attraction strength display order on multiple length scales corresponding to the nanoparticle site

diameter, global filler size, and other intermediate intra-filler length scales. At moderate to strong interfacial attraction, the strongly held adsorbed polymer layer causes damping or averaging of smaller ordering length scales and increases ordering on the overall nanoparticle size scale. Microphase-like peaks in the polymer structure factor exist under steric stabilization (bound layer) and bridging conditions, but not in the depletion regime where large amplitude $k = 0$ fluctuations are more prominent.

3.5 Figures

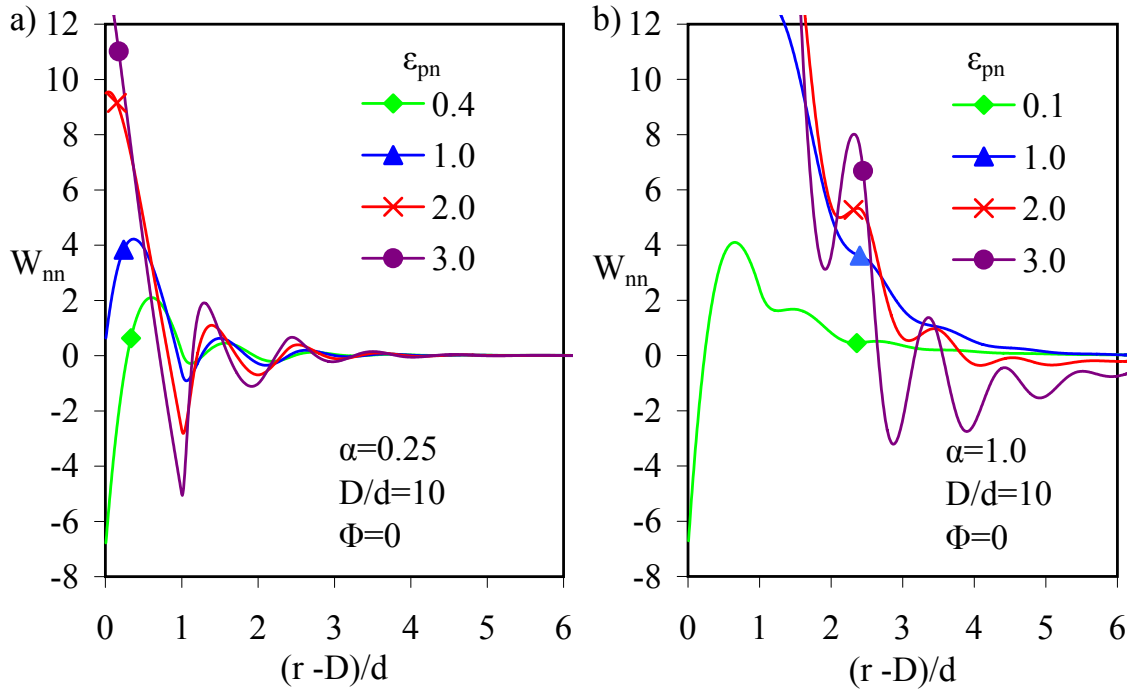

Figure 3.1: Potential of mean force for spherical fillers with $D/d = 10$ at the indicated values of ϵ_{pn} for a) $\alpha = 0.25$ and b) $\alpha = 1.0$.

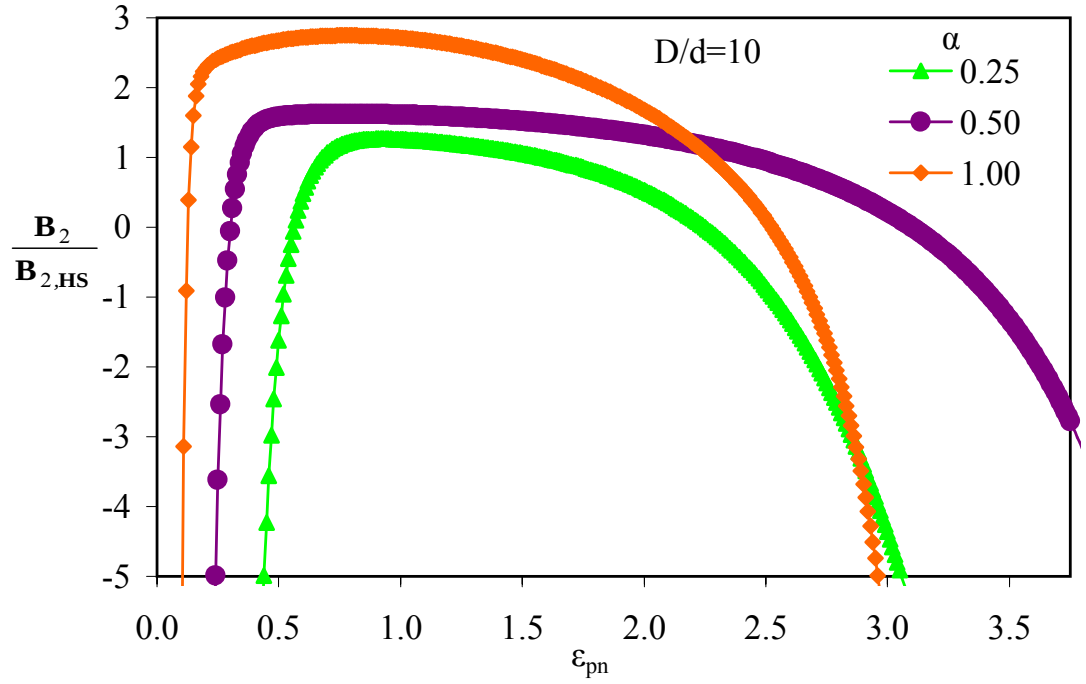

Figure 3.2: Normalized second virial coefficient for spherical fillers with $D/d = 10$.

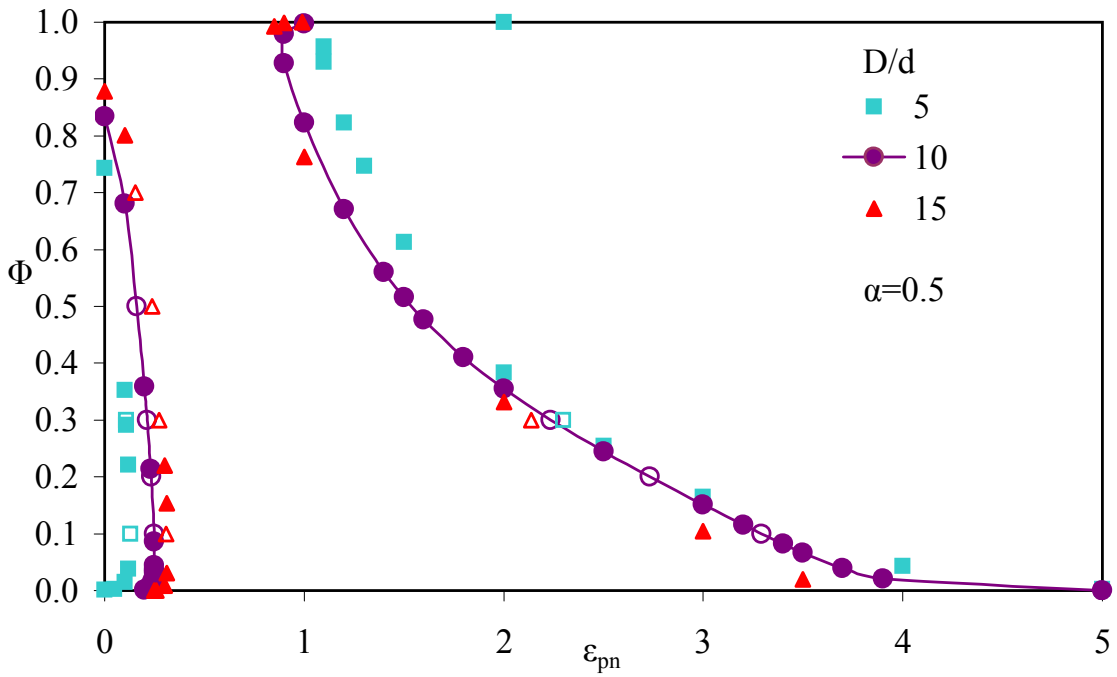

Figure 3.3: Spinodal phase diagram as in Figure 3.4 for fillers of $D/d = 5$, 10, and 15 with $\alpha = 0.5$.

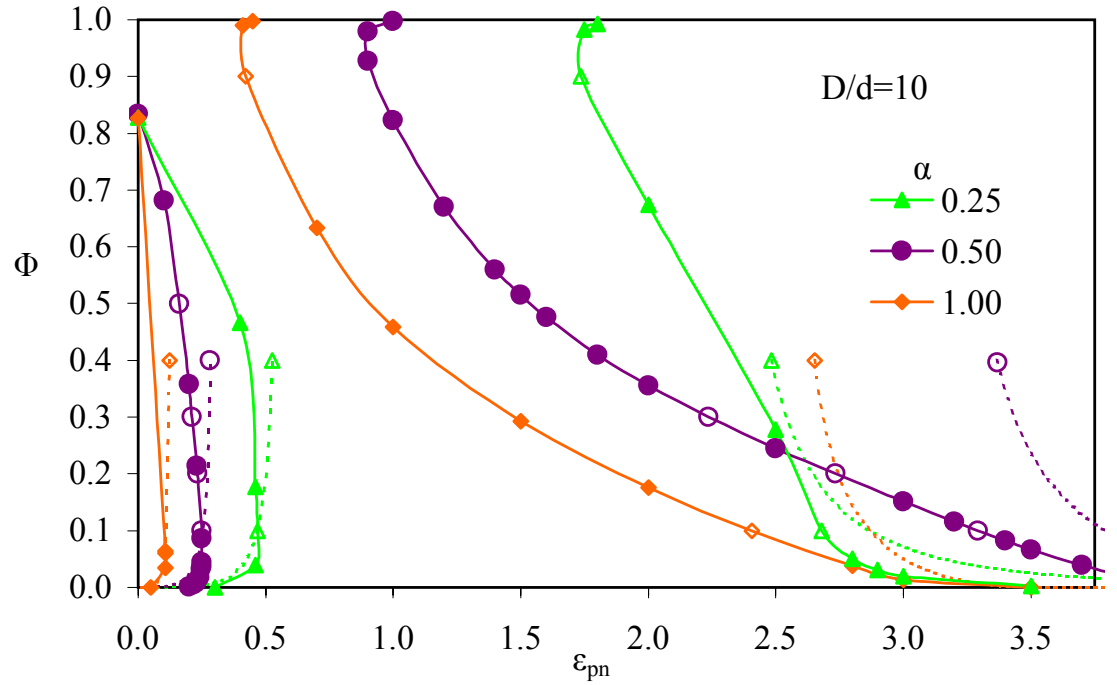

Figure 3.4: Spinodal phase diagram for spherical fillers with $D/d = 10$. Solid symbols represent systems converged incrementing in Φ, while open symbols were incremented in ϵ_{pn}. Dashed lines show the spinodal predicted by a virial analysis.

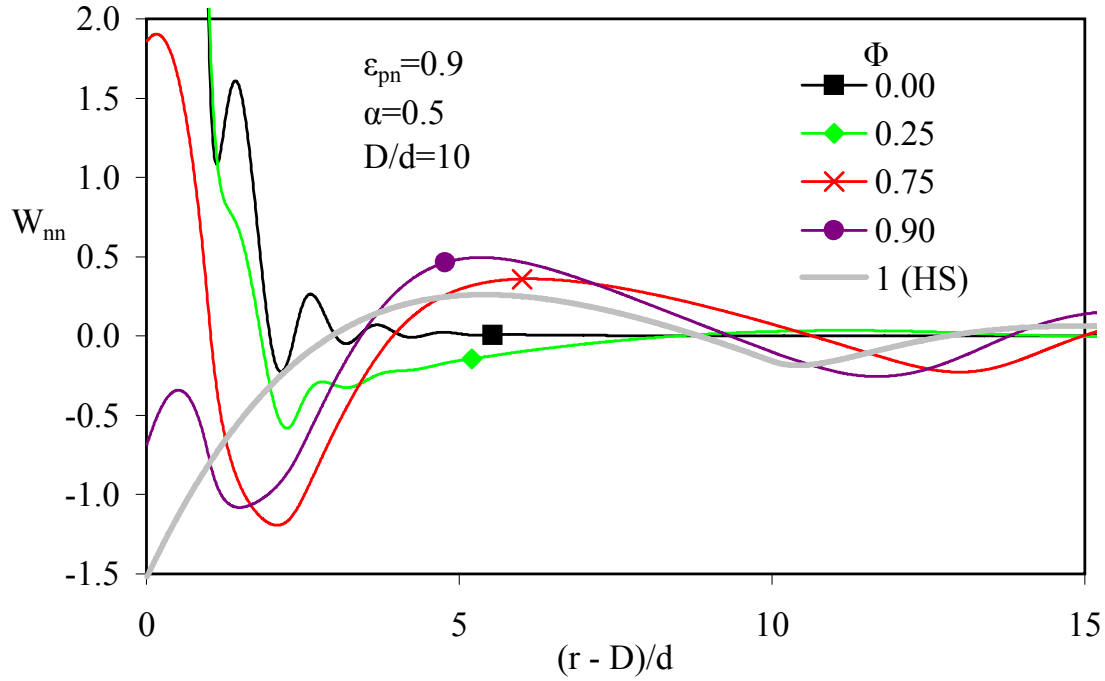

Figure 3.5: Potential of mean force with increasing Φ at $D/d = 10$, $\epsilon_{pn} = 0.9$, and $\alpha = 0.5$.

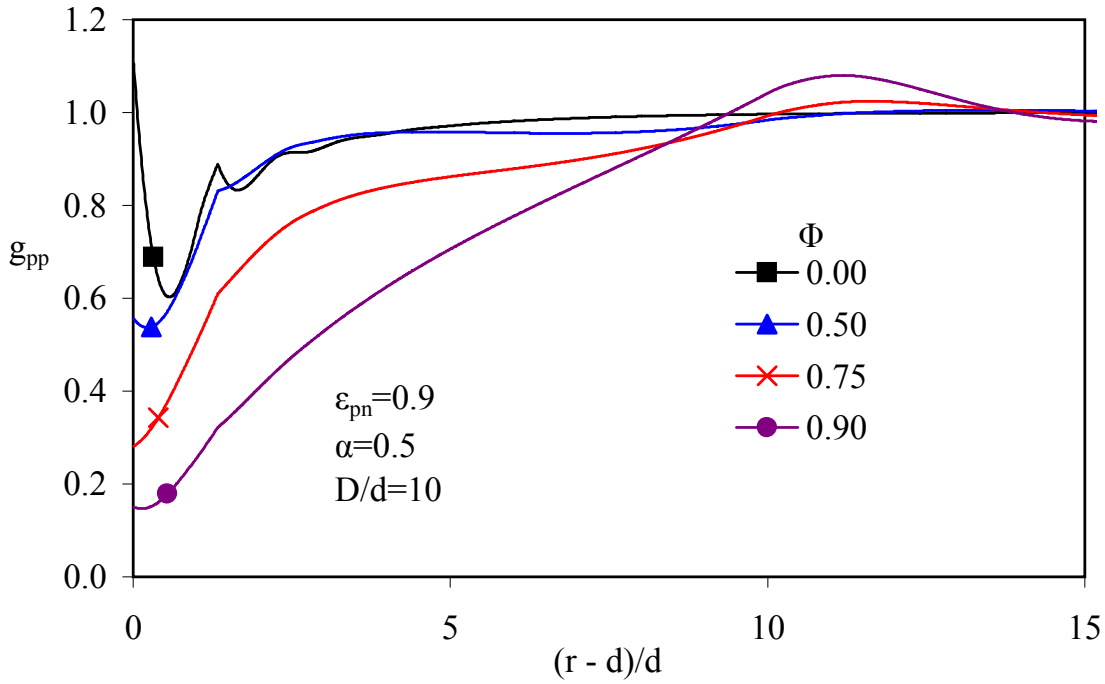

Figure 3.6: Polymer-polymer pair correlation function with increasing Φ at $D/d = 10$, $\epsilon_{pn} = 0.9$, and $\alpha = 0.5$.

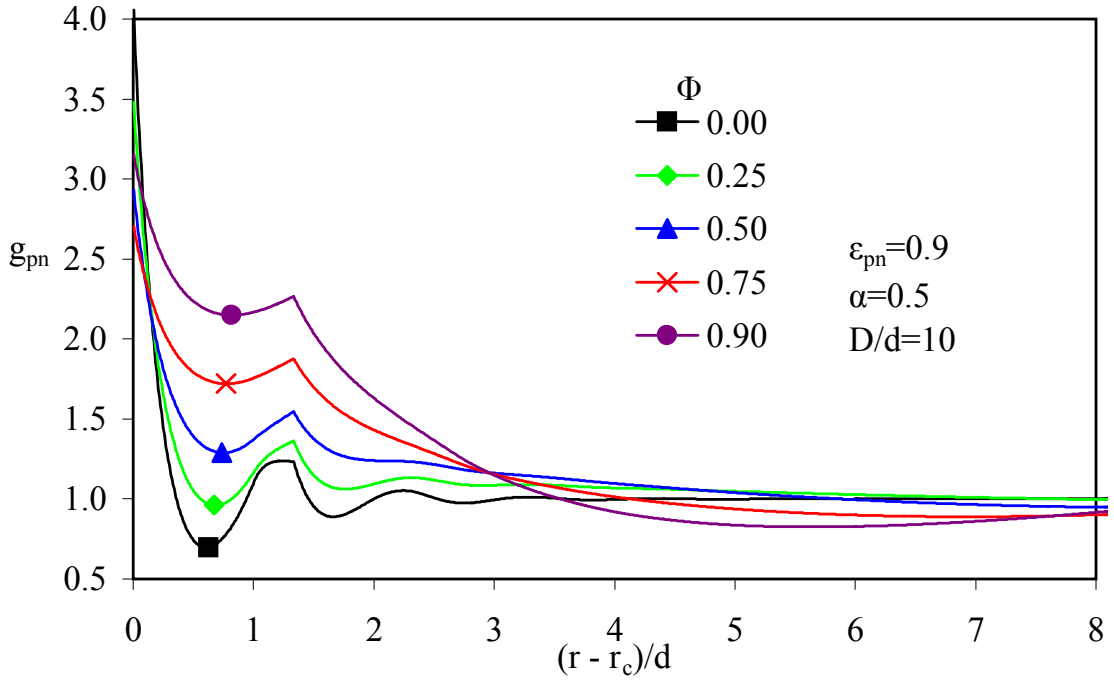

Figure 3.7: Polymer-particle pair correlation function with increasing Φ at $D/d = 10$, $\epsilon_{pn} = 0.9$, and $\alpha = 0.5$.

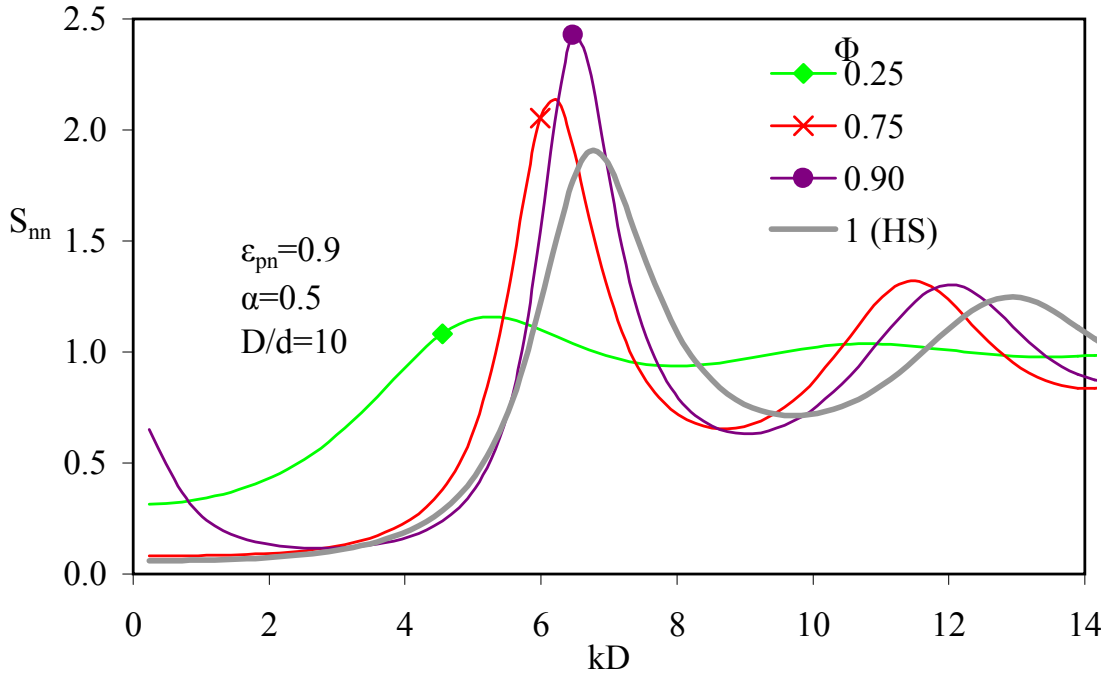

Figure 3.8: Filler collective structure factor with increasing Φ at $D/d = 10$, $\epsilon_{pn} = 0.9$, and $\alpha = 0.5$.

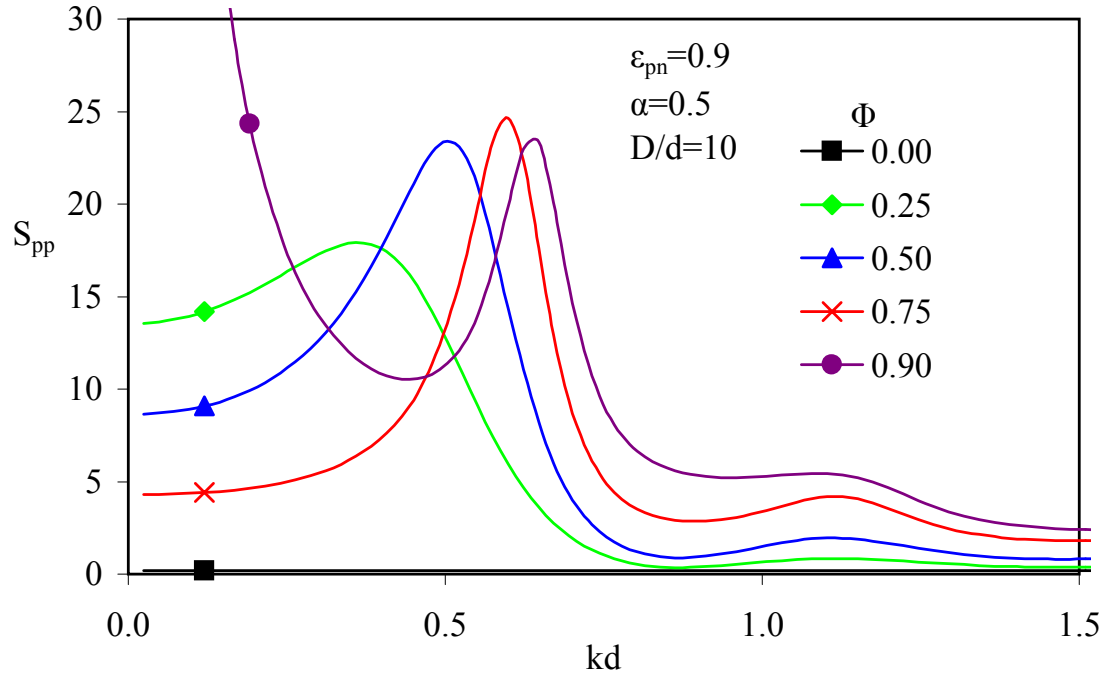

Figure 3.9: Polymer collective structure factor with increasing Φ at $D/d = 10$, $\epsilon_{pn} = 0.9$, and $\alpha = 0.5$.

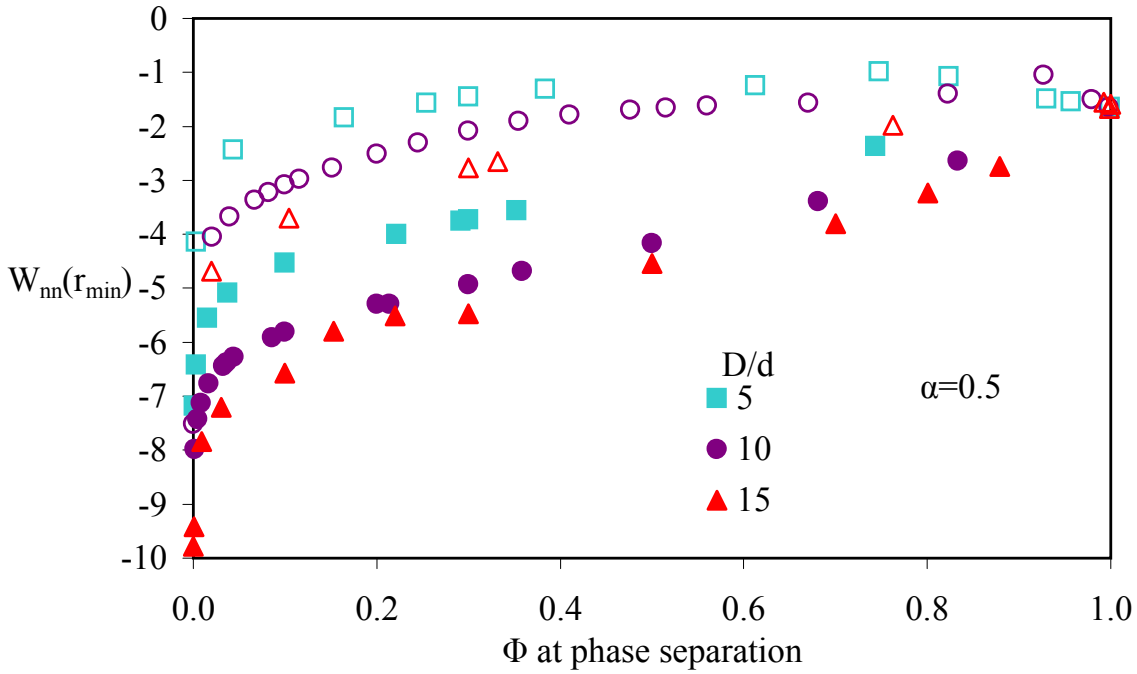

Figure 3.10: Global minimum of the potential of mean force versus Φ for the last converged system before spinodal phase separation, at $\alpha = 0.5$. Filled symbols represent systems on the low ϵ_{pn} (depletion) side of the spinodal, while open symbols are at high ϵ_{pn} (bridging).

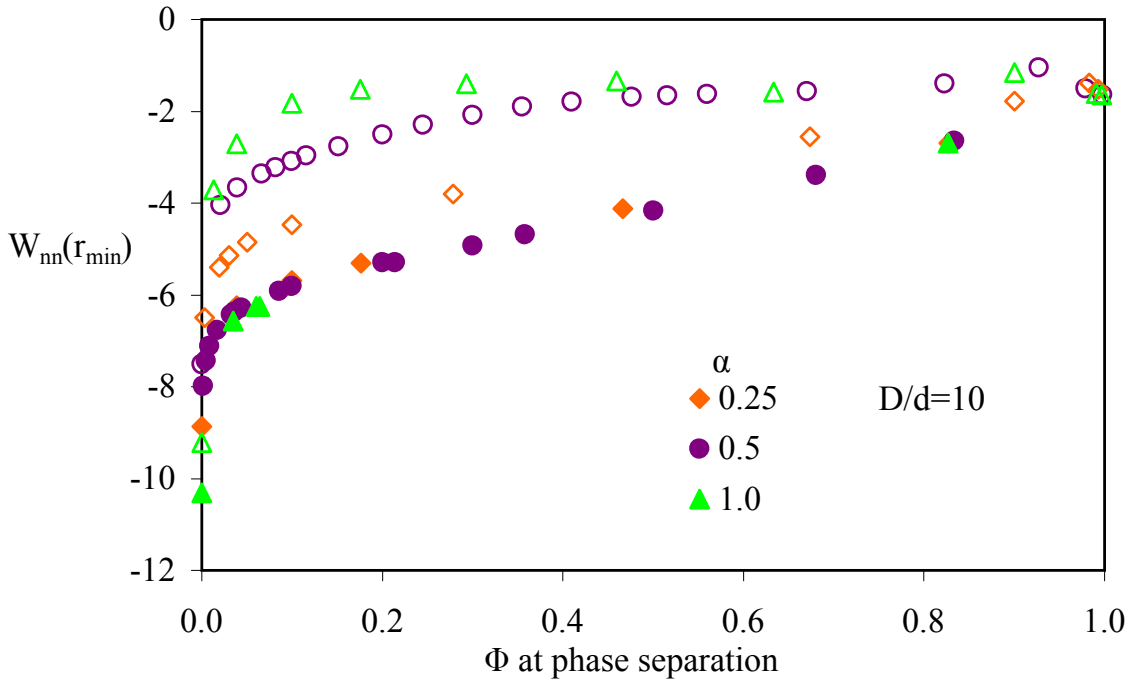

Figure 3.11: Global minimum of the potential of mean force versus Φ for the last converged system before spinodal phase separation, at $D/d = 10$. Filled symbols represent systems on the low ϵ_{pn} (depletion) side of the spinodal, while open symbols are at high ϵ_{pn} (bridging).

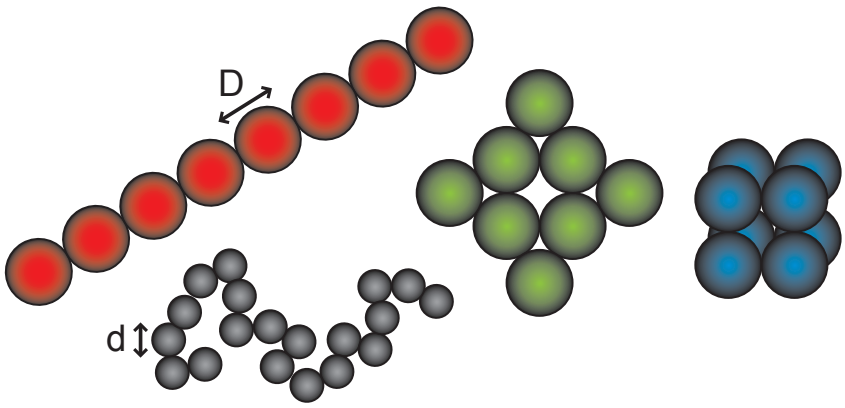

Figure 3.12: From left to right: the rod, disk, and cube shapes, each composed of eight identical sites of diameter D, with radii of gyration $R_g/D = 2.3$, 1.1, and 0.87, respectively. The polymer is a freely jointed chain of $N_p = 100$ monomer sites of diameter $d = D/2$ and $R_g/D = 2.7$.

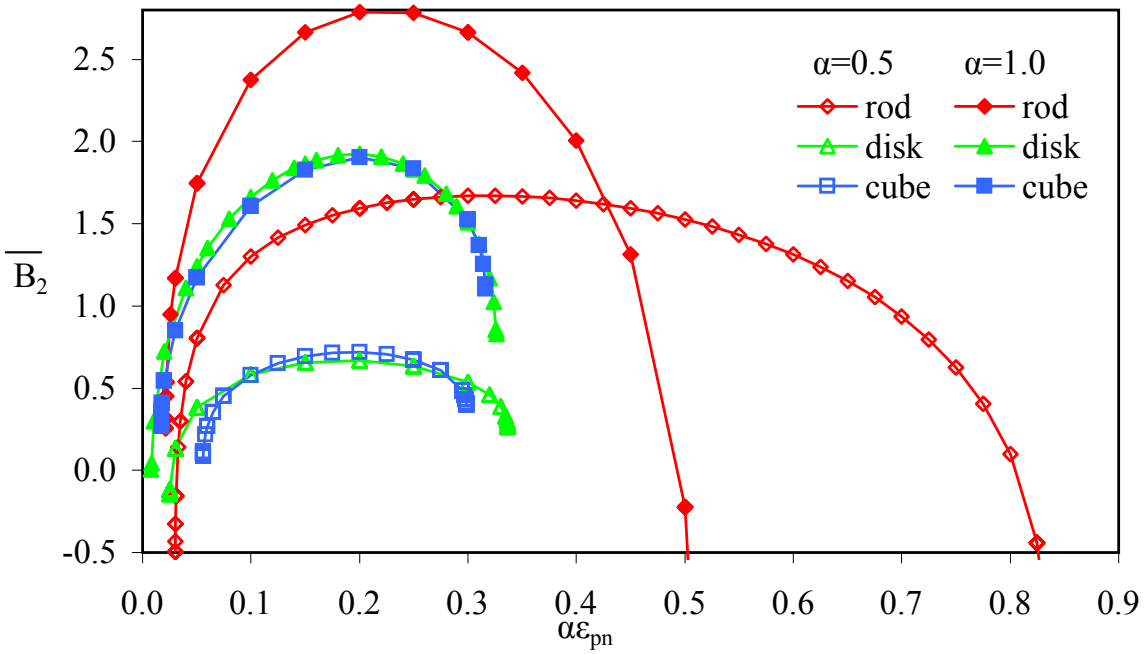

Figure 3.13: Second virial coefficient in the dilute nanoparticle limit, normalized by $4N_n(\pi/6)D^3$, as a function of interfacial attraction strength times spatial range.

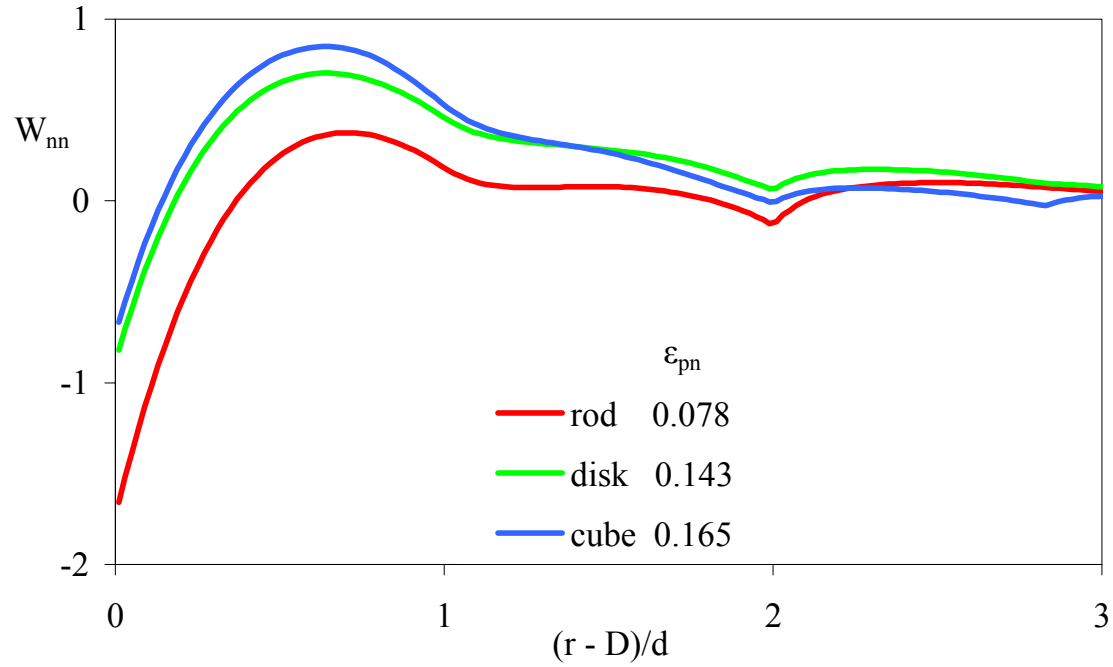

Figure 3.14: Dilute nanoparticle site-site potential of mean force as a function of nanoparticle site surface-to-surface separation when the normalized $\overline{B_2} = 0.5$ for the depletion side of the phase diagram.

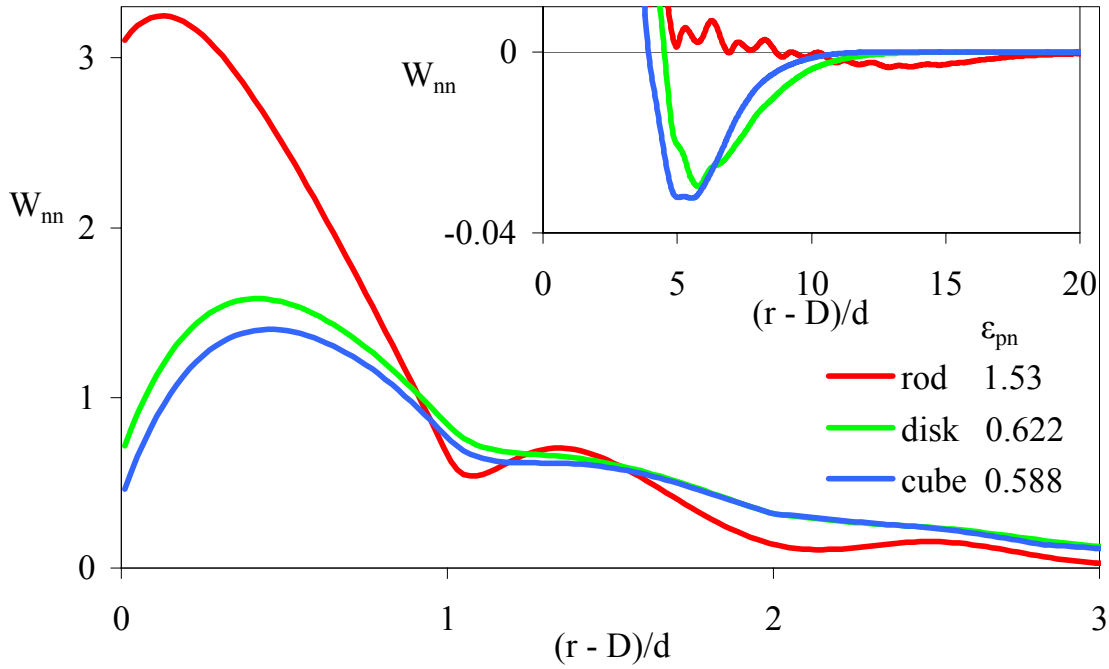

Figure 3.15: Dilute nanoparticle site-site potential of mean force as a function of nanoparticle site surface-to-surface separation when the normalized $\overline{B_2} = 0.5$ for the bridging side of the phase diagram. The inset is an expanded view that shows the existence of weak bridging minima.

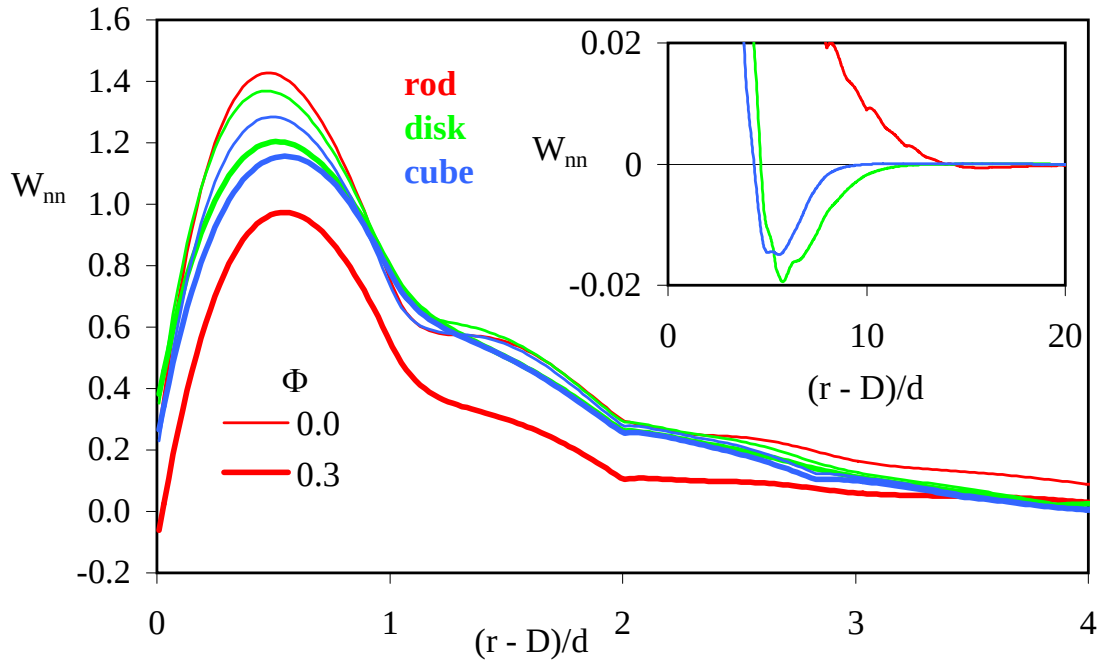

Figure 3.16: Filler site-site potential of mean force in the middle of the miscibility window ($\epsilon_{pn} = 0.5$, $\alpha = 0.5$) in the dilute nanoparticle limit (thin lines) and at $\Phi = 0.3$ (thick lines). The inset shows the small, long range minimum in the dilute filler limit.

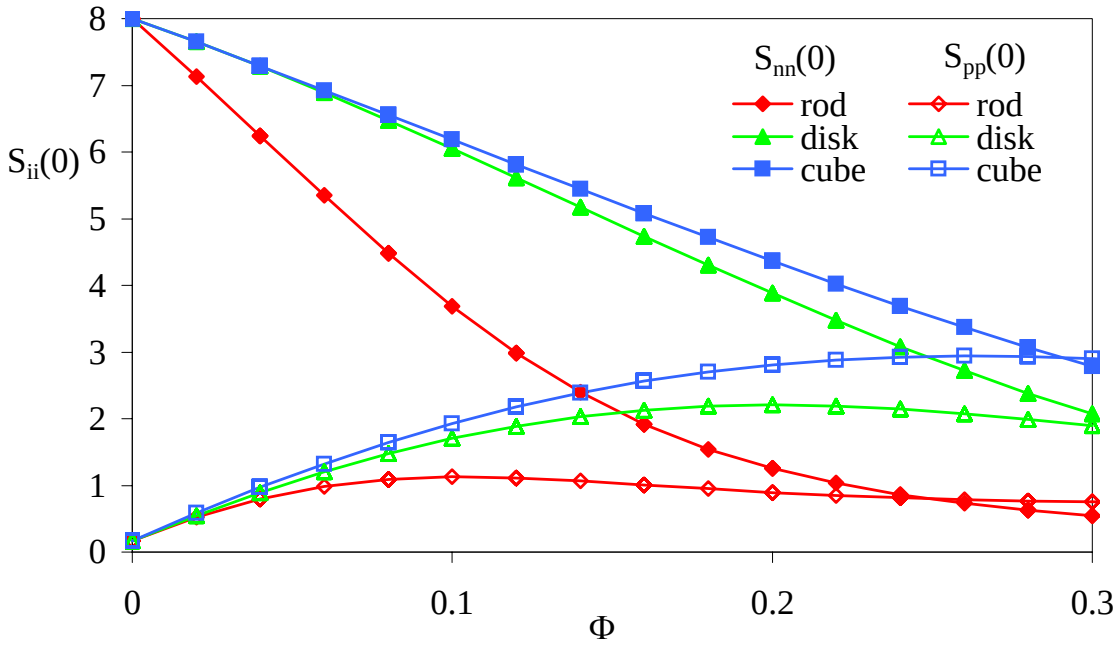

Figure 3.17: Polymer and filler dimensionless osmotic compressibilities as a function of nanoparticle volume fraction at $\alpha = 0.5$ in the middle of the miscibility window ($\epsilon_{pn} = 0.5$).

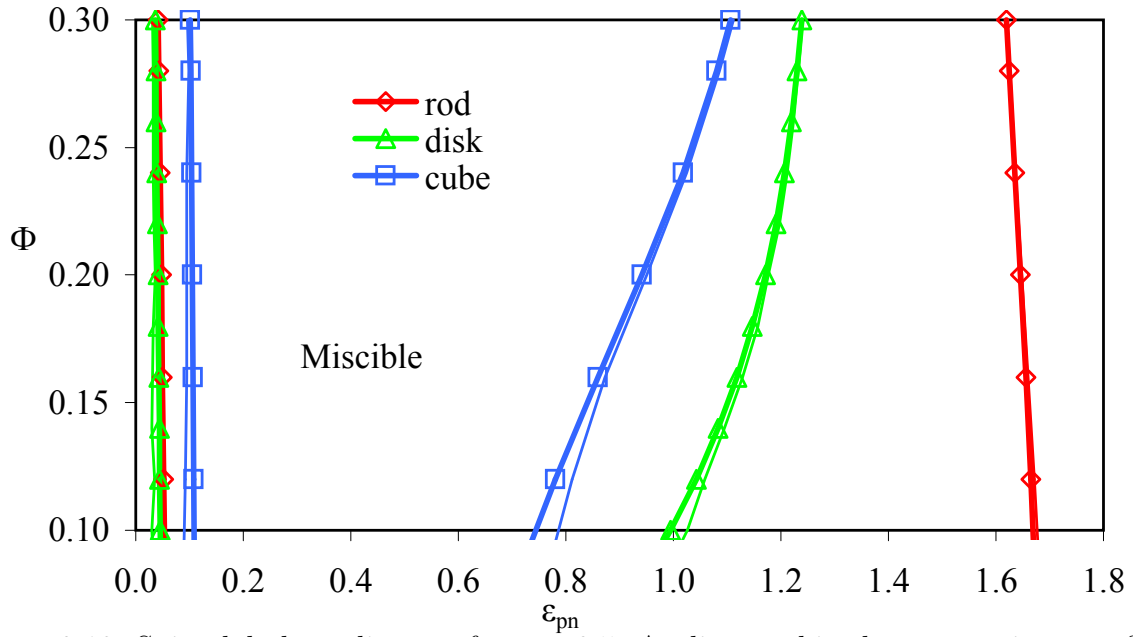

Figure 3.18: Spinodal phase diagram for $\alpha = 0.5$. As discussed in the text, estimates of the spinodal boundaries are obtained based on non-convergence (thick curves) and linear extrapolation of $1/S_{nn}(k = 0)$ to zero (thin curves). At $\Phi = 0.16$, non-convergence occurs at $\epsilon_{pn} = 0.043$, 0.050, and 0.107 for disks, rods and cubes, respectively, and again at 0.86, 1.12, and 1.66 for cubes, disks, and rods, respectively. At $\Phi = 0.3$, non-convergence occurs at $\epsilon_{pn} = 0.036$, 0.042 and 0.102 for disks, rods and cubes, respectively, and again at 1.11, 1.24, and 1.62 for cubes, disks, and rods, respectively.

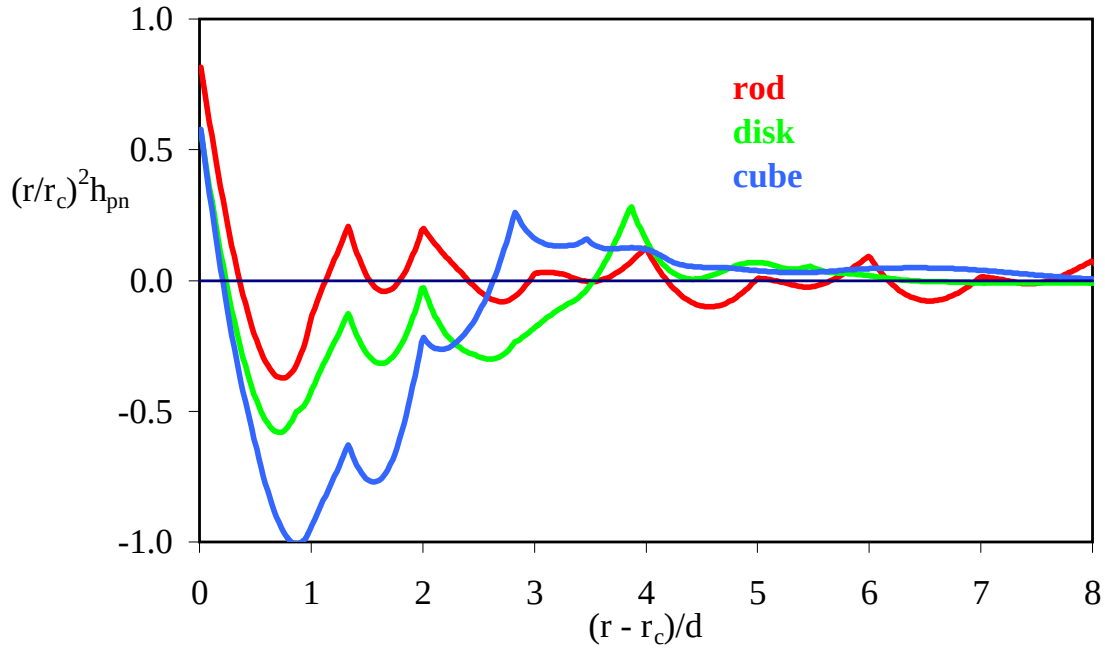

Figure 3.19: Surface area weighted non-random part of interfacial site-site pair correlation function on the depletion side of the phase diagram ($\epsilon_{pn} = 0.2$, $\alpha = 0.5$) at $\Phi = 0.3$. Contact value of $g_{pn} = h_{pn} + 1 \approx 1.84$, 1.61, and 1.60 for rods, cubes, and disks, respectively.

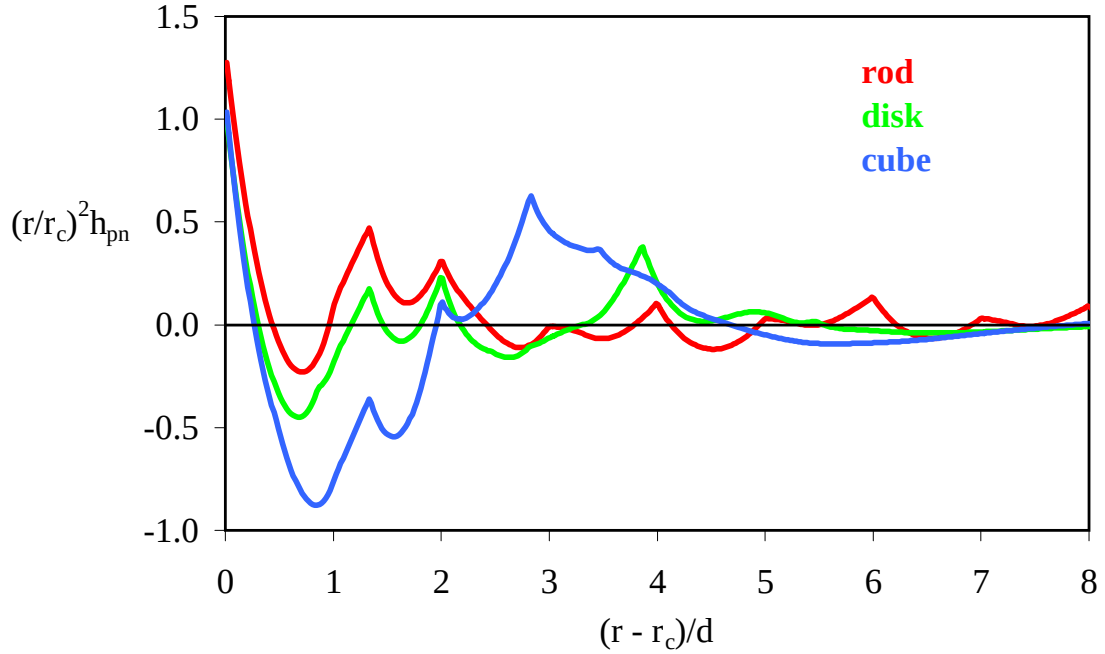

Figure 3.20: Surface area weighted non-random part of the interfacial site-site pair correlation function in the miscibility window at $\epsilon_{pn} = 0.5$, $\alpha = 0.5$, $\Phi = 0.3$. Contact value of $g_{pn} = h_{pn} + 1 \approx 2.32$, 2.09, and 2.04 for rods, cubes, and disks, respectively.

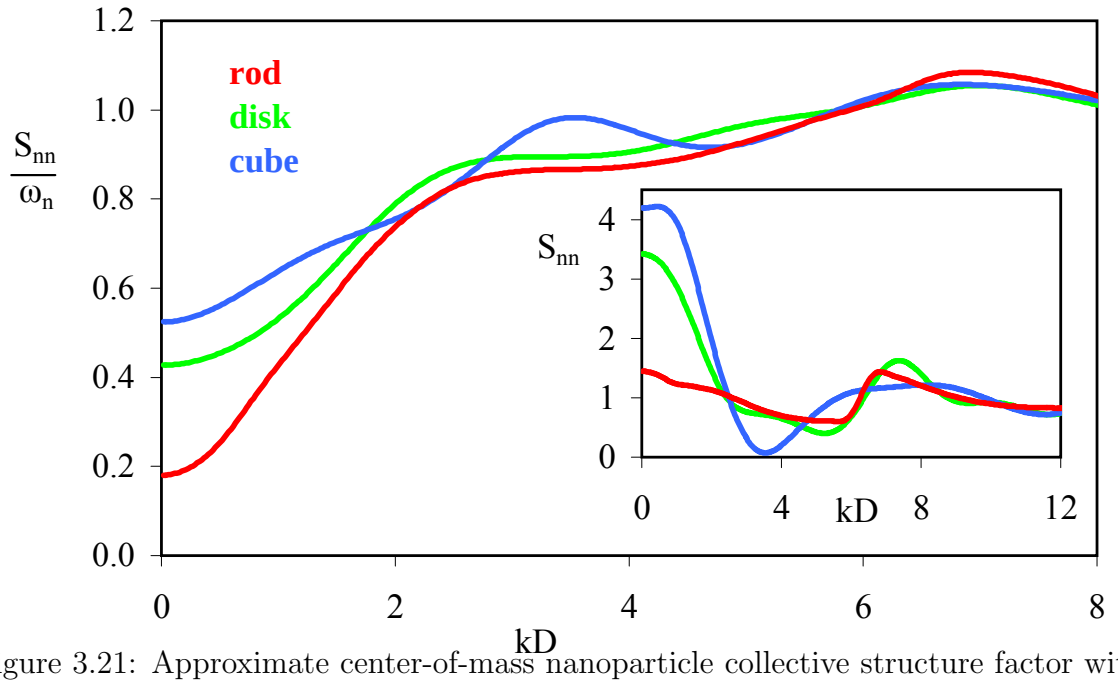

Figure 3.21: Approximate center-of-mass nanoparticle collective structure factor with inset showing the site-site analog on the depletion side of the miscibility window ($\epsilon_{pn} = 0.2$, $\alpha = 0.5$) at $\Phi = 0.3$.

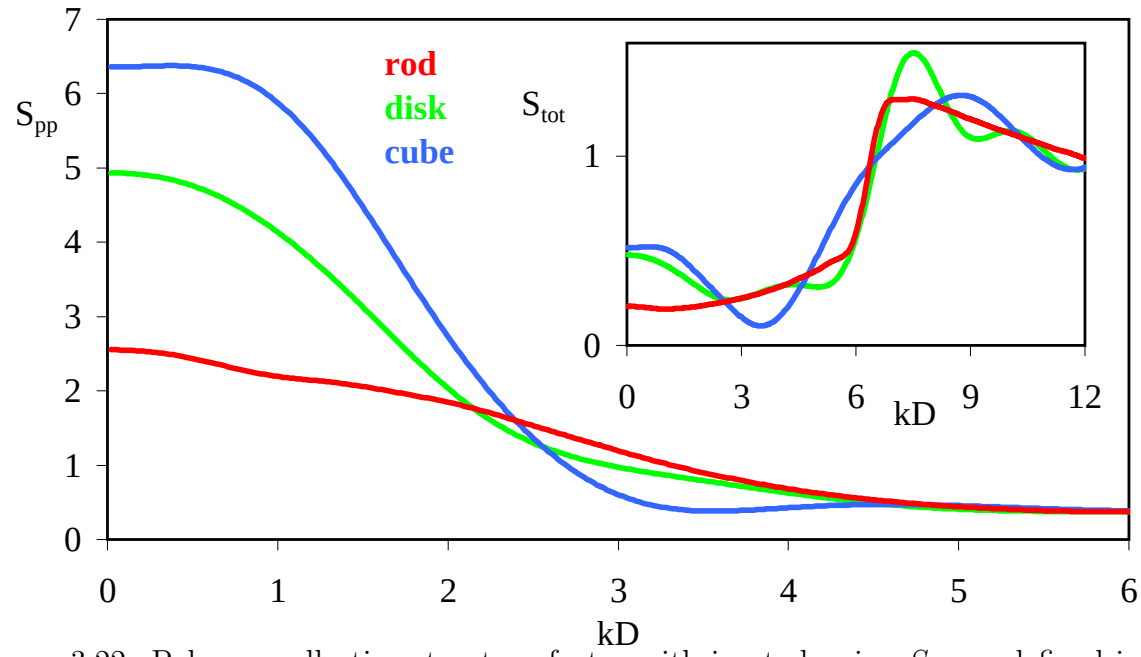

Figure 3.22: Polymer collective structure factor with inset showing S_{tot} as defined in Equation 2.11 on the depletion side of the miscibility window ($\epsilon_{pn} = 0.2$, $\alpha = 0.5$) at $\Phi = 0.3$.

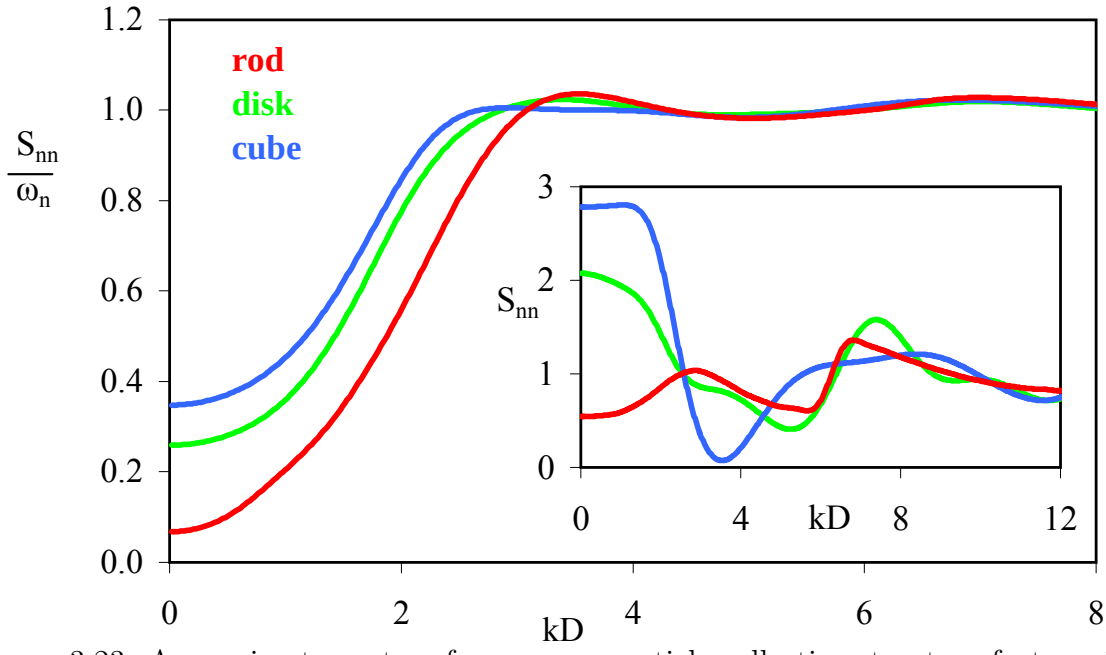

Figure 3.23: Approximate center-of-mass nanoparticle collective structure factor with inset showing the site-site analog in the middle of the miscibility window ($\epsilon_{pn} = 0.5$, $\alpha = 0.5$) at $\Phi = 0.3$.

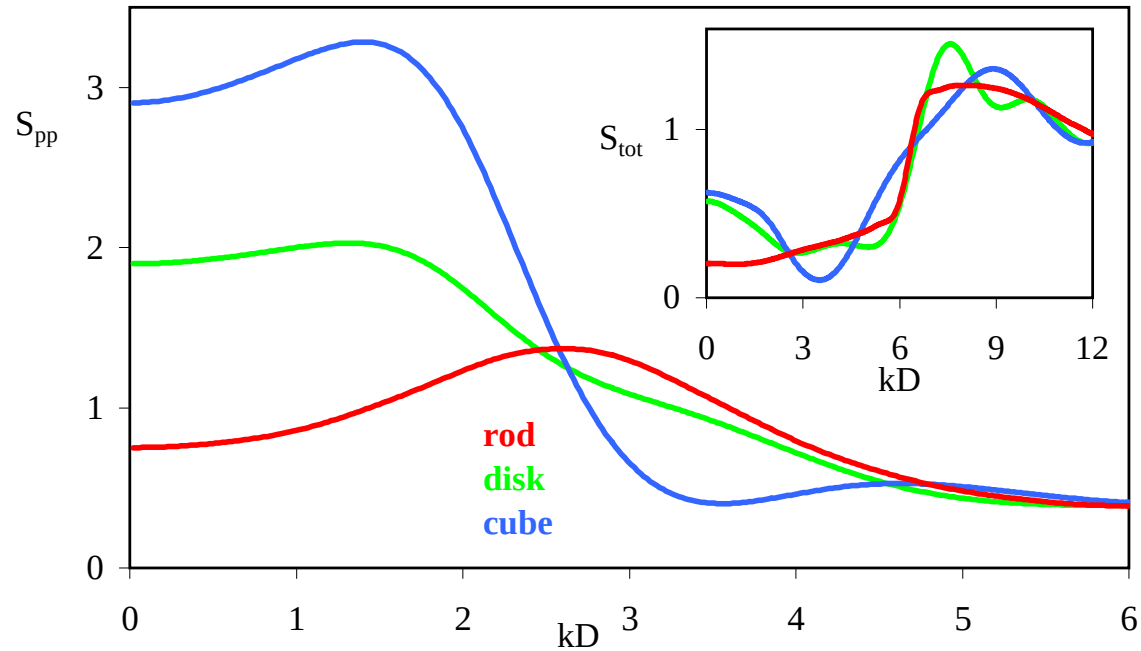

Figure 3.24: Polymer collective structure factor with inset showing S_{tot} as defined in Equation 2.11 in the middle of the miscibility window ($\epsilon_{pn} = 0.5$, $\alpha = 0.5$) at $\Phi = 0.3$.

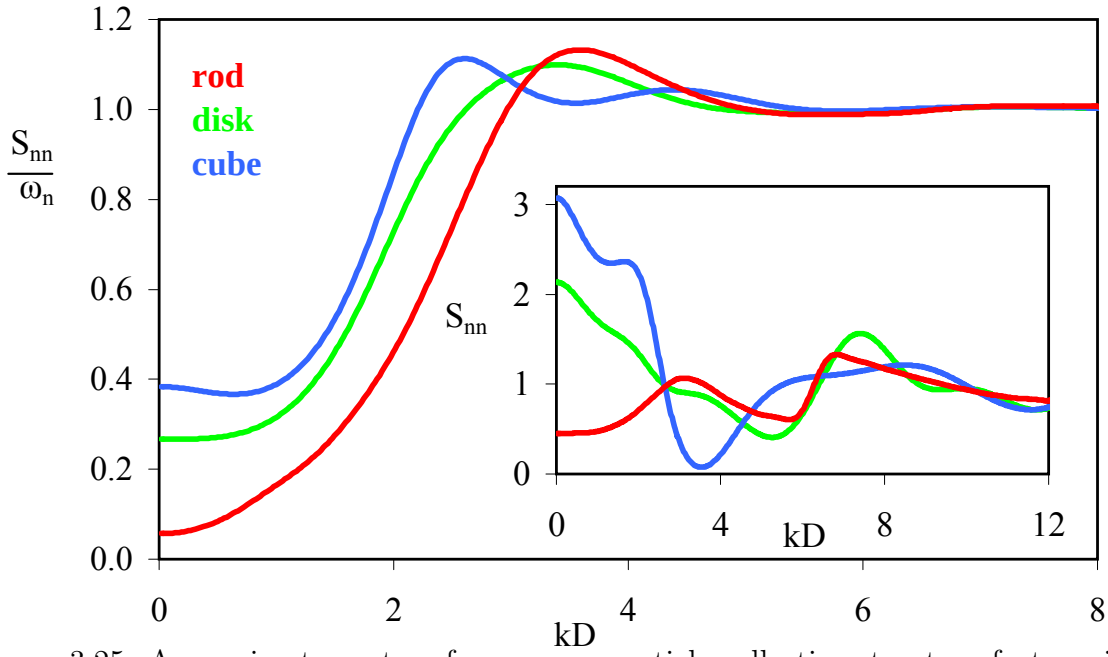

Figure 3.25: Approximate center-of-mass nanoparticle collective structure factor with inset showing the site-site analog on the bridging side of the miscibility window ($\epsilon_{pn} = 0.8$, $\alpha = 0.5$) at $\Phi = 0.3$.

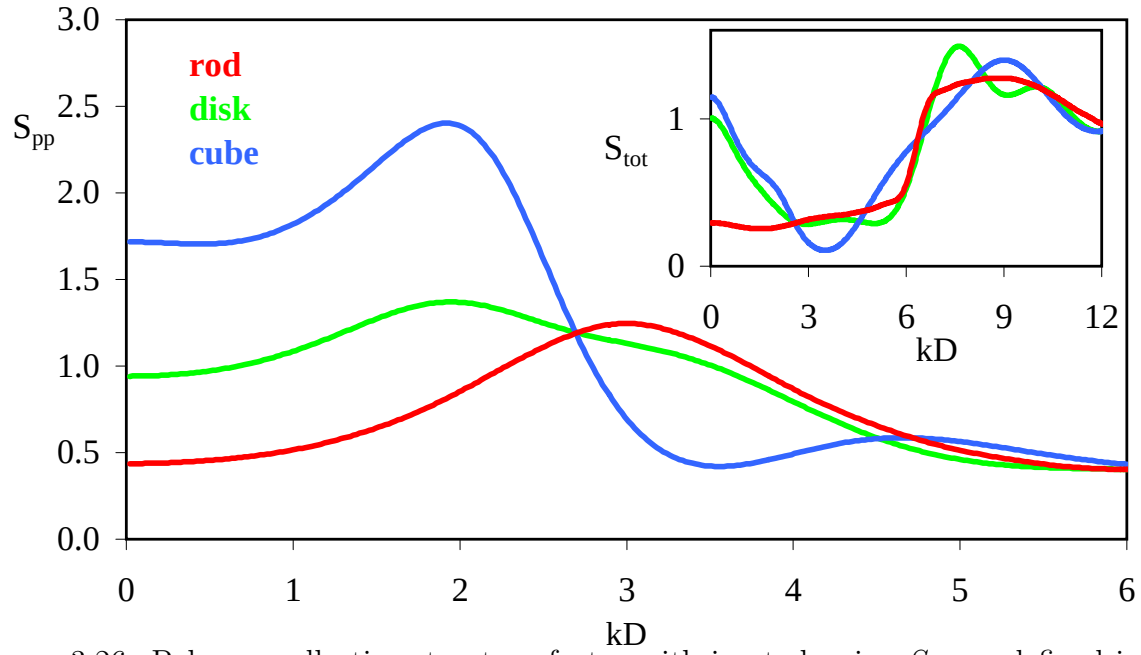

Figure 3.26: Polymer collective structure factor with inset showing S_{tot} as defined in Equation 2.11 on the bridging side of the miscibility window ($\epsilon_{pn} = 0.8$, $\alpha = 0.5$) at $\Phi = 0.3$.

Chapter 4

Comparison to Experiments

The strength (ϵ_{pn}) and spatial range of the monomer-particle attraction play a critical role in determining whether polymers mediate depletion aggregation (entropy-driven, high temperature phase separation), steric stabilization and good dispersion (homogeneous liquid), or local bridging of nanoparticles (enthalpy-driven, low temperature demixing). For intermediate ϵ_{pn} values, thermodynamically stable "bound polymer layers" form around nanoparticles resulting in a repulsive potential of mean force and a "miscibility window" in the phase diagram.[98] This result has recently been qualitatively confirmed for equilibrated silica-polyethyleneoxide (PEO) nanocomposites under index matching conditions which satisfy the hard filler criterion.[115,116] The identification of this experimental system affords the opportunity to use small angle x-ray scattering (SAXS) to probe the theoretical structure predictions for model hard sphere fillers over a wide range of length scales and volume fractions. Scattering of silica nanoparticles in the more hydrophobic, less strongly adsorbing polytetrahydrofuran (PTHF) matrix, and in PEO-ethanol mixtures of various compositions,[117] has also been measured. The chemical formulas of solvent and the two polymers, which can hydrogen-bond with hydroxyl groups on the silica surface, are sketched in Figure 4.1.

The focus of this chapter is to quantitatively confront theory and experiment for the silica-PEO and silica-PTHF nanocomposites, and establish how polymers mediate many body correlations between nanoparticles in the presence of variable interfacial cohesion. For the silica-PEO system, the effect of adding solvent (ethanol) on interfacial cohesion is also examined. A new theoretical model is developed that adjusts the total mixture packing fraction as fillers are added to the homopolymer matrix in

order to mimic equation-of-state effects expected to be operative at constant pressure. Special attention is paid to the packing fraction dependence of the particle osmotic compressibility (amplitude of long wavelength concentration fluctuations), and the intensity and location of the wide angle peak in the nanoparticle structure factor that quantifies the degree of local cage order and its characteristic length scale. The theoretical results for these quantities are shown to compare quite well to experimental observations. Moreover, for the unentangled chains studied, both theory and experiment show little dependence on molecular weight and exhibit a strong dependence on the chemically-specific interfacial attraction strength. A new theoretical model is also proposed and implemented to account for how solvent dilution modifies the effective monomer-filler cohesive attraction.

4.1 Experimental System and Measurements

Details of the experimental sample preparation and SAXS measurements of the collective nanoparticle (silica) structure factor, $S_{nn}(k)$, are documented elsewhere.[115,116] The three polymers studied by Anderson and Zukoski were PEO of molecular weights (MW) 400 and 1000, and polytetrahydrofuran (PTHF) of MW=1000. These low molecular weight polymers are all below the entanglement threshold of the pure polymer melts, thereby allowing the equilibration essential for comparison with the equilibrium theory. The silica particles have a volume averaged diameter of $D = 44 \pm 4$ nm. The polymers are well contrast matched with the nanoparticles, leading to minimal van der Waals attractions between fillers. Scattering experiments were performed at 75^oC.

To create a composite sample, the silica particles were first synthesized in ethanol solution and concentrated to a desired mass fraction. This solution was then mixed with polymer, and the solvent evaporated under conditions chosen to best disperse the particles. For the study on the effect of solvent, ethanol was added to make samples at various specific ethanol:polymer ratios. Filler volume fraction was computed using

the measured composite density, silica density, and particle and polymer (and ethanol if present) masses. The filler structure factor was determined by subtracting the pure polymer scattering intensity from the total composite SAXS intensity, assuming that cross terms can be neglected since the particle x-ray scattering is dominant. The collective nanoparticle structure factor was then determined in the standard manner by dividing the concentrated particle scattering intensity by its volume fraction weighted dilute particle limit analog.

The characteristic ratio for a chain of n backbone bonds, C_n, has been measured for PEO at large MW (110k) using neutron scattering and found to be 5.7 at 74^oC; the structurally similar PTHF should have a similar C_n.[118] Theoretical calculations for PEO yield a characteristic ratio of ~ 5.4 in the long chain limit, which decreases to ~ 5.0 (4.5) for PEO composed of 68 (27) backbone bonds.[119] The backbone chemical bond length is approximately $l_b \approx 0.15$ nm, and the angle between adjacent bonds is 68^o.[109] The number of backbone bonds is $\sim$ 27 for PEO 400, $\sim$ 68 for PEO 1000, and $\sim$ 70 for PTHF 1000. These values motivate the choice of chain length in the theoretical calculations.

4.2 Theoretical Model for Polymer-Nanoparticle Mixture

4.2.1 Choice of Parameters

The mixture model and theory employed is the same as described in Chapter 2.[91–93,98] The spinodal phase boundary is numerically inferred from the small wavevector upturn in the structure factor at values of ϵ_{pn} just before the equations cease to numerically converge. The spinodal phase boundary reported here is the last ϵ_{pn} which could be converged based on increments of 0.0001;[98] the difference between this value and an estimate of the spinodal location obtained by extrapolating $1/S_{nn}(k=0)$ or $1/S_{pp}(k=0)$ to zero (as often done experimentally) is not generally visible on the scale of the plots presented.

Recall that within the present model, the interfacial attraction strength ϵ_{pn} qualitatively determines the free energy change associated with transferring a monomer from the pure monomer fluid environment to the surface of a nanoparticle. In the language of traditional polymer mean field theory, this energy parameter sets the scale of a monomer level bare energetic "χ-parameter", and is expected to change when different polymers are used or upon addition of solvent (see section 4.4).

The degree of polymerization in the calculations is $N = 10$ or 100, the size asymmetry ratio $D/d = 10$, and the spatial range of attraction is $\alpha = 0.5$. These are typical values as motivated in prior studies,[91–93,98] and as such were not fine tuned for comparison to the present experimental data. Note that N=10 is roughly the number of monomers for PEO 400. The strength of the interfacial cohesion is varied widely ($0 \leq \epsilon_{pn} \leq 4$) in order to construct the spinodal phase diagram, and detailed analysis is performed for selected values that are relevant to the nanoparticle structure factors measured experimentally.

To further motivate the chosen values of N, consider the mapping of a polymer chain onto the FJC model. A standard approach is to require that the FJC model reproduces the largest length scales of the real polymer: the end-to-end distance and contour length. This mapping yields a statistical segment length of $C_n l_b \approx 0.75$ nm for PEO. The corresponding number of segments $N = N_{bb}/C_n$, where N_{bb} is the number of backbone bonds. For PEO 400 and 1000, $N_{bb} = 27$ and 68, while $C_n \approx 5$, which implies $N \approx 5$ and 13. However, a mapping based on global chain properties is not the most relevant for dense polymer melts or mixtures where packing effects are controlled by the local chain stiffness. The latter is characterized by the persistence length, $l_p = (C_n + 1)l_b/2 \approx 3l_b$, or one PEO monomer. This mapping then implies $N \approx 10$ and 25 for the two PEO samples, and the FJC "site" corresponds to one monomer yielding roughly $d \approx 0.6$ nm.

Modest changes in persistence length, α, and D/d were briefly investigated but did

not significantly modify the theoretical results, although increasing D/d makes the PRISM equations numerically more difficult to converge. Calculations are reported only for $\alpha = 0.5$ and $D/d = 10$ in order to realize the goal of employing just one material-specific adjustable parameter to perform the quantitative theory-experiment confrontation, while at the same time allowing comparison with prior published PRISM results.[98] Calculations for both $N = 10$ and 100 are presented, focusing on N=100 as in prior studies; these two values of N essentially bracket the relevant values for the two PEO samples studied experimentally, and the sensitivity to N is weak.

4.2.2 Adjusted Packing Fraction Description

An input to the theory is the monomer and particle packing fractions: $\eta_p \equiv \pi\rho_p d^3/6$ and $\eta_n \equiv \pi\rho_n D^3/6$. For simplicity, and due to the lack of a constant pressure mixture equation-of-state, theoretical studies have previously assumed a fixed melt-like total packing fraction of $\eta_t \equiv \eta_p + \eta_n = 0.4$[91–93,98] or 0.5.[94,95] However, recent experiments[115] have been performed well beyond these values, up to filler packing fractions of ~ 0.55. Physically, the interstices between nanoparticle surfaces are expected to be densely filled by monomers in real materials held at constant (atmospheric) pressure. This implies η_t should increase with nanoparticle volume fraction, in analogy with mixtures of small and large hard spheres.[120] This packing effect can be accounted for in a minimalist, but physically motivated and no adjustable parameter, manner. Specifically, for the pure polymer melt $\eta_{p0} = \eta_{t0} = 0.4$ is employed since it yields a realistic dimensionless isothermal compressibility, $S_{pp}(k = 0) \approx 0.2$, based on PRISM theory for a hard core FJC fluid.[73,91–93] The polymer packing fraction outside the volume excluded by nanoparticles is assumed to remain the same as in the pure melt, thereby yielding an "adjusted" total packing fraction of:

$$\eta_t = \eta_n + \eta_{p0}(1 - \eta_n(1 + d/D)^3) \tag{4.1}$$

This equation neglects the consequences of overlap of the excluded volume shells of nearby particles. A more accurate expression for the free volume, which has been employed in the study of hard sphere mixtures, yields a similar η_t at the large D/d and reasonable η_n values studied here.[120,121] The packing fraction of atomic hard sphere mixtures can also in principle be predicted by density functional theory[122] or the PY equation of state at constant pressure.[123] However, there are virtually no simulation nor experimental data for polymer nanocomposite densities as a function of mixture composition that would allow quantitative comparison with the theory, which makes it difficult to justify the use of more complicated adjustments of η_t as a function of η_n in this initial study. Moreover, the accurate computation of an equation-of-state using integral equation theory is generically difficult, and is particularly not appropriate for this model based on a single effective polymer-particle attraction.

As a first test of the adjusted packing fraction concept and demonstration of its importance at high filler volume fractions, the mixture bulk modulus K_B is computed as described in Chapter 2. In the pure polymer melt limit, the dimensionless (units of kT/d^3) $K_B = 4.49$ for $\eta_t = 0.4$, and $K_B(\eta_n = 0) = 29.9$ for $\eta_t = 0.55$. Using $d \approx 0.6$ nm yields reasonable dimensional values of the bulk modulus of the pure polymer.

Calculations of the nanocomposite bulk modulus divided by its pure polymer melt value as a function of nanoparticle volume fraction are shown in Figure 4.2, using $N = 100$, $D/d = 10$, $\alpha = 0.5$ and $\epsilon_{pn} = 0.5$. As discussed previously, the results are not sensitive to the precise values of the latter variables.[91–93] For the fixed η_t model, the bulk modulus decreases rapidly with η_n, and is massively reduced at high filler loadings, trends which are physically implausible for a constant pressure equation-of-state property. In strong contrast, there is a very modest reduction based on the adjusted η_t model. For example, at $\eta_n = 0.1$ the normalized bulk modulus decreases by $\approx 2\%$ for the adjusted model, compared to $\approx 34\%$ (52%) for the constant total packing fraction model of $\eta_t = 0.55$ (0.4). Experiments that measure the bulk modulus

of silica based PNCs are required to quantitatively test these calculations.

The spinodal phase diagram for the adjusted η_t model is compared with that for constant $\eta_t = 0.4$ and 0.55 models in Figure 4.3. In all cases, the phase diagrams show the classic depletion (bridging) phase separation at low (high) interfacial attraction, and a broad miscibility window at intermediate attraction strengths. Qualitatively, the adjusted η_t results are similar to those at $\eta_t = 0.4$ which have been reported previously,[98] although the bridging demixing region shifts to higher interfacial cohesion strengths resulting in a significant widening of the miscibility window. More dramatic changes relative to prior results are found for the fixed $\eta_t = 0.55$ system. Specifically, unusual bridging behavior occurs in the filler packing fraction regime of $\eta_n \sim 0.03$ to 0.21 where enhanced miscibility is predicted with increasing nanoparticle loading. This effect may be due to the initial unrealistically high and rapidly decreasing K_B of this system (or equivalently unrealistically small value of the pure melt dimensionless compressibility at atmospheric pressure), and provides further motivation for use of the adjusted η_t model.

The primary feature of the nanoparticle scattering function is the cage peak which quantifies the filler short range order on a length scale of $2\pi/k^*$, where k^* is the wavevector at the local maximum. Calculations of the intensity of the cage peak of the filler structure factor as a function of η_n at two values of ϵ_{pn} in the miscibility window for the three η_t models are compared in Figure 4.4. The solid line shows the results for the pure hard sphere fluid (vacuum solvent). At the larger $\epsilon_{pn} = 0.6$ for the adjusted η_t model, the bound polymer layer around each particle leads to increased cage scale order relative to pure hard spheres over the entire range of $\eta_n = 0$ to 0.55. At the lower $\epsilon_{pn} = 0.5$, there is slightly less bound polymer around the nanoparticles, and the degree of filler cage ordering is decreased. At very high η_n for this system, the cage peak becomes less intense than that of pure hard spheres. Both constant total mixture packing fraction models result in nonmonotonic behavior at high filler volume

fractions, a trend not seen in the experiments on PEO based nanocomposites as will be discussed below.

Recall that the primary aim is to compare the theoretical results with experiment changing only the interfacial cohesion parameter ϵ_{pn}. The experiments were performed up to $\eta_n \approx 0.55$, so the constant $\eta_t = 0.4$ model is not applicable. For both constant total volume fraction models, the pure hard sphere fluid result must be obtained as $\eta_n \to \eta_t$. However, a significant amount of polymer continues to be present in the experimental system even at $\eta_n \approx 0.55$. This is yet another reason that the adjusted packing fraction model is more appropriate to describe the experimental data.

4.3 Quantitative Comparison to Experiments in Two Polymer Melts

4.3.1 Filler Collective Scattering

Experimental nanoparticle structure factors are presented in Figure 4.5 for silica-PTHF and Figure 4.6 for silica-PEO (MW=1000, $N \approx 23$) at several filler packing fractions;[115] the complementary theoretical results for the adjusted η_t model at the same packing fractions ($\eta_n/\eta_t = 0.37$ and 0.56 for PTHF, and 0.37, 0.65, 0.81 for PEO) are also shown. As more particles are added to the nanocomposite, the structure factor shows enhanced local ordering (larger $S_{nn}(k^*)$) on a smaller length scale (larger k^*). The other interesting feature is $S_{nn}(k = 0)$, the filler dimensionless osmotic compressibility. Typically, the structure factor plateaus at low wavevector, though in the PTHF system at $\eta_n = 0.3$ a small upturn is seen at low k, signaling the system may be near phase separation. These long wavelength filler concentration fluctuations are enormously larger in the less interfacially cohesive PTHF system compared to the PEO-silica mixture.

The theoretical interfacial attraction strength has been adjusted to optimize agreement (by eye) of theory and experiment for $S_{nn}(k)$, to find moderate degrees of attraction: $\epsilon_{pn} = 0.35$ for PTHF, and $\epsilon_{pn} = 0.55$ for PEO. Overall, theory and experiment qualitatively, or nearly quantitatively, agree for all features over all length scales. The

results at fixed $\eta_t = 0.55$ are qualitatively similar, especially at low packing fractions; a representative example at the highest packing fraction (thin line on Figure 4.6) shows the small change compared to the adjusted η_t model. However, as mentioned above, the shape of the $S_{nn}(k^*)$ versus η_n curve does show a qualitative difference between these models. Note that the $\epsilon_{pn} = 0.55$ mixture is in the miscibility window of Figure 4.3, though relatively close to the depletion phase separation boundary (depletion first occurs just below $\epsilon_{pn} = 0.33$). This theoretical result is consistent with the experimental observation[115] of full miscibility to extremely high nanoparticle volume fractions for the silica-PEO mixture. In contrast, the $\epsilon_{pn} = 0.35$ system lies very close to depletion phase separation, and the experimental silica-PTHF system is observed to form a nonequilibrium solid (gel) at $\eta_n \approx 0.3$.

Figures 4.7, 4.8, and 4.9 compare theory and experiment for the three characteristic features of the collective filler structure factor of the PEO and PTHF based nanocomposites: inverse dimensionless osmotic compressibility, $S_{nn}^{-1}(k = 0)$, and the intensity, $S_{nn}(k^*)$, and location, k^*, of the cage peak, respectively. The analogous reference hard sphere fluid results are also shown. Consider first the two PEO systems. The theoretical results based on the adjusted total packing fraction model qualitatively or quantitatively agree with all the experimental trends: (i) little variation with degree of polymerization (N) for the more miscible system, emphasizing the locality of the physics under equilibrium conditions, (ii) reduced long wavelength concentration fluctuations, and (iii) greater cage scale order on a larger length scale (smaller k^*) relative to the pure hard sphere fluid analog. The latter two trends reflect polymer-mediated nanoparticle ordering due to thermodynamically stable bound polymer layers which result in the fillers appearing effectively larger than their bare diameter.[91–93,98] Quantitatively, at intermediate (low) packing fractions $S_{nn}(0)$ ($S_{nn}(k^*)$) is modestly over (under) predicted, and the cage size is a bit too small although the nearly linear variation of k^* with η_n is well captured.

To illustrate the remarkable sensitivity of the nanoparticle collective structure factor to interfacial cohesion strength predicted by the theory, and make contact with the new measurements on the silica-PTHF nanocomposite, calculations for two modestly smaller values of ϵ_{pn} are also shown in Figures 4.7, 4.8, and 4.9. One expects the latter systems have a weaker adsorbed polymer layer, resulting in less cage scale order (lower $S_{nn}(k^*)$) of smaller characteristic length scale (higher k^*), and a greater tendency for depletion aggregation (higher concentration fluctuations, $S_{nn}(k = 0)$). All these expectations are borne out by the calculations and experiments. As ϵ_{pn} decreases, the macroscopic nanoparticle concentration fluctuations do intensify, and are much larger than their pure hard sphere analogs, especially at high η_n. The cage peak weakens indicating reduced local order that is significantly less than the equivalent hard sphere fluid. For $\epsilon_{pn} = 0.35$ and $N = 100$, the magnitudes of $S_{nn}(0)$, $S_{nn}(k^*)$ and k^*, and their dependence on η_n, are remarkably similar to the silica-PTHF data thereby providing a consistent description of nanoparticle collective concentration fluctuations over all scales. Note that the average length scale of order decreases, and k^* is no longer linear with η_n.

Recall that adjusting ϵ_{pn} in the theory corresponds to changing the monomer-level effective attraction between the nanoparticle and polymer. The high sensitivity of the filler collective scattering patterns to the magnitude of the interfacial attraction allows the theory to be used as a tool to deduce ϵ_{pn} which otherwise is not directly measurable experimentally. Since the polymer-polymer and particle-particle interactions are hard core, ϵ_{pn} is proportional to the net reduction in energy upon transferring a monomer from a pure polymer environment to being in contact with the silica surface. Although the chemistry of silica, PEO and PTHF is complex, a simple model for ϵ_{pn} is to assume most of the polymer-particle attraction arises from hydrogen bonding between the hydroxyl group on the silica surface and the oxygen in the polymer. Specifically, PEO $(\text{-}C_2H_4O\text{-})_N$ and PTHF $(\text{-}C_4H_8O\text{-})_N$ are chemically similar except for the ratio of CH_2

groups to oxygen; PEO is 36 wt% oxygen, while PTHF is 22 wt% oxygen (as sketched in Figure 4.1). Hence, a crude estimate of the PTHF attraction is $\approx$ 60% that of PEO, yielding $\epsilon_{pn} = 0.6 \times 0.55 \approx 0.35$ for PTHF. This a priori estimate is remarkably consistent with the adsorption energy required for PRISM theory to reproduce well all the features of the PTHF nanocomposite scattering patterns in Figures 4.7, 4.8, and 4.9.

At lower $N = 10$, the theory compares best to the PTHF data when $\epsilon_{pn} \approx 0.4$ rather than 0.35. This modest difference is likely primarily a reflection of the limitation of the ideal freely jointed chain model used in PRISM theory. As the theoretical model systems which agree well with the PHTF scattering data are very close to the depletion phase boundary (at $\epsilon_{pn} = 0.35$ the $N = 10$ mixture is not miscible beyond $\eta_n = 0.11$), it is not unreasonable that the previously minor effect of N for the PEO mixture is exaggerated for its PTHF analog and coupled to the value of ϵ_{pn}. Within the theory, a primary effect of lowering N is to increase the bulk modulus: the $N = 10$ system appears slightly denser in the sense that interchain packing is better due to less intrachain overlaps,[72,73] and therefore experiences stronger depletion attraction than at $N = 100$. In real constant pressure systems, the bulk modulus should be approximately N-independent, so lowering the $N = 10$ polymer density would likely make the $N = 10$ nanocomposite results even closer to those at $N = 100$. This small second order effect is not further explored because it is not important for the comparisons made here. The $N = 10$, $\epsilon_{pn} = 0.35$ results show the mixture is approaching phase separation since $S_{nn}(0)$ increases sharply with η_n, and the cage peak is more intense and occurs at a higher wavevector than in the miscible case. All these trends reflect local nanoparticle aggregation as a precursor to depletion phase separation.

4.3.2 Polymer Collective Small Angle Scattering

The theory is now employed using the same model parameters determined above to make predictions for the polymer collective concentration fluctuations as encoded in $S_{pp}(k)$. This quantity is amenable to measurement using small angle neutron scattering and deuterium labeling. Figure 4.10 shows the polymer collective structure factor for the PTHF system ($\epsilon_{pn} = 0.35$), while Figure 4.11 shows the corresponding results for PEO ($\epsilon_{pn} = 0.55$). For the PEO system the fillers are surrounded by a strongly held bound polymer layer. As a consequence, an intense low wavevector, or "microphase separation like", peak emerges on a length scale controlled (to first order) by nanoparticle size. Its physical origin is an "imprinting" of filler order on the structurally perturbed adsorbed polymer layers.[91–93,98,101] The microphase peak location, $k^* \approx 2\pi/D$, shifts to higher wavevector, but its amplitude varies nonmonotonically, with increasing nanoparticle concentration. These trends arise from a compression of the bound layer around the filler and increasing inter-filler interference as nanoparticle loading increases. The long wavelength concentration fluctuations for the silica-PEO system (Figure 4.11) first decrease with increasing nanoparticle volume fraction, and then become nearly constant. There is little N dependence of $S_{pp}(k)$ for this miscible system, though lowering N slightly decreases the microphase peak and increases $S_{pp}(0)$.

At $\epsilon_{pn} = 0.35$ relevant to the PTHF mixture, there is less adsorbed polymer and therefore the peak in Figure 4.10 sometimes disappears or is only a shoulder. A feature at nonzero k^* may still exist with significant amplitude but is effectively "buried" under the large amplitude $k = 0$ peak associated with the osmotic compressibility contribution. The $N = 10$, $\eta_n = 0.1$ system is similar to its $N = 100$ analog at large wavevectors, but has even less bound polymer since it is closer to the depletion spinodal. Thus, no discernible shoulder in $S_{pp}(k)$ is seen as it sharply increases towards the $k = 0$ limit; this mixture is nearing spinodal phase separation and at higher η_n is immiscible.

The inset of Figure 4.11 shows the detailed variation of the microphase order parameter, $S_{pp}(k^*)$, with filler volume fraction. For the $\epsilon_{pn} = 0.35$ system that mimics the silica-PTHF nanocomposite, when a local maximum is present at $N = 100$, its intensity grows approximately linearly with η_n at intermediate filler loadings, but this maximum disappears at low and high η_t (and at all η_t for $N = 10$). Thus, a sharp filler scale peak in the polymer scattering may serve as an experimentally measurable indicator of the existence of a bound polymer layer with properties (e.g. local density) distinct from the bulk polymer melt far from filler surfaces. At $\epsilon_{pn} = 0.55$, the microphase order parameter first increases roughly linearly with η_n reflecting the growing amount of perturbed adsorbed polymer. However, $S_{pp}(k^*)$ then goes through a maximum and decreases at very high filler packing fractions. The latter trend occurs at both $N = 10$ and 100, although the value of the peak is somewhat smaller at lower N. This decrease in $S_{pp}(k^*)$ apparently arises from the overlap or sharing of bound layers on different nanoparticles, and the fact that most polymers are associated with filler and their total amount decreases with η_n.

4.3.3 Polymer-Mediated Filler Potential of Mean Force

To gain insight concerning the real space nanoparticle organization, Figures 4.12 and 4.13 present calculations of the filler potential of mean force, $W_{nn}(r) = -ln(g_{nn}(r))$, for the same systems as in Figures 4.10 and 4.11. With increasing nanoparticle volume fraction, the PMF has a deeper contact attraction and lower repulsive barrier, which reflects the many body interference of adsorbed polymer layers around different fillers. Lowering ϵ_{pn} from 0.55 to 0.35 enhances the contact depletion attraction and reduces the monomer scale oscillations in the PMF, presumably due to less bound layer interference between particles. Decreasing N from 100 to 10 exaggerates the monomer scale oscillations in W_{nn} for both ϵ_{pn} values, since the shorter polymer fluid appears more locally dense (higher bulk modulus) when compared at the same theoretical packing

fraction. This leads to qualitatively similar behavior but larger minima in the PMF at lower N.

The inset of Figure 4.13 plots the global minimum of W_{nn} as a function of η_n for both $N = 10$ and 100. At $N = 100$, low η_n and $\epsilon_{pn} = 0.55$, the global minimum of the PMF corresponds to filler "bridging" at an interparticle surface-to-surface separation of roughly two monomer diameters. As η_n increases, the bridging minimum weakens, and the contact aggregation minimum deepens, ultimately becoming the global minimum beyond $\eta_n \approx 0.23$. The global minimum when $\epsilon_{pn} = 0.35$ and 0.4 is always at particle contact since there is less interfacial attraction to overcome entropic depletion and the driving force for bridging is weaker.

Although PRISM is an equilibrium theory, recent progress in the area of sticky colloid suspensions[32,35,124] suggests that when the minimum in $W_{nn}(r)$ becomes sufficiently deep ($\sim 4 - 5kT$) interparticle collisions can become irreversible on the experimental time scale resulting in a kinetically arrested "gel". Based on this scenario, the results in Figures 4.12 and 4.13 suggest that the lower ϵ_{pn} systems (silica-PTHF) may form a gel at relatively low η_n, in contrast to the $\epsilon_{pn} = 0.55$ system (silica-PEO) which should remain stable up to high η_n. This theoretical deduction is qualitatively consistent with rheological measurements[115,125] which find a gel-like transition in silica-PTHF at $\eta_n \approx 0.265$, while PEO samples are fluid. Moreover, the nonequilibrium kinetic arrest appears to be correlated with the greatly enhanced long wavelength nanoparticle concentration fluctuations (large $S_{nn}(k = 0)$) as seen in Figure 4.7, a trend which is properly captured by the theory. Such a connection between gelation due to contact particle aggregation and incipient phase separation has been emphasized in recent studies of suspensions of attractive spherical particles.[126]

4.4 Effect of Solvent Dilution

In the previous section, changing the polymer chemistry is described as one approach to experimentally vary the filler-polymer interfacial adsorption strength. A faster and simpler way of fine-tuning the effective ϵ_{pn} may be to add solvent to the nanocomposite. In principle, dilute polymers in a good solvent will adsorb less strongly (or not at all) compared with those in the melt, as they experience an additional free energy loss upon leaving the good solution to contact the particle surface. The adsorption strength of intermediate concentrations of polymer in a solvent is expected to vary monotonically between these extremes. Conversely, increased adsorption strength is expected for polymers in a poor solvent. The specific version of PRISM theory used to date for nanocomposites has been formulated and tested for dense systems, and dilute polymer-particle mixtures are not explored. Hence, the focus is on particle-polymer-solvent mixtures where the polymer:solvent volume fraction ratio is 0.5 or greater. In such a case, the polymer is expected to retain meltlike characteristics and the FJC model continues to be useful. Even these relatively small amounts of solvent added to a nanocomposite may modify the effective ϵ_{pn} enough to have important effects, especially near a phase boundary where the system is very sensitive to such changes.

4.4.1 Choice of Density and Interfacial Attraction

Scattering data for the specific experimental system of silica in a PEO/ethanol mixture (of various constant polymer:solvent ratios) have been generously provided by So Youn Kim and Charles Zukoski.[117] This section focuses on which theoretical parameters may best model the interactions of these components. The choice of ethanol roughly chemically mimics the polymer monomers, as each are composed of two saturated carbons and an oxygen, as shown in Figure 4.1. The oxygen of ethanol is in a hydroxyl group and should be slightly more able to more strongly hydrogen bond than the oxygen of PEO which is connected to two carbons (except for the OH groups at the polymer

ends). Ignoring this chemical difference as a first approximation, the only difference between the monomer and solvent is size. A theoretical segment is a sphere of diameter d which represents several (~ 3) PEO monomers, each approximately the size of ethanol. Due to its smaller size, and for simplicity, ethanol is represented only implicitly (in the continuum limit), but it fills volume around the nanoparticles in the same manner as polymer. Therefore, the total packing fraction of the system is adjusted as particles are added as described in section 4.2.2. Since only the polymer is explicitly represented, the initial packing fraction is reduced by polymer/(polymer+solvent) volume fraction, f_p (which is held constant as particles are added). In effect, $\eta_{t0} = 0.4$ from the previous sections is replaced by the quantity $0.4 f_p$.

Because the monomers are represented as hard spheres and solvent by vacuum, the interfacial attraction strength ϵ_{pn} actually represents the net enthalpic gain upon transferring a monomer from the bulk to the particle surface. In the previous section this value was $\epsilon_{pn} = 0.55$ for the PEO melt and silica. When the monomer instead originates from the bulk polymer/solvent mixture, the enthalpic considerations upon its placement near the particle surface are: loss of polymer-solvent interactions (strength ϵ_{ps}), loss of nanoparticle-solvent interactions (strength ϵ_{ns}), and gain of solvent-solvent interactions (strength ϵ_{ss}). The former two occur with frequency proportional to the fraction of solvent $(1 - f_p)$ while the latter is proportional to $(1 - f_p)^2$, as described in the following equation.

$$\epsilon_{pn,effective} = \epsilon_{pn,melt} - (1 - f_p)\epsilon_{ps} - (1 - f_p)\epsilon_{ns} + (1 - f_p)^2 \epsilon_{ss} \tag{4.2}$$

Assuming the solvent is chemically the same as the monomer, its interactions with itself and with the monomer can be modeled as athermal ($\epsilon_{ps} = \epsilon_{ss} = 0$) and its interaction with the nanoparticle should then be the same as that of the monomer ($\epsilon_{ns} = \epsilon_{pn,melt}$),

which reduces Equation 4.2 to:

$$\epsilon_{pn,effective} = f_p \epsilon_{pn,melt} = 0.55 f_p \tag{4.3}$$

In this simple zeroth order model with no adjustable parameters, the polymer-filler interfacial attraction strength linearly decreases to zero with polymer/(polymer+solvent) volume fraction.

4.4.2 Effects of Interfacial Attraction and Polymer Density

According to the above section, the theory accounts for the addition of solvent to the polymer nanocomposite by both reducing the polymer number density and changing the effective interfacial adsorption strength. To evaluate how these changes affect the composite structure, calculations were performed based on implementation of these two changes both separately and simultaneously.

Figure 4.14 shows the theoretical inverse of the nanoparticle osmotic compressibility as a function of η_n. The melt case, as discussed and compared to experiment in the previous section, is given by the solid black line, while the pure hard sphere value is given by the black dashed line for reference. Also discussed above, decreasing ϵ_{pn} for the melt case (thin solid lines) dramatically increases $S_{nn}(0)$, especially as the system nears depletion phase separation. At constant $\epsilon_{pn} = 0.55$, decreasing f_p to 0.8 has a negligible effect, but by $f_p = 0.6$, $S_{nn}(0)$ is increased slightly relative to the melt behavior. Though decreasing either f_p or ϵ_{pn} alone increases $S_{nn}(0)$, if these quantities are decreased together according to Equation 4.3 (thick solid lines) the increase in $S_{nn}(0)$ is not nearly as large as predicted based on simply reducing ϵ_{pn}. Local polymer density drives the depletion attraction, so it is reasonable that decreasing the amount of polymer has little effect in the miscible regime but a much greater effect at low ϵ_{pn}, and acts to push the system further from strong depletion behavior.

Figure 4.15 presents the intensity of the nanoparticle structure factor cage peak for the same systems as Figure 4.14, and Figure 4.16 shows its wavevector location k^*. Again, decreasing f_p at constant ϵ_{pn} has only a small effect. $S_{nn}(k^*)$ at moderate to high η_n varies nonmonotonically as ϵ_{pn} is lowered. At first the cage peak amplitude decreases due to a weaker bound layer and less local order. Further lowering ϵ_{pn} near depletion phase separation enhances the cage peak as particles begin to cluster, and the peak moves to larger wavevectors corresponding to a shorter filler ordering length scale with little or no adsorbed polymer. This enhancement of $S_{nn}(k^*)$ due to strong depletion is not observed (or is small) in the case that f_p is reduced along with ϵ_{pn}, as the smaller amount of polymer places this system further from depletion phase separation.

Intuitively, adding solvent decreases the strength of the filler-induced peak in the collective polymer structure factor, shown for a single $\eta_n = 0.3$ in Figure 4.17. The peak in S_{pp} also moves to lower wavevector and can become (depending on η_n) only a shoulder of the zero wavevector peak as f_p is reduced from 1 to 0.5. The primary effect on the filler potential of mean force (shown for $\eta_n = 0.3$ in Figure 4.18) is to decrease the monomer induced oscillations. This weakens both the polymer induced repulsive barrier and bridging minima. Decreasing ϵ_{pn} at a constant $f_p = 1$ should drastically deepen the depletion minimum in the PMF, however, concurrently decreasing f_p acts to keep the contact minimum relatively constant. At $\eta_n = 0.2$, decreasing f_p from 1 to 0.5 lowers $W_{nn}(0)$ from -1 to $-2kT$, and this effect is smaller and nonmonotonic (decreasing then increasing contact value as a function of f_p) at high η_n.

4.4.3 Comparison to Experiment

Nanoparticle collective scattering profiles for the PEO/ethanol/silica system were obtained by So Youn Kim and Charles Zukoski. The theoretical parameters for comparison to this system were set as described above: the melt $\eta_{t0} = 0.4$ and $\epsilon_{pn} = 0.55$, and

η_t is adjusted as a function of η_n as in prior melt work, and as solvent is added both η_{t0} and ϵ_{pn} are reduced linearly towards zero in the dilute polymer limit.

Figure 4.19 shows the comparison of theoretical and experimental results for the inverse of the silica dimensionless osmotic compressibility. This quantity is lowered (more filler concentration fluctuations) as solvent is added by approximately the same amount, and eventually crosses the pure hard sphere result, for both the theory and experiment. The experimental and theoretical particle cage peak intensity in Figure 4.20, and wavevector location in Figure 4.21, also compare favorably. At very low η_n, as observed for the melt, $S_{nn}(k^*)$ is underpredicted and k^* is overpredicted. At high η_n, adding solvent reduces $S_{nn}(k^*)$ by a similar amount for both theory and experiment. The shape of the theoretical $S_{nn}(k^*)$ versus η_n curves at low $f_p = 0.5$ and 0.6 (at first relatively slowly increasing then an upturn at high η_n) implies these systems are experiencing slightly stronger depletion than indicated by the experiment. This is also confirmed by the increase in k^* for the theoretical but not experimental results at these lower values of f_p.

4.5 Summary

This chapter presents a systematic combined theory-experiment quantitative analysis of adsorbing polymer-mediated structural organization of nanoparticles in miscible polymer nanocomposites. The microscopic statistical mechanical theory can qualitatively, and in some cases nearly quantitatively, account for the observed structural effects over a wide range of length scales, filler volume fractions, and variable interfacial cohesion. Prior PRISM theory work explored only a mixture model at constant total packing fraction of 0.4[91–93,98]or 0.5.[94,95] However, the scattering of silica particles in PEO was measured up to nanoparticle packing fractions of 55%, thereby motivating the formulation of a different model for the PNC total packing fraction. Specifically, in order to mimic the expected constant pressure equation-of-state effects, the total

mixture packing fraction is increased as nanoparticles are added to the polymer melt in such a manner that the polymer packing fraction in the space available to monomers is constant. This "adjusted packing fraction" model results in a significantly reduced (and physically sensible) variation of the nanocomposite bulk modulus with filler loading, and improved agreement with the experimental structure factors. The theoretical trend in the particle osmotic compressibility as a function of filler packing fraction is qualitatively similar to experiment, as is the height and location of the particle cage peak in the structure factor. The predicted changes in these structural quantities with decreasing interfacial attraction match well the dramatic effects observed in experiment when the more weakly adsorbing PTHF is used. Both theory and experiments at show little dependence of nanoparticle concentration fluctuations on chain length low molecular weights.

The spinodal phase boundary for the adjusted packing fraction model was obtained and compared to that at constant packing fractions of 0.55 and 0.4. Significant quantitative differences are found, especially on the bridging side of the phase diagram. However, the most striking aspect that a miscibility window exists remains true. A prior comparison of PRISM theory to small angle neutron scattering experiments on a silica-polystyrene nanocomposite up to volume fractions of 0.3 suggested the existence of a "microphase-like" peak on the filler length scale in the collective polymer structure factor.[101] This peak was again found for the theoretical system which modeled best the miscible PEO-silica data, but not for the less strongly adsorbing PTHF-silica analog. The filler potential of mean force was also reported.

Finally, the changes in the particle structure factor are of similar magnitude when solvent is added either experimentally or theoretically. Theoretically changing only polymer volume fraction f_p or only interfacial cohesion strength each present a qualitatively different picture than changing both to account fully for solvent addition. Changing only f_p very modestly affects the nanoparticle structure for the moderate to

high f_p studied here. This confirms that the experimental method of adding solvent can be used to effectively tune the interfacial attraction. Especially near the depletion demixing boundary in the melt, the dilution of polymer (not only the effective change in cohesion) is relevant and must be modeled in order to understand the effect of solvent on polymer nanocomposite structure.

4.6 Figures

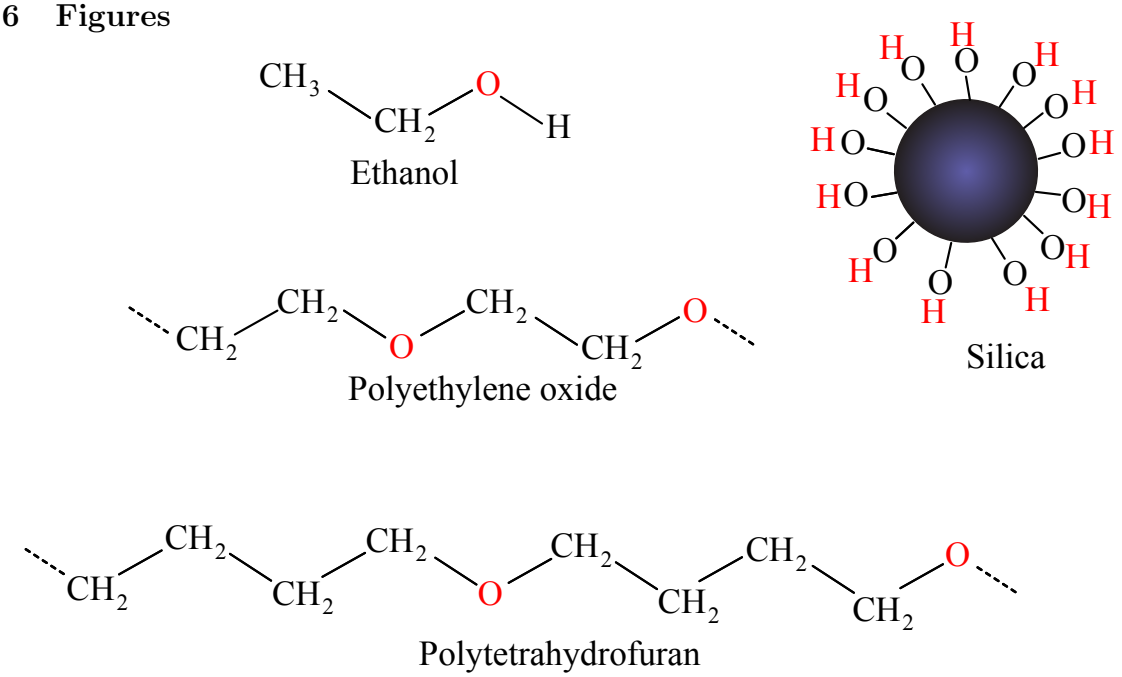

Figure 4.1: Chemical formulas of the solvent and two polymers used in scattering experiments. All are expected to hydrogen bond with hydroxyl groups on the Stöber process silica nanoparticle.

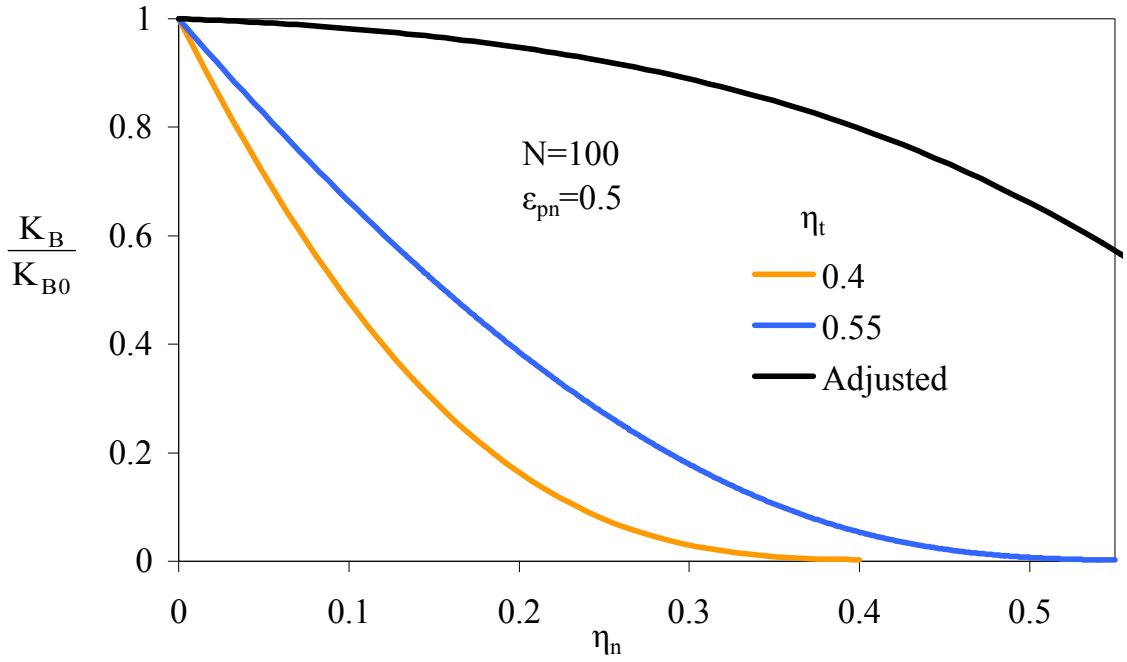

Figure 4.2: Theoretical bulk modulus normalized by its pure polymer melt value as a function of filler packing fraction for the three indicated mixture total packing fraction models. System parameters are: $N = 100$, $D/d = 10$, $\alpha = 0.5$ and $\epsilon_{pn} = 0.5$.

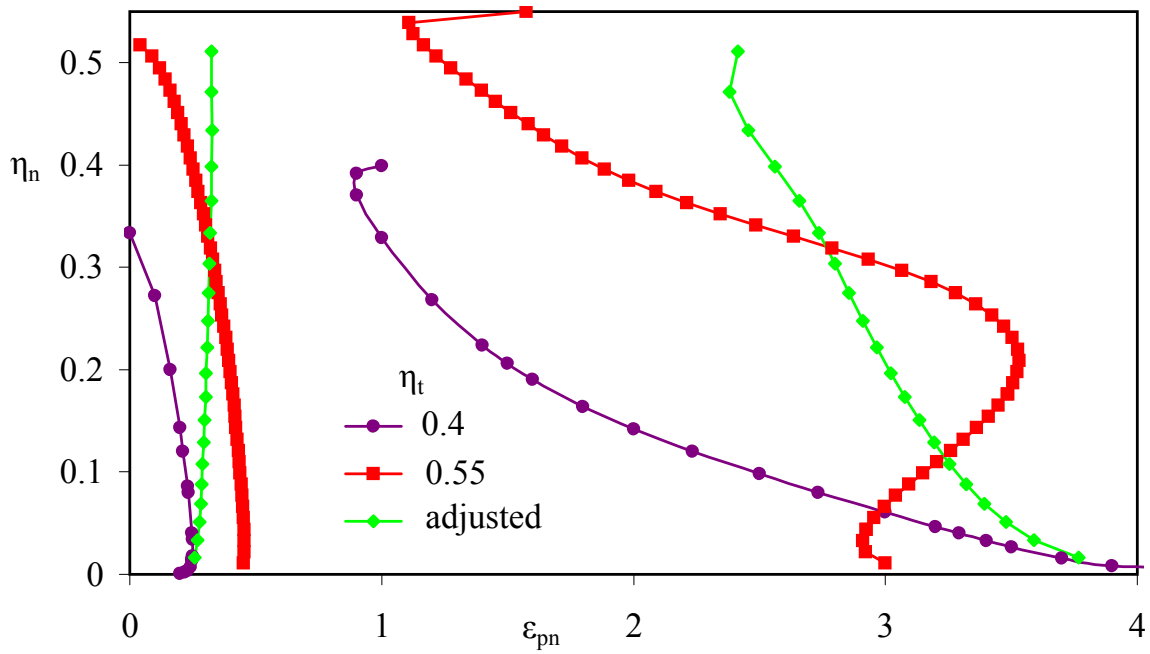

Figure 4.3: Filler packing fraction at the theoretical spinodal phase separation boundary as a function of interfacial attraction strength for the three indicated mixture total packing fraction models, for $N = 100$, $D/d = 10$, and $\alpha = 0.5$.

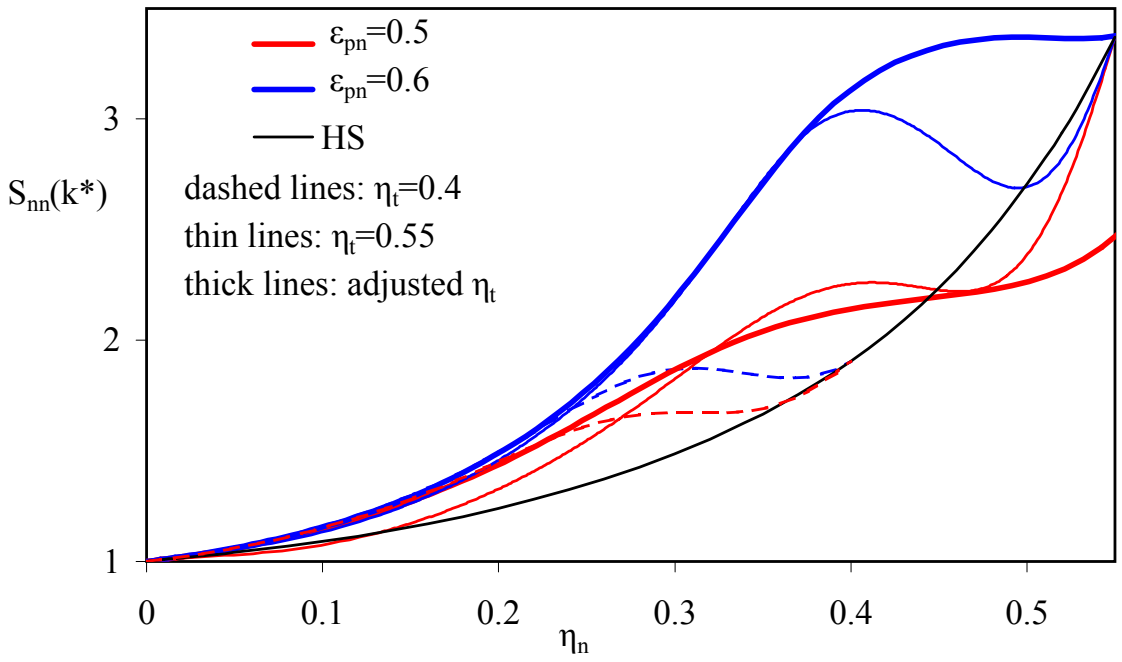

Figure 4.4: Intensity of the nanoparticle wide angle cage peak at $k = k^*$ as a function of filler packing fraction for the three indicated mixture total packing fraction models, for $N = 100$, $D/d = 10$, and $\alpha = 0.5$.

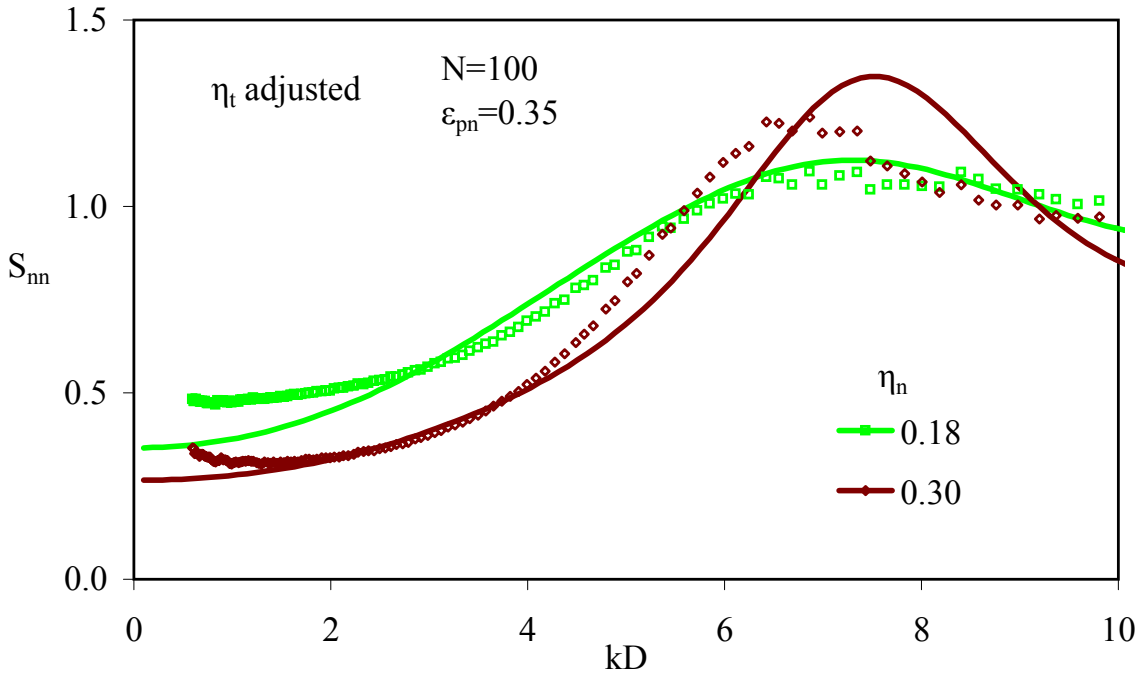

Figure 4.5: Collective nanoparticle structure factor as a function of dimensionless wavevector. Curves are PRISM theory results for $N = 100$, $D/d = 10$, $\alpha = 0.5$, $\epsilon_{pn} = 0.35$ at various filler packing fractions using the adjusted η_t model. Symbols indicate experimental data for silica-PTHF (MW=1000).

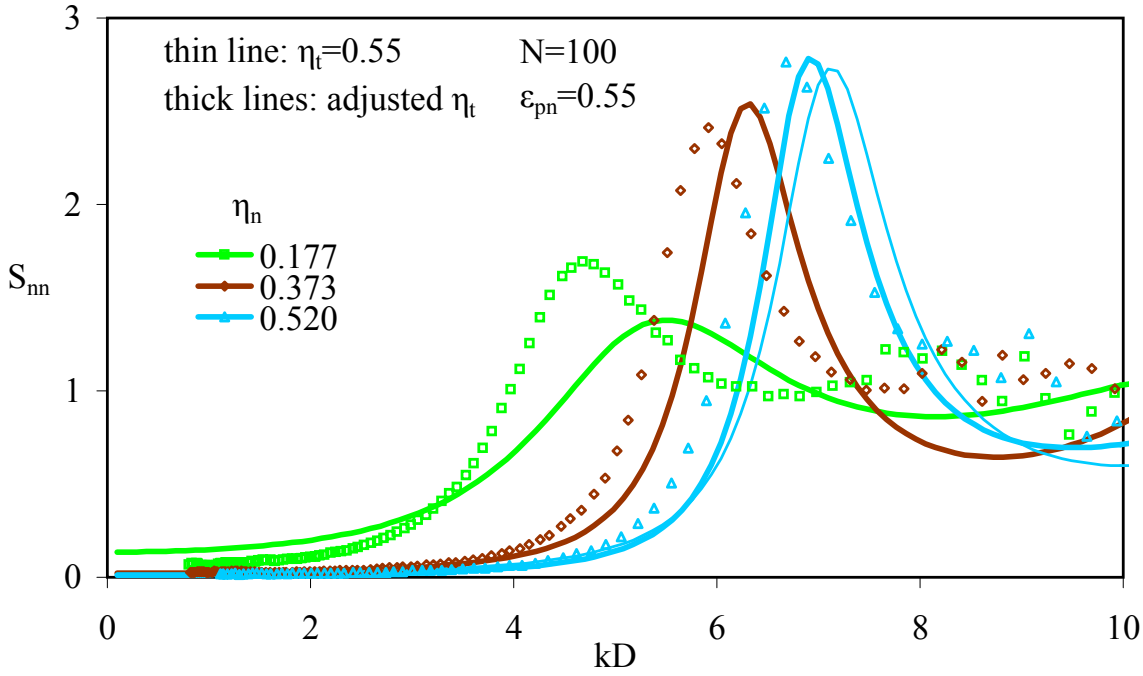

Figure 4.6: Collective nanoparticle structure factor as a function of dimensionless wavevector. Curves are PRISM theory results for $N = 100$, $D/d = 10$, $\alpha = 0.5$, $\epsilon_{pn} = 0.55$ at various filler packing fractions. Thick lines use the adjusted η_t model; thin line for $\eta_n = 0.52$ is at $\eta_t = 0.55$. Symbols indicate experimental data for silica-PEO (MW=1000).

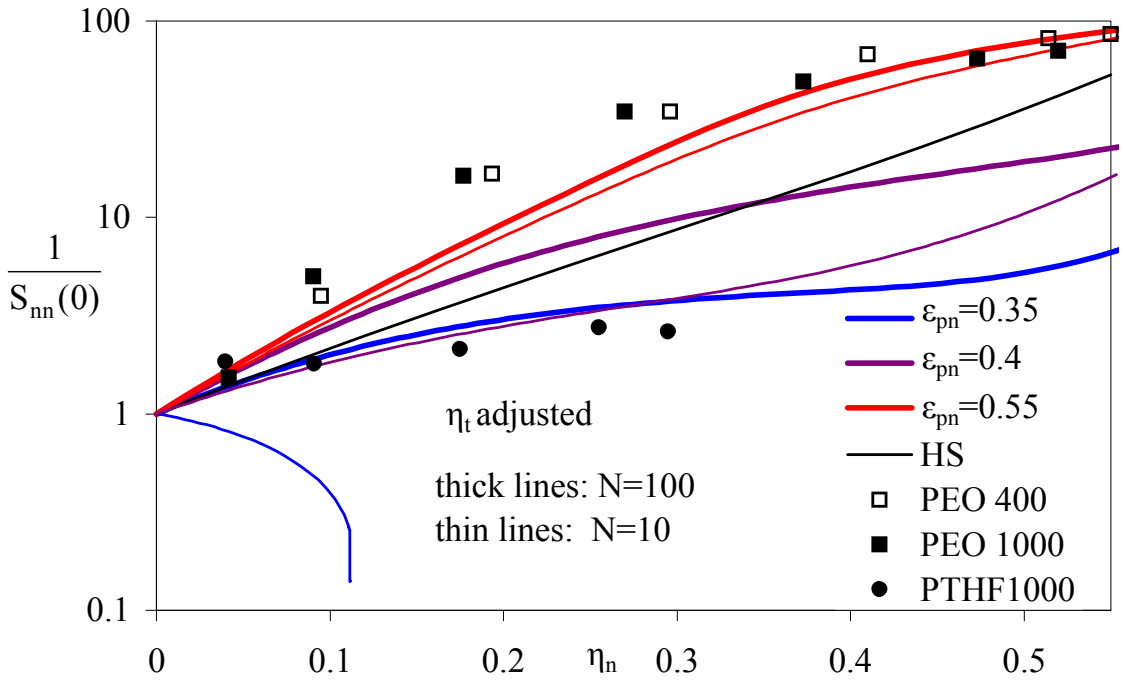

Figure 4.7: Inverse of the nanoparticle dimensionless osmotic compressibility as a function of filler packing fraction. Colored (thick ($N = 100$), thin ($N = 10$)) PRISM curves are for $D/d = 10$, $\alpha = 0.5$ based on the adjusted η_t model; black curve is for a pure hard sphere fluid (polymer replaced by vacuum). Experimental data are for silica-PEO (squares) and silica-PTHF (circles) of MW = 400 (open squares) and 1000 (solid symbols).

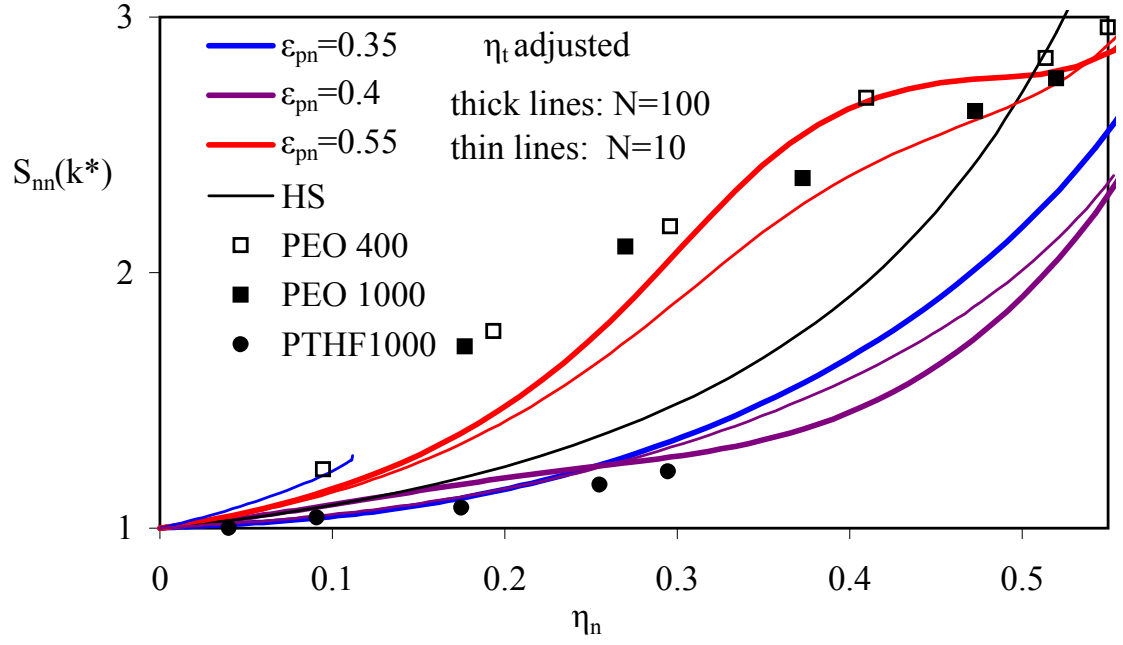

Figure 4.8: Height of the cage peak of the nanoparticle structure factor as a function of filler packing fraction. Colored (thick ($N = 100$), thin ($N = 10$)) PRISM curves are for $D/d = 10$, $\alpha = 0.5$ based on the adjusted η_t model; black curve is for a pure hard sphere fluid (polymer replaced by vacuum). Experimental data are for silica-PEO (squares) and silica-PTHF (circles) of MW = 400 (open squares) and 1000 (solid symbols).

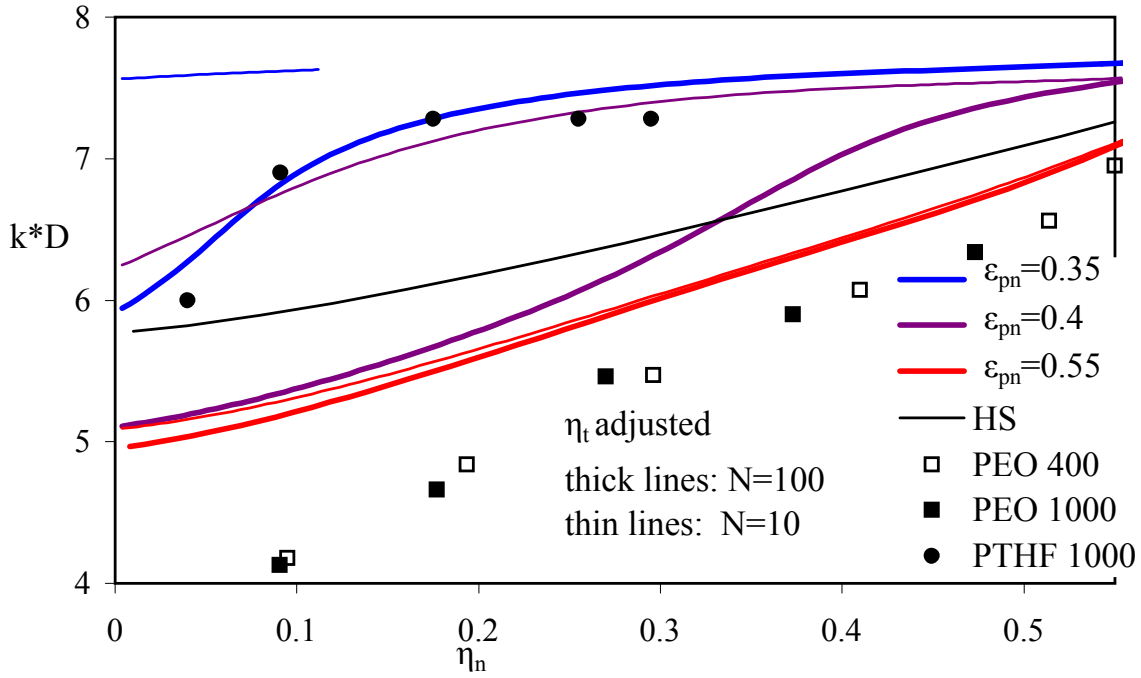

Figure 4.9: Wavevector location of the cage peak of the nanoparticle structure factor as a function of filler packing fraction. Colored (thick ($N = 100$), thin ($N = 10$)) PRISM curves are for $D/d = 10$, $\alpha = 0.5$ based on the adjusted η_t model; black curve is for a pure hard sphere fluid (polymer replaced by vacuum). Experimental data are for silica-PEO (squares) and silica-PTHF (circles) of MW = 400 (open squares) and 1000 (solid symbols).

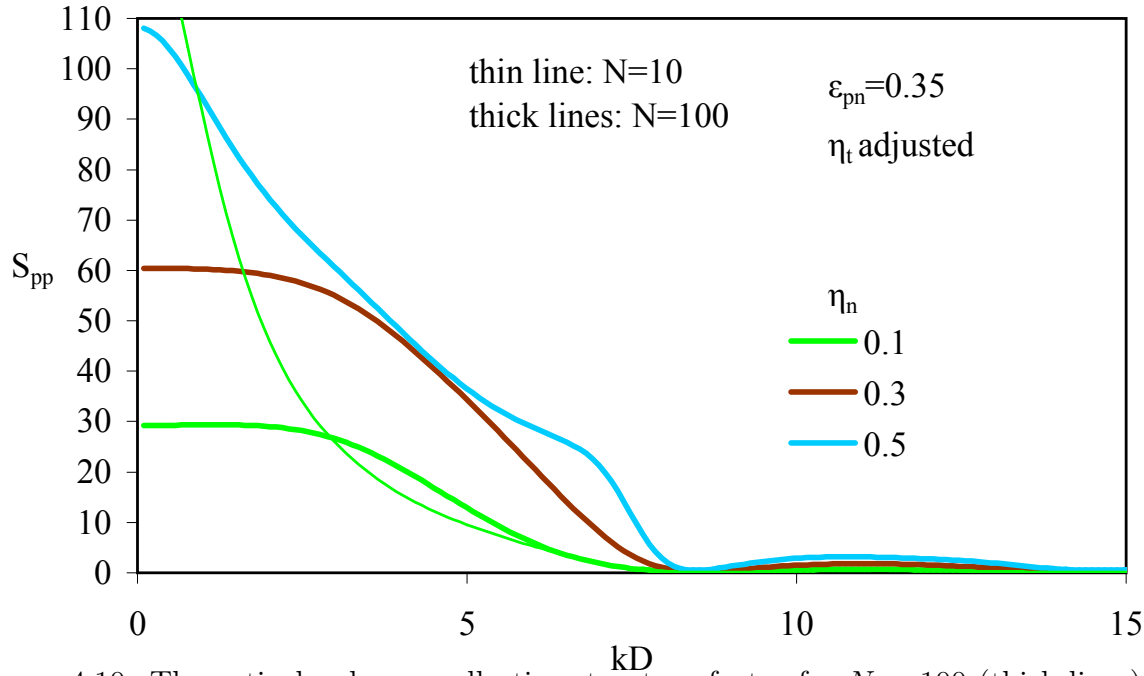

Figure 4.10: Theoretical polymer collective structure factor for $N = 100$ (thick lines) and $N = 10$ (thin line), $D/d = 10$, $\alpha = 0.5$, adjusted η_t model, $\epsilon_{pn} = 0.35$.

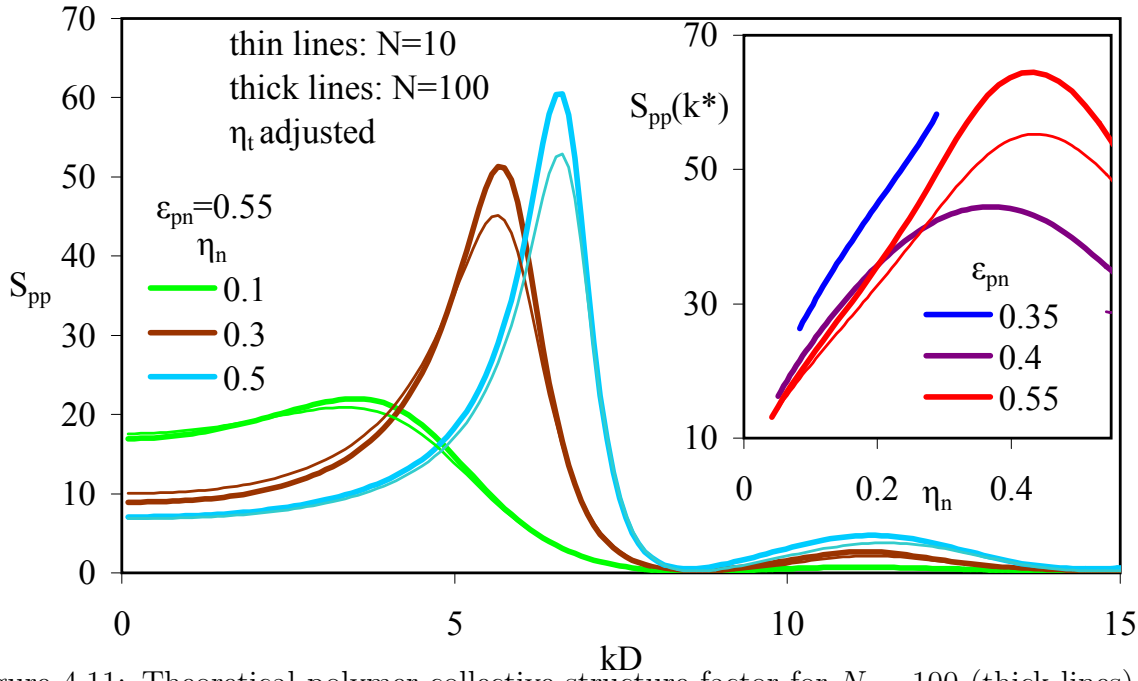

Figure 4.11: Theoretical polymer collective structure factor for $N = 100$ (thick lines) and $N = 10$ (thin lines), $D/d = 10$, $\alpha = 0.5$, adjusted η_t model, $\epsilon_{pn} = 0.55$. Inset shows the intensity of the microphase-like peak (if present) as a function of total packing fraction for three values of ϵ_{pn}.

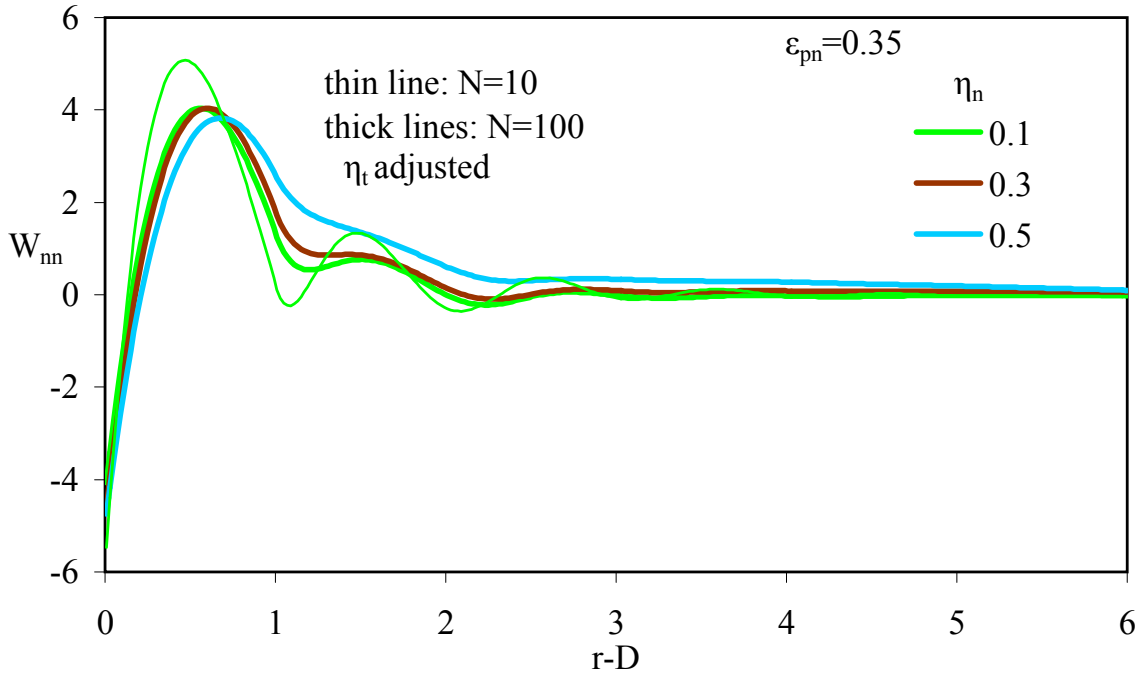

Figure 4.12: Nanoparticle potential of mean force as a function of surface-to-surface separation for $N = 100$ (thick lines) or $N = 10$ (thin line), $D/d = 10$, $\alpha = 0.5$, adjusted η_t model, and $\epsilon_{pn} = 0.35$.

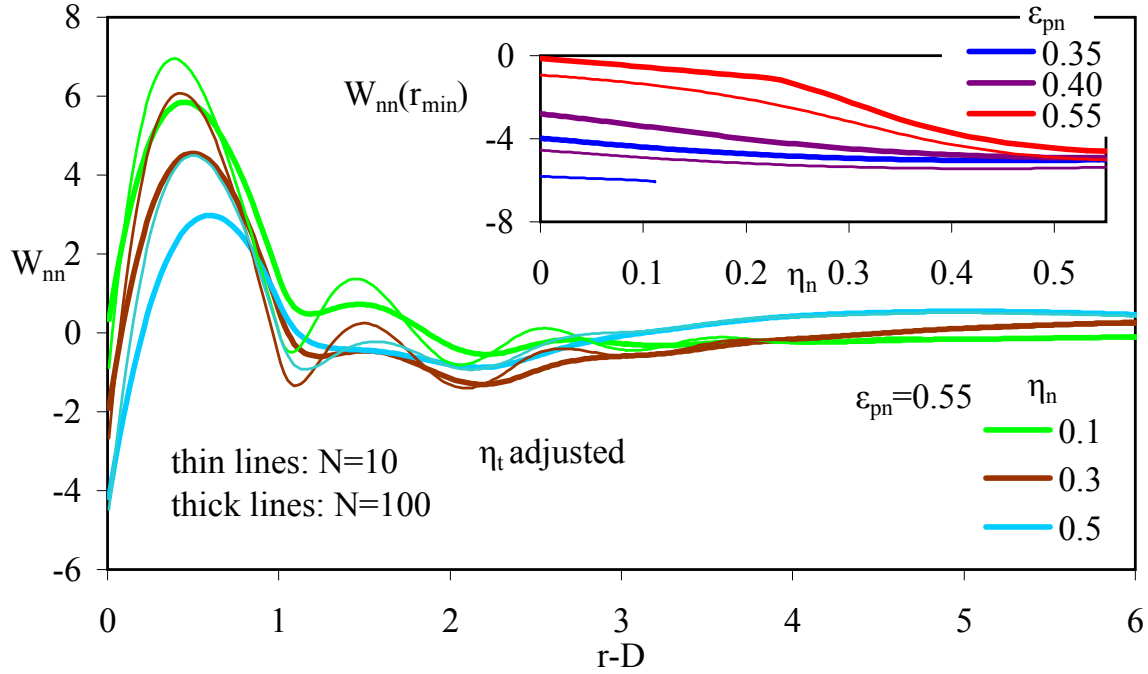

Figure 4.13: Nanoparticle potential of mean force as a function of surface-to-surface separation for $N = 100$ (thick lines) or $N = 10$ (thin lines), $D/d = 10$, $\alpha = 0.5$, adjusted η_t model, and $\epsilon_{pn} = 0.55$. Inset shows the value of the global minimum of W_{nn} as a function of nanoparticle packing fraction for various ϵ_{pn}.

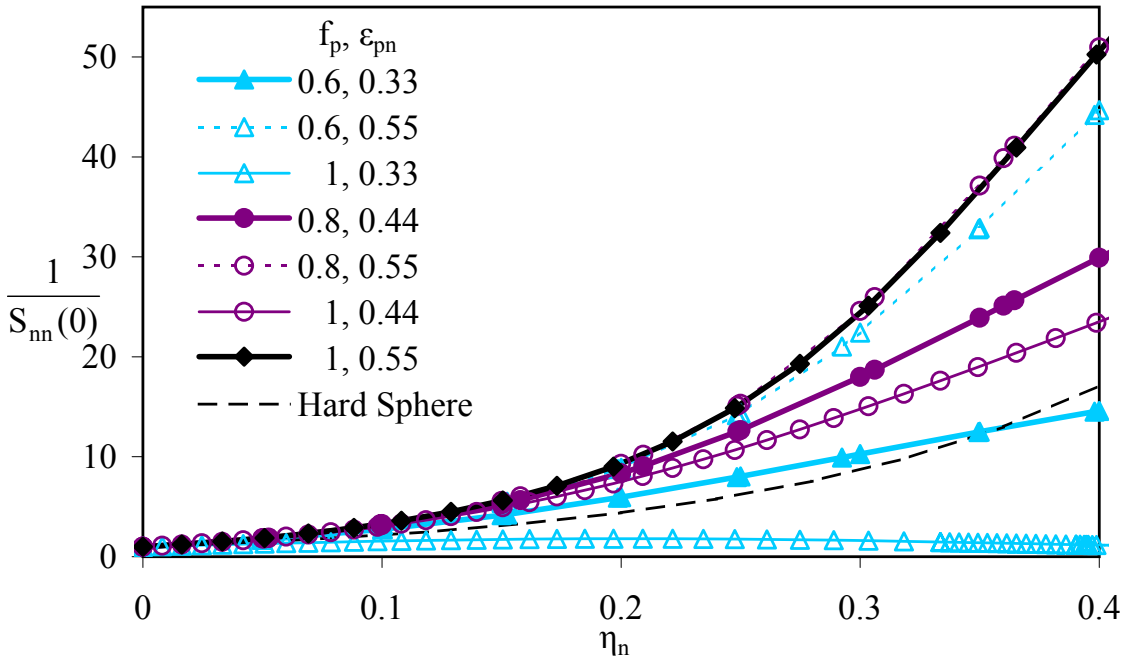

Figure 4.14: Inverse of particle osmotic compressibility versus particle packing fraction, using an adjusted total packing fraction with an initial polymer packing fraction of $\eta_{t0} = 0.4 f_p$ at the indicated values of ϵ_{pn}.

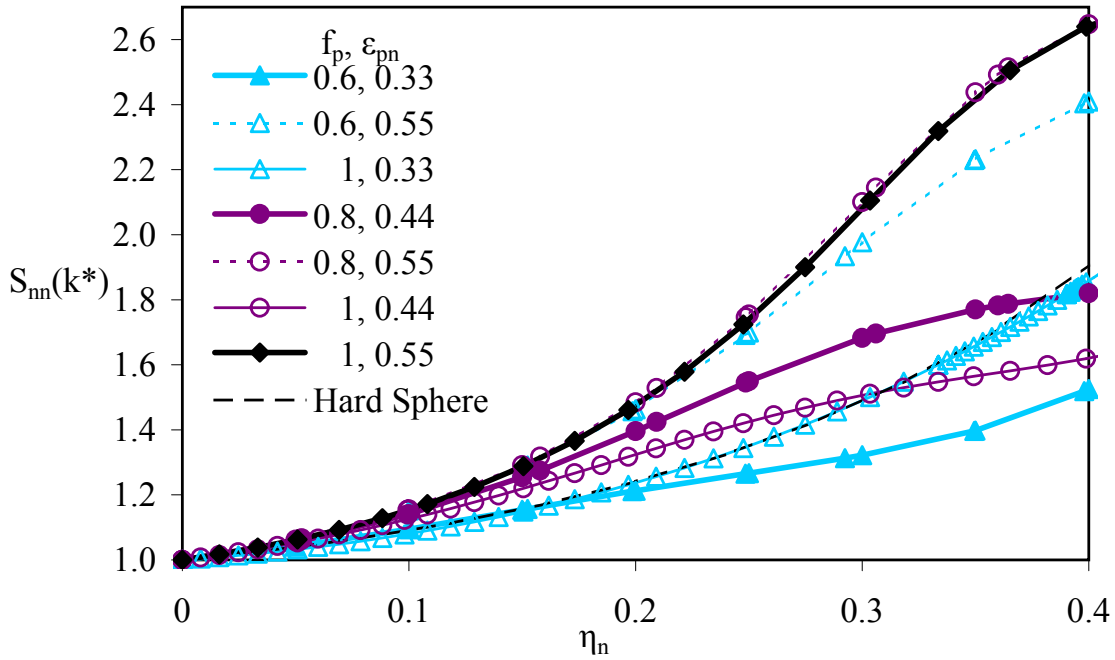

Figure 4.15: Height of cage peak in the particle structure factor versus particle packing fraction, using an adjusted total packing fraction with an initial polymer packing fraction of $\eta_{t0} = 0.4 f_p$ at the indicated values of ϵ_{pn}.

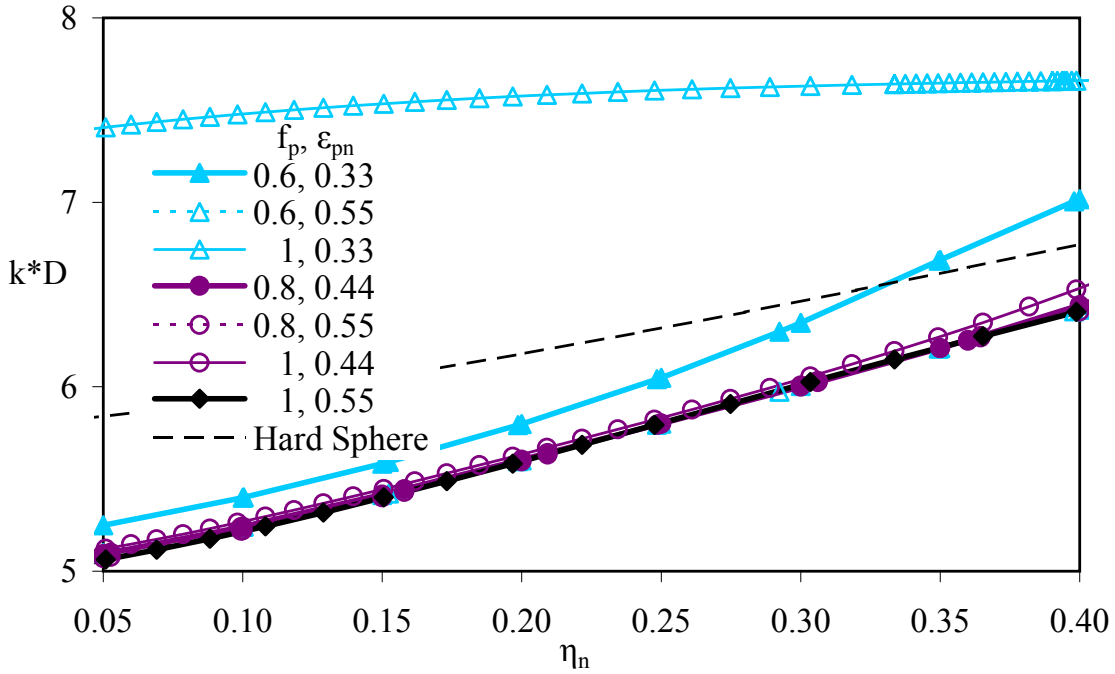

Figure 4.16: Wavevector location of cage peak in the particle structure factor versus particle packing fraction, using an adjusted total packing fraction with an initial polymer packing fraction of $\eta_{t0} = 0.4 f_p$ at the indicated values of ϵ_{pn}.

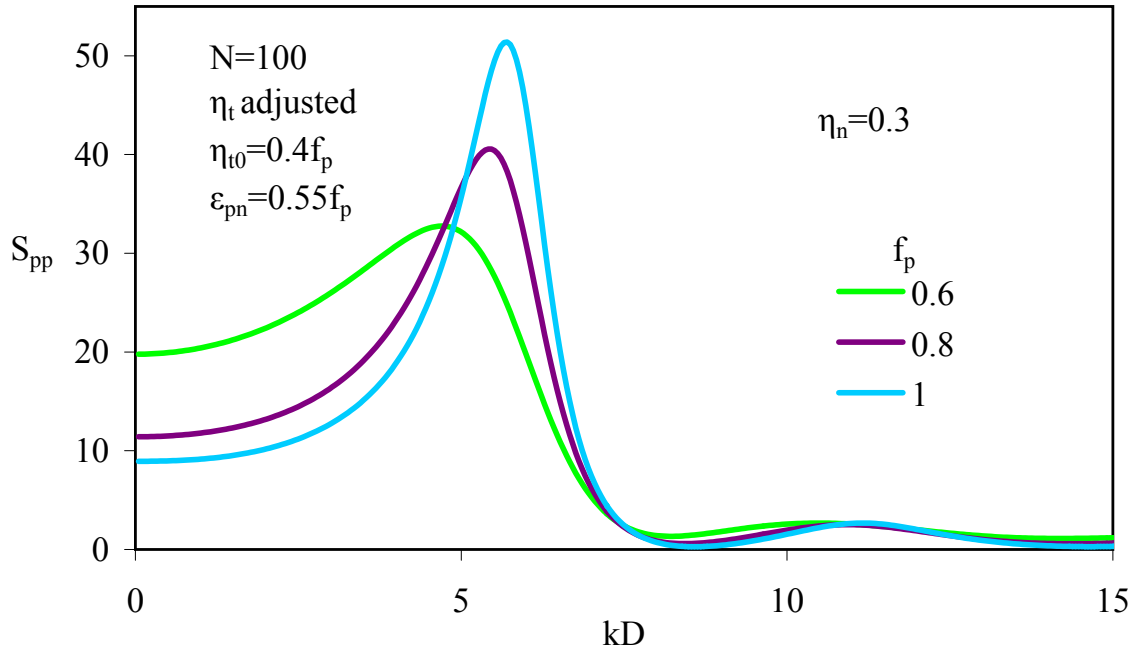

Figure 4.17: Polymer structure factor at particle packing fraction of 0.3, using an adjusted total packing fraction with an initial polymer packing fraction of $\eta_{t0} = 0.4f_p$ and $\epsilon_{pn} = 0.55f_p$.

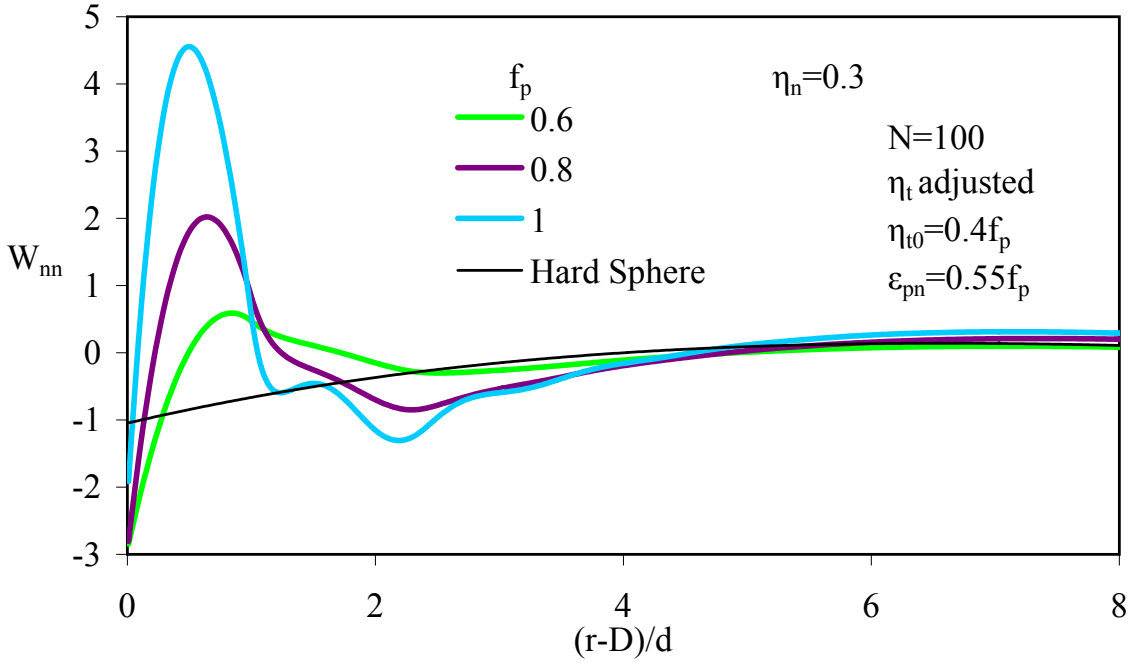

Figure 4.18: Potential of mean force at particle packing fraction of 0.3, using an adjusted total packing fraction with an initial polymer packing fraction of $\eta_{t0} = 0.4f_p$ and $\epsilon_{pn} = 0.55f_p$.

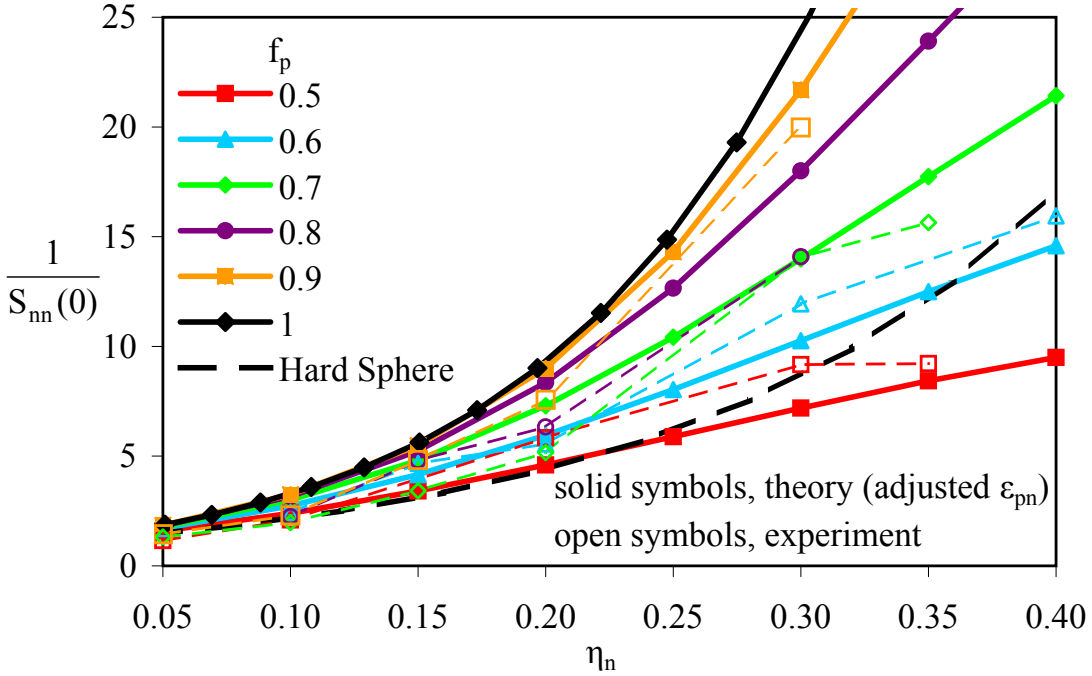

Figure 4.19: Inverse of particle osmotic compressibility versus particle packing fraction, using an adjusted total packing fraction with an initial polymer packing fraction of $\eta_{t0} = 0.4 f_p$ at the indicated values of ϵ_{pn}, compared with experimental scattering data.

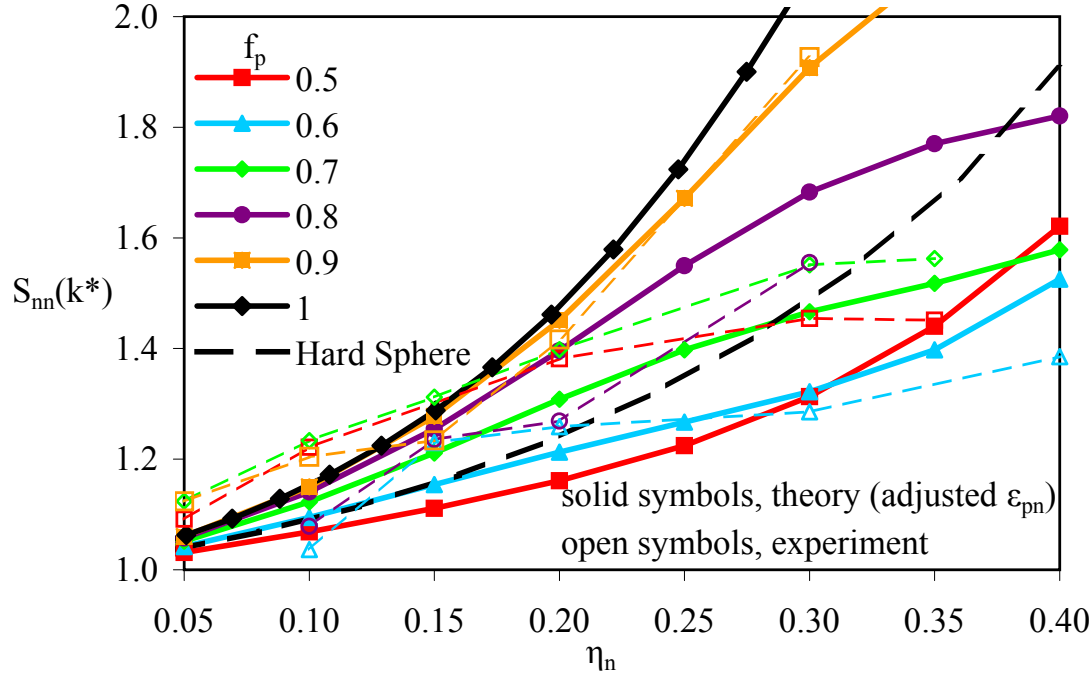

Figure 4.20: Height of cage peak in the particle structure factor versus particle packing fraction, using an adjusted total packing fraction with an initial polymer packing fraction of $\eta_{t0} = 0.4 f_p$ at the indicated values of ϵ_{pn}, compared with experimental scattering data.

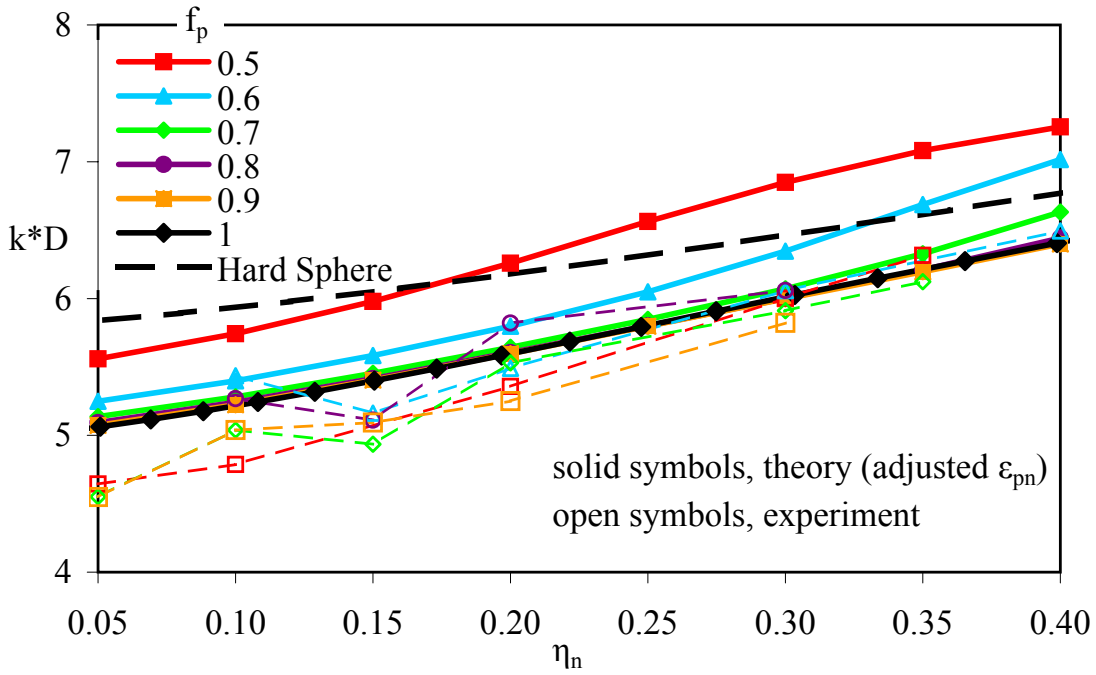

Figure 4.21: Wavevector location of cage peak in the particle structure factor versus particle packing fraction, using an adjusted total packing fraction with an initial polymer packing fraction of $\eta_{t0} = 0.4 f_p$ at the indicated values of ϵ_{pn}, compared with experimental scattering data.

Chapter 5

Miscibility of Rods

The unprecedented strength:weight ratio and interesting electrical and thermal properties of carbon nanotubes make them ideal as polymer additives for multiple potential applications. Many recent experiments have been performed on nanotube/polymer composites, but as with other fillers a key problem is to determine under what conditions the particles and polymer form a homogeneous mixture. The carbon nanotubes have especially strong attractions with each other, and frequently form nanotube bundles in polymers rather than a well dispersed phase. To develop an understanding of the polymer and nanoparticle properties which promote dispersion, PRISM theory was applied to a system of long rods in a polymer melt. The focus is on the effect of adding an attraction between rods in a homopolymer, though the case of a random copolymer with one monomer type more strongly adsorbing on the rod is also briefly addressed, motivated by ongoing experiments by M. Dadmun at Oak Ridge National Laboratory. The main question addressed is whether any rod and polymer chemical parameters can be chosen which allow miscibility of very strongly attracting rods.

5.1 Choice of Model

As described in Chapter 2, the rods are composed of tangentially connected spherical sites. The choice of size, length, and chemical parameters was motivated by carbon nanotubes. Single walled carbon nanotubes (SWCNT) have diameters around 1 nm, while multiwalled nanotubes are somewhat thicker.[15] A typical polymer persistence length is $\sim$ 1 nm or smaller, so a rod site diameter of D/d=2 was chosen to mimic the SWCNT thickness.[109] Rods of aspect ratio or number of sites of $N_n = 10$ and 100 were studied, with the focus on $N_n = 10$, though carbon nanotube aspect ratios are

typically in the hundreds or thousands. The relatively short rods make the PRISM equations numerically easier and faster to converge, and the effect of rod length is not qualitatively important for the properties of interest here.

The polymer-rod and rod-rod attraction strengths, ϵ_{pn} and ϵ_{nn}, were varied for the purpose of understanding the conditions which bracket miscibility. A rod-polymer attraction of spatial range $\alpha_{pn} = 0.5d$ was used, as was typical in prior studies on spherical and small molecular fillers, while rod-rod attraction ranges of $\alpha_{nn} = 0.25d$ and $0.5d$ were studied. Recall that these chemical variables refer to site-site attractions. It is not obvious how to uniquely map the nanotube chemistry onto a rod composed of individual sites. The choice of polymer-rod chemistry in the theoretical study was not quantitatively informed by experiments, and many types of polymers are available which could have a wide range of chemical interactions with carbon nanotubes. Experimental or quantum chemical data are desired to make useful comparisons to specific experimental systems. Knowledge of C_{60} chemistry may aid in understanding the rod site-site attractions because C_{60} "buckyballs" are chemically similar to single walled carbon nanotubes, in the sense that they are composed entirely of aromatic carbon, but exist as spheres and are therefore relevant to theoretical individual rod sites. One experimental study calculated the $C_{60} - C_{60}$ potential, finding an attraction strength of $\sim 10kT$.[127] Fitting an exponential by eye to this reported potential shows a range of ~ 0.15 nm, which maps to $\alpha_{nn} = 0.3d$ if $D = 1$ nm and $D/d = 2$. This value is bracketed by the $\alpha_{nn} = 0.25$ and 0.5 spatial range values studied. The quantitative applicability of the $C_{60} - C_{60}$ potential to multiwalled carbon nanotubes or nanotubes in a polymer melt is not clear. In this initial study, the rod-rod attraction strength was not fixed but rather increased incrementally to establish at what point the rods become immiscible under various conditions. Equilibrium miscibility was not found at the extremely high site-site $\epsilon_{nn} = 10$ for any systems modeled here. However, even if the reported $C_{60} - C_{60}$ potential[127] is a good representation of carbon nanotubes modeled

on a spherical site basis, the results at lower ϵ_{nn} can serve as a guide towards choosing parameters closest to equilibrium miscibility such that the rod-polymer mixture may be kinetically stable even at a higher attraction.

All other model parameters in this chapter are the same as those typically used in prior studies: degree of polymerization $N = 100$, persistence length $l/d = 1.333$, and total packing fraction $\eta_t = 0.4$. A new numerical issue occurs in the computation of the second virial coefficient of long rods. The nanoparticle-nanoparticle closure employed is the HNC, the same as that in the rest of this thesis. However, the solution to the HNC closure for rods shows a very small long range component in $g_{nn}(r)$ even in a vacuum (g_{nn} is not exactly 1 past the longest possible distance at which two rods can interact). Use of the PY closure would not improve the situation because it often yields a negative g_{nn} at some interparticle separations. However, this unphysical feature is so small as to be not visible on the scale of the plots reported, though it does cause an incorrect scaling of the second virial coefficient with rod length. Specifically, B_2 for rods scales approximately with N_n instead of N_n^2. Therefore, instead of normalizing B_2 by 4 times the hard core volume (which scales linearly with N_n and equals B_2 for spheres in a vacuum), in this chapter B_2 is normalized by the value for the hard rods in a vacuum with the HNC closure. This normalized value allows appropriate comparison between rods of various lengths.

5.2 Attractive Rods in Homopolymer Melts

5.2.1 Dilute Potential of Mean Force

The potential of mean force between rods in a weakly or strongly adsorbing homopolymer melt was calculated in order to observe the effect of adding a rod-rod attraction. Figure 5.1 shows W_{nn} for $N_n = 10$ rods in the relatively weakly adsorbing polymer case of $\epsilon_{pn} = 0.5$ and $\alpha_{pn} = 0.5$. With no rod-rod attraction, a modest site-site repulsion exists between rods with oscillations on the scale of the monomer diameter, and the

inset shows very small cusps on intrarod length scales. Adding a site-site rod attraction of $\epsilon_{nn} = 1$ and $\alpha_{nn} = 0.5$ predictably lowers W_{nn} by about $1kT$ near contact. This effect diminishes with distance, and W_{nn} for $\epsilon_{nn} = 1$ and $\alpha_{nn} = 0.5$ is similar to that of the $\epsilon_{nn} = 0$ system beyond $\sim 3d$, albeit with sharper cusps corresponding to the increased probability of rod-rod contact and resulting inter-rod correlations. Decreasing the attraction range to $\alpha_{nn} = 0.25$ at the same $\epsilon_{nn} = 1$ results in qualitatively similar effects of shorter range. Decreasing attraction range while keeping $\alpha_{nn}\epsilon_{nn}$, a measure of total interfacial cohesion, constant may allow a more fair comparison of the effect of attraction range. The $\epsilon_{nn} = 2$ and $\alpha_{nn} = 0.25$ system shows a deeper contact minimum in W_{nn} than that for $\epsilon_{nn} = 1$ and $\alpha_{nn} = 0.5$, but the curves are similar at rod separations of a monomer radius or more.

The same rod-rod attractions are studied in Figure 5.2 for a more strongly adsorbing polymer: $\epsilon_{pn} = 1.5$ and $\alpha_{pn} = 0.5$. The polymer induces a significantly larger repulsion at contact, which is diminished but still present even with the added rod site-site attraction of $2kT$. The repulsion persists for several monomer diameters and is followed by a very weak polymer bridging minimum shown in the inset. Adding a rod attraction of $\epsilon_{nn} = 1$ or 2 at $\alpha_{nn} = 0.25$ lowers the contact value of W_{nn} but has very little effect beyond a monomer radius. In contrast, for a longer range rod attraction of $\epsilon_{pn} = 1$ and $\alpha_{nn} = 0.5$, W_{nn} decreases by a small amount over several monomer diameters. Apparently the longer range rod attraction is less compatible with a repulsive bound polymer layer. Counterintuitively, the small bridging minimum present with no rod attraction or a short range attraction moves to a shorter distance at this longer $\alpha_{nn} = 0.5$.

5.2.2 Second Virial Coefficient

Figure 5.3 presents B_2 for $N_n = 10$ rods with $\alpha_{pn} = \alpha_{nn} = 0.5$ and an increasing rod attraction. As observed in prior spherical filler work, with no interrod attraction a

relatively flat plateau occurs in B_2 at intermediate ϵ_{pn} (at a value greater than that for hard fillers in a vacuum) due to a repulsive polymer layer around each nanoparticle. B_2 drops very sharply at low ϵ_{pn} due to the depletion attraction, and also drops sharply at high ϵ_{pn} due to polymer bridging. Adding an interrod attraction decreases B_2 at all ϵ_{pn}, and hastens the onset of a negative B_2 due to depletion and bridging, with a greater effect on the depletion behavior. The window of positive B_2, expected to correspond with miscibility at low volume fractions, significantly narrows as ϵ_{nn} is increased and no stable window is predicted for $\epsilon_{nn} = 3$ or above (not shown).

B_2 of analogous systems at the shorter rod attraction range of $\alpha_{nn} = 0.25$ is presented in Figure 5.4. The effect of increasing interrod attraction strength on the low ϵ_{pn} (depletion) side of the miscibility window is similar to that at $\alpha_{nn} = 0.5$. However, adding a small, short range rod attraction has little effect at intermediate and high ϵ_{pn}. Apparently the bound polymer layer is much better able to stabilize the nanorods against an attraction of significantly shorter range than the interfacial attraction. The window of positive B_2 is therefore significantly wider for $\alpha_{nn} = 0.25$, and the rods remain miscible past a much larger site-site rod attraction of $4kT$, at which point the B_2 curve begins to separate from its hard rod analog on the bridging side of the diagram.

Longer rods of $N_n = 100$ are more representative of real carbon nanotubes. The analogs of Figures 5.3 and 5.4 at $N_n = 100$ are given in Figures 5.5 and 5.6, respectively. None of the trends at either $\alpha_{nn} = 0.5$ or 0.25 are qualitatively changed. The longer rod length causes a flatter and somewhat lower plateau in B_2 at intermediate ϵ_{pn}, and a more sudden decrease from this plateau towards negative B_2 at both low and high ϵ_{pn}.

A few brief investigations were performed with other parameters to assess what is likely to change the qualitative picture presented above. The B_2 of thinner $D/d = 1$ rods (not shown) has the same qualitative behavior: the miscible window narrows much more quickly with a shorter range rod attraction. However, miscibility deteriorated

much faster with increasing ϵ_{nn}; a better comparison with $D/d = 2$ results was obtained by scaling both α_{pn} and α_{nn} with D. Calculation of B_2 at a shorter range interfacial $\alpha_{pn} = 0.25$ (not shown) reveals that the miscibility window narrows from both sides as ϵ_{nn} is increased when $\alpha_{pn} = \alpha_{nn} = 0.25$, relatively similar to the $\alpha_{pn} = \alpha_{nn} = 0.25$ case. This suggests that the important quantity to increase rod miscibility is not the smaller absolute $\alpha_{nn} = 0.25$ but a shorter range of rod-rod attraction relative to that of the rod-polymer interfacial attraction.

5.2.3 Nonzero Volume Fraction and Scattering

Though the primary focus is on assessing rod miscibility in the dilute limit, the structural effects of increasing rod volume fraction, Φ, are briefly investigated. These effects in the miscible region are in many ways similar to those for spherical nanoparticles. In real space, increasing Φ somewhat decreases the monomer scale order while increasing particle scale order in both g_{pn} and W_{nn}. These results are not shown as the only relevant differences from previously reported calculations are those already noted for the dilute limit W_{nn}.

The collective polymer and rod structure factors are of interest as they are potentially measurable by selective scattering experiments. The approximate center-of-mass rod structure factor based on Equation 2.9 is reported in Figure 5.7 for $N_n = 10$ rods at $\epsilon_{pn} = 1$, $\alpha_{pn} = 0.5$, and $\epsilon_{nn} = 1$ for both $\alpha_{nn} = 0.25$ and 0.5. These systems both have positive B_2 in the dilute limit, though the added $\epsilon_{nn} = 1$ attraction with $\alpha_{nn} = 0.5$ significantly reduces B_2 from the hard rod value, while that at $\alpha_{nn} = 0.25$ does not, as shown in Figures 5.3 and 5.4. The rod CM structure factors show what looks like a typical cage peak, but it is at a relatively low $kD \sim 3 - 4$. There is also a much smaller peak around the single site scale of $k = 2\pi/D$. A shoulder exists at at quite low kD, corresponding to order on the global rod length scale. These features are similar at the two values of α_{nn}, though the smaller α_{nn} system shows a bit more

order on a the main $kD \sim 3-4$ length scale, and decreasing α_{nn} also moves this peak to slightly lower kD (larger length scales). Increasing Φ increases the main peak and decreases the rod osmotic compressibility, as intuitively expected.

Increasing N_n to 100 (not shown) does not appreciably change the $kD \sim 3-4$ peak nor the $kD \sim 7$ peak, but the low kD feature predictably moves to even lower wavevectors. The location of the shoulder and the peaks at $kD \sim 3-4$ and ~ 7 also do not vary with small changes in ϵ_{nn} within the miscible regime (not shown), though at high ϵ_{nn} the peak at $kD \sim 7$ is increased for both apparently due to increased rod contact (higher Φ) and resulting increased site scale order.

Figure 5.8 shows the polymer collective structure factors for the same systems as Figure 5.7. One main filler-scale peak is present in S_{pp}, on the scale of $(1-2)kd$ or $(2-4)kD$, corresponding to the rods imprinting their order on the polymer through the bound layer. This peak increases with rod volume fraction and is very similar at the two values of α_{nn}. The relatively sharp $k = 0$ peak at low Φ is an apparently trivial effect of adding small amounts of long rods to polymer; at low volume fractions, these uncorrelated rods appear to the polymer as long linear holes which increase polymer concentration fluctuations or compressibility. Increasing Φ allows the rods to pack closer and form a smaller mesh size, and the polymer correlated with the mesh of rods experiences a decrease in compressibility. Note at $\Phi = 0.2$ the "microemulsion" form of the scattering profile, i. e. maxima at both $k = 0$ and $k^* \neq 0$.

5.3 Rods in Copolymer Melts

A brief investigation of the effect of copolymer chemistry on rod miscibility was performed motivated by recent experiments on carbon nanotubes in a polystyrene or polyvinylphenol homopolymer or a random copolymer of these with varying composition.[26] The nanotubes were functionalized such that they could hydrogen bond with the phenolic monomer. The propensity of nanotubes to form large bundles was assessed

in both polystyrene and polyvinylphenol homopolymers and in the random copolymer of varying composition. Surprisingly, nanotube bundling was the least (the nanotubes were closest to miscibility) at an intermediate copolymer composition rather than in the strongest interfacial attraction case of pure polyvinylphenol.

The monomers of polystyrene and polyvinylphenol differ only in the presence of the hydroxyl group on polyvinylphenol. Although the hydroxyl group certainly changes the monomer-monomer attractions, this difference should be small compared to the specific and strong H-bonding interaction possible between the polyvinylphenol and functionalized carbon nanotubes. Therefore, the model AB copolymer, in which the only difference between A and B monomers is their chemical interaction with filler, is likely applicable. As in the experiments, the A and B monomers are randomly arranged in the chain. The copolymer degree of polymerization is $N = 100$, and the nanotubes are composed of $N_n = 10$ tangentially connected spheres of diameter $D/d = 2$ with a rod-rod exponential attraction of range $\alpha_{nn} = 0.25$ or 0.5 and of varying strength ϵ_{nn} as motivated previously.

Polymer-polymer interactions are all purely hard core. This choice avoids any possibility of polymer microphase separation: without particles present, the system is a homopolymer melt. For this initial study, the range of the exponential interfacial attraction between any monomer and the nanotube is fixed at $\alpha_{pn} = 0.5$. The A and B types of monomers are therefore different only in their interfacial attraction strengths with the rod, ϵ_{An} and ϵ_{Bn}. The fraction of A monomers, f_A, is varied from 0.01 (nearly a homopolymer of B monomers) to 0.99 (nearly a homopolymer of A monomers).

Only the dilute limit is explored here, and the second virial coefficient is reported as a measure of rod miscibility. Of primary interest is whether the miscibility is ever a non-monotonic function of copolymer composition: can a copolymer disperse the nanotubes better than either homopolymer?

Figure 5.9 shows the normalized rod B_2 versus ϵ_{An} for various copolymer compo-

sitions in the case that $\epsilon_{Bn} = 0$ and there is no rod-rod attraction. At $f_A = 0.99$, the results are essentially the same as those for homopolymer, with a stabilized plateau region in B_2 at intermediate ϵ_{An}, and a sharply decreasing B_2 due to depletion at low ϵ_{An} and polymer bridging at high ϵ_{An}. Increasing the fraction of the nonadsorbing B monomer monotonically decreases miscibility; at $f_A < 0.25$, the system would have a large negative B_2 due to the dominance of entropic depletion and the PRISM equations could not be converged.

To better explore the entire copolymer composition range, ϵ_{Bn} was increased slightly such that even the $f_A = 0.01$ system could be converged, and analogous results to those of Figure 5.9 for $\epsilon_{Bn} = 0.1$ are given by the solid lines in Figure 5.10. All B_2 lines meet at $\epsilon_{An} = 0.1$, which is the homopolymer case. For ϵ_{An} above this value, increasing the fraction of more adsorbing A monomers increases B_2 in the miscible regime. However, with increasing ϵ_{An} the B_2 drops more sharply due to bridging for intermediate copolymer compositions, and the curves cross. Therefore, at high ϵ_{An} a nonmonotonic trend is predicted such that copolymers of $f_A = 0.25$ to 0.75 are less miscible than either homopolymer alone. At low and intermediate ϵ_{An} the trend is monotonic.

Figure 5.10 also shows the effect of increasing rod attraction strength ϵ_{nn} with $\alpha_{nn} = 0.5$. In all cases the added rod attraction decreases B_2 by a relatively similar amount for various compositions at all ϵ_{An}. Figure 5.11 compares some of the calculations from Figure 5.10 with their analogs at $\epsilon_{nn} = 0.25$. As expected from the homopolymer results, B_2 under bridging conditions is not as affected by the added short range rod attraction as it is by that at $\alpha_{nn} = 0.5$. This effect is similar at all copolymer compositions.

Under no conditions studied here is the experimentally observed situation of increased miscibility at moderate random copolymer composition observed. This may be because the model is too simple, or the equilibrium calculations may not apply to

the experiments which are actually always in a nonequilibrium state as evidenced by the presence of nanotube aggregates at all copolymer compositions. However, the potential of the theory to capture new physics due to the copolymer architecture which cannot be predicted by a weighted average of homopolymer results is confirmed by the observation of decreased miscibility of intermediate copolymer compositions in the bridging regime.

5.4 Summary

The miscibility and structure of thin rods in a polymer melt was investigated, motivated by experiments using carbon nanotubes as filler. The overall goal is to determine under what conditions attractive rods can be dispersed in the polymer. With no rod-rod attraction, the second virial coefficient versus interfacial cohesion plots show a plateau region at intermediate cohesion in which B_2 is greater than the result for hard rods in vacuum. At low cohesion strength, entropic depletion behavior causes a sharp decrease in B_2, while at high interfacial cohesion a weak but relatively long range bridging attraction causes a somewhat slower decrease in B_2. The miscibility window is narrowed from both sides as rod-rod attraction is added in the case that both the interfacial and rod-rod attractions are of the same spatial range. Shortening the range of rod-rod attraction increases miscibility. For the short range rod-rod attraction, the transition from positive to negative B_2 at low polymer-rod interfacial attraction still occurs more readily (at higher interfacial attraction strength) as rod-rod attraction is increased. However, in that case the transition to negative B_2 at high polymer-rod attraction strength, driven by polymer-induced enthalpic bridging of rods, is relatively invariant to inter-rod attraction strength. Increasing rod length slightly reduces the stabilizing consequences of polymer adsorption and the attendant steric repulsion. Polymer and rod collective structure factors were calculated, and the polymer $S_{pp}(k)$ shows evidence of imprinting of rod order via the adsorbed polymer layer. Rod miscibility was

also investigated in a random copolymer melt in which one type of monomer is more adsorbing than the other. This does not change the general qualitative picture, and increased miscibility at a shorter interrod attraction range still holds. Interestingly, for intermediate copolymer compositions, the transition to bridging occurs earlier than expected based on the results of either homopolymer alone.

5.5 Figures

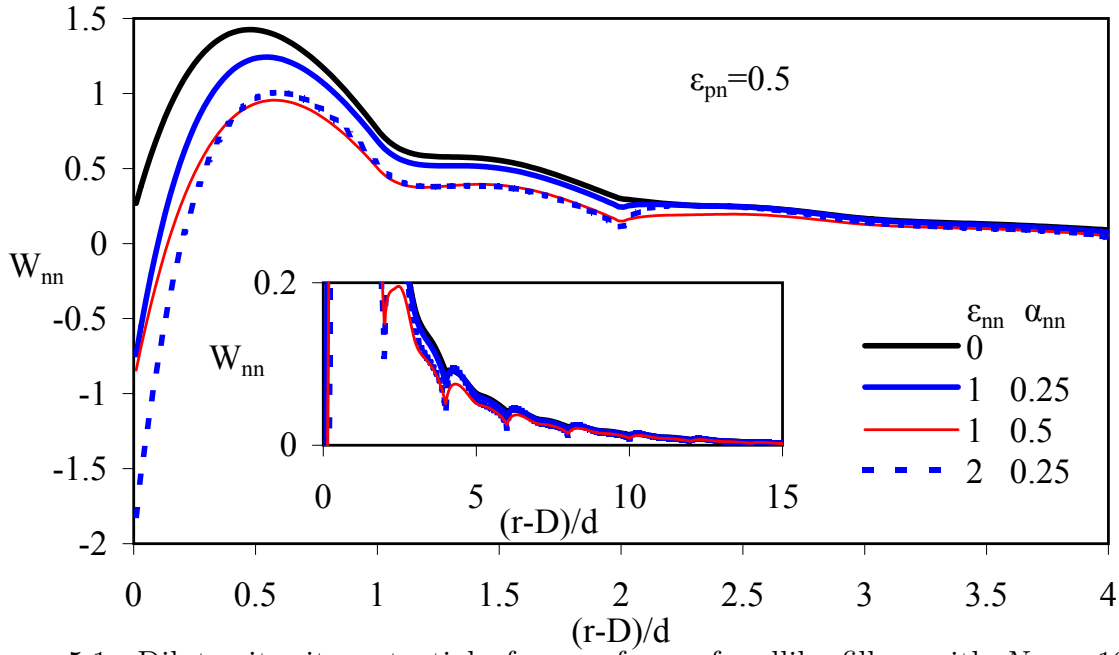

Figure 5.1: Dilute site-site potential of mean force of rodlike fillers with $N_n = 10$, $\alpha_{pn} = 0.5$ and $\epsilon_{pn} = 0.5$. Inset shows the long length scale features which are visible to a rod site separation of order of half the rod length.

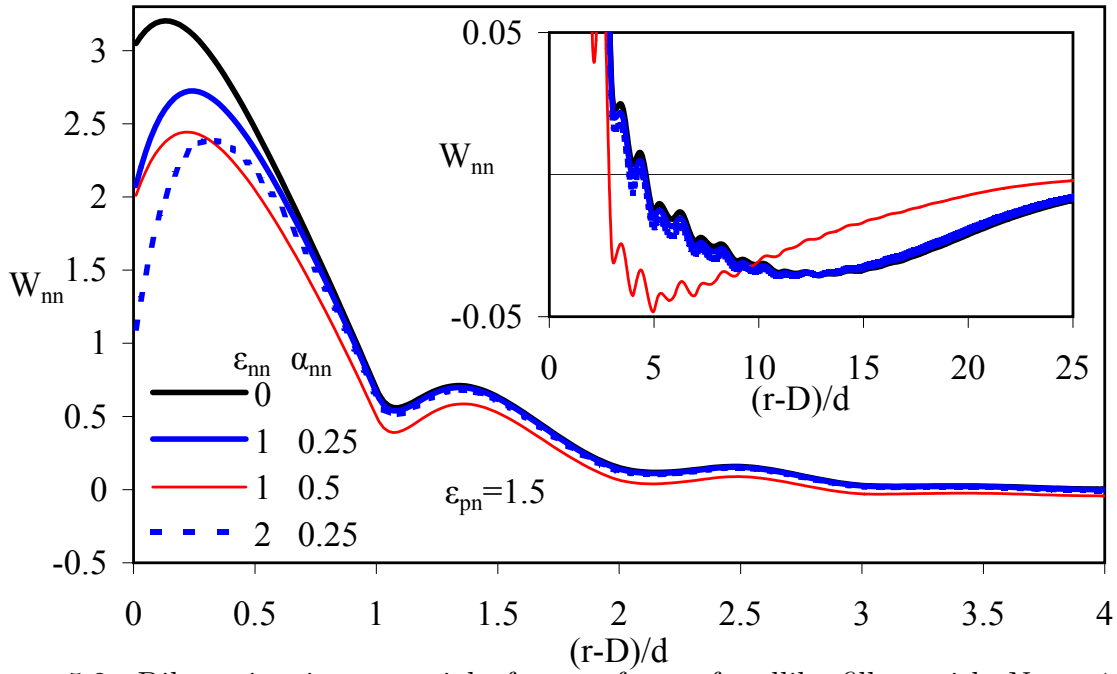

Figure 5.2: Dilute site-site potential of mean force of rodlike fillers with $N_n = 10$, $\alpha_{pn} = 0.5$ and $\epsilon_{pn} = 1.5$. Inset shows the long length scale features.

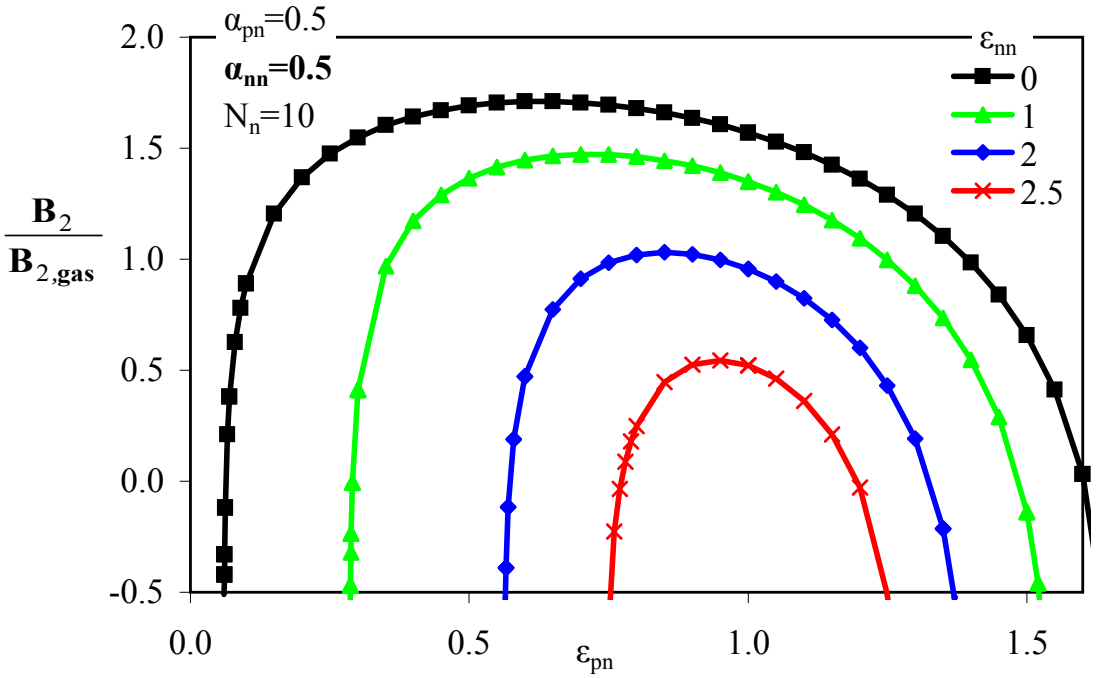

Figure 5.3: Second virial coefficient of rodlike fillers normalized by the value for pure hard rods in a vacuum, with $N_n = 10$, $\alpha_{pn} = 0.5$ and $\alpha_{nn} = 0.5$.

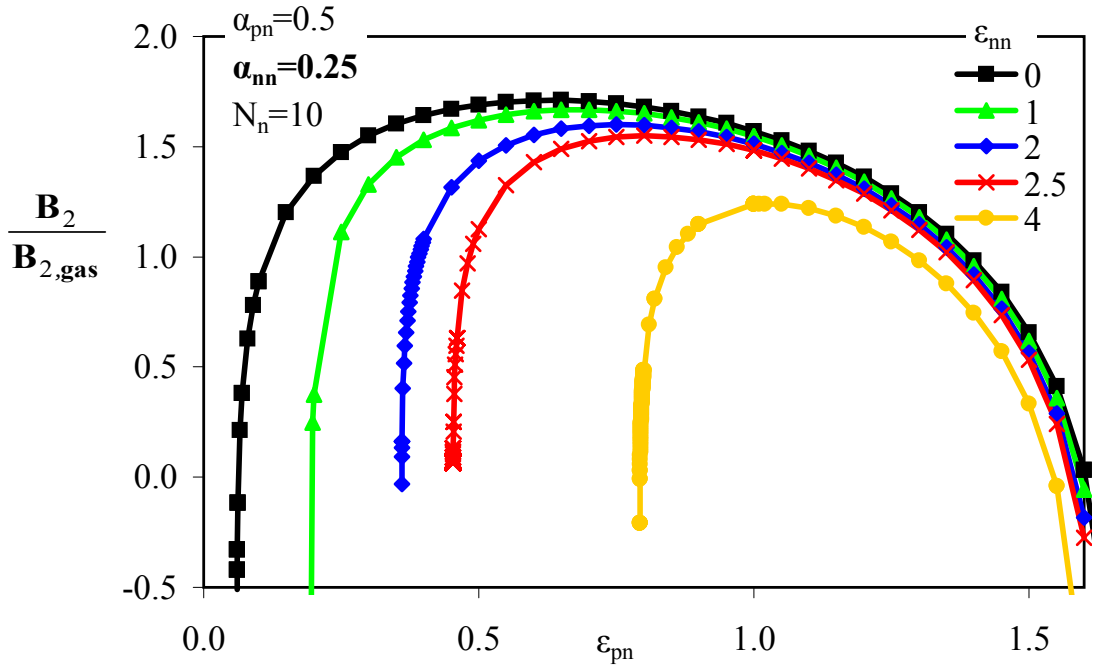

Figure 5.4: Second virial coefficient of rodlike fillers normalized by the value for pure hard rods in a vacuum, with $N_n = 10$, $\alpha_{pn} = 0.5$ and $\alpha_{nn} = 0.25$.

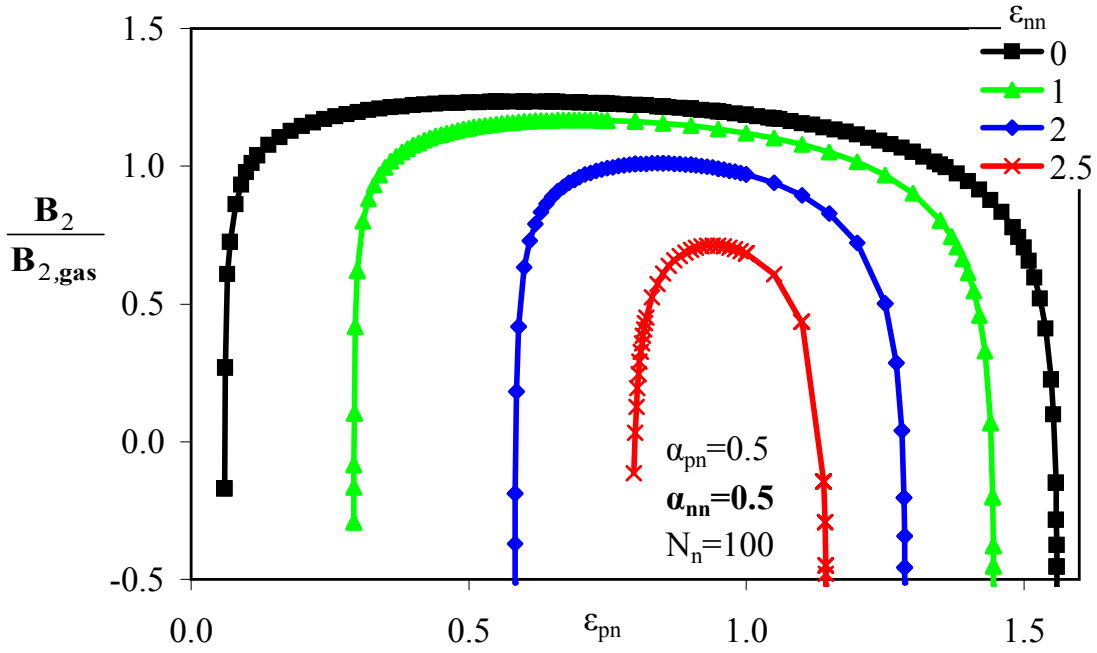

Figure 5.5: Second virial coefficient of rodlike fillers normalized by the value for pure hard rods in a vacuum, with $N_n = 100$, $\alpha_{pn} = 0.5$ and $\alpha_{nn} = 0.5$.

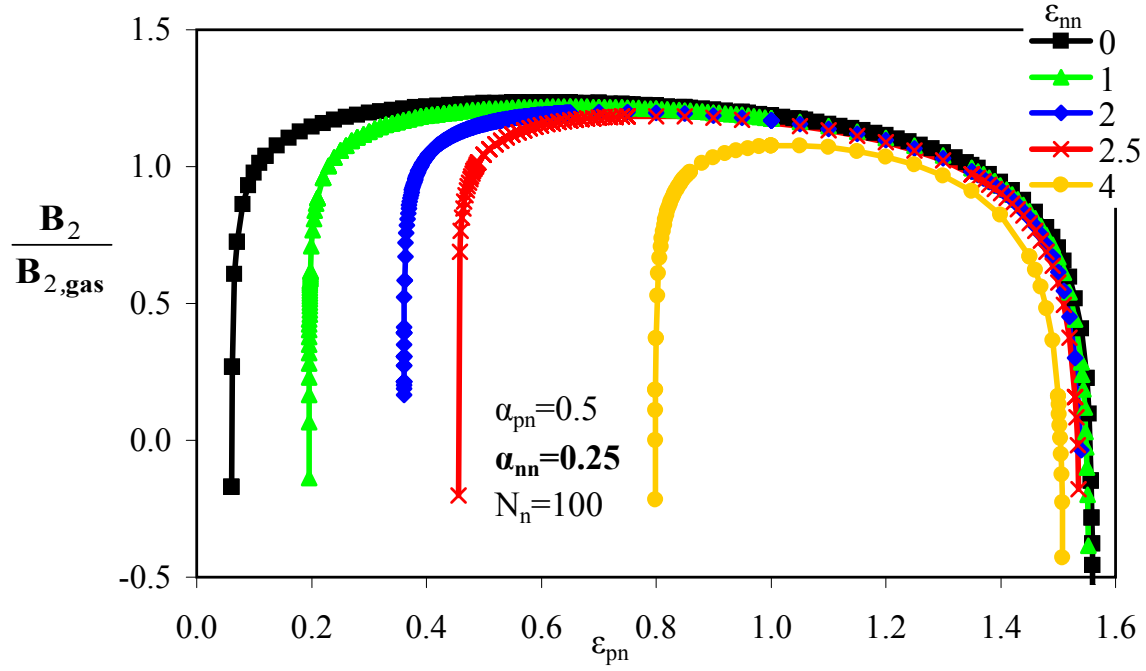

Figure 5.6: Second virial coefficient of rodlike fillers normalized by the value for pure hard rods in a vacuum, with $N_n = 100$, $\alpha_{pn} = 0.5$ and $\alpha_{nn} = 0.25$.

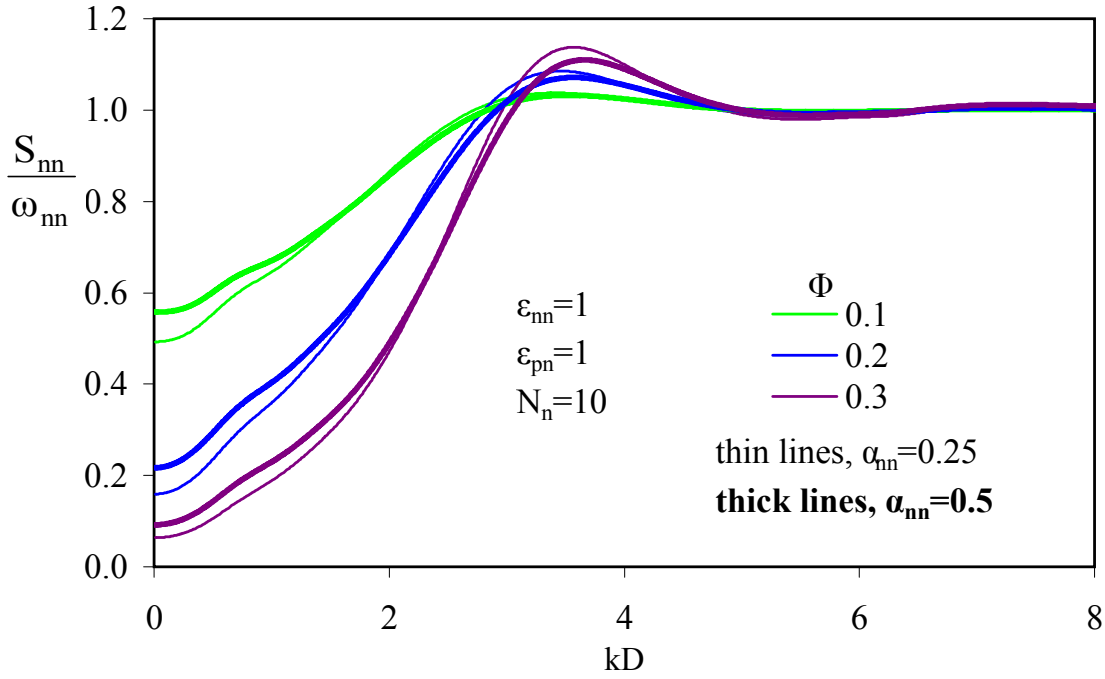

Figure 5.7: Approximate rod center-of-mass structure factor for $N_n = 10$ at $\alpha_{pn} = 0.5$, $\epsilon_{pn} = 1$, $\epsilon_{nn} = 1$, and various rod volume fractions.

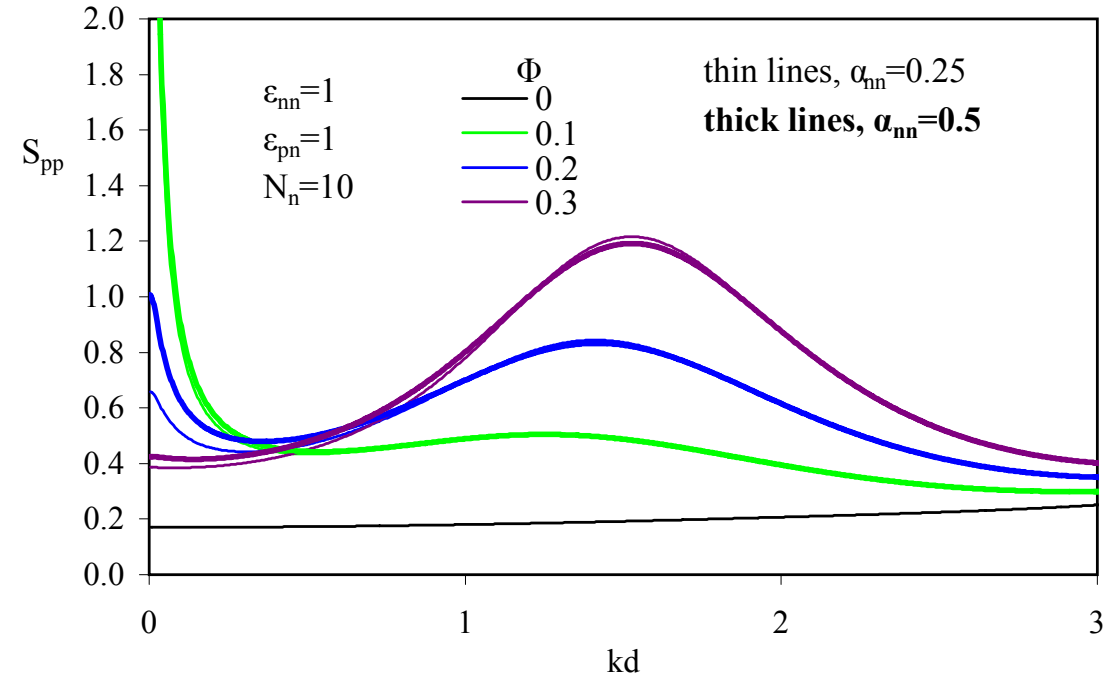

Figure 5.8: Polymer collective structure factor with $N_n = 10$ rod fillers at $\alpha_{pn} = 0.5$, $\epsilon_{pn} = 1$, $\epsilon_{nn} = 1$, and various rod volume fractions.

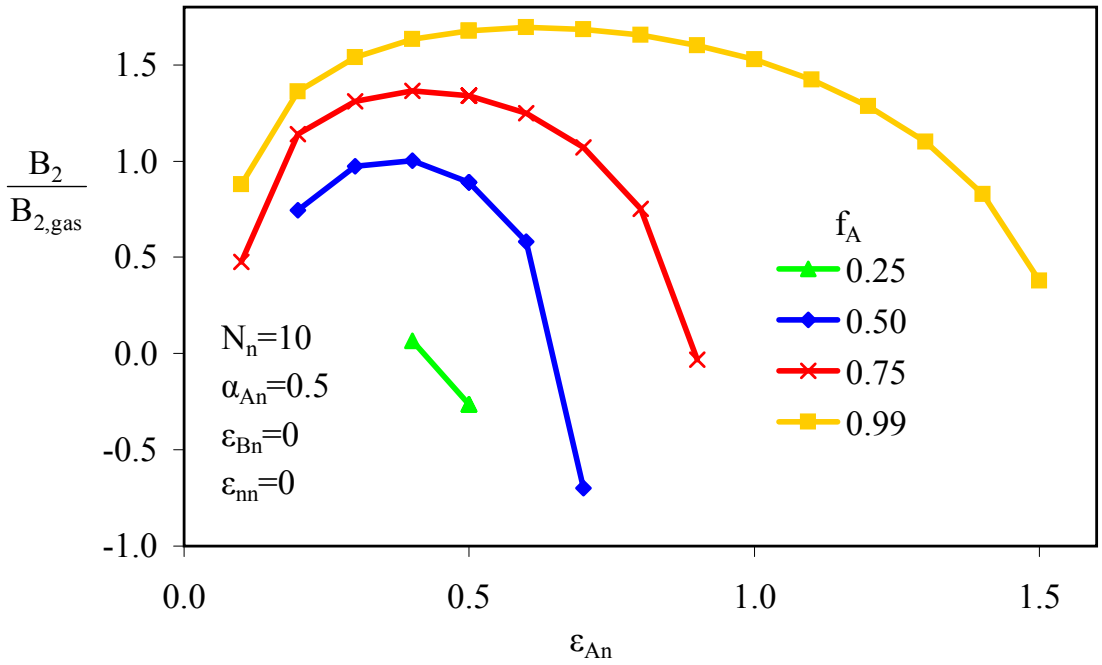

Figure 5.9: Second virial coefficient of $N_n = 10$ rods in a random AB copolymer melt normalized by the value for pure hard rods in a vacuum, with $\epsilon_{Bn} = 0$, $\epsilon_{nn} = 0$, and $\alpha_{An} = 0.5$.

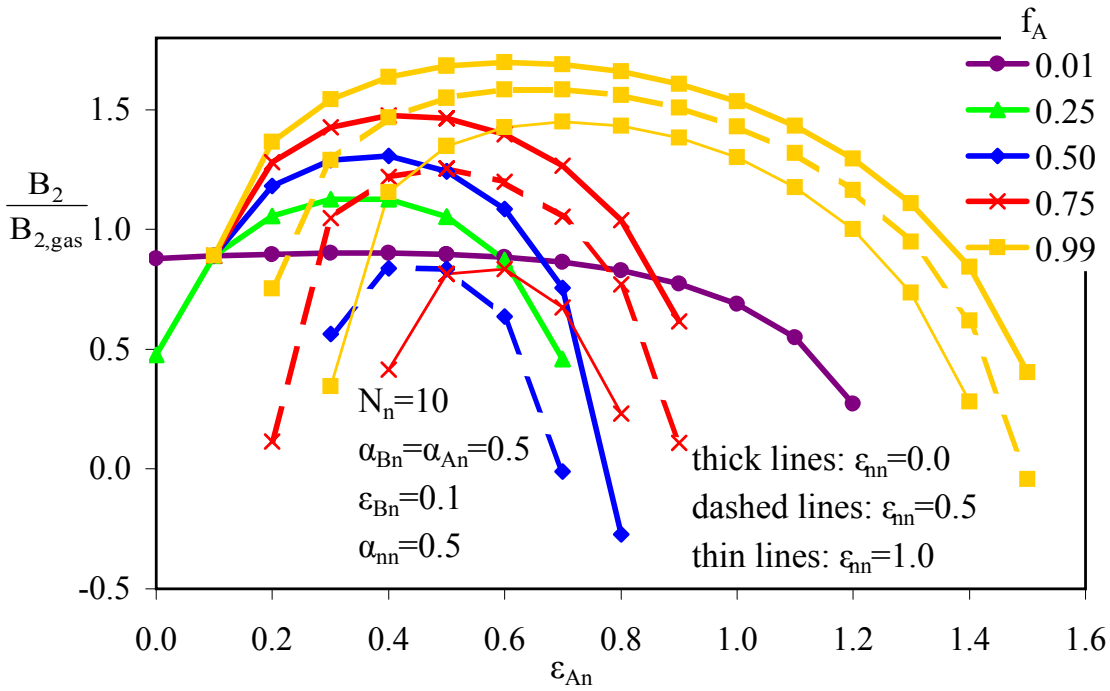

Figure 5.10: Second virial coefficient of $N_n = 10$ rods in a random AB copolymer melt normalized by the value for pure hard rods in a vacuum, with $\epsilon_{Bn} = 0.1$, $\alpha_{An} = \alpha_{Bn} = 0.5$, and $\alpha_{nn} = 0.5$.

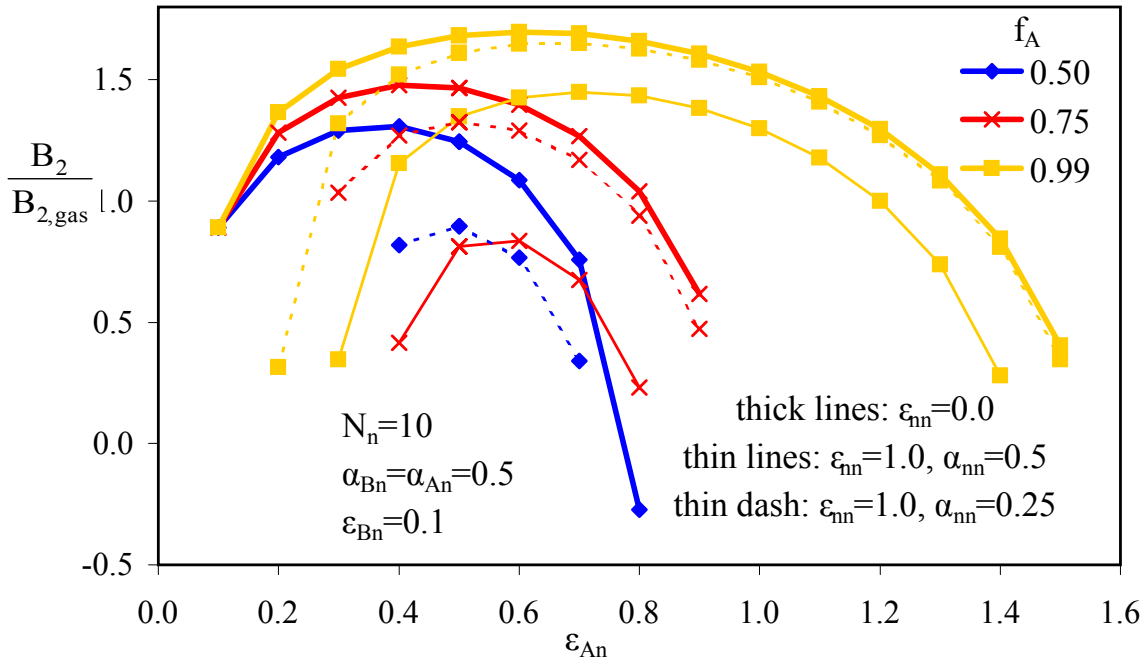

Figure 5.11: Second virial coefficient of $N_n = 10$ rods in a random AB copolymer melt normalized by the value for pure hard rods in a vacuum, with $\epsilon_{Bn} = 0.1$ and $\alpha_{An} = \alpha_{Bn} = 0.5$.

Chapter 6

Chemical Heterogeneity

Nanocomposites in which the polymer or particle are made up of chemically different parts are described here as "chemically heterogeneous". A recent experimental example of a possible heterogeneous diatomic molecule like filler is that of CdS nanocrystals grown on Fe_3O_4 nanocrystals.[22] Heterogeneous spherical "Janus" particles, one hemisphere (or other fractions of the sphere) of which is chemically modified, can also be created.[24] Added to a homopolymer melt, such particles may cluster or microphase separate. The implications of adding such fillers to a heterogeneous polymer melt are not explored in these initial studies. Instead, polymer chemical heterogeneity is addressed in the most basic manner by considering sphere-sphere interactions in copolymer melts and polymer blends. Although the microphase separation of copolymers in the presence of fillers is of broad experimental and theoretical interest,[74] polymer microphase separation is avoided here. Rather, the primary purpose of this study is to understand how the interfacial polymer-filler behavior such as the adsorbed polymer layer is affected by chemical heterogeneity. Therefore, the consequences of changing only monomer-filler interactions with identical monomer-monomer interactions are explored.

The several types of heterogeneous systems studied in this chapter are presented conceptually in Figure 6.1. Spherical fillers in several heterogeneous polymer melts are studied. Each heterogeneous polymer has two types of monomer, which were identical in the pure polymer limit but one of which was more strongly attracted to the filler. Three heterogeneous polymer types created are: an alternating copolymer, a random copolymer of varying composition, and a blend of two polymers in equal ratios. Diatomic fillers in which one site is more attractive towards the homopolymer than the other are studied, as are diatomic fillers whose sites interact with the polymer

identically but experience an additional direct site-site attraction for one of the types of sites.

6.1 Heterogeneous Polymers with Spherical Fillers

To explore the effect of polymer chemical heterogeneity on nanocomposite structure, spherical fillers in the dilute limit are studied in a random AB copolymer, an alternating AB copolymer, and a blend of A and B polymers. In this initial study, the particle interactions are hard core ($\epsilon_{nn} = 0$), D/d=5, and the fraction of A monomers f_A (fraction of the total polymer, a quantity not affected by particle volume fraction) is fixed at 0.5 for the alternating copolymer and polymer blend. The random copolymer calculations are mainly for $f_A = 0.5$, though f_A is varied across the entire range from 0.01 to 0.99. In all cases, each polymer is a freely jointed chain of 100 beads and the polymer-polymer interactions are entirely hard core. Therefore, in absence of fillers all polymer "mixtures" are a homopolymer melt. This choice avoids the possibility of polymer microphase or macrophase separation. The only difference between A and B monomer types is their attractive interaction strengths ϵ_{An} and ϵ_{Bn} with the nanoparticle; the range of both of these interactions is fixed at the value typically used in homopolymer work, $\alpha_{pn} = 0.5$.

6.1.1 Monomer-Filler Correlation Functions

Figure 6.2 shows both polymer-particle pair correlation functions for a random copolymer of $f_A = 0.5$ and $\epsilon_{Bn} = 0.5$. In the $\epsilon_{An} = 0.5$ homopolymer case (black line), g_{pn} is ~ 3 at contact and decays to one after a short distance, with small monomer scale oscillations, corresponding to moderate interfacial adsorption. Decreasing ϵ_{An} to zero decreases g_{An} (thin blue line) at contact to ~ 2 and slightly increases g_{Bn} (thick blue line), though the shape of both curves remains similar and they are almost equivalent after one monomer diameter from the surface. The average of g_{An} and g_{Bn} (not shown)

for this $\epsilon_{An} = 0$, $\epsilon_{Bn} = 0.5$ case is approximately equal to the homopolymer g_{pn} at an averaged $\epsilon_{pn} = 0.25$ (dashed blue line). Increasing ϵ_{An} to 3 (red lines) dramatically increases g_{An} at contact and lowers g_{Bn}. For this case, g_{An} remains larger than g_{Bn} for almost 2 monomer diameters, and averaging the two yields an increased contact value and other small differences versus the averaged $\epsilon_{pn} = 1.75$ homopolymer result.

The above results are put into context by comparison with Figure 6.3, which shows the same $\epsilon_{Bn} = 0.5$, $\epsilon_{An} = 0$ and 3 results for the alternating copolymer case. Again the contact value of g_{An} is decreased and that of g_{Bn} increased when $\epsilon_{An} = 0$. However, these curves cross around half a monomer diameter from the surface, and the A monomer is very slightly more likely to be one monomer diameter from the particle than the B monomer. At $\epsilon_{An} = 3$, the difference from the random copolymer case is more clear; the g_{An} and g_{Bn} curves start in the same manner, though their contact values are not quite as far apart, then cross at a fraction of a monomer diameter distance, and cross again between 1 and 2 d from the surface before becoming approximately equal after $2d$. This curve crossing is caused by the alternating nature of the copolymer; where A monomers are highly likely to be at the particle surface, the B monomers to which they are directly connected are more likely to be a short distance from the surface. In the random copolymer case, however, there are some locally blocky structures where some lengths of the chain are composed of several A monomers in a row. This allows a continuous excess of g_{An} over g_{Bn} or the averaged homopolymer g_{pn} for several monomer diameters. In the random sequence case these stretches of A will preferentially adsorb on the particles, causing a much greater f_A near the filler surface than in the bulk, which cannot be the case for alternating copolymers on length scales larger than d. Therefore, the average interaction of a nanoparticle with the surrounding polymer will be closer to the more adsorbing monomer's ϵ for the random copolymer case versus the alternating case. This explains why the average of the alternating copolymer g_{An} and g_{Bn} is more similar to the averaged homopolymer

result than is the average of these quantities for the random copolymer.

Obviously, the polymer blend contains longer continuous stretches of A monomers (the entire polymer length) than the random copolymer. These monomers can completely separate themselves from the B monomers, driven by preferential adsorption on the filler. Figure 6.4 reveals a much larger length scale over which g_{An} and g_{Bn} remain distinct for the blend. The blue lines are analogous to those of Figures 6.2 and Figure 6.3 ($\epsilon_{Bn} = 0.5$, $\epsilon_{An} = 0$), and show an increased g_{Bn} and decreased g_{An} versus these other cases, which persists further than the fluidlike monomer scale oscillations and is visible until $\sim 8d$. In essence, "surface segregation" or "preferential wetting" occurs. By the time ϵ_{An} is increased to 0.75, g_{Bn} is so much reduced that it becomes (unphysically) negative at a short distance. The focus here is therefore on the random and alternating copolymer systems.

6.1.2 Potential of Mean Force

The dilute particle potential of mean force in either a random (solid lines) or alternating (dashed lines) copolymer melt is given in Figure 6.5 for $f_A = 0.5$, $\epsilon_{Bn} = 0.5$, and $\epsilon_{An} = 0$ to 3. At $\epsilon_{An} = 0$, the alternating and random copolymer results are similar and show typical depletion behavior. For the alternating copolymer, increasing ϵ_{An} monotonically increases W_{nn} at contact and at short distances, though at large $\epsilon_{An} = 2$ and 3 a very small bridging minimum develops at $\sim 2d$. For the random copolymer, increasing ϵ_{An} initially increases W_{nn} similarly, but at $\epsilon_{An} = 2$ and 3 the random copolymer behavior is starkly different; the contact value decreases and a deep, long range ($\sim 3d$) bridging minimum develops. Though there are overlaid small monomer scale oscillations, W_{nn} remains < 0 for several monomer diameters, a qualitatively different picture than the typical behavior discussed in Chapter 3 of multiple bridging minima caused by monomer scale oscillations above and below zero. Apparently, as particles come together in the random copolymer, stretches of A monomers along the

chain can form a strongly adsorbing bridge extending over several monomer diameters, a situation not possible in the alternating copolymer case nor for the homopolymer case until ϵ_{pn} is large (larger than the average of ϵ_{An} and ϵ_{Bn} of a strongly bridged random polymer). A conceptual picture of bridging between particles in the alternating copolymer, random copolymer, and polymer blend is presented in Figure 6.6.

Figure 6.7 shows that the alternating copolymer results in Figure 6.5 are similar to the homopolymer at an averaged ϵ_{pn}. At high ϵ_{An}, the alternating copolymer PMF has a smaller contact repulsion, increased repulsion between 1 and $2d$, and reduced bridging strength. These differences are due to the layering of A and then B monomers around the particle surface; the steric constraint of a less adsorbing B monomer attached to every A frustrates the preferential packing of A on the surfaces between two nearby particles.

As expected from the pair correlation functions, a much longer range PMF is predicted for the polymer blend case of Figure 6.8. The $\epsilon_{An} = 0$, $\epsilon_{Bn} = 0.5$ system has a depletion minimum similar to that of the random, alternating, and averaged homopolymer cases. However, beyond a very small repulsion, a very broad bridging minimum develops, in qualitative contrast to all prior results. It seems that, although the adsorption strength is not large and the depletion attraction remains, since the A and B homopolymers can fully separate, the more adsorbing species accumulates near the particles and prefers to bridge the fillers which allows the less adsorbing polymer the greatest possible entropy. For the $\epsilon_{An} = 0.75$, $\epsilon_{Bn} = 0.5$ system, a much deeper bridging minimum is observed.

Figure 6.9 explores the effect of random copolymer composition on W_{nn} for the $\epsilon_{An} = 3$, $\epsilon_{Bn} = 0$ copolymer. At $f_A = 0.01$, near the $\epsilon_{pn} = 0$ homopolymer limit, a typical depletion attraction is observed, while repulsion followed by small bridging minima is seen at $f_A = 0.99$ near the $\epsilon_{pn} = 3$ homopolymer limit. The results at intermediate f_A are not simple interpolations between these limits; instead, a strong and

broad bridging behavior is predicted. Decreasing f_A from 0.99 to 0.25 monotonically lowers $W_{nn}(r)$; the decrease in W_{nn} is largest at contact and persists until $\sim 2.5d$. Even at the relatively low $f_A = 0.25$, stretches of several A monomers will be present in the random copolymer. These adsorbing patches are preferentially pushed to the particle surface by the nonadsorbing monomer resulting in even more strong bridging than in the purely adsorbing homopolymer.

The overall conclusion is that both copolymer composition and sequence play crucial roles in determining the polymer-induced PMF between nanoparticles.

6.2 Heterogeneous Diatomic Fillers

Heterogeneous diatomic fillers in a homopolymer melt were studied as a simple example of filler chemical heterogeneity. Two joined, but chemically distinct, particles can be produced experimentally, such as the recent Fe_3O_4/CdS systems of McDaniel and Shim.[23] A heterogeneous diatomic may exhibit different site sizes, filler-polymer interactions, filler-filler interactions, or a combination of these. To simplify discussion, only AB diatomic fillers where A and B are tangentially connected spheres of the same size of D/d=5 are considered. The A and B sites have either different polymer attraction strengths and no filler-filler attraction ($\epsilon_{pA} \neq \epsilon_{pB}$, $\epsilon_{nn} = 0$), or have the same polymer attraction strength but one added direct site-site attraction ($\epsilon_{pA} = \epsilon_{pB} = \epsilon_{pn}$, $\epsilon_{BB} \neq 0$,$\epsilon_{AA} = 0$). Results for these systems are compared with the homogeneous hard diatomic results. In all cases, the attractions exponentially decay with range $\alpha_{pn} = \alpha_{nn} = 0.5d$. In the dilute limit, when the direct or effective attractions cause B-B site-site contact, the A-A sites connected to them can also be in contact (or more likely, near contact with an adsorbed polymer layer between them) or at a distance of up to $3D$, as shown conceptually in Figure 6.10. Increasing the particle volume fraction could potentially cause micellization or clustering of particles, as sketched in Figure 6.10. These possibilities are assessed by calculation of the potential of mean

force, and of the collective structure factors at finite volume fractions.

6.2.1 Correlations in the Dilute Limit

Diatomics with one site of intermediate interfacial attraction strength $\epsilon_{pA} = 1$ and the other site of widely varying $\epsilon_{pB} = 0$ to 5 were compared to probe the range of possible behaviors. The B site-polymer pair correlation function of the diatomic fillers is given in Figure 6.11, with the A site analog in the inset. Increasing ϵ_{pB} intuitively increases g_{pB} at contact and somewhat increases the monomer scale oscillations in g_{pB}, presumably due to increased density and monomer ordering near the surface for the more strongly adsorbing polymer. At the highest ϵ_{pB} studied, the monomer oscillations are so large that g_{pB} becomes negative near contact, an unphysical result. Therefore, this system is presented only to add to the qualitative picture of the very high ϵ_{pB} bridging limit, and is not discussed in the next section. The inset of Figure 6.11 shows that g_{pA} is hardly changed as ϵ_{pB} is varied from 0 to 5 at constant ϵ_{pA}. Apparently neither an excess nor shortage of polymer on one side of the diatomic appreciably affects the local statistical packing of the polymer on the other side.

The filler site-site potentials of mean force for the same diatomics are shown in Figures 6.12, 6.13, and 6.14. The insets are rescalings of the main panel to show long range behavior. For the case of constant polymer attraction strength, the A-A site-site correlations in Figure 6.12 show that changing ϵ_{pB} has only a small effect. Because of the moderate ϵ_{pA} used, each A site is surrounded by a bound polymer layer, creating an A-A repulsion at short distances for all cases. Where the B sites experience depletion conditions ($\epsilon_{pB} = 0$) or bridging conditions ($\epsilon_{pB} = 5$), a small, broad decrease in $W_{AA}(r)$ from $\sim 1 - 10d$ exists versus $W_{AA}(r)$ of the most miscible $\epsilon_{pB} = 2$ system. This corresponds to an increased probability of A sites being near each other when there is a strong attraction between the B sites to which they are attached; this effect persists to $3D$ in the dilute limit as shown in Figure 6.10.

Figure 6.13 shows the B-B site potential of mean force for increasing ϵ_{pB}. Similar to spherical particle results in Chapter 3, a depletion attraction is observed at $\epsilon_{pB} = 0$, with weak and then strong bridging attractions at $\epsilon_{pB} = 2$ and 5. A small long range repulsion is also present out to $\sim 7d$, presumably caused by the steric hindrance of the attached and repulsive (due to their bound polymer layer) A sites. The A-B PMF of Figure 6.14 shows behavior generally between that of A-A and B-B results. When $\epsilon_{pB} = 0$, the A site has a bound polymer layer which weakly repels the B site at short distances, while at higher ϵ_{pB} both sites have a strongly held bound layer. At $\epsilon_{pB} = 2$, W_{AB} is repulsive, while at very high $\epsilon_{pB} = 5$, bridging minima develop. The $\epsilon_{pB} = 0$ strong B-B depletion system shows a decreased W_{AB} until $5d = D$, due to the A-B interactions which occur when 2 B sites are in contact. Similarly, two bridged B sites separated by a polymer layer for the $\epsilon_{pB} = 5$ system result in cause a decreased W_{AB} until $\sim 7d$ which corresponds to the intermolecular A-B distance plus the approximate bound layer distance between bridged B particles.

6.2.2 Effect of Volume Fraction on the Nanoparticle Potential of Mean Force

Diatomic filler structure was studied up to high particle volume fractions with a constant total packing fraction of 0.4. The $\epsilon_{pA} = 1$, $\epsilon_{pB} = 0$ system with a strong B-B depletion attraction and A-A bound polymer induced repulsion is the main focus. This is compared with the averaged $\epsilon_{pn} = 0.5$ homogeneous diatomic case, the site-site PMF of which is given in Figure 6.15. Though this is a homogeneous diatomic particle, the PMF is reported as that between one labeled site on each diatomic for a clearer comparison with the heterogeneous site-site potentials of mean force. At $\Phi = 0$, this system is almost entirely repulsive. The main effects of increasing Φ are to decrease the repulsion strength and add a small bridging attraction (except at the highest $\Phi = 0.9$ where the polymer has little effect), decrease the monomer scale oscillations, and induce a small oscillation on the scale of the particle site diameter.

The heterogeneous diatomic A-A correlations for $\epsilon_{pA} = 1$ and $\epsilon_{pB} = 0$ in Figure 6.16 are similar. Because of the higher attraction between the A site and polymer versus the averaged homogeneous diatomic, the A-A potential of mean force shows a larger bridging attraction as Φ is increased, and small polymer scale bump in W_{AA} is still present even at $\Phi = 0.9$. The corresponding B-B correlations in Figure 6.17 show a strong depletion attraction as expected at $\epsilon_{pB} = 0$. Increasing Φ creates a filler site scale oscillation and decreases the importance of monomer packing, which decreases the monomer scale oscillations and increases $W_{BB}(0)$. Overall, W_{AA} and W_{BB} are similar to that of spheres at an intermediate ϵ_{pn} and at a low ϵ_{pn}, respectively.

The effect of an added attraction between B sites only, $\epsilon_{BB} = 5$, was studied at constant $\epsilon_{pn} = 0.5$. The A-A potential of mean force is given in Figure 6.18; recall that the homogeneous diatomic results for the analogous system without a filler attraction are presented in Figure 6.15. As there is no added A-A attraction, these results are quite similar at all Φ. However, as expected, the B-B PMF in Figure 6.19 shows a strong attraction at contact and slightly reduced short range repulsion. As Φ is increased, a B-B correlation of increasing strength around $5d = D$ develops, corresponding to aggregation of B sites.

6.2.3 Scattering Patterns

6.2.3.1 Filler collective structure

The collective scattering structure factor of one site of a homogeneous diatomic filler at $\epsilon_{pn} = 0.5$ and $\Phi = 0.1 - 0.9$ is given in Figure 6.20. A typical site scale cage peak is observed which grows in intensity and wavevector as particles are added and packing correlations increase. A small shoulder at the highest Φ is observed at approximately half the wavevector (ordering on double the real space distance) of the site cage peak, indicating a small degree of order on the diatomic molecule size scale. The analogous heterogeneous diatomic $\epsilon_{pA} = 1$, $\epsilon_{pB} = 0$ results are given in Figure 6.21 (A-A structure

factors) and Figure 6.22 (B-B structure factors). The A-A scattering profile shows a more intense site scale peak of increasing wavevector as Φ is increased, similar to the homogeneous diatomic result. However, the low wavevector shoulder observed for the homogeneous system forms in the heterogeneous A-A structure factor at a lower volume fraction $\Phi \approx 0.5$, and as Φ is further increased it moves to slightly smaller wavevector and becomes an intense peak which is larger than the cage peak by $\Phi = 0.9$. The B-B structure factors (Figure 6.22) also show cage and low wavevector peaks. As the B sites experience a depletion attraction, their cage ordering is on a smaller length scale (larger wavevector) than for S_{AA}, and this peak moves to smaller wavevectors as Φ is increased. The low wavevector peak in S_{BB} is more intense and at slightly larger wavevector than for S_{AA}. Taken together, these structure factor results suggest microphase separation like behavior in which there is some local cage scale order and also larger scale, possibly micelle-like, filler organization.

The microphase order discussed above is also seen in the differentially attracting heterogeneous filler with $\epsilon_{pn} = 0.5$, $\epsilon_{AA} = 0$, and $\epsilon_{BB} = 5$. The A-A and B-B structure factors are shown in Figures 6.23 and 6.24, respectively. Here the A-A site scale cage peak is similar to that of homogeneous diatomics, though it is somewhat broader, and increases in strength and wavevector with increasing Φ. The A-A structure factor shows a low wavevector microphase peak only at high Φ, which is not as strong as that for the differential polymer adsorption $\epsilon_{pA} = 1$, $\epsilon_{pB} = 0$ case. The B-B structure shows qualitatively different behavior. The site cage peak of S_{BB} is at higher wavevector due to the close correlations between sites with a strong contact attraction, and the location of the S_{BB} peak does not decrease with Φ as it did for the $\epsilon_{pA} = 1$, $\epsilon_{pB} = 0$ system. The low wavevector peak in S_{BB} at $\epsilon_{BB} = 5$ is the strongest of any system, and as Φ increases the peak moves to slightly lower k and its height increases to ~ 6 at $\Phi = 0.9$.

6.2.3.2 Polymer collective structure

The filler imprints its spatial order on the collective polymer structure factor via the adsorbed layer. The polymer structure factor for homogeneous diatomic filler is shown in Figure 6.25. A filler-scale peak develops by $\Phi = 0.3$, and increases in intensity and wavevector (from $kD \sim 3 - 5$) with volume fraction until it is lost under the zero wavevector contribution at high $\Phi = 0.9$. This length scale of ordering corresponds to the size of the filler sites plus their bound polymer layers. Figure 6.26 shows S_{pp} with the heterogeneous filler of $\epsilon_{pA} = 1$ and $\epsilon_{pB} = 0$. The site plus adsorbed polymer scale peak is at most a shoulder until $\Phi = 0.5$, is at slightly larger k than the homogeneous case, and persists at $\Phi = 0.9$. A new peak on a larger length scale is significantly more intense than the site scale peak, with an intensity ~ 90 at $2\pi/kD \sim 4$ when $\Phi = 0.9$. This length scale corresponds to two diatomics end-to-end which could correspond to the distance between adsorbed polymer on either side of a small spherical or tubular shaped micelle. The low wavevector and site scale peaks in S_{pp} are also seen for heterogeneously attracting fillers of $\epsilon_{pn} = 0.5$, $\epsilon_{AA} = 0$, and $\epsilon_{BB} = 5$ in Figure 6.27. These microphase peaks are both similar to those of the polymer induced B-B depletion attraction ($\epsilon_{pA} = 1$, $\epsilon_{pB} = 0$) system except they are less intense at very high Φ; for example S_{pp} for $\epsilon_{BB} = 5$ at $\Phi = 0.9$ the low wavevector peak intensity is ~ 60 and the site scale peak becomes only a shoulder.

6.2.3.3 Osmotic compressibilities

Figure 6.28 compares the filler site dimensionless osmotic compressibility $S_{AA}(k \to 0) \equiv S_{AA}(0) = S_{BB}(0)$ of two heterogeneous nanoparticles of $\epsilon_{pA} = 0.5$, $\epsilon_{pB} = 0$ and $\epsilon_{pA} = 1$, $\epsilon_{pB} = 0$ to the homogeneous fillers of $\epsilon_{pn} = 0.25$ and 0.5. The heterogeneous nanoparticles have a low Φ peak (for $\epsilon_{pA} = 0.5$) or shoulder (for $\epsilon_{pA} = 1$) in $S_{AA}(0)$ which is absent from the analogous homogeneous filler results. At high Φ, the behavior is qualitatively the same; the $\epsilon_{pA} = 1$, $\epsilon_{pB} = 0$ heterogeneous system result decreases

and merges with its homogeneous averaged ϵ_{pn} analog at $\Phi \sim 0.7$; the $\epsilon_{pA} = 0.5$, $\epsilon_{pB} = 0$ heterogeneous filler curve crosses its homogeneous analog at $\Phi \sim 0.5$ and then stays slightly below until they merge at $\Phi = 1$.

The polymer osmotic compressibility as a function of filler volume fraction of the heterogeneous diatomic composites is shown in Figure 6.29 and also exhibits a peak at low Φ. The analogous homogeneous result at $\epsilon_{pn} = 0.5$ also shows a peak, although it is much weaker, and there is no peak at at $\epsilon_{pn} = 0.25$. Both heterogeneous filler system curves cross their homogeneous analogs at intermediate Φ, and remain at a somewhat lower values until they meet in the dilute polymer limit at $S_{pp}(0) = N = 100$. The increased particle and filler compressibilities at low Φ for the heterogeneous PNCs may signal the formation of nanoparticle aggregates or micelles, while at very high Φ discrete micelles may not be possible as particles at relatively close distances span the system.

6.3 Summary

The addition of chemical heterogeneity to one of the species of a polymer nanocomposite can qualitatively change dispersion and spatial structure. The comparison of various heterogeneous polymer types, in which one type of monomer is more strongly adsorbing than the other, shows that these systems can exhibit qualitatively different behavior than a simple homopolymer. An alternating copolymer shows a small layering effect; the more strongly adsorbing monomer is likely to be near the particle surface, so the other monomers are more likely to be a short distance away. This causes a small excess repulsion compared to the homopolymer case with an average interfacial attraction. However, the overall depletion-stabilization-bridging progression seen in homopolymers as ϵ_{pn} is increased is similar for alternating copolymers as adsorption strength is increased for one of its monomer types. In contrast, random copolymers and the polymer blend can mediate a novel strong, long-range bridging behavior. The

deep bridging minimum may start at contact (for low f_A of a random copolymer) or around $1d$ and persist to $\sim 3d$ for random copolymers, while it is longer range ($\sim 6d$) for the polymer blend. These length scales are apparently due to the runs of several adsorbing monomers of random copolymers of intermediate f_A, and the longer entire polymer length over which adsorbing monomers are correlated in the blend. Obviously, the alternating copolymer has no stretches of more than one adsorbing monomer, and therefore the very strong, long range bridging behavior is not observed. The random copolymer and polymer blend calculations reveal that a very large monomer adsorption energy is not needed to induce a strong bridging minimum, and bridging is stronger at an adsorbing monomer fraction of 0.25 than at 0.5 for the highly heterogeneous random AB copolymer. These results collectively indicate that the nonadsorbing or less strongly adsorbing monomers are crucial to this newly observed heterogeneous polymer bridging behavior. The more adsorbing polymers are driven to the filler surface both by energetic considerations and the entropic gain of less adsorbing monomers not near the particle surface, thereby creating a longer range polymer layer than seen in the homopolymer case and a very strong bridging attraction when this layer is shared between fillers.

AB heterogeneous diatomic fillers dissolved in a homopolymer melt were also studied, focusing on systems with an effective B-B attraction due to nonadsorption of polymer onto B sites or systems with equal filler site-polymer adsorption strengths but a direct B-B attraction. In contrast to the homogeneous diatomic scattering profile which exhibits only one primary ordering length scale, distinct peaks or shoulders on both the site and larger length scales are predicted in the heterogeneous diatomic S_{AA}, S_{BB}, and S_{pp} partial collective structure factors at intermediate and high Φ. The low wavevector peak suggests the formation of groups of correlated particles, possibly micelles. Very small spherical micelles caused by a B-B attraction may be expected to show little longer length scale B-B order. Because the B-B structure factor microphase-

like peaks are as intense or larger under most conditions than the A-A peaks, and were at similar kD, a tubelike or toroidal micelle or other more complex average structure may exist. Certainly a qualitatively different packing of heterogeneous diatomics is expected relative to homogeneous diatomics at any value of ϵ_{pn}. Together, these computational results point towards the details of copolymer architecture or filler chemical interactions as key considerations in the design of heterogeneous polymer nanocomposites.

6.4 Figures

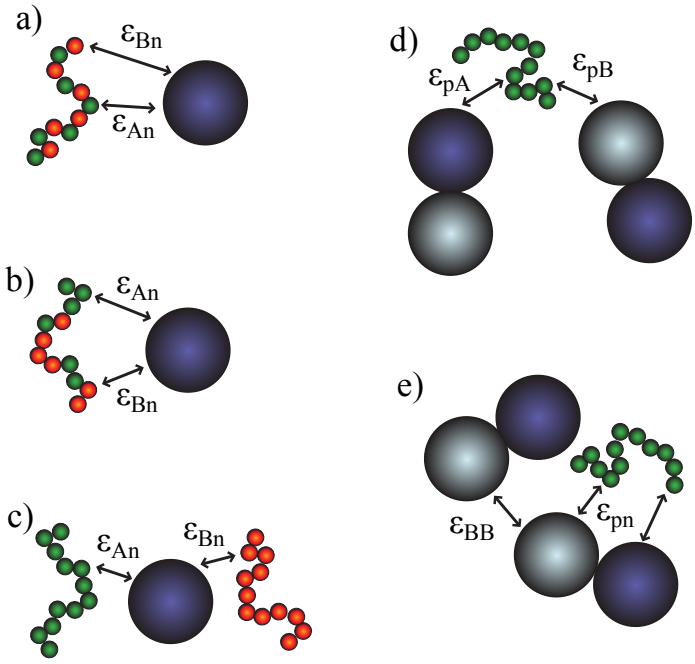

Figure 6.1: Conceptual cartoon of chemically heterogeneous systems, where the attraction strength between i and j sites is given by ϵ_{ij} and all unlabeled site-site interactions are hard core: a) alternating AB copolymer and hard spherical nanoparticle b) random AB copolymer and hard spherical nanoparticle c) A/B polymer blend and hard spherical nanoparticle d) homopolymer and AB diatomic nanoparticle with variable site-polymer adsorption strengths e) homopolymer and AB diatomic nanoparticle with one added site-site attraction.

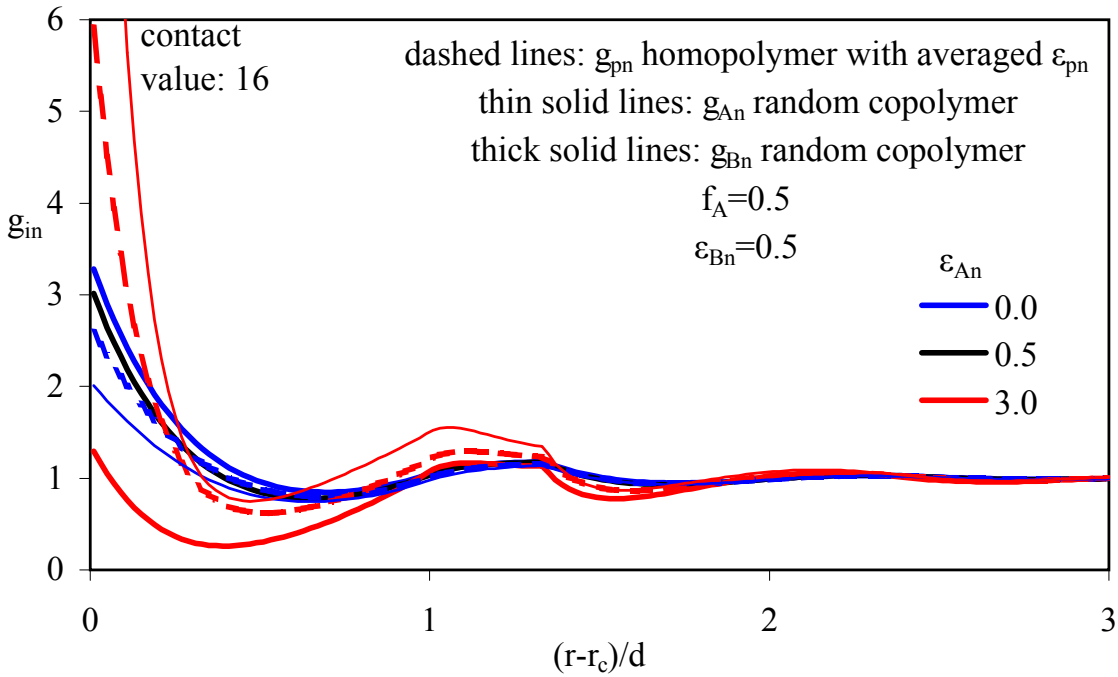

Figure 6.2: Type A and B monomer-particle correlation functions as a function of the dimensionless surface-to-surface separation of a monomer and nanoparticle for dilute ($\Phi \to 0$) hard spheres in a random AB copolymer, with $f_A = 0.5$ and $\epsilon_{Bn} = 0.5$ at the indicated values of ϵ_{An}, compared with the homopolymer result for $\epsilon_{pn} = (\epsilon_{An} + \epsilon_{Bn})/2$.

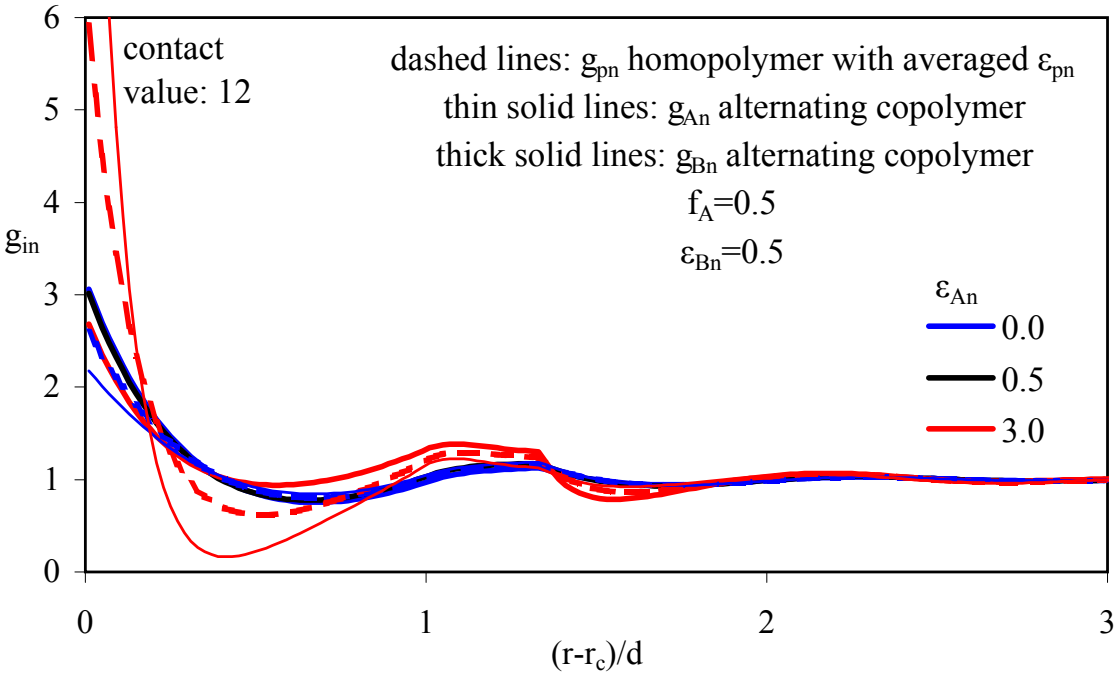

Figure 6.3: Type A and B monomer-particle correlation functions for dilute hard spheres in an alternating AB copolymer, with $f_A = 0.5$ and $\epsilon_{Bn} = 0.5$ at the indicated values of ϵ_{An}, compared with the homopolymer result for $\epsilon_{pn} = (\epsilon_{An} + \epsilon_{Bn})/2$.

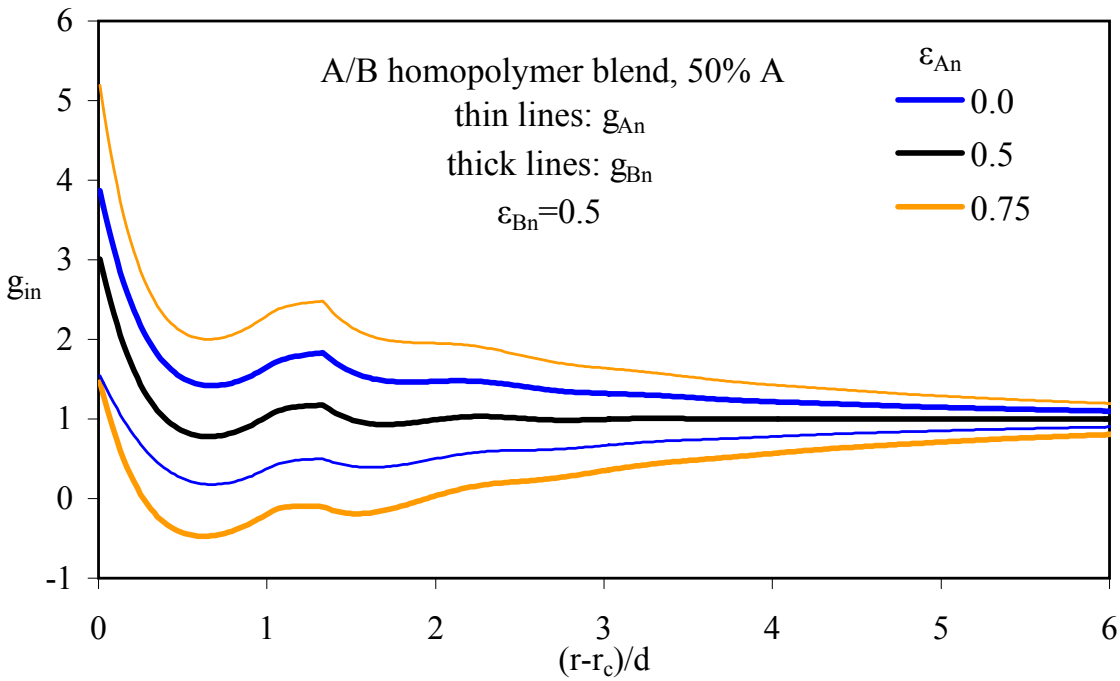

Figure 6.4: Type A and B monomer-particle correlation functions for dilute hard spheres in a blend with equal amounts of A and B polymer and $\epsilon_{Bn} = 0.5$ at the indicated values of ϵ_{An}.

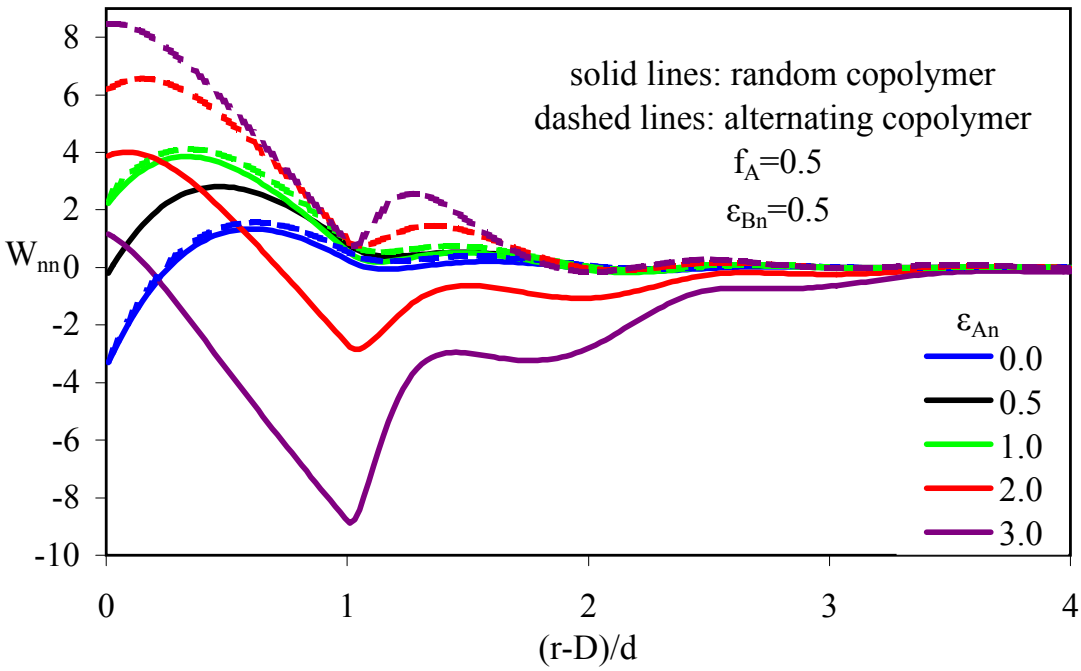

Figure 6.5: Potential of mean force for dilute hard spheres in a random or alternating AB copolymer, with $f_A = 0.5$ and $\epsilon_{Bn} = 0.5$ at the indicated values of ϵ_{An}.

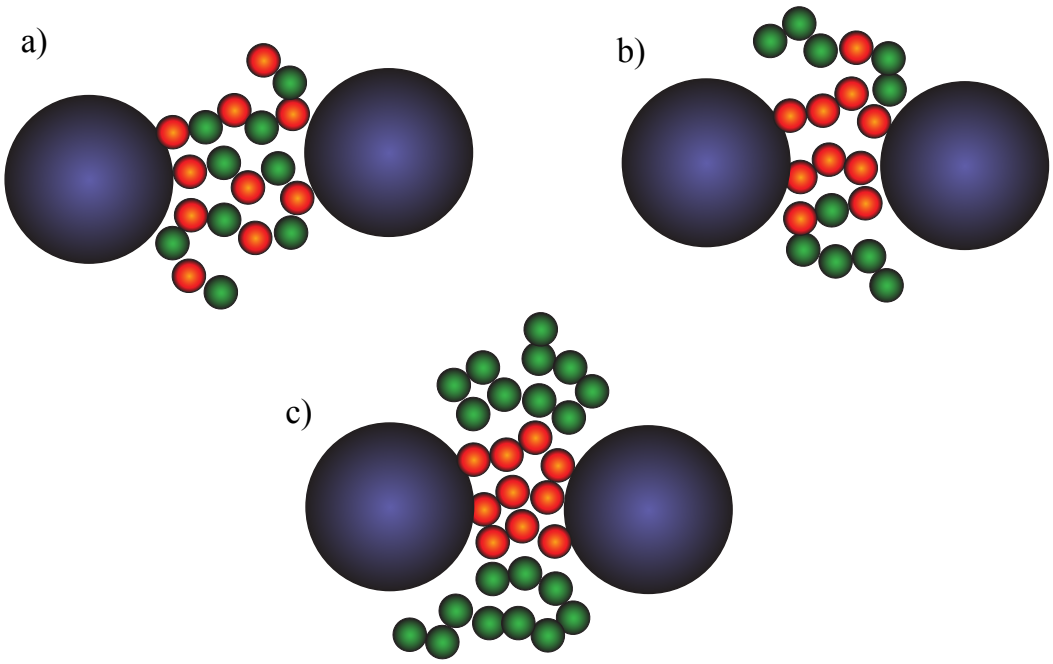

Figure 6.6: Sketches of polymer bridging between particles for the alternating copolymer, random copolymer, and polymer blend.

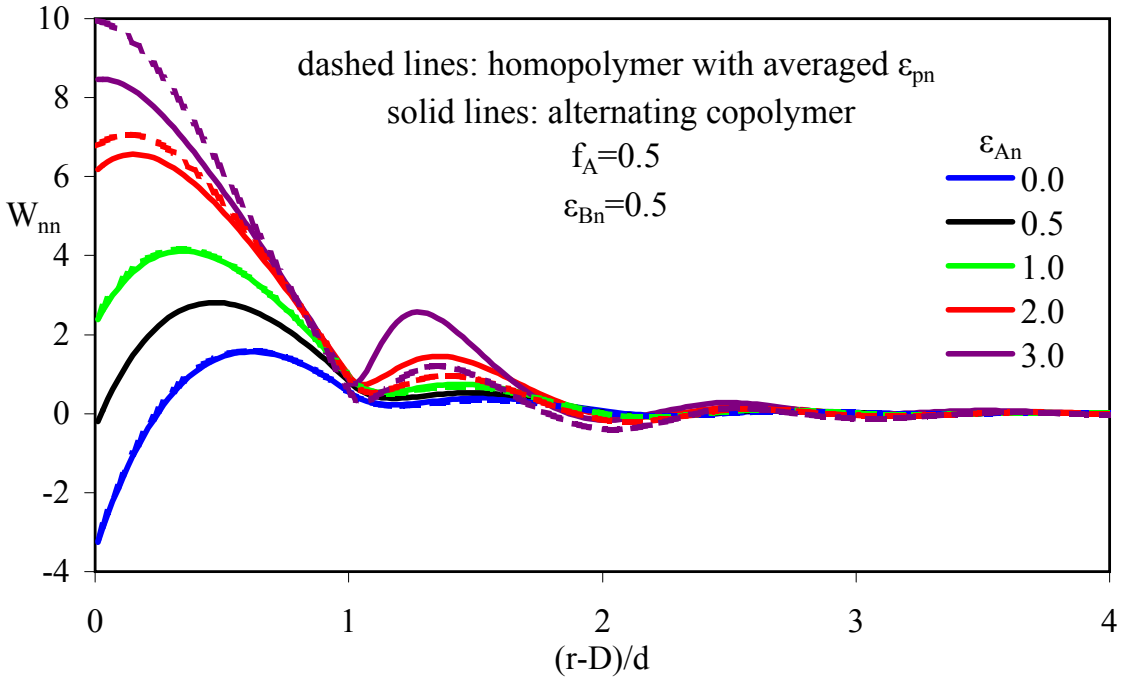

Figure 6.7: Potential of mean force for dilute hard spheres in an alternating AB copolymer, with $f_A = 0.5$ and $\epsilon_{Bn} = 0.5$ at the indicated values of ϵ_{An}, compared with the homopolymer result for $\epsilon_{pn} = (\epsilon_{An} + \epsilon_{Bn})/2$.

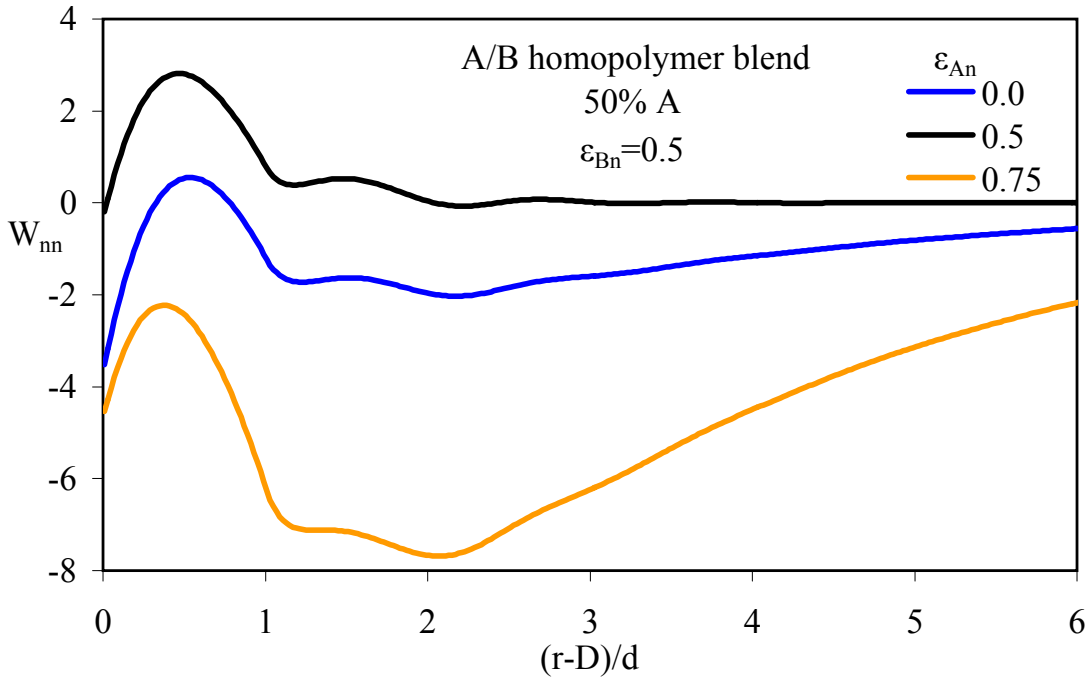

Figure 6.8: Potential of mean force for dilute hard spheres in a blend of equal amounts of A and B polymer, with $\epsilon_{Bn} = 0.5$ at the indicated values of ϵ_{An}.

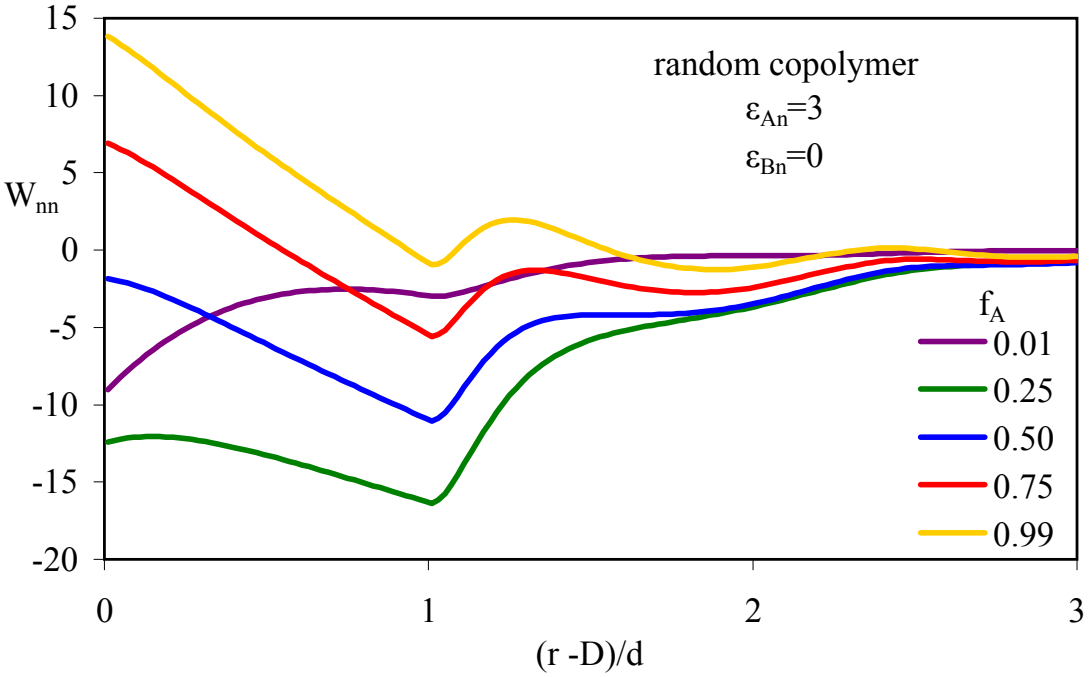

Figure 6.9: Potential of mean force for dilute hard spheres in a random AB copolymer, with various f_A at $\epsilon_{An} = 3$ and $\epsilon_{Bn} = 0$.

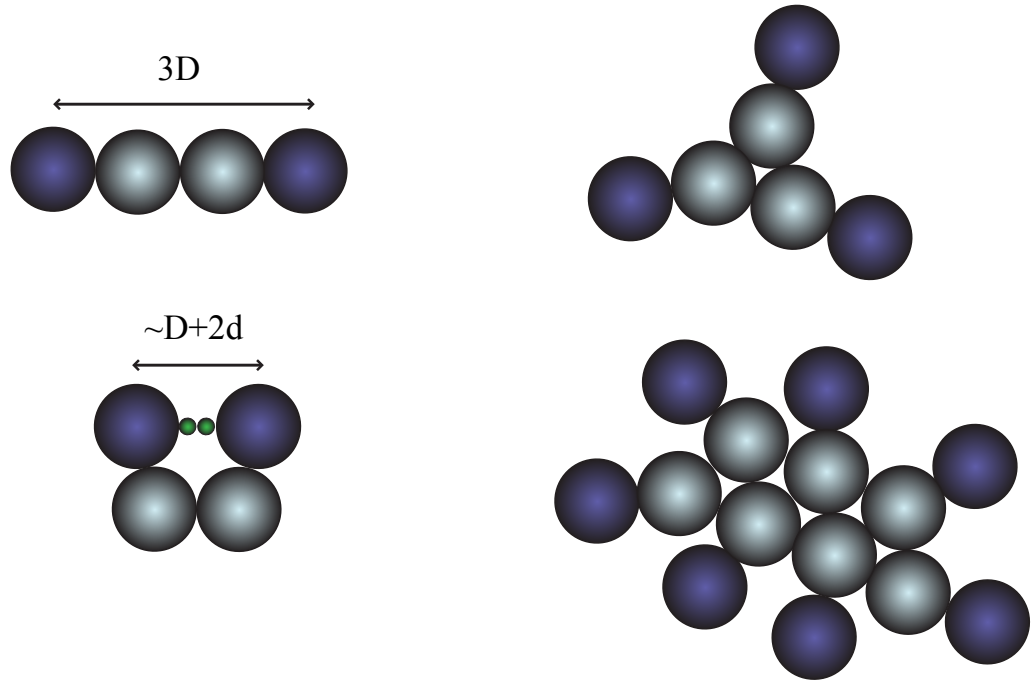

Figure 6.10: Conceptual sketch of heterogeneous diatomic fillers showing the length scales of interaction of the nonattractive sites when the attractive sites are in contact, and of possible small or large clusters.

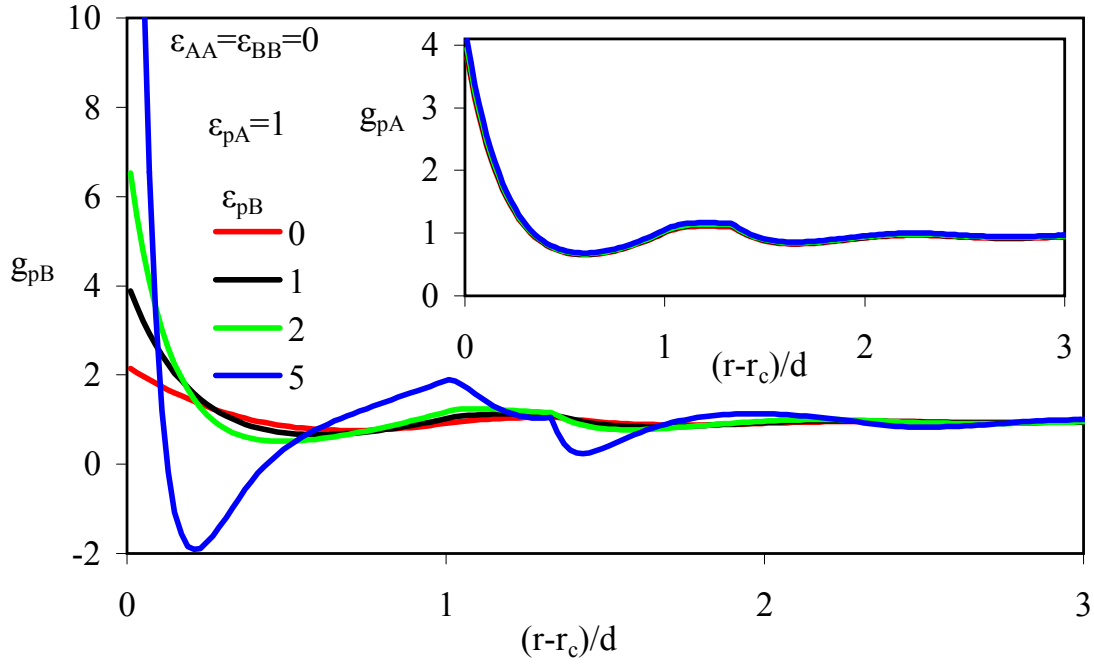

Figure 6.11: Polymer-particle site B correlation function (inset polymer-particle site A correlation function) for dilute hard diatomics in a homopolymer, with $\epsilon_{pA} = 1$ at the indicated values of ϵ_{pB}; at $\epsilon_{pB} = 5$, contact value is 30.

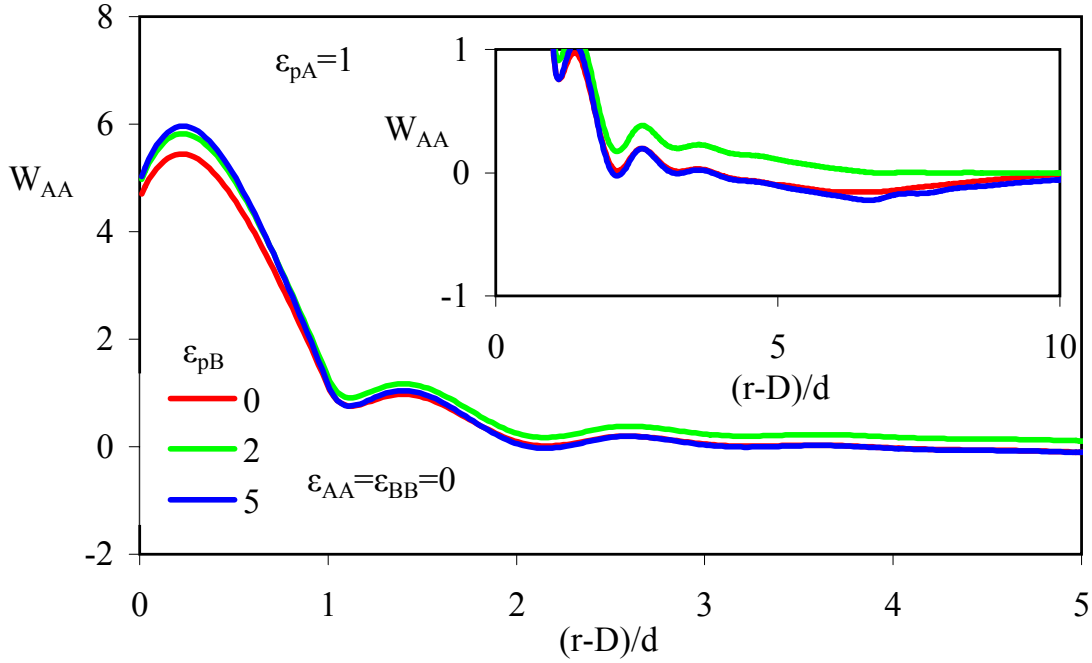

Figure 6.12: A-A site potential of mean force for dilute hard diatomics in a homopolymer, with $\epsilon_{pA} = 1$ at the indicated values of ϵ_{pB}.

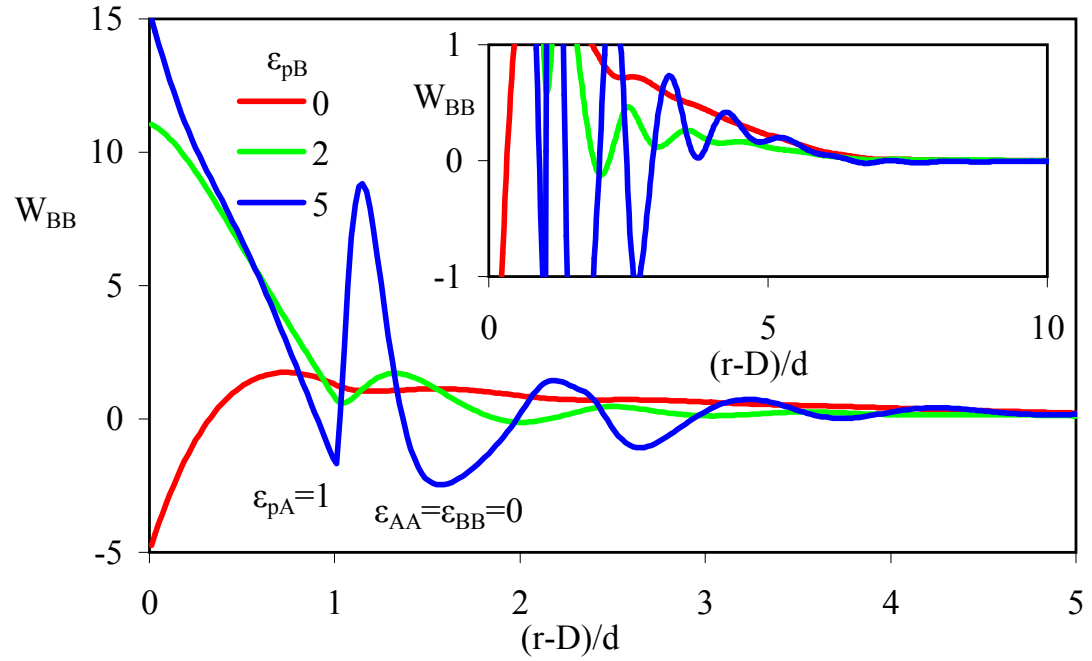

Figure 6.13: B-B site potential of mean force for dilute hard diatomics in a homopolymer, with $\epsilon_{pA} = 1$ at the indicated values of ϵ_{pB}.

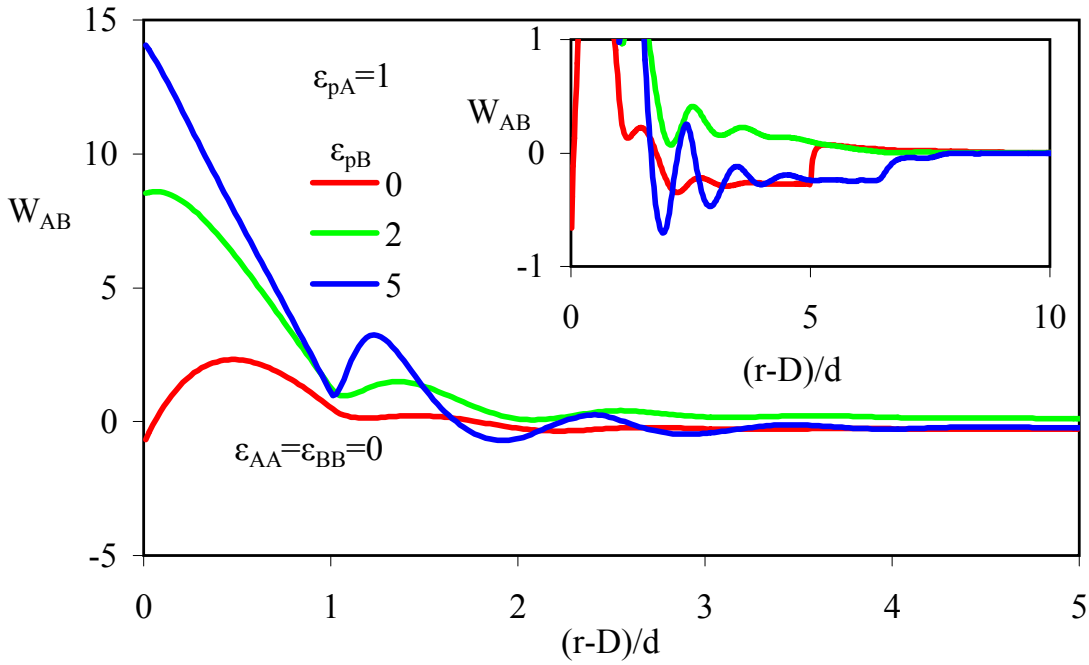

Figure 6.14: A-B site potential of mean force for dilute hard diatomics in a homopolymer, with $\epsilon_{pA} = 1$ at the indicated values of ϵ_{pB}.

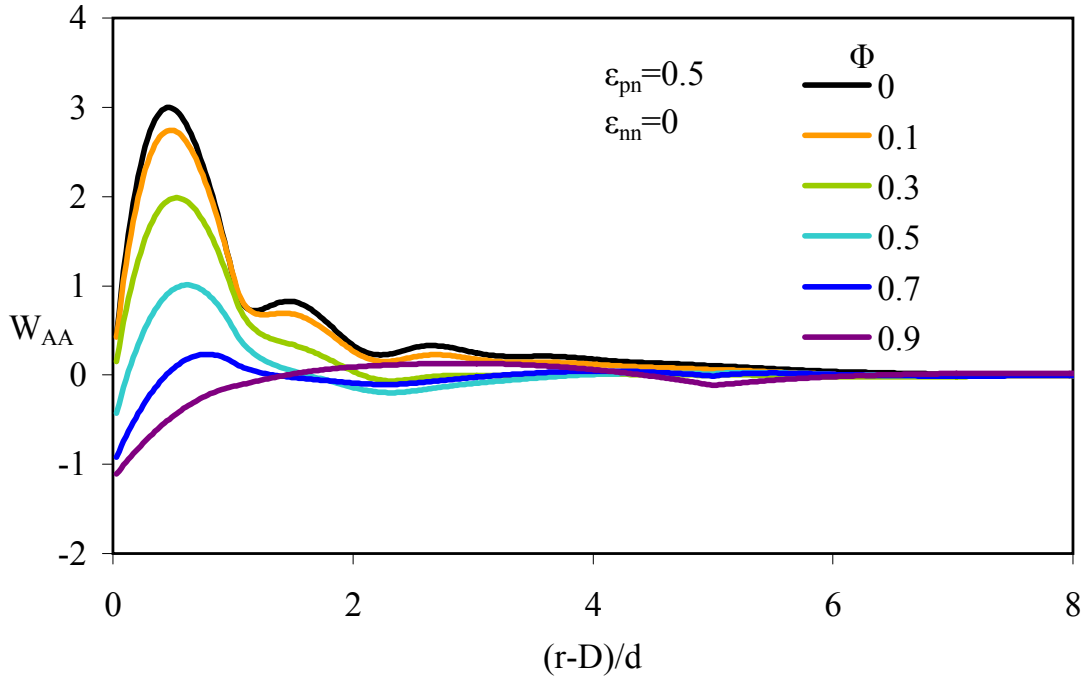

Figure 6.15: A-A site potential of mean force (equal to A-B and B-B site potential of mean force) for hard diatomics of various volume fractions in a homopolymer, with $\epsilon_{pA} = \epsilon_{pB} = 0.5$.

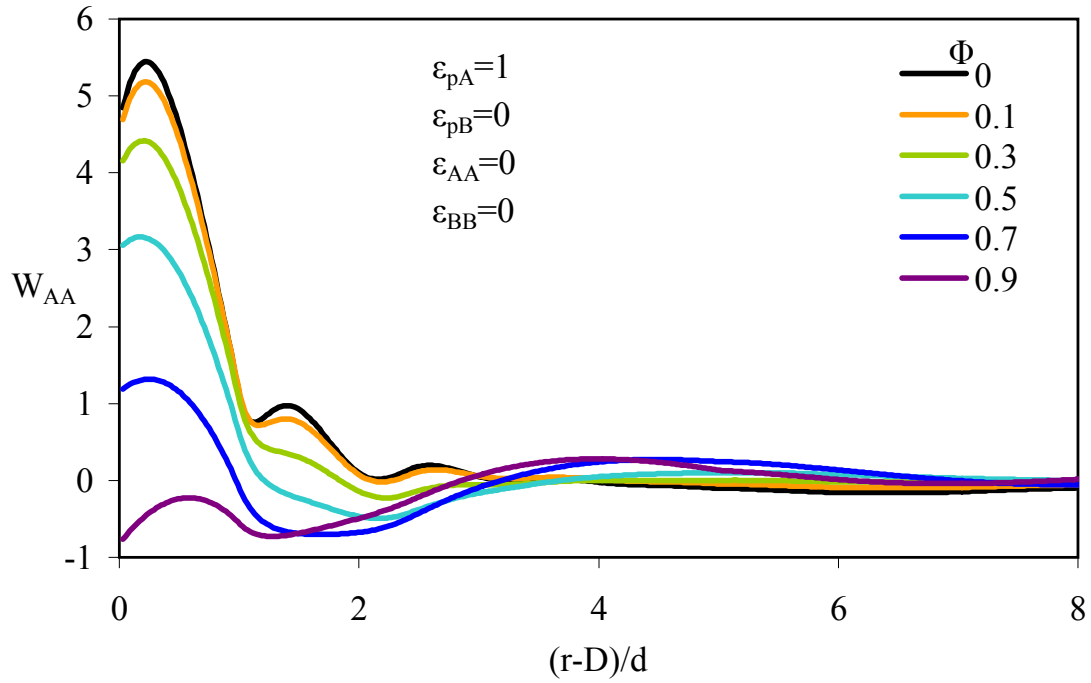

Figure 6.16: A-A site potential of mean force for hard diatomics of various volume fractions in a homopolymer, with $\epsilon_{pA} = 1$ and $\epsilon_{pB} = 0$.

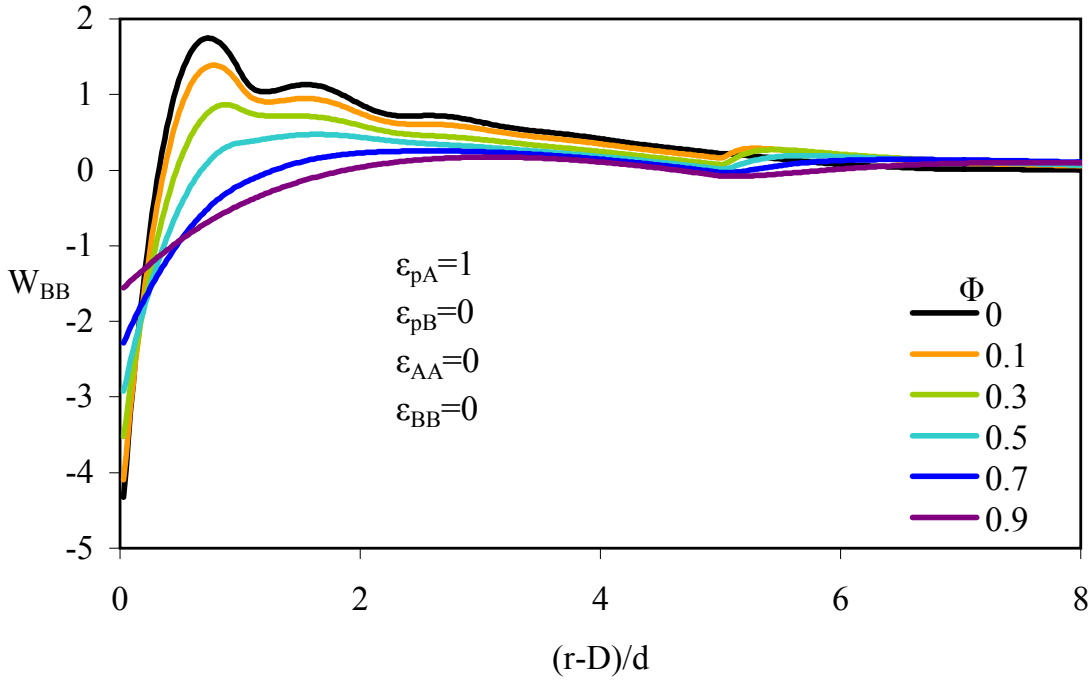

Figure 6.17: B-B site potential of mean force for hard diatomics of various volume fractions in a homopolymer, with $\epsilon_{pA} = 1$ and $\epsilon_{pB} = 0$.

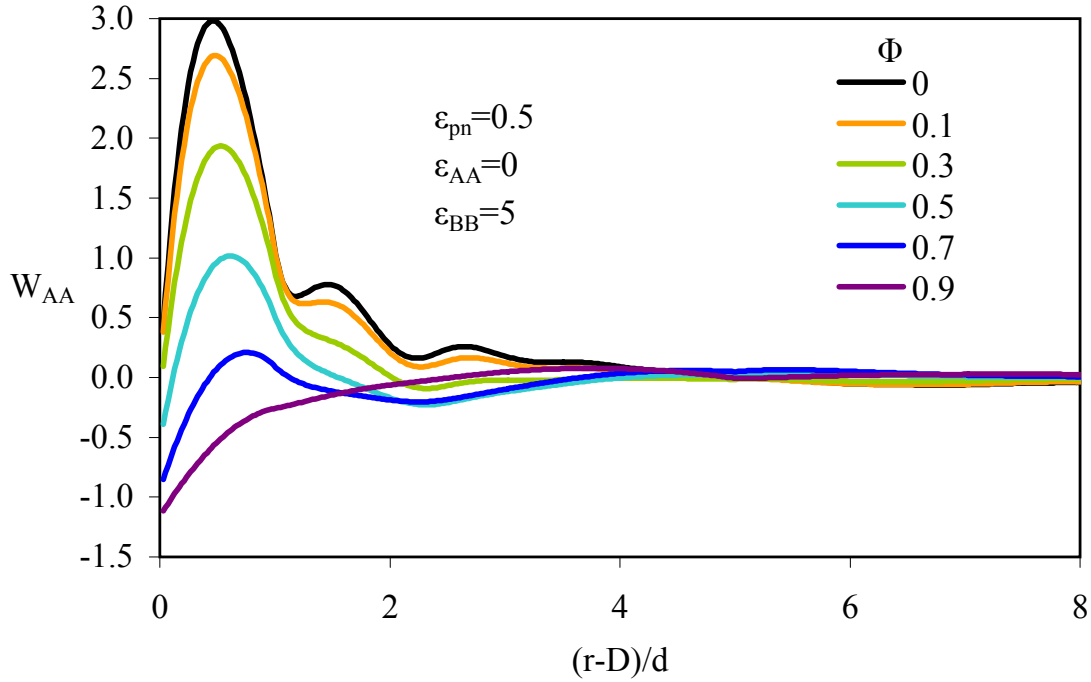

Figure 6.18: A-A site potential of mean force for diatomics of various volume fractions in a homopolymer, with $\epsilon_{BB} = 5$, $\epsilon_{AA} = 0$, and $\epsilon_{pA} = \epsilon_{pB} = 0.5$.

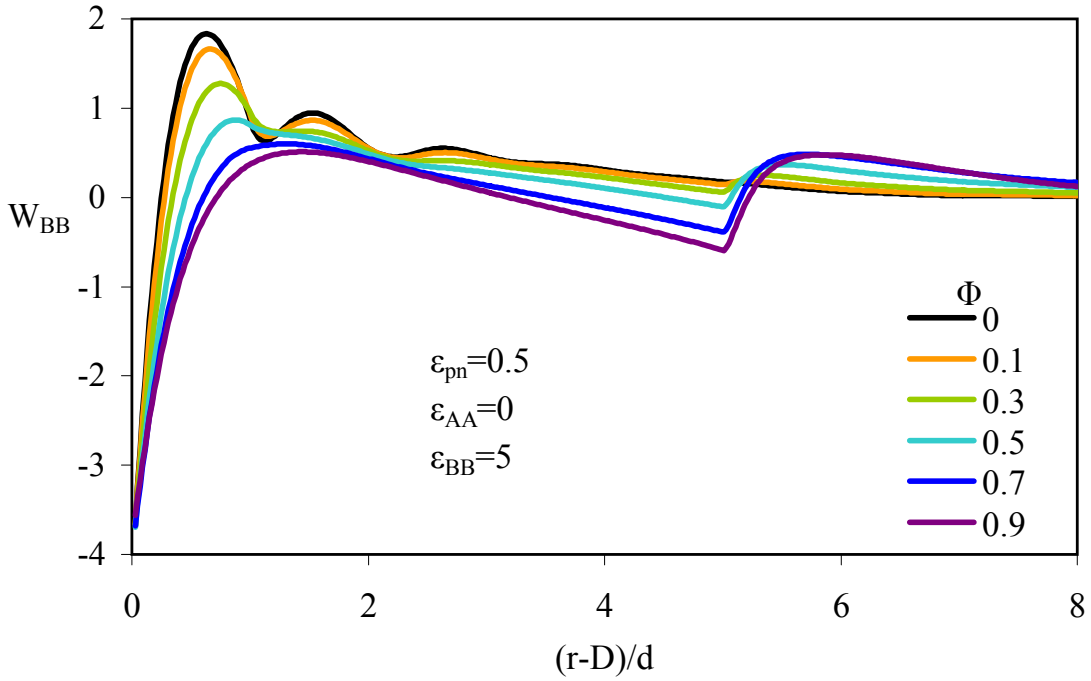

Figure 6.19: B-B site potential of mean force for diatomics of various volume fractions in a homopolymer, with $\epsilon_{BB} = 5$, $\epsilon_{AA} = 0$, and $\epsilon_{pA} = \epsilon_{pB} = 0.5$.

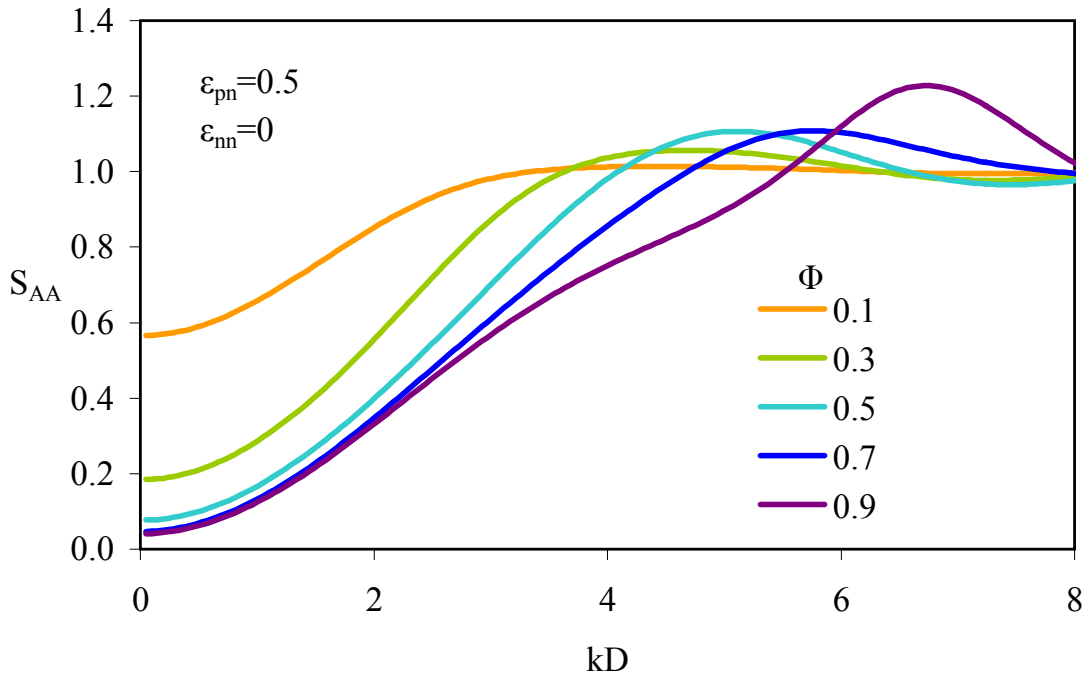

Figure 6.20: A-A site structure factor (equal to B-B site structure factor) for hard diatomics of various volume fractions in a homopolymer, with $\epsilon_{pA} = \epsilon_{pB} = 0.5$.

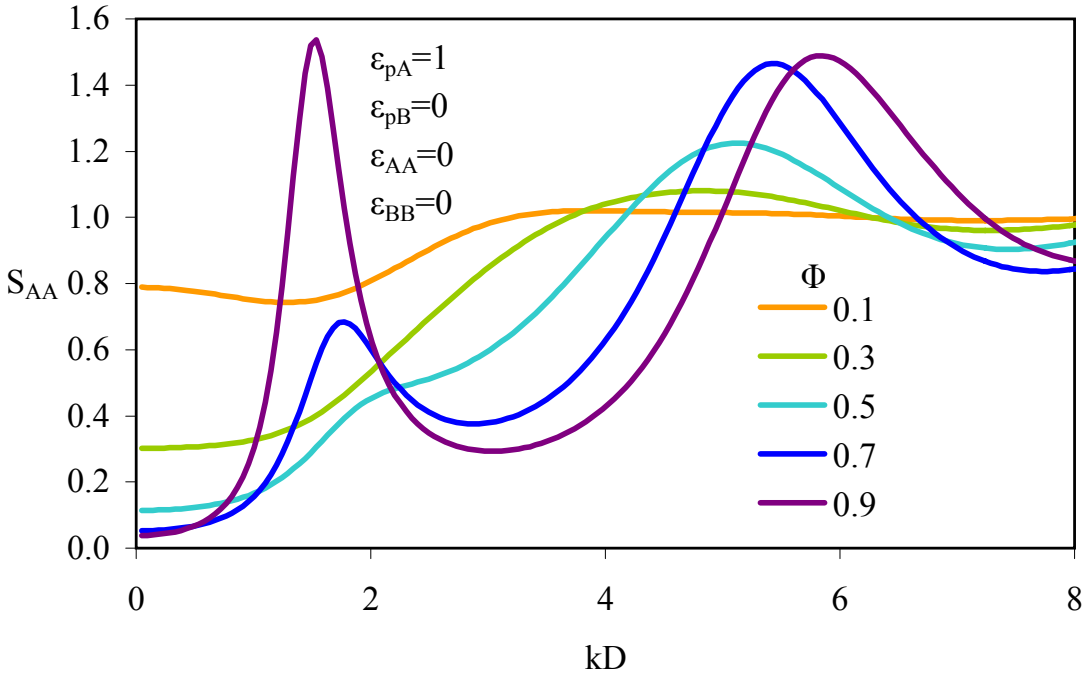

Figure 6.21: A-A site structure factor for hard diatomics of various volume fractions in a homopolymer, with $\epsilon_{pA} = 1$ and $\epsilon_{pB} = 0$.

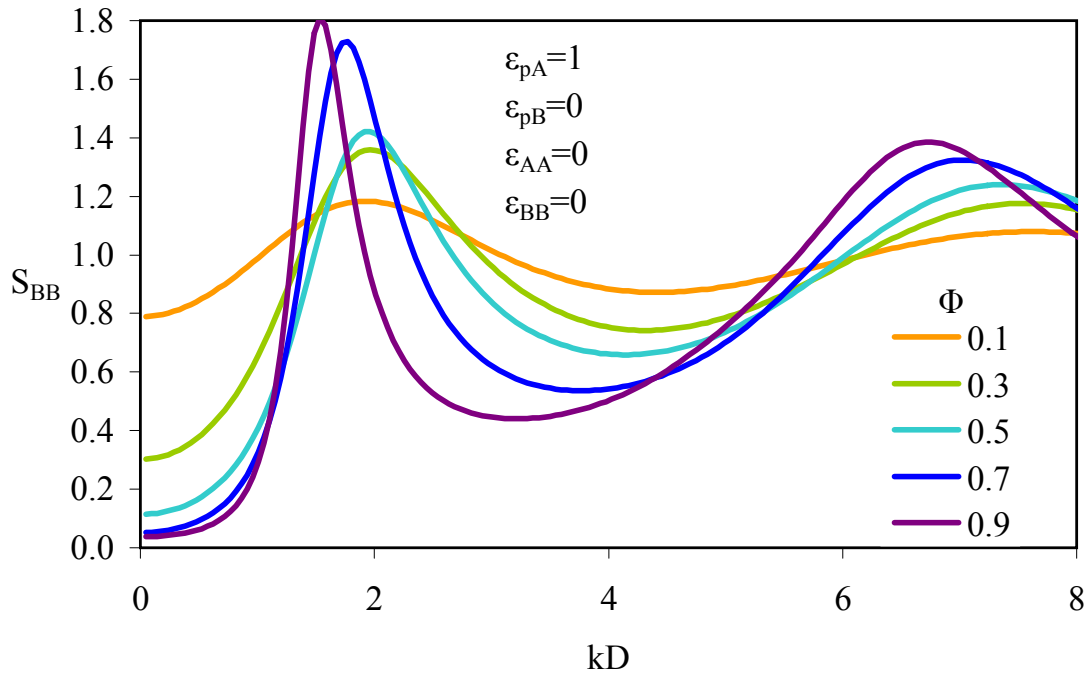

Figure 6.22: B-B site structure factor for hard diatomics of various volume fractions in a homopolymer, with $\epsilon_{pA} = 1$ and $\epsilon_{pB} = 0$.

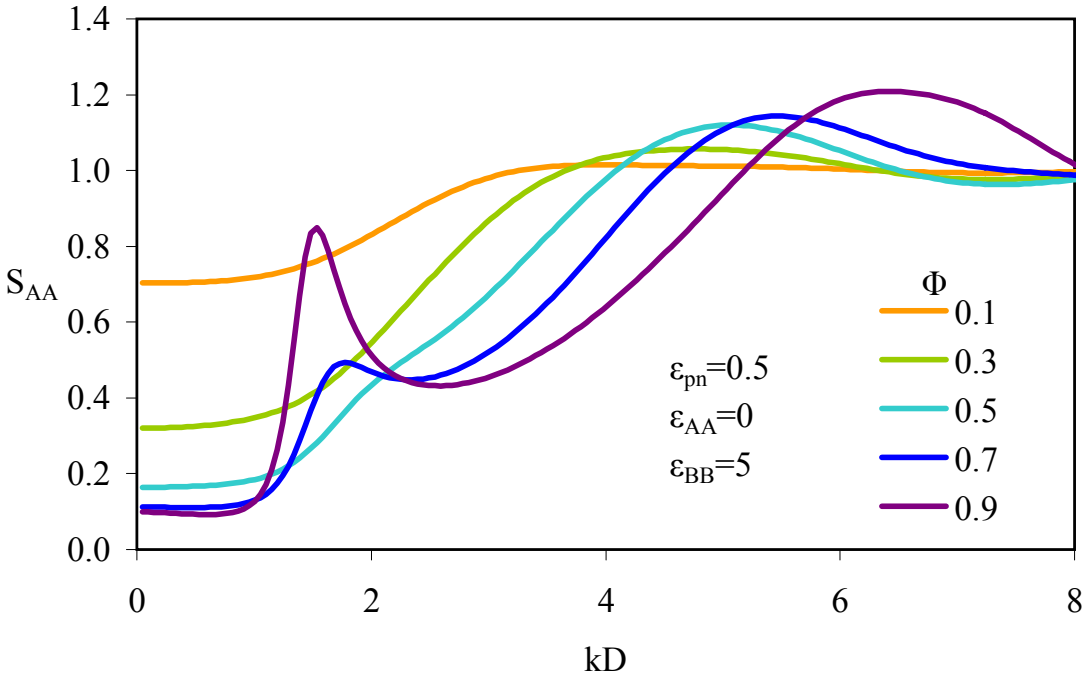

Figure 6.23: A-A site structure factor for diatomics of various volume fractions in a homopolymer, with $\epsilon_{BB} = 5$, $\epsilon_{AA} = 0$, and $\epsilon_{pA} = \epsilon_{pB} = 0.5$.

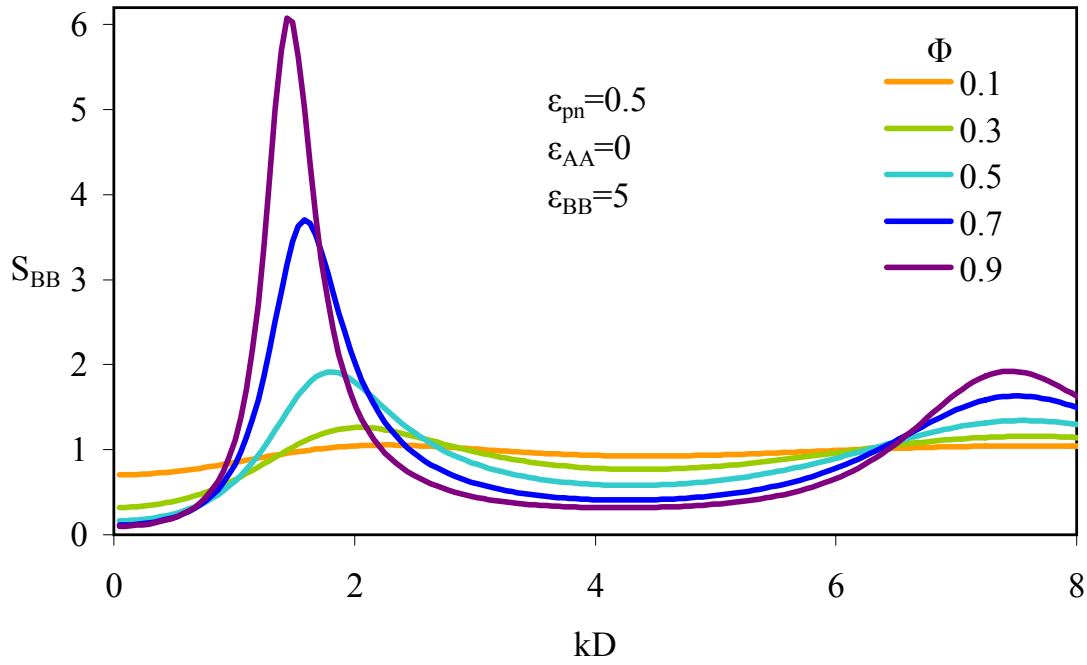

Figure 6.24: B-B site structure factor for diatomics of various volume fractions in a homopolymer, with $\epsilon_{BB} = 5$, $\epsilon_{AA} = 0$, and $\epsilon_{pA} = \epsilon_{pB} = 0.5$.

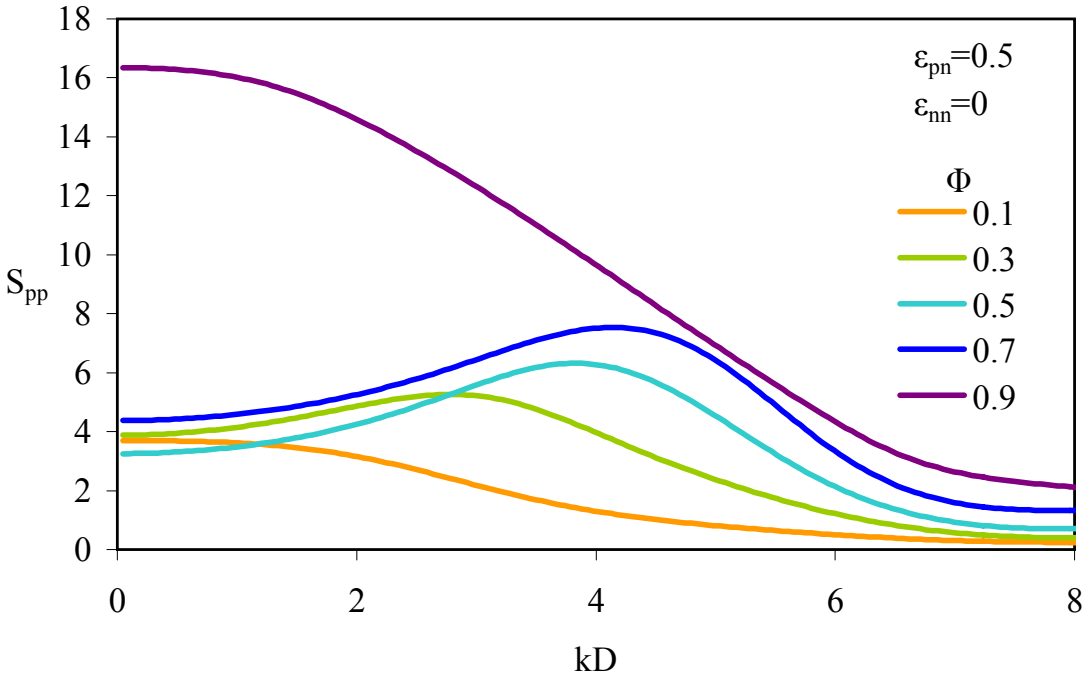

Figure 6.25: Homopolymer collective structure factor with various volume fractions of hard diatomics with $\epsilon_{pA} = \epsilon_{pB} = 0.5$.

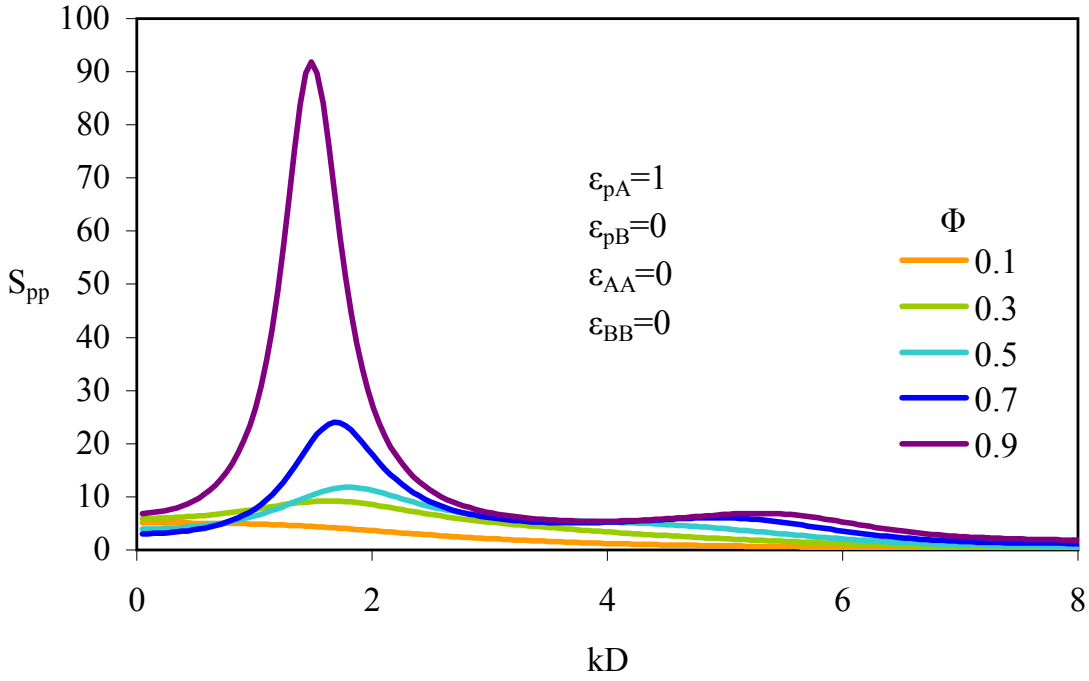

Figure 6.26: Homopolymer collective structure factor with various volume fractions of hard diatomics with $\epsilon_{pA} = 1$ and $\epsilon_{pB} = 0$.

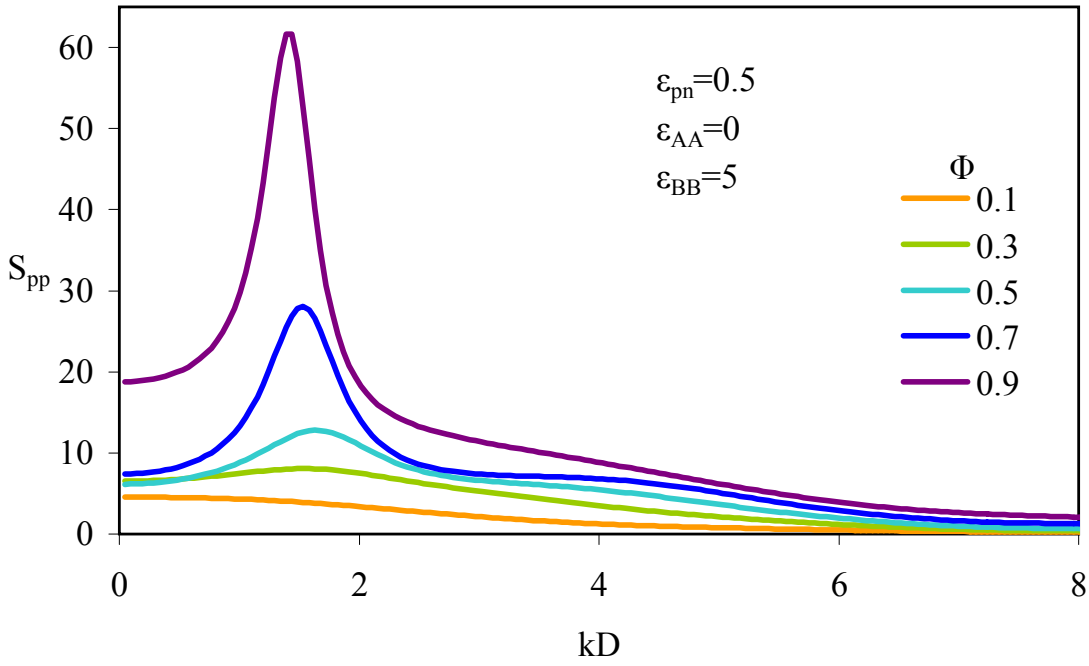

Figure 6.27: Homopolymer collective structure factor with various volume fractions of diatomics with $\epsilon_{BB} = 5$, $\epsilon_{AA} = 0$, and $\epsilon_{pA} = \epsilon_{pB} = 0.5$.

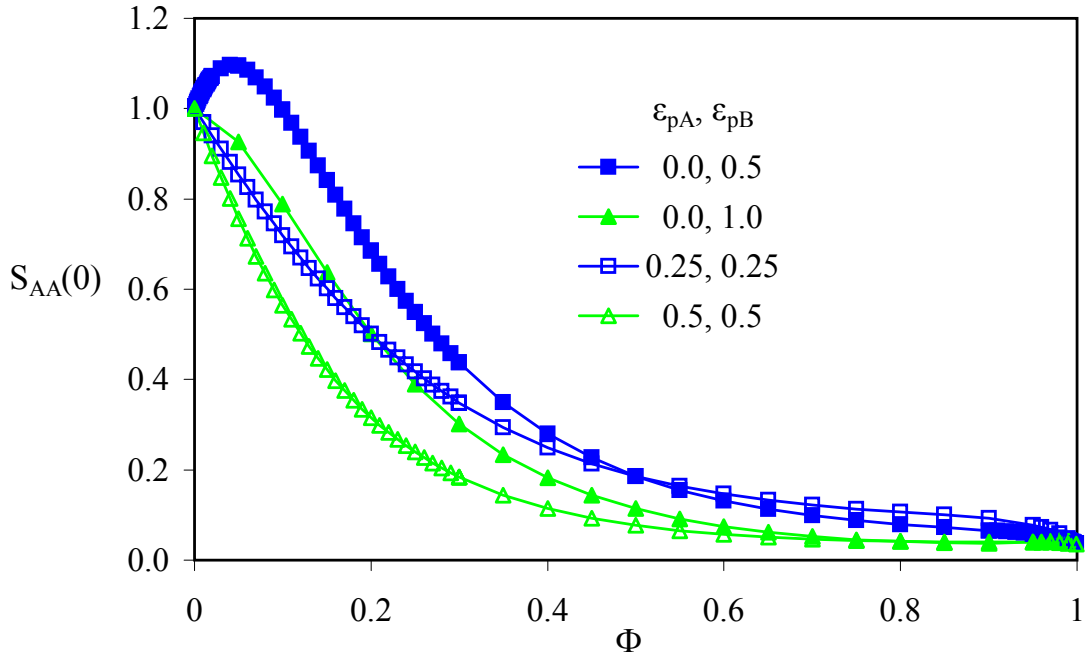

Figure 6.28: Filler site osmotic compressibility $S_{AA}(0) = S_{BB}(0)$ versus volume fraction in homopolymer for hard diatomics at the indicated values of ϵ_{pA} and ϵ_{pB}.

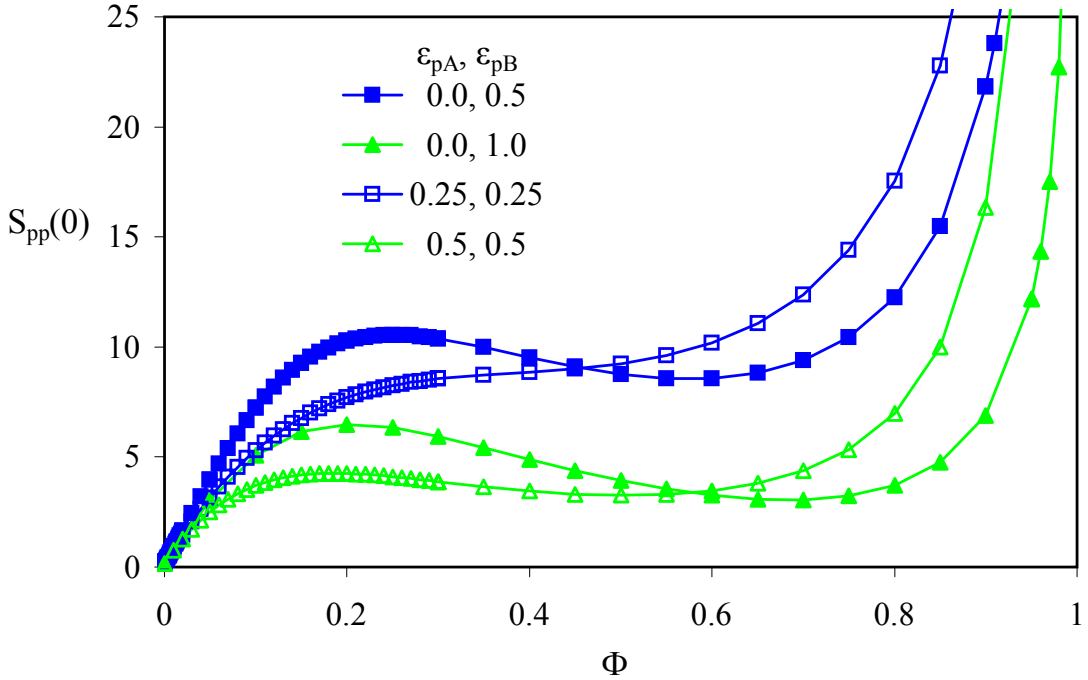

Figure 6.29: Polymer osmotic compressibility versus volume fraction of hard diatomics at the indicated values of ϵ_{pA} and ϵ_{pB}.

Chapter 7

Conclusions and Future Work

The Polymer Reference Interaction Site Model (PRISM) liquid state theory has been extended and applied to many types of polymer nanocomposites. A basic model is that of hard spheres in a polymer melt with a variable interfacial attraction. If the interfacial cohesion strength is small, the well known depletion attraction in the two particle limit leads to particle aggregation and phase separation at finite volume fractions. At a moderate interfacial attraction, a bound polymer layer is adsorbed on each particle, the effective particle potential is repulsive, and the system can be miscible at all volume fractions. However, very strongly adsorbing polymer can cause a particle-particle attraction through the formation of polymer bridges. In this case, a short range polymer-mediated repulsion due to the bound layer is followed by one or more bridging minima in the potential of mean force. The volume fraction of bridging induced phase separation is a complex function of the spatial range of the interfacial attraction.

Quantitative comparison of the calculations with small angle x-ray scattering experiments demonstrates that the theoretical approach properly accounts for the effects of adsorbed polymer layers on nanoparticle concentration fluctuations over all length scales for a wide range of volume fractions. Important differences in experimental results are observed when a less strongly adsorbing polymer is used, and are reproduced by the theory by lowering interfacial cohesion strength. The mixture total packing fraction is increased as particles are added to the polymer melt in order to account for equation-of-state effects which are important at very high filler loadings. A distinctive microphase separation like peak in the collective polymer structure factor is predicted. Addition of solvent not only decreases polymer density but also decreases the effective interfacial cohesion strength, the consequences of which have been measured experi-

mentally and shown to be properly accounted for by the theory.

The comparisons to experiment specifically place the polyethyleneoxide(PEO)-silica and polytetrahydrofuran(PTHF)-silica systems on the generic theoretical phase diagram. In contrast to the PEO-silica mixture, the PTHF-silica nanocomposite is predicted to be very near depletion phase separation and will not display the polymer microphase peak observed for miscible systems. Hence, this peak may be used as an experimental indicator of the presence of a bound polymer layer and the attendant steric stabilization. The theoretical potential of mean force for the PEO and PTHF nanocomposites were also computed and indicate the PTHF system has a very strong depletion minimum which is consistent with the experimental observation of nonequilibrium gelation at high enough filler loadings.

A good solvent (ethanol) was added to the experimental PEO-silica system with various constant polymer:solvent ratios, and the results compared to the theory at accordingly lower polymer packing fractions (the solvent was modeled implicitly). Decreasing polymer packing fraction alone had only small effects on the theoretical results, but concurrently decreasing polymer adsorption to account for the decreased enthalpic gain of polymer-nanoparticle contact showed a larger effect in good agreement with the experiments. This suggests the interfacial attraction strength can be modified experimentally by small amounts of solvents, and points towards addition of poor solvents to a nanocomposite near depletion phase separation as a possible route to increased miscibility.

Motivated by polymer nanocomposites made with carbon nanotubes, clay platelets and other novel nonspherical fillers, which have been the focus of many recent experiments, PRISM theory was extended and applied to study the equilibrium properties of hard and attractive rodlike particles, and pseudo one- two- and three-dimensional hard particles (rod, disk, cube) of fixed space-filling volume, in a dense adsorbing homopolymer melt. The theory is further extended to chemically heterogeneous species for the

first time including the systems: attractive rods in a random copolymer composed of two monomers with different interfacial adsorption strengths; spheres in a random copolymer, alternating copolymer, or polymer blend where the two types of monomers have different interfacial adsorption strengths; and "Janus" diatomic particles in a homopolymer in which one filler site can be either more attracted to the polymer or to itself than the other site.

For the pseudo one- two- and three-dimensional nanoparticles, the second virial coefficient, nanoparticle potential of mean force, osmotic compressibilities, and spinodal demixing boundaries have been determined. The entropic depletion attraction between nanoparticles is dominant for weakly adsorbing polymer, while strongly adsorbing chains induce a bridging attraction. Intermediate interfacial cohesion results in the formation of a sterically stabilizing adsorbed polymer layer around each nanoparticle, which can partially damp inter-filler collective order on various length scales and increase order on an averaged length scale. The details of depletion, stabilization, or bridging behavior are shape dependent and often, but not always, trends are monotonic with increasing filler dimensionality. Distinctive nanoparticle shape dependent low angle features are predicted for the collective polymer structure factor associated with competing macrophase fluctuations and microphase-like ordering. The influence of nonzero mixture compressibility on the scattering profiles was established.

A detailed study of thin attractive rod fillers was performed in search of design rules for dispersing nanotubes in polymer melts. The potential of mean force and the second virial coefficient, B_2, were calculated as a function of polymer-rod and rod-rod attraction strengths. The transition from positive to negative B_2 at low polymer-rod interfacial attraction (entropic depletion) occurs more readily (at higher attraction strength) as rod-rod attraction is increased. The transition to negative B_2 at high polymer-rod attraction strength, driven by polymer-induced bridging, is also hastened by the added rod-rod attraction if it is of the same spatial range as the interfacial

attraction. However, if the rod-rod attraction is of shorter range, this transition is relatively invariant to inter-rod attraction strength. Using a random copolymer in which one monomer type is more strongly adsorbing increases the strength of the bridging attraction at intermediate copolymer compositions. Overall, the most miscible attractive rod systems are those in a moderately adsorbing homopolymer and which have a short spatial range of rod-rod attraction compared to polymer-rod attraction.

Copolymers were also studied with a spherical filler in the dilute limit. The potential of mean force in an alternating AB copolymer melt is similar to that in a homopolymer at an interfacial attraction strength which is the average of the A and B monomer-filler attraction strengths. The only noticeable difference is a small layering effect for the alternating copolymer such that more of the strongly adsorbing monomer is in contact with particle, with a layer of the less adsorbing monomer a short distance away. In contrast, the random copolymer shows a much stronger and longer range bridging behavior than the averaged interfacial attraction homopolymer, or even a homopolymer composed of only the more adsorbing monomer. A blend of more and less strongly adsorbing homopolymers also mediates a very strong and even longer range bridging attraction via a preferential wetting mechanism. This intense bridging is produced by the existence of groups of strongly adsorbing monomers along the chain (present in significant amounts for the random copolymer even at a 25% strongly adsorbing monomer composition) against the background of a less adsorbing monomer type which, due to entropic considerations, acts to further push the adsorbing sections onto the particles.

A brief investigation of heterogeneous (Janus) diatomic fillers in a homopolymer showed qualitatively different behavior versus the homogeneous diatomic case. When polymer adsorbs on only one side of a diatomic particle, the other side experiences a depletion attraction and may form the interior of multiparticle clusters. Both the filler and polymer structure factors show order on the diatomic site scale as well as a larger

scale corresponding to diatomic clusters. The larger length scale order is also present for equally polymer-attracting diatomics with an added direct attraction of one type of diatomic site, although it is not as prevalent at low volume fractions in this case. This represents a qualitatively new clustering or micelle formation not observed for homogeneous diatomic particles.

Other heterogeneous systems would likely also exhibit qualitatively new behaviors. One interesting type of chemically heterogeneous filler amenable to future studies is a rod with chemically different end sites. The theoretical parameters could be set to represent specific experimental systems of interest. Carbon nanotubes, for example, are known to be differentially reactive to functionalization at the ends,[21] allowing the possibility of nanotubes with ends that are more or less attractive to each other, or which have a different polymer interaction than the bare nanotubes. Another similar particle created recently consists of a gold nanorod with polymer tethers added to both ends, which changes the end-end interactions.[25] If the ends attract each other enough, they may assemble into clusters and ultimately create a rod network within the homopolymer matrix, mimicking the behavior of triblock copolymers of similar architecture. Another experimentally relevant filler model is a relatively simple diatomic or other small molecular nanoparticle which is heterogeneous in site size and possibly in chemistry. In one experimental example of combined shape and chemical heterogeneity, CdS is nucleated on approximately spherical Fe_3O_4 seeds; the CdS growth can be controlled to yield few to many small spherical CdS crystals on each seed or one to several rodlike CdS protrusions.[23] Used as polymer fillers, such anisotropic shapes could organize into clusters based on entropic considerations as a different polymer induced depletion may be expected for the small and large parts of the nanocrystals. If modeled by PRISM theory, evidence of structures such as rod networks or micelles of shape heterogeneous diatomics might be found in the potential of mean force and the rod and polymer collective structure factors, in which case the parameters which

control this behavior could be established.

The investigation of many shapes and chemistries of PNC systems has already provided some guidelines to produce various desirable and undesirable behaviors. One simple example is that a short range rod-rod attraction compared to the polymer-rod attraction should allow greater miscibility. Another finding is that controlled clusters of fillers in a PNC are possible with either a differential polymer interfacial attraction or direct filler site-site attraction. Signatures of such behavior are predicted in both filler and polymer structure factors, which can be measured by selective scattering experiments. However, the aspherical nanoparticle and chemically heterogeneous PNC results remain to be confirmed by simulations or experiments which can tune (at least in some cases) the filler and polymer interactions. Such confirmation could pinpoint an experimental system in the theoretical parameter space and allow insights into the possibilities and limitations of the theory.

This theoretical work examined the structure and phase behavior of PNCs. Further theory and simulation are needed to describe the mechanical behavior and its correlation with structure and miscibility, which is relevant to the final PNC reinforcement but also to the production and processing of the material. The assumption of only small effects of fillers on polymer chain conformation, especially for aspherical nanoparticles and chemically heterogeneous systems, has yet to be tested in detail. Although signatures of impending nonequilibrium behavior are discussed here, additional work is required to specifically address possible kinetically driven behaviors and inhomogeneous systems. The ability of the theory to predict spherical filler concentration fluctuations at all length scales provides hope for its use in collaboration with experiments in the design of novel composites.

References

[1] Ash, B., Schadler, L., and Siegel, R., "Glass transition behavior of alumina–polymethylmethacrylate nanocomposites," *Materials Letters*, Vol. 55, 2002, pp. 83–87.

[2] Ash, B. J., Siegel, R. W., and Schadler, L. S., "Glass-transition temperature behavior of alumina/PMMA nanocomposites," *Journal of Polymer Science: Part B: Polymer Physics*, Vol. 42, 2004, pp. 4371–4383.

[3] Bansal, A., Yang, H., , Li, C., Benicewicz, B. C., Kumar, S. K., and Schadler, L. S., "Controlling the thermomechanical properties of polymer nanocomposites by tailoring the polymer-particle interface," *Journal of Polymer Science: Part B: Polymer Physics*, Vol. 44, 2006, pp. 2944–2950.

[4] Tsagaropoulos, G. and Eisenberg, A., "Dynamic mechanical study of the factors affecting the two glass transition behavior of filled polymers. Similarities and differences with random ionomers," *Macromolecules*, Vol. 28, 1994, pp. 6067–6077.

[5] Ash, B. J., Siegel, R. W., and Schadler, L. S., "Mechanical behavior of alumina/poly(methyl methacrylate) nanocomposites," *Macromolecules*, Vol. 37, 2004, pp. 1358–1369.

[6] Sternstein, S. S. and Zhu, A.-J., "Reinforcement mechanism of nanofilled polymer melts as elucidated by nonlinear viscoelastic behavior," *Macromolecules*, Vol. 35, 2002, pp. 7262–7273.

[7] Goel, V., Chatterjee, T., Bonbalski, L., Yurekli, K., Matyjaszewski, K., and Krishnamoorti, R., "Viscoelastic properties of silica-grafted poly(styrene-acrylonitrile) nanocomposites," *Journal of Polymer Science: Part B: Polymer Physics*, Vol. 44, 2006, pp. 2014–2023.

[8] Zhu, Z., Thompson, T., Wang, S.-Q., von Meerwall, E. D., and Halasa, A., "Investigating linear and nonlinear viscoelastic behavior using model silica-particle-filled polybutadiene," *Macromolecules*, Vol. 38, 2005, pp. 8816–8824.

[9] Mackay, M. E., Dao, T. T., Tuteja, A., Ho, D. L., Horn, B. V., Kim, H.-C., and Hawker, C. J., "Nanoscale effects leading to non-Einstein-like decrease in viscosity," *Nature Materials*, Vol. 2, 2003, pp. 762–766.

[10] Berriot, J., Montes, H., Lequeux, F., Long, D., and Sotta, P., "Evidence for the shift of the glass transition near the particles in silica-filled elastomers," *Macromolecules*, Vol. 35, 2002, pp. 9756–9762.

[11] Montes, H., Lequeux, F., and Berriot, J., "Influence of the glass transition temperature gradient on the nonlinear viscoelastic behavior in reinforced elastomers," *Macromolecules*, Vol. 36, 2003, pp. 8107–8118.

[12] Vieweg, S., Unger, R., Heinrich, G., and Donth, E., "Comparison of dynamic shear properties of styrene-butadiene vulcanizates filled with carbon black or polymeric fillers," *Journal of Applied Polymer Science*, Vol. 73, 1999, pp. 495–503.

[13] Wang, M.-J., "Effect of polymer-filler and filler-filler interactions on dynamic properties of filled vulcanizates," *Rubber Chemistry and Technology*, Vol. 71, 1998, pp. 520–589.

[14] Wang, M.-J., "The role of filler networking in dynamic properties of filled rubber," *Rubber Chemistry and Technology*, Vol. 72, 1999, pp. 430–448.

[15] Winey, K. I. and Vaia, R. A., "Polymer nanocomposites," *MRS Bulletin*, Vol. 32, 2007, pp. 314–319.

[16] Shi, X., Hudson, J. L., Spicer, P. P., Tour, J. M., Krishnamoorti, R., and Mikos, A. G., "Injectable nanocomposites of single-walled carbon nanotubes and biodegradable polymers for bone tissue engineering," *Biomacromolecules*, Vol. 7, 2006, pp. 2237–2242.

[17] Mackay, M. E., Tuteja, A., Duxbury, P. M., Hawker, C. J., Horn, B. V., Guan, Z., Chen, G., and Krishnan, R. S., "General strategies for nanoparticle dispersion," *Science*, Vol. 311, 2006, pp. 1740–1743.

[18] Chatterjee, T. and Krishnamoorti, R., "Dynamic consequences of the fractal network of nanotube-poly(ethylene oxide) nanocomposites," *Physical Review E*, Vol. 75, 2007, pp. 050403.

[19] Putz, K., Krishnamoorti, R., and Green, P. F., "The role of interfacial interactions in the dynamic mechanical response of functionalized SWNT-PS nanocomposites," *Polymer*, Vol. 48, 2007, pp. 3540–3545.

[20] Hunter, D. L., Kamena, K. W., and Paul, D. R., "Processing and properties of polymers modified by clays," *MRS Bulletin*, Vol. 32, 2007, pp. 323–327.

[21] Krishnamoorti, R., "Strategies for dispersing nanoparticles in polymers," *MRS Bulletin*, Vol. 32, 2007, pp. 341–347.

[22] Kwon, K.-W., Lee, B. H., and Shim, M., "Structural evolution in metal oxide/semiconductor colloidal nanocrystal heterostructures," *Chemistry of Materials*, Vol. 18, 2006, pp. 6357–6363.

[23] McDaniel, H. and Shim, M., "Size and growth rate dependent structural diversification of Fe_3O_4/CdS anisotropic nanocrystal heterostructures," *ACS Nano*, Vol. 3, 2009, pp. 434–440.

[24] Hong, L., Jiang, S., and Granick, S., "Simple Method to Produce Janus Colloidal Particles in Large Quantity," *Langmuir*, Vol. 22, 2006, pp. 9495–9499.

[25] Nie, Z., Fava, D., Kumacheva, E., Zou, S., Walker, G. C., and Rubinstein, M., "Self-assembly of metal-polymer analogues of amphiphilic triblock copolymers," *Nature Materials*, Vol. 6, 2007, pp. 609–614.

[26] Rasheed, A., Dadmun, M. D., Ivanov, I., Britt, P. F., and Geohegan, D. B., "Improving dispersion of single-walled carbon nanotubes in a polymer matrix using specific interactions," *Chemistry of Materials*, Vol. 18, 2006, pp. 3513–3522.

[27] Eisenriegler, E., "Small mesoscopic particles in dilute and semidilute solutions of nonadsorbing polymers," *Journal of Chemical Physics*, Vol. 113, 2000, pp. 5091–5097.

[28] Odijk, T., "Many-body depletion interactions among protein spheres in a semidilute polymer solution," *Journal of Chemical Physics*, Vol. 106, 1997, pp. 3402–3406.

[29] Patel, N. and Egorov, S. A., "Interactions between colloidal particles in polymer solutions: A density functional theory study," *Journal of Chemical Physics*, Vol. 121, 2004, pp. 4987–4997.

[30] Patel, N. and Egorov, S. A., "Interactions between nanocolloidal particles in polymer solutions: Effect of attractive interactions," *Journal of Chemical Physics*, Vol. 123, 2005, pp. 144916.

[31] Patel, N. and Egorov, S. A., "Interactions between sterically stabilized nanoparticles in supercritical fluids: A simulation study," *Journal of Chemical Physics*, Vol. 126, 2007, pp. 054706.

[32] Bergenholtz, J., Poon, W. C. K., and Fuchs, M., "Gelation in model colloid-polymer mixtures," *Langmuir*, Vol. 19, 2003, pp. 4493–4503.

[33] Chen, Y.-L. and Schweizer, K. S., "Depletion interactions in suspensions of spheres and rod-polymers," *Journal of Chemical Physics*, Vol. 117, 2002, pp. 1351–1362.

[34] Chen, Y.-L., Schweizer, K. S., and Fuchs, M., "Phase separation in suspensions of colloids, polymers and nanoparticles: Role of solvent quality, physical mesh, and nonlocal entropic repulsion," *Journal of Chemical Physics*, Vol. 118, 2003, pp. 3380–3890.

[35] Chen, Y.-L. and Schweizer, K. S., "Microscopic theory of gelation and elasticity in polymer-particle suspensions," *Journal of Chemical Physics*, Vol. 120, 2004, pp. 7212–7222.

[36] Chen, Y.-L. and Schweizer, K. S., "Collective structure and dynamics in dense colloid-rod polymer suspensions," *Langmuir*, Vol. 18, 2002, pp. 7354–7363.

[37] Chen, Y.-L., Kobelev, V., and Schweizer, K. S., "Barrier hopping, viscous flow, and kinetic gelation in particle-polymer suspensions," *Physical Reveiw E*, Vol. 71, 2005, pp. 041405.

[38] Poon, W. C. K., "The physics of a model colloid-polymer mixture," *Journal of Physics: Condensed Matter*, Vol. 14, 2002, pp. R859–R880.

[39] Dickman, R. and Yethiraj, A., "Polymer-induced forces between colloidal particles. A Monte Carlo simulation," *Journal of Chemical Physics*, Vol. 100, 1994, pp. 4683–4690.

[40] Doxastakis, M., Chen, Y.-L., and de Pablo, J. J., "Potential of mean force between two nanometer-scale particles in a polymer solution," *Journal of Chemical Physics*, Vol. 123, 2005, pp. 034901.

[41] Yethiraj, A., "Polymer melts at solid surfaces," *Advances in Chemical Physics*, Vol. 121, 2002, pp. 89–139.

[42] Eisenriegler, E., "Universal density-force relations for polymers near a repulsive wall," *Physical Review E*, Vol. 55, 1997, pp. 3116–3123.

[43] Hooper, J. B., Pileggi, M. T., McCoy, J. D., Curro, J. G., and Weinhold, J. D., "Density functional theory of simple polymers in a slit pore. II. The role of compressibility and field type," *Journal of Chemical Physics*, Vol. 112, 2000, pp. 3094–3103.

[44] Joanny, J. F., Liebler, L., and DeGennes, P. G., "Effects of polymer solutions on colloid stability," *Journal of Polymer Science: Polymer Physics Edition*, Vol. 17, 1979, pp. 1073–1084.

[45] McCoy, J. D. and Curro, J. G., "Conjectures on the glass transition of polymers in confined geometries," *Journal of Chemical Physics*, Vol. 116, 2002, pp. 9154–9157.

[46] Scheutjens, J. M. H. M. and Fleer, G. J., "Effect of polymer adsorption and depletion on the interaction between two parallel surfaces," *Advances in Colloid and Interface Science*, Vol. 16, 1982, pp. 361–380.

[47] Yethiraj, A. and Hall, C. K., "Integral equation theory for the adsorption of chain fluids in slitlike pores," *Journal of Chemical Physics*, Vol. 95, 1991, pp. 3749–3755.

[48] Surve, M., Pryamitsyn, V., and Ganesan, V., "Polymer-bridged gels of nanoparticles in solutions of adsorbing polymers," *Journal of Chemical Physics*, Vol. 125, 2006, pp. 064903.

[49] Vacatello, M., "Monte Carlo simulations of polymer melts filled with solid nanoparticles," *Macromolecules*, Vol. 34, 2001, pp. 1946–1952.

[50] Vacatello, M., "Chain dimensions in filled polymers: An intriguing problem," *Macromolecules*, Vol. 35, 2002, pp. 8191–8193.

[51] Zhang, Q. and Archer, L. A., "Monte Carlo simulation of structure and nanoscale interactions in polymer nanocomposites," *Journal of Chemical Physics*, Vol. 121, 2004, pp. 10814–10824.

[52] Smith, J. S., Bedrov, D., and Smith, G. D., "A molecular dynamics simulation study of nanoparticle interactions in a model polymer-nanoparticle composite," *Composites Science and Technology*, Vol. 63, 2003, pp. 1599–1605.

[53] Bedrov, D., Smith, G. D., and Smith, J. S., "Matrix-induced nanoparticle interactions in a polymer melt: A molecular dynamics simulation study," *Journal of Chemical Physics*, Vol. 119, 2003, pp. 10438–10447.

[54] Desai, T., Keblinski, P., and Kumar, S. K., "Molecular dynamics simulations of polymer transport in nanocomposites," *Journal of Chemical Physics*, Vol. 122, 2005, pp. 134910.

[55] Starr, F. W., Schrøder, T. B., and Glotzer, S. C., "Effects of a nanoscopic filler on the structure and dynamics of a simulated polymer melt and the relationship to ultrathin films," *Physical Review E*, Vol. 64, 2001, pp. 021802.

[56] Starr, F. W., Schrøder, T. B., and Glotzer, S. C., "Molecular dynamics simulation of a polymer melt with a nanoscopic particle," *Macromolecules*, Vol. 35, 2002, pp. 4481–4492.

[57] Starr, F. W., Douglas, J. F., and Glotzer, S. C., "Origin of particle clustering in a simulated polymer nanocomposites and its impact on rheology," *Journal of Chemical Physics*, Vol. 119, 2003, pp. 1777–1788.

[58] Pryamitsyn, V. and Ganesan, V., "Origins of linear viscoelastic behavior of polymer-nanoparticle composites," *Macromolecules*, Vol. 39, 2006, pp. 844–856.

[59] Salaniwal, S., Kumar, S. K., and Douglas, J. F., "Amorphous solidification in polymer-platelet nanocomposites," *Physical Review Letters*, Vol. 89, 2002, pp. 258301.

[60] Sinsawat, A., Anderson, K. L., Vaia, R. A., and Farmer, B. L., "Influence of polymer matrix composition and architecture on polymer nanocomposite formation: Coarse-grained molecular dynamics simulation," *Journal of Polymer Science B: Polymer Physics*, Vol. 41, 2003, pp. 3272–3284.

[61] Knauert, S. T., Douglas, J. F., and Starr, F. W., "The effect of nanoparticle shape on polymer-nanocomposite rheology and tensile strength," *Polymer Science: Part B: Polymer Physics*, Vol. 45, 2007, pp. 1882–1897.

[62] Hall, L. M., Jayaraman, A., and Schweizer, K. S., "Molecular theories of polymer nanocomposites," *Current Opinion in Solid State and Materials Science*, web published, September 23, 2009.

[63] Chen, X., Cai, J., Liu, H., and Hu, Y., "Depletion interaction in colloid/polymer mixtures: Application of density functional theory," *Molecular Simulation*, Vol. 32, 2006, pp. 877–885.

[64] Bymaster, A., Jain, S., and Chapman, W. G., "Microstructure and depletion forces in polymer-colloid mixtures from an interfacial statistical associating fluid theory," *Journal of Chemical Physics*, Vol. 128, 2008, pp. 164910.

[65] Kim, S. C. and Lee, C. H., "Depletion interactions between colloidal particles in polymer solutions: Density functional approach," *Molecular Physics*, Vol. 104, 2006, pp. 1487–1495.

[66] Ganesan, V., Khounlavong, L., and Pryamitsyn, V., "Equilibrium characteristics of semiflexible polymer solutions near probe particles," *Physical Review E*, Vol. 78, 2008, pp. 051804.

[67] Surve, M., Pryamitsyn, V., and Ganesan, V., "Nanoparticles in solutions of adsorbing polymers: Pair interactions, percolation, and phase behavior," *Langmuir*, Vol. 22, 2006, pp. 969–981.

[68] Surve, M., Pryamitsyn, V., and Ganesan, V., "Universality in structure and elasticity of polymer-nanoparticle gels," *Physical Review Letters*, Vol. 96, 2006, pp. 177805.

[69] Kyrylyuk, A. V. and van der Schoot, P., "Continuum percolation of carbon nanotubes in polymeric and colloidal media," *PNAS*, Vol. 105, 2008, pp. 8221–8226.

[70] Surve, M., Pryamitsyn, V., and Ganesan, V., "Dispersion and Percolation Transitions of Nanorods in Polymer Solutions," *Macromolecules*, Vol. 40, 2007, pp. 344–354.

[71] Kim, K., Utracki, L. A., and Kamal, M. R., "Numerical simulation of polymer nanocomposites using self-consistent mean-field model," *Journal of Chemical Physics*, Vol. 121, 2004, pp. 10766.

[72] Curro, J. G., Schweizer, K. S., Grest, G. S., and Kremer, K., "A comparison between integral equation theory and molecular dynamics simulations of dense, flexible polymer liquids," *Journal of Chemical Physics*, Vol. 91, 1989, pp. 1357–1364.

[73] Schweizer, K. S. and Curro, J. G., "Integral equation theories of the structure, thermodynamics, and phase transitions of polymer fluids," *Advances in Chemical Physics*, Vol. 98, 1997, pp. 1–142.

[74] Bockstaller, M. R., Mickiewicz, R. A., and Thomas, E. L., "Block copolymer nanocomposites: Perspectives for tailored functional materials," *Advanced Materials*, Vol. 17, 2005, pp. 1331–1349.

[75] Balazs, A. C., "Predicting the morphology of nanostructured composites," *Current Opinion in Solid State and Materials Science*, Vol. 7, 2003, pp. 27–33.

[76] Sides, S. W., Kim, B. J., Kramer, E. J., and Fredrickson, G. H., "Hybrid particle-field simulations of polymer nanocomposites," *Physical Review Letters*, Vol. 96, 2006, pp. 250601.

[77] Curro, J. G. and Schweizer, K. S., "Integral equation theory for compressible polymer alloys: Thermodynamics, scattering, and miscibility of gaussian chains," *Macromolecules*, Vol. 24, 1991, pp. 6736–6747.

[78] Honnell, K. G., Curro, J. G., and Schweizer, K. S., "Local structure of semiflexible polymer melts," *Macromolecules*, Vol. 23, 1990, pp. 3496–3505.

[79] Schweizer, K. S. and Curro, J. G., "Equation of state of polymer melts: Numerical results for athermal freely jointed chain fluids," *Journal of Chemical Physics*, Vol. 89, 1988, pp. 3350–3362.

[80] Koshy, R., Desai, T., Keblinski, P., Hooper, J., and Schweizer, K. S., "Density fluctuation correlation length in polymer fluids," *Journal of Chemical Physics*, Vol. 119, 2003, pp. 7599–7603.

[81] Fuchs, M. and Schweizer, K. S., "Structure and thermodynamics of colloid-polymer mixtures: A macromolecular approach," *Europhysics Letters*, Vol. 51, 2000, pp. 621–627.

[82] Fuchs, M. and Schweizer, K. S., "Macromolecular theory of solvation and structure in mixtures of colloids and polymers," *Physical Review E*, Vol. 64, 2001, pp. 021514.

[83] Fuchs, M. and Schweizer, K. S., "Structure of colloid-polymer suspensions," *Journal of Physics: Condensed Matter*, Vol. 14, 2002, pp. R239–R269.

[84] Khalatur, P., Zherenkova, L., and Khokhlov, A., "Aggregation of colloidal particles induced by polymer chains: The RISM integral equation theory," *Physica A*, Vol. 247, 1997, pp. 205–234.

[85] Yethiraj, A., Hall, C. K., and Dickman, R., "Interaction between colloids in solutions containing dissolved polymer," *Journal of Colloid and Interface Science*, Vol. 151, 1992, pp. 102–117.

[86] Kulkarni, A. M., Chatterjee, A. P., Schweizer, K. S., and Zukoski, C. F., "Depletion interactions in the protein limit: Effects of polymer density fluctuations," *Physical Review Letters*, Vol. 83, 1999, pp. 4554–4557.

[87] Ramakrishnan, S., Fuchs, M., Schweizer, K. S., and Zukoski, C. F., "Entropy driven phase transitions in colloid-polymer suspensions: Tests of depletion theories," *Journal of Chemical Physics*, Vol. 116, 2002, pp. 2201–2212.

[88] Shah, S. A., Chen, Y. L., Schweizer, K. S., and Zukoski, C. F., "Phase behavior and concentration fluctuations in suspensions of hard spheres and nearly ideal polymers," *Journal of Chemical Physics*, Vol. 118, 2003, pp. 3350–3361.

[89] Shah, S. A., Chen, Y.-L., Ramakrishnan, S., Schweizer, K. S., and Zukoski, C. F., "Microstructure of dense colloid-polymer suspensions and gels," *Journal of Physics: Condensed Matter*, Vol. 15, 2003, pp. 4751–4778.

[90] Hooper, J. B., "Molecular Theory of the Structure, Thermodynamics, and Miscibility of Polymer Nanocomposites," Ph.D. Dissertation, University of Illinois at Urbana-Champaign, 2005.

[91] Hooper, J. B. and Schweizer, K. S., "Contact aggregation, bridging, and steric stabilization in dense polymer-particle mixtures," *Macromolecules*, Vol. 38, 2005, pp. 8858–8869.

[92] Hooper, J. B. and Schweizer, K. S., "Theory of phase separation in polymer nanocomposites," *Macromolecules*, Vol. 39, 2006, pp. 5133–5142.

[93] Hooper, J. B. and Schweizer, K. S., "Real space structure and scattering patterns of model polymer nanocomposites," *Macromolecules*, Vol. 40, 2007, pp. 6998–7008.

[94] Zhao, L., Li, Y.-G., and Zhong, C., "Integral equation theory study on the structure and effective interactions in star polymer nanocomposite melts," *Journal of Chemical Physics*, Vol. 126, 2007, pp. 014906.

[95] Zhao, L., Li, Y.-G., Zhong, C., and Mi, J., "Structure and effective interactions in polymer nanocomposite melts: An integral equation theory study," *Journal of Chemical Physics*, Vol. 124, 2006, pp. 144913.

[96] Hooper, J. B., Schweizer, K. S., Desai, T. G., Koshy, R., and Keblinski, P., "Structure, surface excess and effective interactions in polymer nanocomposite melts and concentrated solutions," *Journal of Chemical Physics*, Vol. 121, 2004, pp. 6986–6997.

[97] Hall, L. M., "Statistical Mechanical Theory of Polymer Nanocomposites: Structure and Miscibility Studies with Various Types of Fillers," M.S. Thesis, University of Illinois at Urbana-Champaign, 2007.

[98] Hall, L. M. and Schweizer, K. S., "Many body effects on the phase separation and structure of dense polymer-particle melts," *Journal of Chemical Physics*, Vol. 128, 2008, pp. 234901.

[99] Hall, L. M., Anderson, B. J., Zukoski, C. F., and Schweizer, K. S., "Concentration fluctuations, local order and the collective structure of polymer nanocomposites," *Macromolecues*, web published, August 27, 2009.

[100] Hall, L. M. and Schweizer, K. S., "Structure and phase behavior of polymer nanocomposites with aspherical fillers," *Soft Matter*, submitted, September, 2009.

[101] Sen, S., Xie, Y., Kumar, S. K., Yang, H., Bansal, A., Ho, D. L., Hall, L., Hooper, J. B., and Schweizer, K. S., "Chain conformations and bound-layer correlations in polymer nanocomposites," *Physical Review Letters*, Vol. 2007, 98, pp. 128302.

[102] Schweizer, K. S. and Curro, J. G., "Integral equation theory of the structure and thermodynamics of polymer blends," *Journal of Chemical Physics*, Vol. 91, 1989, pp. 5059–5081.

[103] Krakoviack, V., Hansen, J. P., and Louis, A. A., "Relating monomer to centre-of-mass distribution functions in polymer solutions," *Europhysics Letters*, Vol. 58, 2002, pp. 53–59.

[104] Pagonabarraga, I. and Cates, M. E., "A practical density functional for polydisperse polymers," *Europhysics Letters*, Vol. 55, 2001, pp. 348–354.

[105] DeGennes, P. G., *Scaling Concepts in Polymer Physics*, Cornell University Press, Ithaca, 2nd ed., 1979.

[106] Frischknecht, A. L., McGarrity, E. S., and Mackay, M. E., *Macromolecules*, submitted, 2009.

[107] Sung, B. J. and Yethiraj, A., "Integral equation theory of random copolymer melts," *Macromolecules*, Vol. 38, 2005, pp. 2000–2008.

[108] Henderson, D., Duh, D.-M., Chu, X., and Wasan, D., "An expression for the dispersion force between colloidal particles," *Journal of Colloid and Interface Science*, Vol. 185, 1997, pp. 265–268.

[109] Rubinstein, M. and Colby, R. H., *Polymer Physics*, Oxford University Press, New York, 1st ed., 2003.

[110] Chuev, G. N. and Fedorov, M. V., "Wavelet treatment of structure and thermodynamics of simple liquids," *Journal of Chemical Physics*, Vol. 120, 2004, pp. 1191–1196.

[111] Zerah, G., "An efficient Newton's method for the numerical solution of fluid integral equations," *Journal of Computational Physics*, Vol. 61, 1985, pp. 280–285.

[112] Hindmarsh, A. C., Brown, P. N., Grant, K. E., Lee, S. L., Serban, R., Shumaker, D. E., and Woodward, C. S., "SUNDIALS: Suite of nonlinear and differential/algebraic equation solvers," *ACM Transactions on Mathematical Software*, Vol. 931, 2005, pp. 363–369.

[113] Peplow, A. T., Beardmore, R. E., and Bresme, F., "Algorithms for the computation of solutions of the Ornstein-Zernike equation," *Physical Review E*, Vol. 74, 2006, pp. 046705.

[114] Beardmore, R. E., Peplow, A. T., and Bresme, F., "A numerical bifurcation analysis of the Ornstein-Zernike equation with hypernetted chain closure," *SIAM Journal on Scientific Computing*, Vol. 29, 2007, pp. 2442–2463.

[115] Anderson, B. J. and Zukoski, C. F., "Rheology and microstructure of an unentangled polymer nanocomposite melt," *Macromolecules*, Vol. 41, 2008, pp. 9326–9334.

[116] Anderson, B. J. and Zukoski, C. F., "Nanoparticle stability in polymer melts as determined by particle second virial measurement," *Macromolecules*, Vol. 40, 2007, pp. 5133–5140.

[117] Kim, S. Y., Hall, L. M., Schweizer, K. S., and Zukoski, C. F., in preparation, 2009.

[118] Smith, G. D., Yoon, D. Y., Jaffe, R. L., Colby, R. H., Krishnamoorti, R., and Fetters, L. J., "Conformations and structures of poly(oxyethylene) melts from molecular dynamics simulations and small-angle neutron scattering experiments," *Macromolecules*, Vol. 29, 1996, pp. 3462–3469.

[119] Wick, C. D. and Theodorou, D. N., "Connectivity-altering Monte Carlo simulations of the end group effects on volumetric properties for poly(ethylene oxide)," *Macromolecules*, Vol. 37, 2004, pp. 7026–7033.

[120] Biben, T. and Hansen, J. P., "Phase separation of asymmetric binary hard-sphere fluids," *Physical Review Letters*, Vol. 66, 1991, pp. 2215–2218.

[121] Lekkerkerker, H. N. W. and Stroobants, A., "On the spinodal instability of highly asymmetric hard sphere suspensions," *Physica A*, Vol. 195, 1993, pp. 387–397.

[122] Roth, R., Evans, R., and Louis, A. A., "Theory of asymmetric nonadditive binary hard-sphere mixtures," *Physical Review E*, Vol. 64, 2001, pp. 051202.

[123] Hansen-Goos, H. and Roth, R., "A new generalization of the Carnahan-Starling equation of state to additive mixtures of hard spheres," *Journal of Chemical Physics*, Vol. 124, 2006, pp. 154506.

[124] Dawson, K. A., "The glass paradigm for colloidal glasses, gels, and other arrested states driven by attractive interactions," *Current Opinion in Colloid and Interface Science*, Vol. 7, 2002, pp. 218–227.

[125] Anderson, B. J., in preparation, 2009.

[126] Lu, P. J., Zaccarelli, E., Cuilla, F., Schofield, A. B., Sciortino, F., and Weitz, D. A., "Gelation of particles with short-range attraction," *Nature*, Vol. 453, 2008, pp. 499–504.

[127] Girifalco, L. A., "Interaction potential for carbon (C60) molecules," *Journal of Physical Chemistry*, Vol. 95, 1991, pp. 53705371.

Author's Biography

Lisa Michelle Hall was born in Dayton, Ohio, where she attended Archbishop Alter High School, graduating in the year 2000. She moved to Terre Haute, Indiana to study chemical engineering and chemistry at Rose-Hulman Institute of Technology. Her last two undergraduate summers were spent in Research Experience for Undergraduates programs, first with Jane Lipson at Dartmouth College and then with Ulrich Wiesner at Cornell University. She graduated from Rose-Hulman in 2004 and then began her graduate studies at the University of Illinois in Urbana-Champaign. She plans to work as a postdoctoral associate with Amalie Frischknecht at Sandia National Labs.